



HAL
open science

Contribution to the Development of Axial Flux *Machines* for Small Wind *Turbine Applications*

Mostafa Hatoum

► **To cite this version:**

Mostafa Hatoum. *Contribution to the Development of Axial Flux Machines for Small Wind Turbine Applications*. Electromagnetism. Normandie Université, 2023. English. NNT : 2023NORMLH09 . tel-04220337v2

HAL Id: tel-04220337

<https://normandie-univ.hal.science/tel-04220337v2>

Submitted on 21 Mar 2024

HAL is a multi-disciplinary open access archive for the deposit and dissemination of scientific research documents, whether they are published or not. The documents may come from teaching and research institutions in France or abroad, or from public or private research centers.

L'archive ouverte pluridisciplinaire **HAL**, est destinée au dépôt et à la diffusion de documents scientifiques de niveau recherche, publiés ou non, émanant des établissements d'enseignement et de recherche français ou étrangers, des laboratoires publics ou privés.



Normandie Université



THÈSE

Pour obtenir le diplôme de doctorat

Spécialité GENIE ELECTRIQUE

Préparée au sein de l'Université Le Havre Normandie

Contribution to the Development of Axial Flux Machines for Small Wind Turbine Applications

Présentée et soutenue par
MOSTAFA HATOUM

Thèse soutenue le 20/09/2023
devant le jury composé de

M. JEAN-PHILIPPE LECOINTE	PROFESSEUR DES UNIVERSITES, UNIVERSITE ARTOIS	Rapporteur du jury
M. PETER SERGEANT	PROFESSEUR, GHENT UNIVERSITY DE PINTELAAN (BEL)	Rapporteur du jury
M. NICOLAS ZIEGLER	DOCTEUR, ERNEO - MONTPELLIER	Membre du jury
M. DANIEL MATT	PROFESSEUR DES UNIVERSITES, UNIVERSITE MONTPELLIER 2 SCIENCES ET TECH DU LANGUEDOC	Président du jury
M. GEORGES BARAKAT	PROFESSEUR DES UNIVERSITES, Université Le Havre Normandie	Directeur de thèse
M. YACINE AMARA	PROFESSEUR DES UNIVERSITES, Université Le Havre Normandie	Co-directeur de thèse

Thèse dirigée par **GEORGES BARAKAT** (Groupe de Recherche en Electrotechnique et Automatique du Havre) et **YACINE AMARA** (Groupe de Recherche en Electrotechnique et Automatique du Havre)



Contribution au Développement des Machines à Flux Axial pour l'Éolien de Petite Puissance

Résumé :

Le travail accompli dans cette thèse traite la problématique de la conception des générateurs de petite puissance pour des applications éoliennes. Dans les premières phases de la conception, il a été nécessaire de développer des outils de pré-dimensionnement rapide de la machine tout en gardant une précision acceptable avant de vérifier les performances en utilisant une méthode plus précise comme les éléments finis. Ainsi, des outils de dimensionnement analytique et de constantes localisées ont été développés pour modéliser la machine magnétiquement et thermiquement. Pour la partie magnétique, une méthode analytique issue de la résolution formelle des équations de Maxwell a été développée, ainsi qu'un modèle de réseau de reluctance maillé, et pour la partie thermique un modèle thermique nodal. Le modèle reluctant développé a été testé sur une machine à reluctance variable à flux axial dans le cas du linéaire et non linéaire pour une version multicouche et pour une version quasi-3D. Parmi les 2 modèles, analytique et reluctant, le modèle analytique a été choisi pour le pré-dimensionnement magnétique de la machine et une topologie à flux axial à rotor interne et 2 stators à aimants montés en surface a été choisie pour cette machine. Les performances thermiques ont été évaluées par le biais d'un modèle thermique nodal, et les performances magnétiques par un modèle éléments finis. Le comportement mécanique du disque rotorique était étudié à l'aide d'un modèle éléments finis mécanique.

Mots clés : *Flux axial, Machines à aimants permanents, Machines à reluctance variable, Éolien, Modélisation multi-physique, Éléments finis 3D, Simulation mécanique*

Contribution to the development of Axial Flux Machines for Small Wind Turbine Applications

Abstract:

The work done in this thesis deals with the design of small power generators for wind turbine applications. In the early stages of the design, it was necessary to develop tools for rapid machine pre-sizing while maintaining acceptable accuracy before verifying the performance using a more accurate method such as finite elements. Thus, analytical and lumped parameter sizing tools have been developed to model the machine magnetically and thermally. For the magnetic part, an analytical method based on the formal solution of Maxwell's equations was developed, as well as a model of a mesh based reluctance network, and for the thermal part a nodal thermal model. The reluctance network model was tested on an axial flux switched reluctance machine for both linear and nonlinear ferromagnetic material and for a multi-slice version and a quasi-3D version. Between the analytical model and the reluctance network model, the analytical model was chosen for the magnetic pre-sizing of the machine and a double stator single rotor axial flux topology with surface mounted permanent magnets was chosen. The thermal performance of the machine was evaluated using a nodal thermal model, and magnetic performance was evaluated by a finite element model. The mechanical behavior of the rotor disc was studied using a mechanical finite element model.

Keywords: *Axial flux, Permanent magnet machines, Switched reluctance machines, Wind turbine, Multi-physics modeling, 3D finite elements, Mechanical simulation*

Table of Contents

General Introduction	13
Chapter 1: State of the Art Review on Axial Flux Machines.....	17
I. Introduction.....	18
II. Presentation of the Axial Flux Machine.....	18
III. Axial Flux Machine Types.....	19
1. Axial Flux Machines with Permanent Magnets	19
a) Axial-Flux Permanent Magnet Machines (AFPMs).....	19
b) Axial-Flux-Switching Permanent Magnet Machines (AFSPM)	21
c) Axial-Flux Vernier Permanent Magnet Machines (AFVPMM).....	22
2. Axial Flux Machines without Permanent Magnets	23
a) Axial-Flux Switched Reluctance Machines (AFSRMs).....	23
b) Axial-Flux Induction Machines (AFIM)	24
c) Axial Flux Wound Rotor Machines (AFWRM).....	24
3. Axial Flux Machines with additional Radial Flux Path	25
IV. Axial Flux Machine Configurations.....	26
1. Single Stator Single Rotor (SSSR).....	27
2. Double Stator Single Rotor (DSSR).....	27
3. Single Stator Double Rotor (SSDR).....	27
4. Multi Stator Multi Rotor (MSMR).....	28
5. Comparison	28
V. Recent Designs of Axial Flux Machines.....	30
VI. Materials used in Axial Flux Machines	50
1. Soft ferromagnetic materials	51
2. Ferromagnetic alloys	52
3. Soft magnetic composites (SMCs).....	52
4. Hard magnetic materials.....	54
5. Insulating materials	55
VII. Problems with Axial Flux Machines.....	55
1. Magnetic problems	55
a) Skewing	55
b) Lamination.....	56
2. Thermal problems	56
a) End windings heat	56
b) Insulation heat.....	57

c)	Demagnetization.....	57
d)	Mechanical loss	57
3.	Mechanical problems	58
a)	Axial attraction force	58
b)	Centrifugal force.....	58
c)	Vibration.....	59
VIII.	Problematic of the Thesis	59
IX.	Conclusion.....	60
	References.....	60
	Chapter 2: Multiphysics Modelling of Axial Flux Machines.....	69
I.	Introduction.....	70
II.	Analytical Modelling of Axial Flux Machines	70
1.	Assumptions and solved equations	70
2.	Solution in the different regions.....	72
a)	Region I (slots)	72
b)	Region II (slot opening).....	73
c)	Region III (air gap).....	73
d)	Region IV (magnets)	74
3.	Continuity conditions	74
d)	From region I to region II	74
e)	From region II to region III	74
f)	From region III to region IV.....	74
4.	Determination of the vector potential constants.....	75
5.	Flux & EMF	76
6.	Electromagnetic torque	77
III.	Mesh Based Generated Reluctance Network Method.....	78
1.	Overview of the modelling approach	78
a)	Flux Tube.....	78
b)	Model Equations.....	80
c)	Modeling of Sources.....	81
d)	Numbering of Blocks.....	84
e)	Boundary Conditions.....	84
f)	Motion processing	87
g)	Non-linear characteristic of ferromagnetic material.....	89
h)	Local and global quantities computation.....	92

i) Algorithm.....	93
2. Multi-slice MBGRN Modelling of Axial Flux Machines.....	102
a) Studied machine	102
b) Assessment and comparison of the multi-slice MBGRN with the full 3D FEA for the linear BH curve case	105
c) Non-linear BH curve case.....	117
d) Application of the method on a surface mounted PM machine	119
3. Quasi-3D Reluctance Network.....	120
a) Algorithm.....	120
b) Studied Machine	122
c) Error computation.....	122
d) Linear BH curve conditions.....	122
e) Nonlinear BH curve case	123
f) Q3DRN model validity evaluation by parameter variation.....	124
IV. Magnetic Finite Element Method [25][19][26].....	126
1. Maxwell's equations	126
2. Magneto-static Formulations [27][28]	126
a) Magnetic scalar formulation ϕ	127
b) Magnetic vector formulation \mathbf{A}	127
3. Magneto-dynamic Formulations [29][28].....	128
a) A-V formulation	128
b) T- ϕ formulation	129
V. Thermal Model.....	129
1. Heat Transfer Mechanisms.....	129
a) Conduction.....	129
b) Convection.....	130
c) Radiation.....	130
2. Methods of Thermal Modelling	130
3. Lumped Parameter Method.....	130
VI. Mechanical Finite Element Method [38][39][40]	132
1. Strong formulation	132
2. Weak formulation.....	133
VII. Conclusion.....	133
References	134

Chapter 3: Design of an Axial Flux Machine for Low Power Wind Turbine Applications 139

I.	Introduction.....	140
II.	3D Aspect of Axial Flux Machines.....	140
III.	Magnetic Study	141
1.	Pre-sizing and Parametric Sweep Analysis using the Analytical Model	141
2.	Validation of the Final Design Using Finite Elements	147
a)	Magnetic Flux Density	149
b)	Joule Losses	153
c)	Iron Losses.....	155
d)	Flux & EMF.....	158
e)	Electromagnetic torque & power.....	158
f)	Cogging torque	160
g)	Attraction forces	162
IV.	End Winding Inductance.....	163
V.	PM Eddy Current Loss.....	164
VI.	Thermal Study of the Designed Machine.....	170
VII.	Mechanical Study of the Designed Machine.....	171
1.	Deflection of the Rotor Disk	171
2.	Mechanical Loss.....	173
VIII.	Performance Summary	174
IX.	Conclusion.....	176
	References	176
	General Conclusion.....	181

List of Figures

Fig. 1.1: A basic axial flux machine [1]	19
Fig. 1.2: AFPM machine [3]	20
Fig. 1.3: AFSPMM [3]	22
Fig. 1.4: AFSPMM operating principal. (a) Case 1. (b) Case 2. (c) Case 3	22
Fig. 1.5: AFVPMM [30]	23
Fig. 1.6: AFSRM [3]	24
Fig. 1.7: AFIM [3]	24
Fig. 1.8: AFWR machine cross section [36]	25
Fig. 1.9: AFPM machine configurations a) SSSR. b) DSSR. c) SSSDR. d) MSMR [41]	27
Fig. 1.10: Topology of the proposed AF-SFMM in [53]	30
Fig. 1.11: Single stack AFPM machine designed in [54]	31
Fig. 1.12: proposed AFDSTPMM. (a) 2D cross-section of the machine. (b) 3D cross-section of rotor. (c) 3D cross-section of the machine. (d) 2D equivalent electromagnetic structure of the machine [56]	32
Fig. 1.13: a) 3D model of the proposed machine using a coreless rotor structure. b) Appearance of the prototype using existing SMC for the stator core. c) Manufactured stators using HB2 and two newly developed SMCs (HX3.5, HX4) [57]	32
Fig. 1.14: The internal structure of the AFRC unit [58]	33
Fig. 1.15: Exploded view of the proposed DR-HEAFPMVM. 1—Stator split-tooth, 2—stator maintooth, 3—armature windings, 4—DC excitation windings, 5—PMs, and 6—rotor back iron [59]	33
Fig. 1.16: Proposed design. (a) LR-AFPMG. (b) AFPMG [60]	34
Fig. 1.17: (a) Axial slice of air-gap area. Left: conventional case. Right: two-layer case. (b) Two-layer machine PD-2: outer layer is 1/12 model and inner layer is 1/10 model. (c) 2-D linear model of the slice at the average diameter for the baseline design. (d) 3-D model of the baseline design [61]	35
Fig. 1.18: Topology of the axial-radial flux permanent magnet machine. 1—Stator core, 2—Windings, 3—Radial PMs, 4—Radial rotor back iron, 5—Axial PMs, 6—Axial rotor back iron [62]	35
Fig. 1.19: View containing the active elements of the superconducting machine [63]	36
Fig. 1.20: (a) AFMSM topology (b) General rotor pole shape (c) Sinusoidal rotor pole shape [65]	37
Fig. 1.21: Proposed machine in [66] (a) Exploded view of the Halbach rotor (b) Non-overlapping coils on PCB	37
Fig. 1.22: Exploded view of the line-start AFPM motor [67]	38
Fig. 1.23: (a) Machine design with coreless stator windings (b) Machine prototype and its main components [68]	38
Fig. 1.24: Internal stator double external rotor AFPM machine topology [69]	39
Fig. 1.25: Structure of the rotor (half side in axial direction): (a) rotor with spoke-type (ST) permanent magnets; (b) rotor with two-layer spoke-type (TLST) permanent magnets and flux barriers. (c) Improved air gap flux density waveform at no-load [70]	40
Fig. 1.26: Three dimensional model and an NN version of the MAGNUS topology employing a reduced number of concentrated coils in combination with a very large number of rotor poles [71]	40
Fig. 1.27: (a) Commercialized generator (b) Designed axial-flux permanent magnet generator (c) Radial-flux permanent magnet generator (d) Proposed hybrid-flux PM generator	41
Fig. 1.28: Efficiency characteristics	41
Fig. 1.29: Left: cross-sectional view of the novel AMM brushless permanent magnet motor topology. Right: 3-D view of the stator core with open slots and the rotor magnet structure [73]	42
Fig. 1.30: (a) Isometric view of one pole of the proposed AFM (b) 6-4 Ferrite surface PMSM with concentrated winding (c) 24-4 Ferrite surface PMSM with distributed winding (d) 24-4 NdFeB surface PMSM with distributed winding [74]	43
Fig. 1.31: Topologies of DSAFSPM Machines. (a) Basic model. (b) Proposed model. 1-Stator. 2-Phase-group winding. 3-Rotor pole. 4-Ferrite permanent magnet [75]	44
Fig. 1.32: Magnax yokeless axial flux motor	45
Fig. 1.33: Electrical Performance of P400 R motor with 800V controller @450ARMS [79]	46
Fig. 1.34: YASA 750 structure and performance [79]	46
Fig. 1.35: Turntide's TX switched reluctance axial flux motor	47

Fig. 1.36: Motor efficiency vs torque at various speeds	47
Fig. 1.37: Stator assembly process of the surface mounted PM machine	48
Fig. 1.38: Rotor assembly process of the surface mounted PM machine	48
Fig. 1.39: Stator of the flux switching machine without magnets	49
Fig. 1.40: Winding of the flux switching machine	49
Fig. 1.41: Rotor of the flux switching machine.....	50
Fig. 1.42: Assembled flux switching machine.....	50
Fig. 1.43: Hub and shaft of the flux switching machine	50
Fig. 1.44: Classification of main types of soft magnetic materials [85].....	51
Fig. 1.45: Comparison of manufacturing processes of a magnetic circuit by sheet rolling and by powder metallurgy [85].....	53
Fig. 1.46: Wind generator prototype with teeth made of SMC material	54
Fig. 1.47: Different skewing methods employed in AFPM designs [92]	56
Fig. 2.1: Modeled pattern of the machine	71
Fig. 2.2: Flux tube [18]	79
Fig. 2.3: (a) Permeance network (b) Permeance network branch with flux source [19]	80
Fig. 2.4: RN model of a magnet [19].....	82
Fig. 2.5: MMF distribution [21].....	83
Fig. 2.6: Direction of numbering in FE method [20]	84
Fig. 2.7: Application of tangential flux conditions [19]	85
Fig. 2.8: Application of normal flux conditions [19].....	86
Fig. 2.9: Periodicity condition [19].....	86
Fig. 2.10: Anti-periodicity condition [19]	87
Fig. 2.11: Interpolation nodes and their connections [20].....	88
Fig. 2.12: Algorithm used for taking saturation into account	92
Fig. 2.13: Computation of torque using Maxwell tensor method in a meshed reluctance network [19].....	93
Fig. 2.14: Functional block diagram of the algorithm	94
Fig. 2.15: Detailed block diagram of the proposed method	95
Fig. 2.16: Different cases for the computation of clasement.....	97
Fig. 2.17: Example showing the connections of each element with delimitation of regions	98
Fig. 2.18: MMF distribution function.....	100
Fig. 2.19: Axial-field switched reluctance machine topology and multi-slice model principle.....	103
Fig. 2.20: Geometrical parameters illustrated on one magnetic pattern	104
Fig. 2.21: Winding configuration of the machine.....	104
Fig. 2.22: Magnetic flux density in the middle of the air gap for both models	106
Fig. 2.23: Self-Inductance of phase A for both models.....	106
Fig. 2.24: Stator phase currents	108
Fig. 2.25: Comparison between 2D reluctance network (slice 1) and 2D finite elemnts for magnetic flux density, phase flux and torque	110
Fig. 2.26: Comparison between 2D reluctance network (slice 2) and 2D finite elements for magnetic flux density, phase flux and torque	112
Fig. 2.27: Comparison between 2D reluctance network (slice 3) and 2D finite elements for magnetic flux density, phase flux and torque	114
Fig. 2.28: Normal and tangential magnetic flux density in the middle of the air gap at $x=0$ for both models.	114
Fig. 2.29: Electromagnetic torque for both models.....	115
Fig. 2.30: Electromagnetic torque comparison between both models for 5 slices	116
Fig. 2.31: Electromagnetic torque comparison between both models for 7 slices	117
Fig. 2.32: Radial component of air gap magnetic flux density as a function of radius and angle	117
Fig. 2.33: Normal and tangential magnetic flux density in the middle of the air gap at $x=0$ for both models incorporating saturation.....	118
Fig. 2.34: Electromagnetic torque for both models incorporating saturation	118
Fig. 2.35: Modeled half of the studied axial flux surface mounted PM machine	119
Fig. 2.36: Normal component of the magnetic flux density at the middle of the air gap at $x=0$ for both models	120

Fig. 2.37: Tangential component of the magnetic flux density at the middle of the air gap at $x=0$ for both models	120
Fig. 2.38: Connection of slices by reluctances	121
Fig. 2.39: Normal and tangential magnetic flux density in the middle of the air gap at $x=0$ for both models in linear conditions	123
Fig. 2.40: Electromagnetic torque for both models in linear conditions	123
Fig. 2.41: Normal and tangential magnetic flux density in the middle of the air gap at $x=0$ for both models in nonlinear conditions	124
Fig. 2.42: Electromagnetic torque for both models in nonlinear conditions	124
Fig. 2.43: Electromagnetic torque for $K_t=1.5$ and 2.1 in linear and nonlinear BH curve conditions	125
Fig. 2.44: Electromagnetic torque characteristic for different K_t s	125
Fig. 2.45: Conductance network for each node [35]	131
Fig. 3.1: Torque as a function of external radius R_e and internal radius R_i	143
Fig. 3.2: Total active weight as a function of external radius R_e and internal radius R_i	143
Fig. 3.3: Torque mass density as a function of external radius R_e and internal radius R_i	144
Fig. 3.4: Torque mass density as a function of stator slot height	144
Fig. 3.5: 3D view of the machine	145
Fig. 3.6: The geometrical parameters of the machine	145
Fig. 3.7: Winding configuration	145
Fig. 3.8: Axial flux magnetic gear [8]	147
Fig. 3.9: Meshing of the whole machine	148
Fig. 3.10: Meshing of the modeled part	148
Fig. 3.11: Zoom on the air gap region mesh	149
Fig. 3.12: Magnetic flux density in the magnets at no load (normal component)	150
Fig. 3.13: Magnetic flux density in the magnets at no load (tangential component)	150
Fig. 3.14: Magnetic flux density in the air gap at no load (normal component)	151
Fig. 3.15: Magnetic flux density in the air gap at no load (tangential component)	151
Fig. 3.16: Magnetic flux density in the magnets at load (normal component)	152
Fig. 3.17: Magnetic flux density in the magnets at load (tangential component)	152
Fig. 3.18: Magnetic flux density in the air gap at load (normal component)	153
Fig. 3.19: Magnetic flux density in the air gap at load (tangential component)	153
Fig. 3.20: An example of a HB, dBdt surface [11]	156
Fig. 3.21: Example of B(H) curve of M330-35A steel [11]	156
Fig. 3.22: Flux per phase	158
Fig. 3.23: EMF per phase	158
Fig. 3.24: Instantaneous torque	159
Fig. 3.25: Torque characteristic for different rotor positions	160
Fig. 3.26: Electromagnetic power	160
Fig. 3.27: Cogging torque using the analytical model	161
Fig. 3.28: Cogging torque using the finite element model	162
Fig. 3.29: Tangential magnetic flux density in the middle of the air gap at 1.5° rotor position	162
Fig. 3.30: Attraction force at no load	163
Fig. 3.31: Qualitative curves describing magnet loss variation as a function of magnet segmentation [33] ..	164
Fig. 3.32: Meshing of a magnet; (a) perspective, (b) top view, (c) bottom view	166
Fig. 3.33: Eddy current density in the magnets	167
Fig. 3.34: Density of eddy currents in magnets at the inner radius	167
Fig. 3.35: Density of eddy currents in magnets at the outer radius	168
Fig. 3.36: PM Eddy current loss variation as a function of frequency	169
Fig. 3.37: Impact of PM eddy currents on air gap magnetic flux density (normal component)	169
Fig. 3.38: Impact of PM eddy currents on air gap magnetic flux density (tangential component)	170
Fig. 3.39: Thermal nodal network	171
Fig. 3.40: The studied structure and its mesh	172
Fig. 3.41: Deflection of the rotor disk to axial attraction force	173

List of Tables

<i>Tab. 1.1: Different bearingless machine configurations</i>	20
<i>Tab. 1.2: Radial-axial flux machines found in literature</i>	25
<i>Tab. 1.3: Comparison between different AFPM Topologies [41][43][46][49]</i>	28
<i>Tab. 1.4: Comparison between NS and NN AFPM topologies [49]</i>	29
<i>Tab. 1.5: Saturation flux density B_{sat} and Curie temperature T_c for the soft magnetic materials used in electrical machines [86]</i>	51
<i>Tab. 1.6: Physical properties of common soft magnetic materials [87]</i>	51
<i>Tab. 1.7: Main physical properties of magnets proposed in [91]</i>	54
<i>Tab. 1.8: Electrical insulation classes according to the maximum temperature</i>	55
<i>Tab. 2.1: Geometrical parameters of the studied AFSRM</i>	104
<i>Tab. 2.2: Errors on important quantities for the proposed method</i>	115
<i>Tab. 2.3: Computation time comparison between both methods</i>	115
<i>Tab. 2.4: Errors on important quantities for the proposed method</i>	118
<i>Tab. 2.5: Computation time comparison between both methods</i>	119
<i>Tab. 2.6: Geometrical parameters of the studied machine</i>	119
<i>Tab. 2.7: Precision and computation time for the proposed method</i>	123
<i>Tab. 2.8: Precision and computation time for the proposed method</i>	124
<i>Tab. 2.9: Precision on torque computation and computation time (sec/resolution) comparison for the different tooth width ratios</i>	125
<i>Tab. 3.1: Dimensional Characteristics of the machine</i>	145
<i>Tab. 3.2: PM Eddy current loss for different frequencies and speeds</i>	168
<i>Tab. 3.3: Thermal conductivities of the different regions</i>	170
<i>Tab. 3.4: Thicknesses of different machine elements</i>	171
<i>Tab. 3.5: Temperatures in the different regions</i>	171
<i>Tab. 3.6: Mechanical properties used in the simulation</i>	173
<i>Tab. 3.7: Machine's performances</i>	175

General Introduction

The wind energy sector is rapidly growing, as countries around the world seek to reduce their carbon emissions and transition to cleaner, renewable energy sources with major players including manufacturers of wind turbines such as Vestas, Siemens Gamesa, and GE Renewable Energy, and developers of wind energy projects such as Iberdrola, Enel, and EDF Renewables. Significant progress is being made in the search for suitable conversion devices to make this energy more competitive as companies head towards increasing electrical energy production thus introducing new constraints such as the size of the nacelle, the maintenance of offshore wind farms and the installed power density. These new constraints give rise to the investigation of new energy conversion chains better suited to mass production by wind farms. More precisely, this concerns the search of new or relatively new generator structures and suitable gear if necessary that can meet the requirements and expectations set by this ever developing technology. In this context, it is not sufficient to study new and emerging generator topologies, but also to develop tools allowing to quickly explore several designs in the early phases of the design process while at the same time preserving an acceptable accuracy. This pre-design phase is of great importance as it depicts the path of the entire development process of the proposed solution. The research of new generator structures and the related design code are the main focus of the work done in this thesis, which consists, on one hand, in the study of the performance of an axial flux permanent magnet synchronous machine, and on the other hand in the development of a light and sufficiently precise pre-sizing tools used for analysis and exploration of potential design candidates.

In order to achieve these goals, the thesis will be divided into three chapters as follows:

In the first chapter, a state of the art review on axial flux machines is conducted where the axial flux machine concept is first presented through a simple single stator single rotor structure with permanent magnets in the rotor; the machines geometry, flux path, torque and operating principle are exposed. This is followed by a classification of machines based on the presence or not of magnets; this includes classical permanent magnet machines, flux switching machines, Vernier machines, switched reluctance machines, induction machines and axial flux machines with additional radial flux path. Another classification is also presented and is based on the number of stator and rotor disks followed by a comparison between the different configurations illustrating advantages, disadvantages and applications; the machines are classified into single stator single rotor structures, double stator single rotor structures, single stator double rotor structures and multi stator multi rotor structures. Recent axial flux machine designs found in the literature are then listed spanning different machine types and giving the reader a broader perspective on what is being designed commercially and what is being tested in research laboratories. The materials used in the design of axial flux machines are listed; these materials span soft ferromagnetic materials, ferromagnetic alloys, soft magnetic composites, hard magnetic materials and insulating materials. Magnetic, thermal and mechanical problems that arise in these machines are addressed; the problems treated are skewing, lamination, end winding heat evacuation, insulation heat evacuation, demagnetization, mechanical loss, axial attraction force, centrifugal force and vibration. Finally the problematic of the thesis is stated.

In the second chapter, an explanation of the used analytical pre-sizing model is given, where the equation to be solved in the different regions of a permanent magnet machine is stated and its solution in terms of the magnetic vector potential is given; the expressions of these vector potential is used to determine the magnetic flux density in the different regions

and then these 2 local quantities are used to determine the expressions of global quantities like flux, EMF and torque. Then, the mesh based generated reluctance network (MBGRN) method is explained illustrating the concept of flux tube, the model equations, the modelling of magnetic sources such as magnets and coils, the numbering of the reluctance blocks, the integration of boundary conditions, the method used for motion processing, modelling of the non-linear characteristic of ferromagnetic material and the equations to compute local and global quantities. The algorithm used to implement the method in MATLAB is then detailed illustrating the different steps starting from the meshing of the structure and ending with the post processing of the results. After that, a 2D multi-slice version of the method is applied to a switched reluctance machine for both linear and non-linear magnetic materials to assess magnetic flux density and torque where the precision and computation time of the method were compared to the 3D finite element method. The same process is then repeated with a quasi-3D version where the slices are connected by means of reluctances in the radial direction and the approach. Finally, the robustness of the method is tested by varying the stator to rotor tooth width ratio and computing electromagnetic torque for both linear and non-linear magnetic materials conditions where the accuracy and speed of the obtained results were compared with 3D finite elements. This is followed by an explanation of the finite elements method presenting Maxwell's equations and the different formulations used to solve them in both magneto-static and magneto-dynamic simulation set ups; these formulations are the magnetic vector potential and the magnetic scalar potential for magneto-statics and A-V and T- φ formulations for magneto-dynamics. Finally the explanation of the finite element method used in mechanical simulations is explained, exposing both strong and weak formulations used to compute the displacement that a material experiences when a force or stress is applied.

In the third chapter, the 3D aspect of axial flux machines is first presented as it is important to take it into account in any modelling approach to achieve accurate results. The methodology used in the machine design is then presented justifying the choice of the topology, the winding configuration and electrical and geometrical parameters, and the adopted design is simulated using a finite elements model in order to determine electromagnetic performance indicators; these being magnetic flux density, coil flux, back-EMF, mean power, mean torque, torque ripple, iron losses, PM Eddy current loss, mechanical loss, attraction forces. Also the analytical model was used to evaluate cogging torque and a lumped parameter thermal model was used to evaluate the temperatures in the regions of interest of the machine. An FE mechanical simulation was conducted to evaluate rotor disk deflection and finally the machine's performance indicators are summarized in a table.

The thesis ends with a general conclusion that summarizes the work carried out and outlines the research perspectives.

Chapter

1

Chapter 1: State of the Art Review on Axial Flux Machines

- 1. Introduction**
- 2. Presentation of the Axial Flux Machine**
- 3. Axial Flux Machine Configurations**
- 4. Axial Flux Machine Types**
- 5. Recent Designs of Axial Flux Machines**
- 6. Materials Used in Axial Flux Machines**
- 7. Problems with Axial Flux Machines**
- 8. Problematic of the Thesis**
- 9. Conclusion**

I. Introduction

Following the 1831 experiment by Michael Faraday that gave birth to the axial flux concept, not much has happened until the 1970's. The experiment consisted of a disk fixed on an axis having one electrical contact on its periphery and the other one on the axis. The disk is placed in a magnetic field generated by magnets in the axial direction. This concept was then abandoned, mainly because of the large attraction force between the disk and the magnets, the manufacturing difficulties and the high construction cost. Meanwhile, radial flux machines took over until recent developments in permanent magnet material, thus renewing interest in axial flux machines and opening a new field of research.

In this chapter, a study of axial flux machines is carried out through a state of the art review covering different aspects of these machines. First, the axial flux machine is presented to give a general idea of the concept. This is followed by a classification by machine type (with magnets, without magnets, with additional radial flux path) and by machine configuration (stator and rotor disk placement and number of disks). The attention is then turned to recent axial flux machine designs, showcasing both laboratory and commercial designs developed in the past 10 years. Materials used in the design of axial flux machines are listed, these materials include soft ferromagnetic materials, ferromagnetic alloys, soft magnetic composites, hard magnetic materials and insulating materials. The most common magnetic, thermal and mechanical problems that arise in axial flux machines and that can possibly degrade machine performance are then presented. Finally the problematic of the thesis is stated.

II. Presentation of the Axial Flux Machine

An axial flux machine is composed of at least one stator and one rotor and can be constructed with magnets or with no magnets at all, but windings have to be always integrated in either the stator or the rotor. From a geometrical perspective, these machines have a compact pancake form with a limited axial length and are basically 2 discs facing each other, one fixed and the other free to rotate about the machines axis. Magnetically they are distinguished by their inherent 3D flux path that is mainly axial (in the direction of the machines axis or shaft) with minor radial and tangential components, and can produce torque that is proportional to their outer diameter cubed, giving them the upper hand on radial flux machines whose torque is proportional to their outer diameter squared. They have a high power and torque density and are used in applications ranging from small power ratings to multi-megawatt ratings as those integrated in the nacelles of wind turbines.

The operating principle of axial flux machines can be explained considering the case of a surface mounted permanent magnet machine that has magnets on the rotor and windings in the stator (Fig. 1.1). In this machine, the rotor flux travels from a rotor north pole, crosses the air gap and reaches a stator tooth, then loops inside the stator yoke, exits the stator from another tooth, then enters the air gap and reaches a rotor south pole, then loops inside the rotor yoke. When the machine's windings are energized they generate a flux that crosses the air gap surface and interacts with the rotor flux to generate 2 forces: one is tangential that creates torque and the other one is axial which is responsible for the magnetic attraction between the stator and rotor discs.

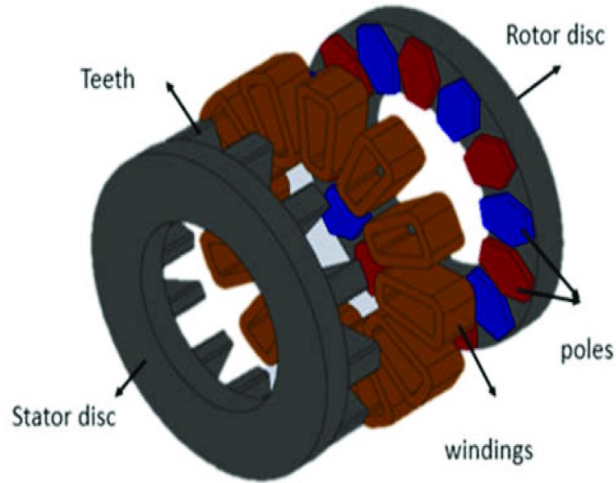


Fig. 1.1: A basic axial flux machine [1]

III. Axial Flux Machine Types

Electrical machines, in general, can be classified into DC machines, AC machines and universal machines, with different variants for each type. In the following, the most common variants of axial flux machines will be presented.

1. Axial Flux Machines with Permanent Magnets

a) Axial-Flux Permanent Magnet Machines (AFPMS)

AFPM machines (Fig. 1.2) attract the most attention from researchers with designs as early as 1987 [2]. They can be identified by the magnets in the rotor and the windings in the stator. The magnets can be either surface mounted or in a spoke configuration and even inserted in the rotor. The stator is usually made of soft magnetic composites (SMCs) or rolled laminated steel to avoid large eddy currents.

Ironless AFPM machines are suited for high-speed traction systems [3]. But at high speeds, the rotor exhibits a large centrifugal force thus requiring a carbon fiber sleeve or a retainment ring to ensure mechanical integrity. Also, it is possible to overcome the stress on PMs caused by these forces, by fixing them using stainless steel screws [4].

The power of general AFPM machines, and nearly all axial flux machines, can be calculated as follows [5]:

$$P_{em} = \frac{\pi}{480} n B_{\delta av} \frac{NI}{D_{av}} (D_o - D_i)^2 (D_o + D_i) \quad (1.1)$$

Where:

n is the rotor speed

$B_{\delta av}$ is the average magnetic flux density per pole

N is the total turns of coils

I is the current in the coils

D_o and D_i are the outer and inner diameters respectively

D_{av} is the average diameter

AFPM machines are characterized by [3]: their compactness, high power density, high efficiency, high torque-to-weight ratio and simple structure and control strategy. On the other hand they require large amounts of PMs and have a high torque ripple where reduction by teeth skewing is a challenge due to manufacturing complexity. AFPM machines find applications in EVs, HEVs, ships, and aircraft.

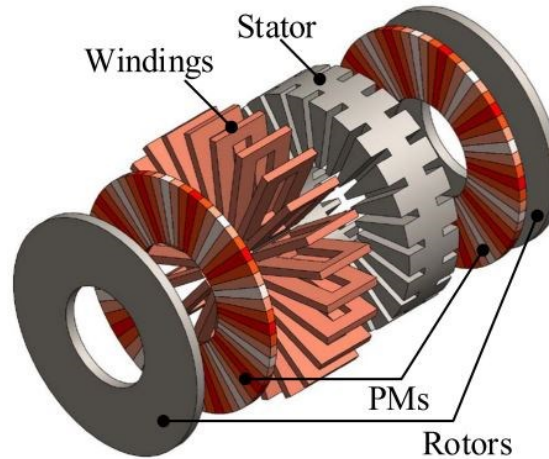


Fig. 1.2: AFPM machine [3]

AFPM machines suffer from losses and failures that are due to mechanical bearings used to hold the shaft. To overcome these challenges machines with magnetic bearings instead of mechanical bearings are proposed incorporating both motor and magnetic suspension capabilities in a single structure, thus obtaining machines with no mechanical wear, no lubrication, broader speed range and torque dense designs [6].

Applications include centrifugal pumps, ventricular assist devices, artificial hearts, reaction wheels and flywheels [7].

Classification of magnetic bearing machines is possible based on the number of actively regulated rotor degrees of freedom (DOF). Machines configurations found in literature are listed in the following table:

Tab. 1.1: Different bearingless machine configurations

DOF	Quantities Regulated	Configurations	References
1	Axial forces and motor torque	Double-sided slotted armature with either non-salient or salient rotor Single-sided slotted and coreless designs Several structures rely on a combined armature winding supplied by a single three-phase inverter to generate both the axial force and the torque	[8], [9], [10], [11], [12], [13]

2	Radial forces	Ironless stator	[14], [15], [16]
3	Axial and tilt motions	Single-sided slotted structure	[17], [18], [19]
5	Axial force and drive torque production and radial and tilt forces	Double-sided machines	[20], [21], [22], [23], [24]

b) Axial-Flux-Switching Permanent Magnet Machines (AFSPM)

AFSPM machines (Fig. 1.3), are in a way, the combination of AFPM machines and AFSRMs; PMs and windings are included in the stator and the rotor is passive with salient poles. PMs on the stator can be replaced with a high-temperature superconductor [25]. The operation principal is illustrated in Fig. 1.4 where 3 cases are present:

Case 1 (upper rotor teeth and stator teeth are aligned and lower rotor teeth and stator slots are aligned): magnetic flux mainly flows through the upper rotor teeth.

Case 2 (parts of the upper rotor teeth/lower rotor teeth and stator teeth are aligned): magnetic flux flows the upper teeth and the lower teeth.

Case 3 (lower rotor teeth and stator teeth are aligned and upper rotor teeth and stator slots are aligned): magnetic flux mainly flows through the lower rotor teeth.

The double-rotor single-stator topology has a larger back EMF, high torque, and larger axial thrust force in the rotor than the double-stator single-rotor topology [26].

Higher torque can be achieved by inserted PMs [27], also using segmented rotors with inserted PMs can increase torque density and reduce cogging torque [28]. Extending rotor teeth can also reduce cogging torque but it makes the machine heavier [29].

AFSPMs are characterized by [3]: intense air-gap flux density and improved torque if inserted PMs, the rotor can be manufactured as a whole as PMs are on the stators rather than on the rotors. On the other hand they have a high cogging torque and torque ripple and possible harmonics in flux linkage.

AFIMs, AFSRMs, and AFSPMMs are usually applied in EVs and HEVs. AFIMs and AFSRMs, the major merits are no need for PMs and low cost. Their torque-to-volume ratios are relatively small [3].

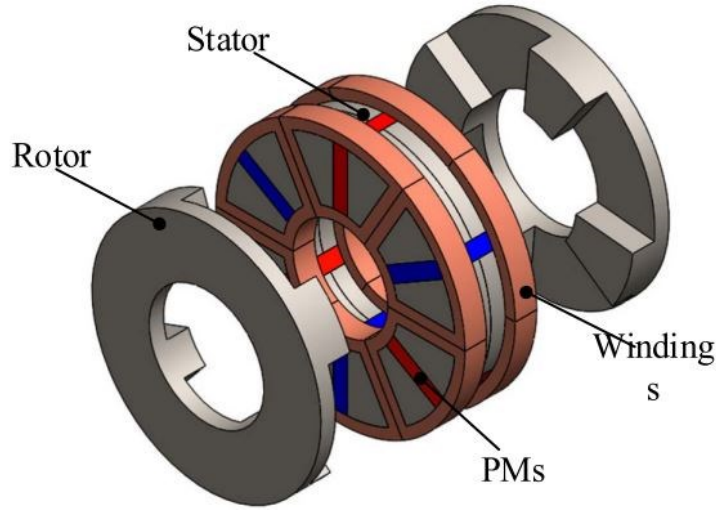


Fig. 1.3: AFSPMM [3]

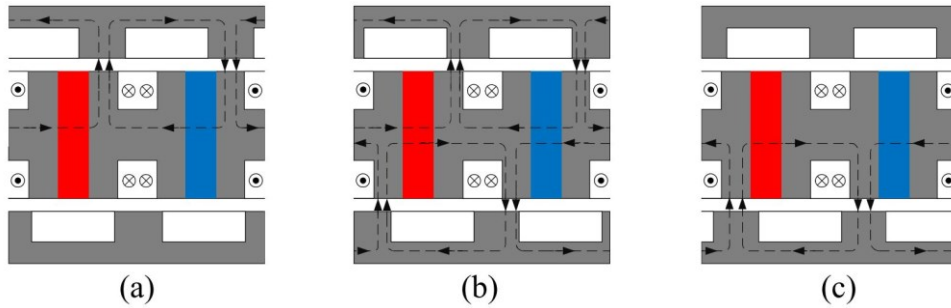


Fig. 1.4: AFSPMM operating principal. (a) Case 1. (b) Case 2. (c) Case 3

c) Axial-Flux Vernier Permanent Magnet Machines (AFVPMM)

AFVPMMs are inspired from magnetic gears. In a magnetic gear, a high-speed rotating magnetic field is produced by magnets in the air-gap and is then modulated by flux modulation segments to meet the low-speed level of the gear. The gear's PMs interact with the modulated field to produce torque. These machines can also be considered as magnetically geared machines. Integrating a magnetic gear in the structure of an electric machine increases torque density and allows for multiple rotating shafts at different speeds, thus finding applications in direct drive and EV applications.

The main elements of an AFVPMM (Fig. 1.5) are a stator with armature windings and a rotor with PMs. There is a constraint on 3 parameters that has to be met, these are the number of stator teeth N_t , the number of pole pairs of the armature windings p_s , and the number of pole pairs of PMs p_r ; these parameters have to satisfy the following condition:

$$p_s = |N_t - p_r| \quad (1.2)$$

The main working harmonics of the AFVPMM are p_r , $N_t - p_r$ and $N_t + p_r$. Having 3 working harmonics greatly improve torque density. Also, Spoke type PM is employed to concentrate magnetic flux in the air gap, thus increasing torque density.

AFVPMMs are characterized by [3]: low speed, high torque, very suitable for direct-drive systems, higher power density than AFPM machines, high space utilization. On the other

hand they have large flux leakage, low power factor, large torque ripple, not suitable for applications requiring precise control, not suitable for high speed applications.

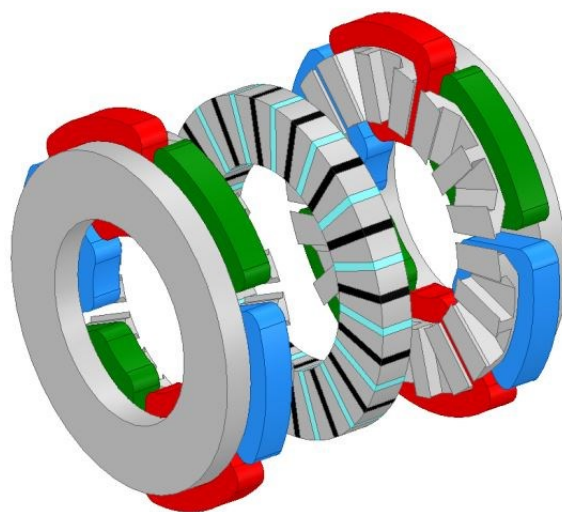


Fig. 1.5: AFVPM [30]

2. Axial Flux Machines without Permanent Magnets

a) Axial-Flux Switched Reluctance Machines (AFSRMs)

AFSRMs (Fig. 1.6) are doubly salient machines not requiring PMs, with the rotor made only of magnetic material and supported by nonmagnetic material and can be categorized into inner rotor and outer rotor types. Torque production in these machines is due to the tendency of the rotor to align itself with the minimum reluctance path, thus torque is dependent on material characteristic. This property can be exploited to improve torque by using, for example, grain-oriented steel known for its magnetic properties in the rolling direction [31]. These machines have very high torque ripple due to their salient nature but it can be reduced, for example, by displacing rotor poles [32].

AFSRMs are characterized by [3]: short flux paths reducing magnetic circuit reluctance, full use of winding flux due to increased air-gap area, robust and simple structure without PMs reducing manufacturing costs, high-speed capability and high power density making them a candidate for traction applications. On the other hand, they have high torque ripple resulting in vibration and acoustic noise and making them not suitable for applications where precise control is required. Also, torque and efficiency of AFSR machines are usually less than that of AFPM machines of the same frame size.

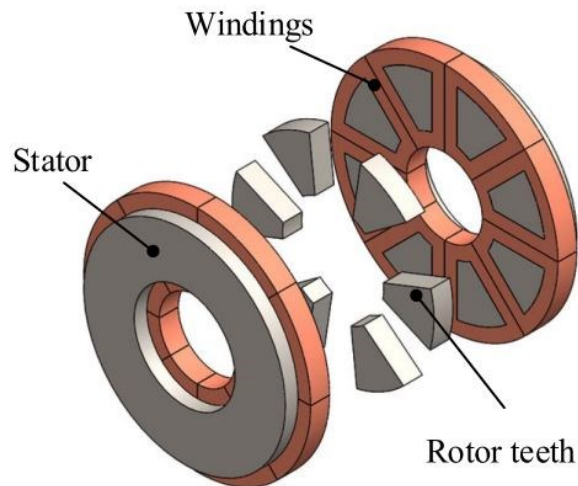


Fig. 1.6: AFSRM [3]

b) Axial-Flux Induction Machines (AFIM)

AFIMs structure consists of a rotor with armature windings and a stator with excitation windings (Fig. 1.7), and are categorized into squirrel-cage types and wound-rotor types. From [33], it is observed that the power of these machines is proportional to the product of speed, MMF and maximum air-gap flux density. These machines are suitable for electrical vehicle (EV) applications because of their minimum design volume, coverage of all torque-speed operating points [34] and the possibility to eliminate rotor back iron reducing axial force and material utilization [35].

AFIMs are characterized by [3]: cheaper manufacturing cost, no demagnetization risk, good heat dissipation, high active materials utilization, small inertia resulting in small mechanical time constant, wide speed range making them suited for medium and high-speed applications, high starting torque. On the other hand, their efficiency is lower than AFPM machines.

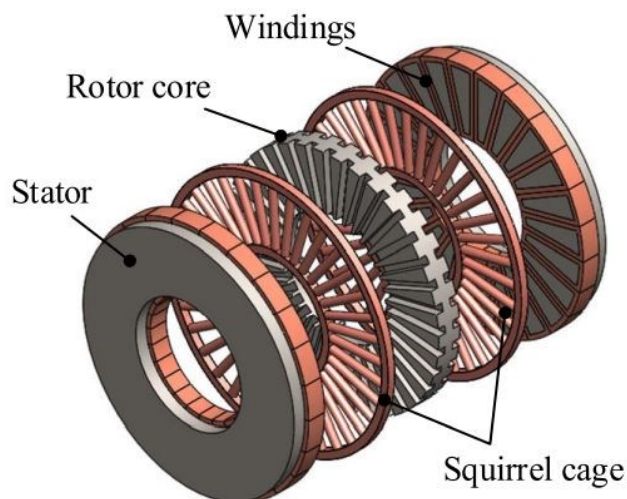


Fig. 1.7: AFIM [3]

c) Axial Flux Wound Rotor Machines (AFWRM)

AFWRMs are constructed with windings in both rotor and stator as can be seen in Fig. 1.8 showing a cross section of the AFWR machine. In these machines, the flux of the rotor poles can be controlled by varying the field current through the rotor windings, this allows to control the output voltage of the machine keeping it at a constant value [36]. AFWRMs are advantageous for controlling the inductor flux as it is not possible to use flux weakening over the whole speed range of the machine. Also, using a winding to generate flux is less costly than using a permanent magnet, but on the other hand, a winding cannot reach the energy density of a rare earth permanent magnet.

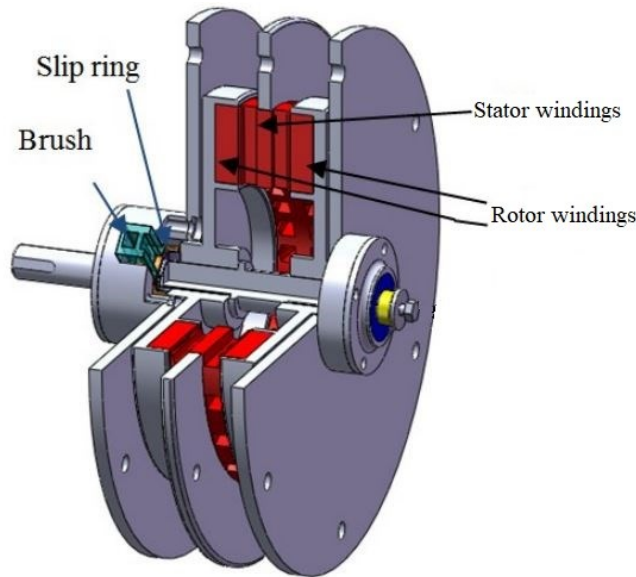


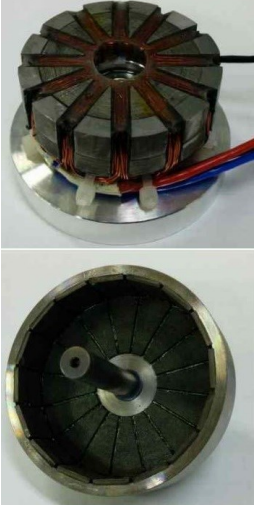
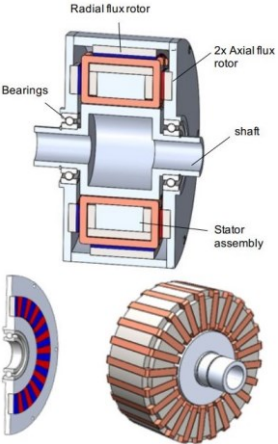
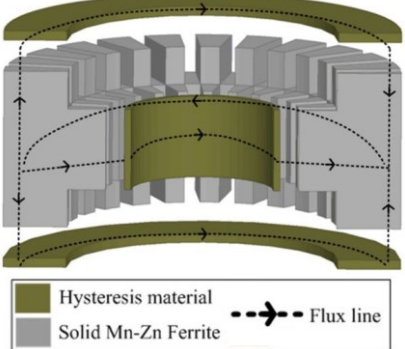
Fig. 1.8: AFWR machine cross section [36]

3. Axial Flux Machines with additional Radial Flux Path

To be able to produce torque, end-windings of RF machines require an axial flux path, and end-windings of AF machines require a radial flux path. Radial-axial flux machines use both the radial and axial flux paths for torque production, thus improving the torque density. But manufacturing is always a challenge with the conventional AF and RF lamination techniques. Some of the work reported in literature on radial-axial flux machines is summarized in the following table:

Tab. 1.2: Radial-axial flux machines found in literature

Structure	Description	Reference
<p>Radial stator (Distributed winding)</p> <p>Axial stator (Concentrated winding)</p> <p>Rotor core</p> <p>Magnetization Direction</p> <p>Nd-Fe-B</p>	<p>400 Nm/18000 RPM efficiency-shifting radial-axial hybrid permanent magnet synchronous motor that can realize two high efficiency regions of 97.6 % and 92 % at low and high speeds for EV application. The motor has two stators (radial and axial) to rotate one shared rotor. The rotor employs two combined topologies: inner</p>	<p>[37]</p>

	<p>surface-inset-mounted and outer V-shaped interior-mounted</p>	
	<p>Hybrid flux permanent-magnet (PM) machine with a high-power density that combines radial and axial flux machines with integrated windings. An overhang structure of the PMs and additional magnetic cores are employed to increase power density</p>	<p>[38]</p>
	<p>Combined radial-axial flux PM Vernier machine for a low-speed high-torque direct-drive application with a potential to generate 1.5 times the torque of the baseline machine that it replaced</p>	<p>[39]</p>
	<p>Combined radial-axial flux hysteresis machine using soft magnetic ferrite (Mn–Zn) for the stator core achieving 40% higher torque than an axial flux machine of the same form factor</p>	<p>[40]</p>

IV. Axial Flux Machine Configurations

In the previous section, axial flux machines have been classified based on the type of electromagnetic interaction between the active parts. In this section, a different way to classify these machines is presented which is based on the number of stator and rotor disks and their positioning relative to each other. Even though it is difficult to classify axial flux machines that way but we will list the most common configurations which are illustrated by the 4 categories in Fig. 1.9:

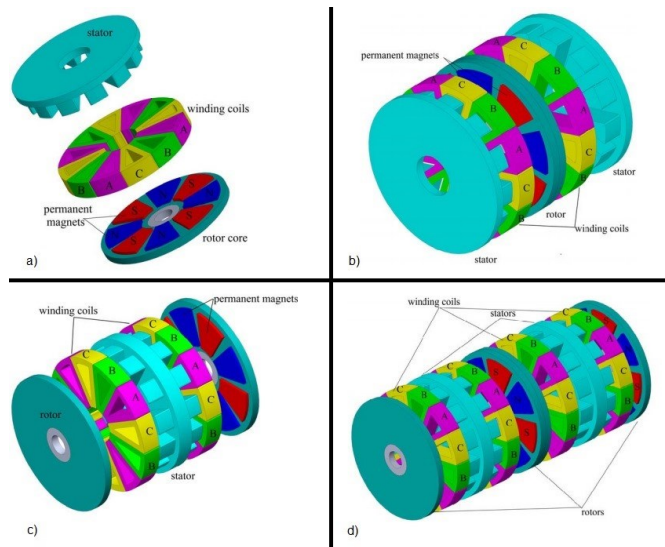


Fig. 1.9: AFPM machine configurations a) SSSR. b) DSSR. c) SSSR. d) MSMR [41]

1. Single Stator Single Rotor (SSSR)

This is the simplest structure of axial flux machines [42]. The rotor can be constructed as to have axially magnetized permanent magnets glued on its surface or buried inside it and arranged in an N-S alternating manner; The stator can be cored or coreless and can be slotted or slot-less [43]. The coreless configuration eliminates iron losses and cogging torque making it suitable for low wind speed power generation applications, it also reduces the complexity of manufacturing as does the slot-less configuration [44]. The compactness and high torque of the SSSR machine makes it a good candidate for industrial traction, servo electromechanical drives, military, transportation industries, and gearless elevators [45]. Its major drawbacks are low power and imbalanced axial force between stator and rotor [46].

2. Double Stator Single Rotor (DSSR)

Also called internal rotor machine, it's configured with a rotor sandwiched between 2 stators that can be slotted (SS type) or slot-less (NS-type) [47]. The stator can also be cored or coreless; Slotted stators reduce air gap length, thus increasing flux density and reducing required PM and machine cost, but at the same time they increase torque pulsations (which can be reduced by rotating a stator with respect to the other) as well as mutual and leakage inductances; Windings in slot-less stators are gramme type or air gap winding and in slotted stators distributed or concentrated pole windings; Magnets can be surface mounted (increasing power density and reducing machine axial length) or inserted into the rotor [43]. Interior PM configurations have higher leakage flux of PM ends as well as a higher armature reaction than surface mounted ones but better protects PMs against mechanical impact, wear, and corrosion [48]. Flux can cut through the rotor disk or flow circumferentially along it [41]. The steel rotor disk can be eliminated based on main flux path [48]. Axial forces between the stator and rotor are equilibrated since the rotor is at equal distance from both the stators [46].

3. Single Stator Double Rotor (SSDR)

Also called internal stator machine, it's configured with a stator sandwiched between 2 rotors that can be slotted or slot-less. The flux flows either axially through the stator or circumferentially in the stator yoke. In a slot-less machine short end windings are observed, (resulting in reduced copper loss and better heat dissipation) and leakage and mutual inductances are lower thus eliminating flux ripple, cogging torque, high-frequency rotor loss, and stator teeth (recognized as slot effects) [41]. Concentrated pole windings are used in SSDRs [43]. Slotted SSDRs can have an NN type TORUS or an NS type TORUS PM arrangement. In the first arrangement, poles from either rotor of the same magnetic orientation face each other and in the second, poles of opposite orientation face each other. In NN structure, the winding is short in axial and radial directions and thus stator yoke is thicker [41]. In NS structure, the flux is completely axial and thus stator core can be eliminated, also iron and copper losses are lower and power density is higher [46]. Rotor back iron in the NS type is much smaller than the NN type resulting in higher torque densities (torque quality can be improved in NN type by displacement of stator and magnets positions) [49]. Drum windings are required for NS configuration increasing end winding length and external diameter [50]. Magnets can be glued on the surfaces of both rotor disks in an alternating NS arrangement or glued so as to have an all N arrangement on one disk and an all S arrangement on the other [43]. When less cogging torque and torque ripple are tolerated, it is preferred to use coreless SSDRs [41], they could attain a very high efficiency when using strong PMs due to the absence of iron loss.

4. Multi Stator Multi Rotor (MSMR)

An MSMR configuration is obtained by stacking different DSSR or SSDR machines on the same mechanical shaft, thus enhancing torque and power density without increasing machine diameter. MSMR designs can be slotted or slot-less, cored or coreless, NN or NS topologies [41]. Winding configuration is important to achieve sinusoidal EMF and is dependent on the application. In direct-driven applications, tooth concentrated winding is more efficient than distributed winding because it results in regular and short coil ends, less winding losses and reduced structure size [43]. MSMR machines are used for ship propulsions, pumps, and high-speed PM generators [51].

5. Comparison

The following tables compare the different axial flux machine configuration stated above.

Tab. 1.3: Comparison between different AFPM Topologies [41][43][46][49]

Topology	Advantages	Disadvantages	Applications
SSSR	Simple and easy to manufacture-design/Efficiency similar to DSSR and SSDR/Space utilization lower than DSSR and SSDR/lowest rotor back-iron thickness and highest operating speed range- flux weakening capability amongst SSSR, DSSR and SSDR	Low Power Production/High attraction forces between the stator and rotor/Highest leakage flux, armature reactance and inductance amongst	Low Power Applications

		SSSR, DSSR and SSDR	
DSSR	Rotor core can be eliminated since the flux path is not circumferential/Manufacturing is simpler and easier than SSDR/Since the rotor is in the middle the forces of attraction between the stator and rotor are equilibrated/Higher torque density/PMS protected against mechanical impact, wear and corrosion/More fault tolerant characteristics/The slotted structure has a lower copper loss due to smaller end windings and better flux guides/Cooling system better than SSDR/Smaller size and lower weight than SSDR counterpart/Power factor higher than SSSR/Highest torque density amongst SSSR, DSSR and SSDR	High Copper Losses due to long end windings/Higher inductance is produced which leads to reduced efficiency/Higher leakage flux and armature reaction	Low to medium power applications
SSDR	Lower iron and copper losses/Slotted two stator single rotor has the highest torque and power densities, high torque to weight ratio and high efficiency than any other structures/The rotation of fans around the stator windings work as a cooling fan for the windings/More space is available for winding than DSSR/No cogging torque/Relatively low moment of inertia/Smother transient operation/Power factor higher than SSSR	Effective air gap area is larger than DSSR machine/Attraction forces of are larger	Low to medium power applications
MSMR	High Power can be produced within same radial length of the machine	Axial length of the machine is increased	High power applications

Tab. 1.4: Comparison between NS and NN AFPM topologies [49]

Topology	NS DSSR/SSSR	NN DSSR/SSSR
Rotor/stator back-iron	+	++
Torque density	++	+
Inductance	++	+
Reluctance path length	++	+

V. Recent Designs of Axial Flux Machines

Axial flux machines have been a hot topic of interest in the recent years due to the progress made in the fabrication of rare earth magnets. Consulting the literature, several designs can be found that spans all kinds of axial flux structures and covers different machine types.

In [52] the authors design a 3 phase 12-slot/8-pole switched reluctance machine (SRM) and compares its torque ripple with its 6-slot/4-pole counterpart. The authors also compare its weight/power ratio and weight/torque ratio with other motor drives commonly used in electric vehicle (EV) applications. They concluded that the proposed SRM has a lower torque ripple than the 6/4 variant and a lower weight/power ratio and weight/torque ratio than other motor drives.

In [53] Qin *et al.* propose a novel axial field switched flux memory machine (AF-SFMM) as shown in Fig. 1.10 and analyses it by a combined analytical method (quasi-3D finite element method with a magneto motive force–permeance-based method, and a virtual-linear hysteresis model for the magnets). The authors claim that the design benefits from good heat dissipation, high rotor robustness, and improved power density compared with conventional axial flux permanent magnet (AFPM) machines with rotor side magnets; they also claim that the proposed machine can flexibly regulate air gap flux as a result of using low coercive force permanent magnets (PM) materials.

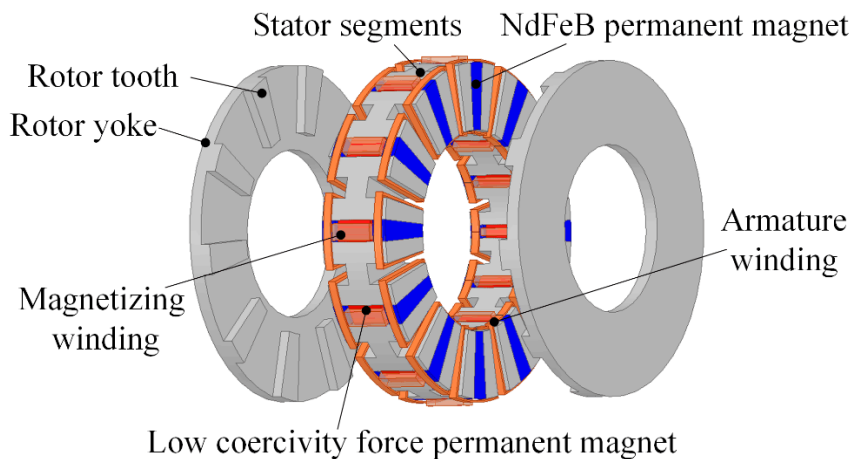


Fig. 1.10: Topology of the proposed AF-SFMM in [53]

The authors in [54] designed two single stack AFPM machines with and without gap between rotor poles respectively (Fig. 1.11) using the Diameter to Length (D^2L) method. Both machines have the same output power of 1469.64W. Power fluctuates in the single stack AFPM machine without gap, Back EMF's are the same for both machines at 140V and finally magnetic flux density is higher in the machine without gap (1.96T) than in the machine with gap (1.495T).

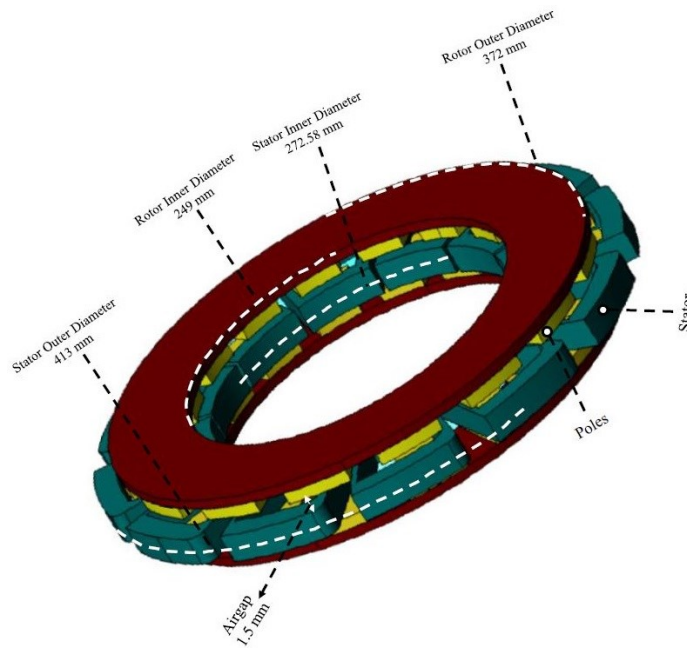


Fig. 1.11: Single stack AFPM machine designed in [54]

Ismagilov *et al.* [55] compared various axial flux electrical machines by means of numerical simulation and they concluded that ironless axial flux machines with Halbach array have the smallest weight of active parts amongst axial flux electrical machines.

Zhao *et al.* [56] present a novel axial-flux dual-stator toothless permanent magnet machine (AFDSTPMM) for flywheel energy storage (Fig. 1.12). The machine's rotor consist of a flywheel and a PM array linked together by a core (Fig. 1.12b). Parameters related to stator windings and PMs were optimized and performance was evaluated and compared with 2 other machines having a Halbach array rotor and a spoke PM rotor respectively. Results showed a higher back EMF for the proposed model than for the other 2 configurations (4.51V for Halbach, 4.46V for spoke and 5V for the proposed machine). Average torque of the proposed machine was also higher than the other 2 machines (4.85N.m for Halbach, 4.76N.m for spoke and 4.98N.m for the proposed machine).

Tsunata *et al.* [57] proposes a coreless rotor axial flux machine (Fig. 1.13) where permeability does not easily affect torque. Sensitivity to material properties is investigated through simulation of machines with different virtual soft magnetic composite (SMC) materials having different iron loss and permeability. The obtained results are then used to extract guidelines for developing SMC material, which are used to improve efficiency of axial flux machines. Finally, and by following the obtained guidelines, the authors develop 3 prototypes; 2 having stators constructed with new SMCs (HX3.5 and HX4) and 1 with conventional SMC stator (HB2). Efficiencies of all 3 machines are evaluated for 6 operating points. The axial flux machine with HX4 SMC achieves an efficiency of over 90% over a wide operating range, with the highest efficiency being 96%.

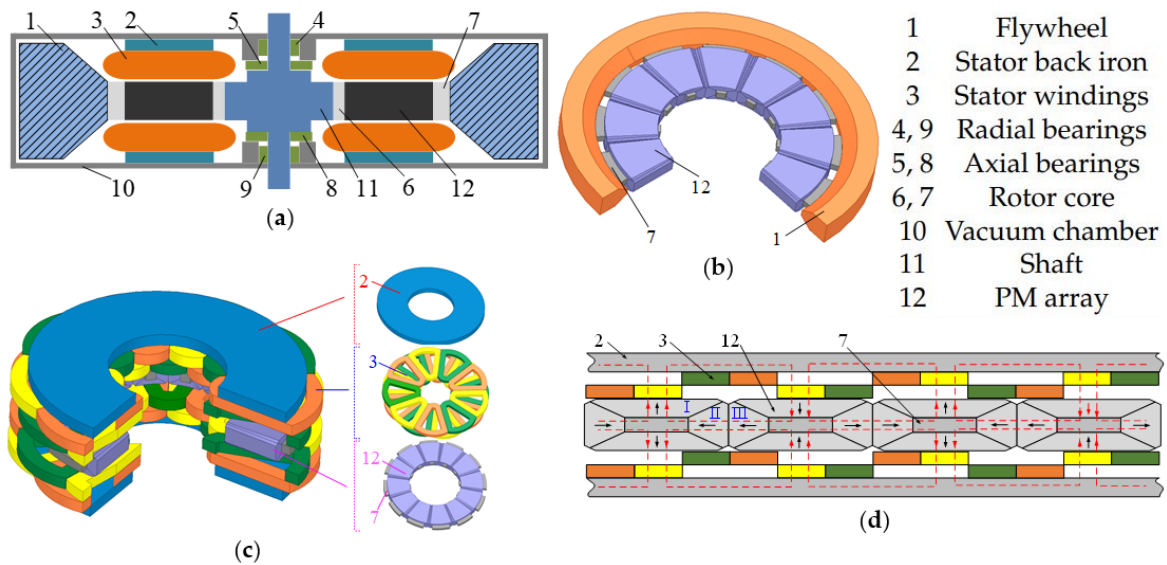


Fig. 1.12: proposed AFDSTPMM. (a) 2D cross-section of the machine. (b) 3D cross-section of rotor. (c) 3D cross-section of the machine. (d) 2D equivalent electromagnetic structure of the machine [56]

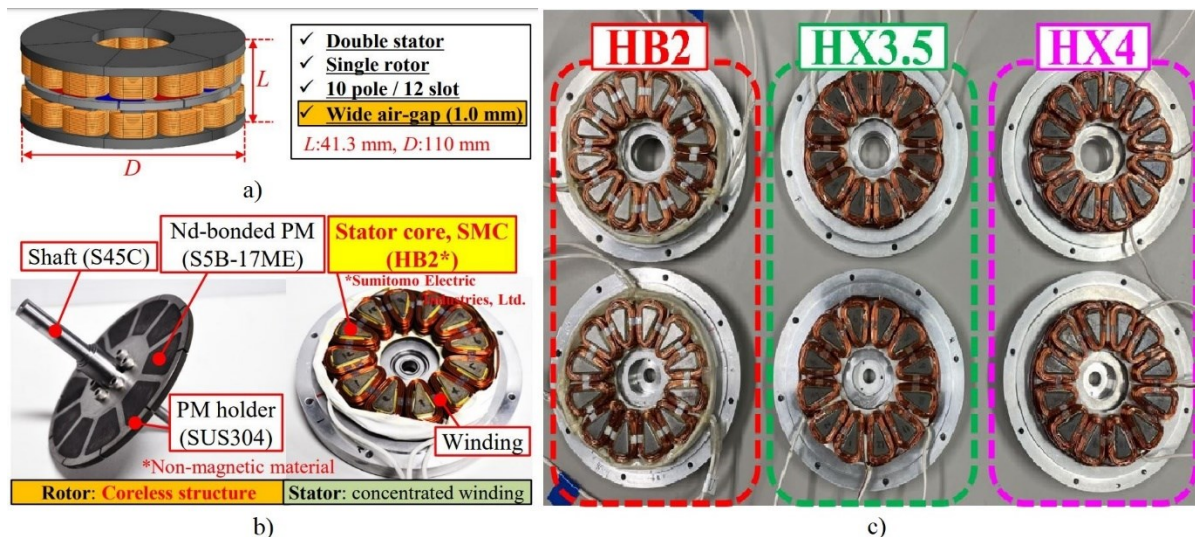


Fig. 1.13: a) 3D model of the proposed machine using a coreless rotor structure. b) Appearance of the prototype using existing SMC for the stator core. c) Manufactured stators using HB2 and two newly developed SMCs (HX3.5, HX4) [57]

In [58], the authors present an optimized design a novel 1500 W axial flux machine consisting of 1 stator and 2 successive rotors as indicated in Fig. 1.14 for a special hybrid electric vehicle arrangement known as a four-quadrant rotary converter. Optimization of permanent magnets' material, shape, and thickness was performed through 3D FEM simulations in the RMXprt/Maxwell environment. The results show an increase in the overall theoretical efficiency of the outer rotor unit from 90.2% to 94.4% following the optimization.

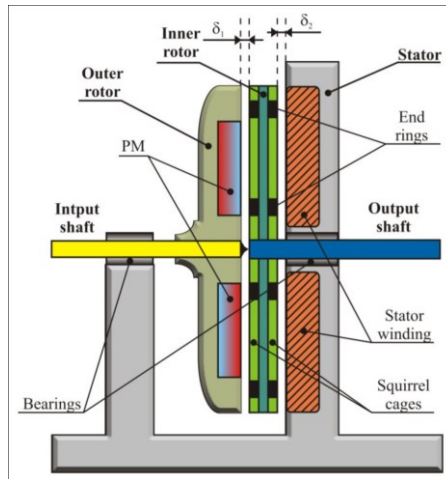


Fig. 1.14: The internal structure of the AFRC unit [58]

Jia *et al.* [59] propose a new dual-rotor hybrid-excited axial-flux permanent magnet vernier machine with modular stator and consequent-pole PM rotor (Fig. 1.15) for low-speed, high torque density applications combining yokeless and segmented armature Torus NS configuration and split-teeth stator cores. The tooth-wound non-overlapping armature windings and direct current (DC) excitation windings are, respectively, arranged in stator main-teeth and split-teeth to obtain the modulated and adjustable air-gap flux densities, resulting in high torque density and outstanding flux-weakening capability also increasing the space utilization ratio to enable flux regulation without decreasing torque capability. It has been found that the DC excitation winding can effectively weaken the amplitude of the armature phase flux linkage almost linearly by bypassing the main flux, and by comparing three pole ratios (PRs), it is concluded that the design with the PR of 8/1 possesses higher torque density (up to 39.3 kNm/m³), higher machine efficiency (up to 94%), and a significant flux-weakening ratio (up to 77%) throughout the flux-weakening regions.

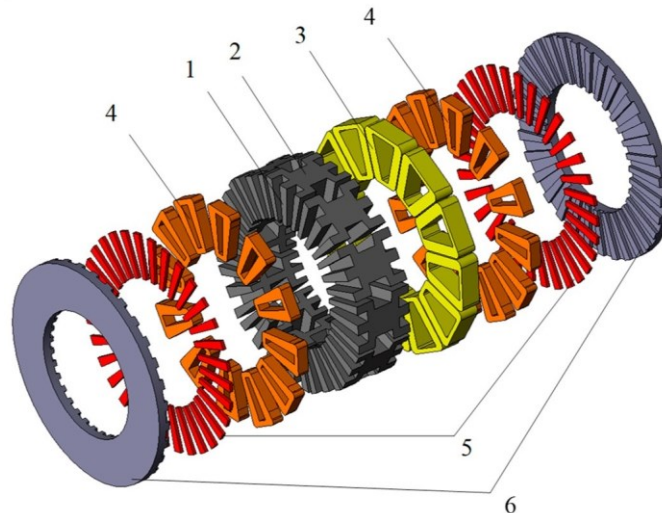


Fig. 1.15: Exploded view of the proposed DR-HEAFPMVM. 1—Stator split-tooth, 2—stator maintooth, 3—armature windings, 4—DC excitation windings, 5—PMs, and 6—rotor back iron [59]

[60] proposes a linear-rotating axial flux permanent magnet generator (LR-AFPMG) for direct drive wave energy conversion (DDWEC) combining the merits of magnetic lead

screw and axial flux generator (Fig. 1.16). Four AFPMG configurations were compared (12s10p, 12s11p, 12s13p, 12s14p) on the basis of average torques, cogging torques and on-load back EMFs, and the results show that the output voltage and power density of the power generation system can be improved using this topology and 12s13p configuration is an ideal candidate for DDWEC.

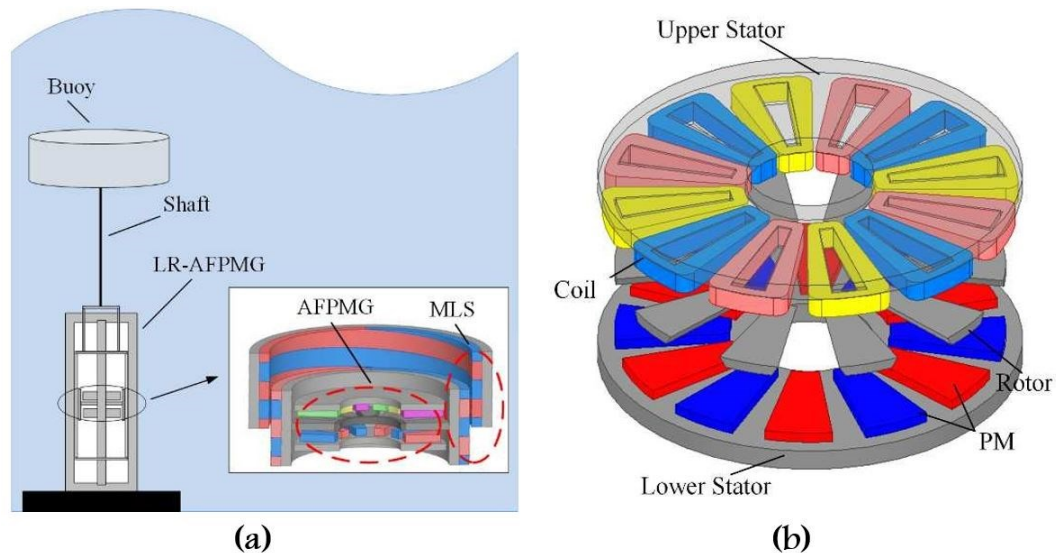


Fig. 1.16: Proposed design. (a) LR-AFPMG. (b) AFPMG [60]

Zhou and Gerling [61] propose a multi-layer structure that adopts concentric rings consisting of multiple layers instead of the conventional single layer. The authors compare the proposed structure with a conventional axial flux machine (Fig. 1.17) marking an improvement in output power density, compactness and constant power speed range. The air-gap area of the proposed structure can be extended to the complete inner radial space except the necessary area for end winding and shaft. Compared to a conventional axial flux machine, the output power was increased by 7%, the usage of rare-earth magnets was reduced by 12% and torque density was increased by 16%. The results of a study on a two layer machine showed that the speed range and output power on higher range haven been significantly improved (3.4 time increase on speed and 2.4 times on power).

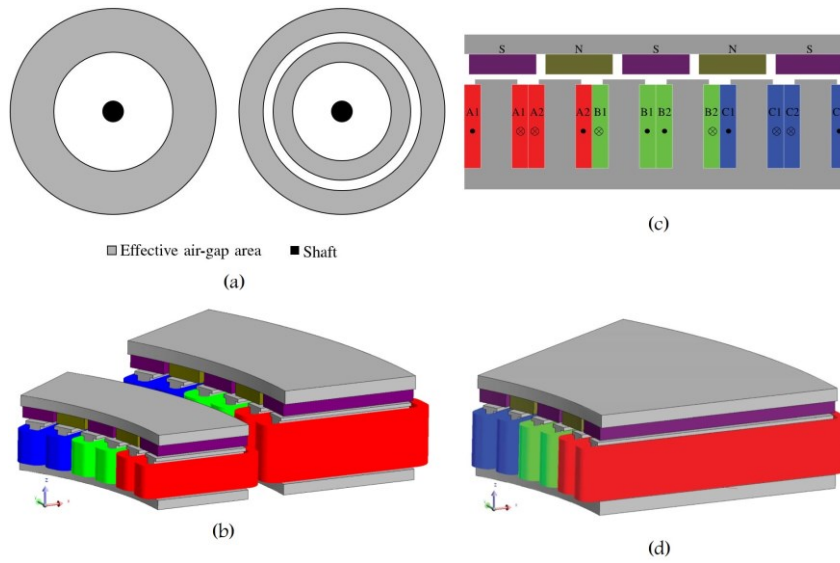


Fig. 1.17: (a) Axial slice of air-gap area. Left: conventional case. Right: two-layer case. (b) Two-layer machine PD-2: outer layer is 1/12 model and inner layer is 1/10 model. (c) 2-D linear model of the slice at the average diameter for the baseline design. (d) 3-D model of the baseline design [61]

Huang *et al.* proposed in [62] a novel axial-radial flux permanent magnet machine with Halbach-Array PMs (Fig. 1.18) achieving a high torque density and improving copper utilization. The radial rotor balances axial forces, preventing tilt and deformation of axial rotors and the Halbach-Array PMs suppress air-gap flux density harmonics and reduces attraction forces on axial rotors. Comparison results with a radial flux and an axial flux machine showed that the proposed structure had the highest torque, the highest torque density and the highest back-EMF. On the other hand it had the highest cogging torque, the highest back-EMF THD, the second highest torque ripple after the radial flux machine and the lowest torque-to-PM volume.

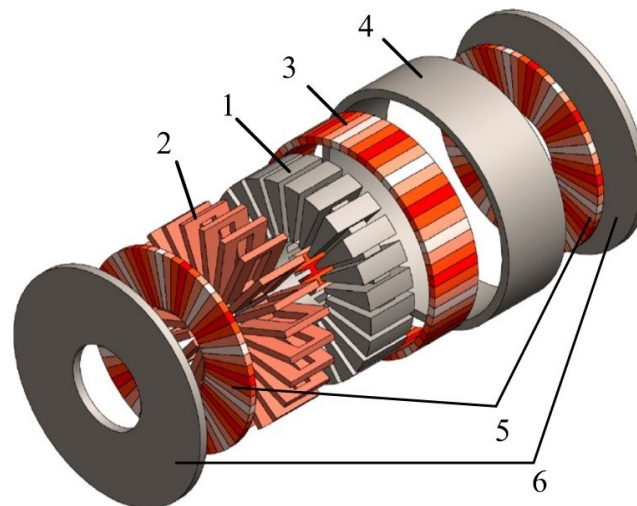


Fig. 1.18: Topology of the axial-radial flux permanent magnet machine. 1—Stator core, 2—Windings, 3—Radial PMs, 4—Radial rotor back iron, 5—Axial PMs, 6—Axial rotor back iron [62]

Colle *et al.* present in [63] and [64] the design and test of a 50 kW 5000 RPM superconducting aircraft generator (Fig. 1.19). The design steps included electromagnetic design, thermal design and superconducting system optimization. This latter was performed for the 50 kW machine as well as for a 1 MW machine. As a result the highest power-to-mass ratio is obtained with an operating temperature of 66 K for the 50 kW machine (0,6 kW/kg) and at 50 K for the 1 MW machine (6 kW/kg). It was concluded that the cooling temperature (depicting the mass of the machine and its cooling system) is dependent on the power of the machine. Also, the authors observed that the superconducting technology is more interesting for a MW-class machine as the mass of the cooler doesn't increase a lot with power (50 kg for 50 kW and 80 kg for 1 MW).

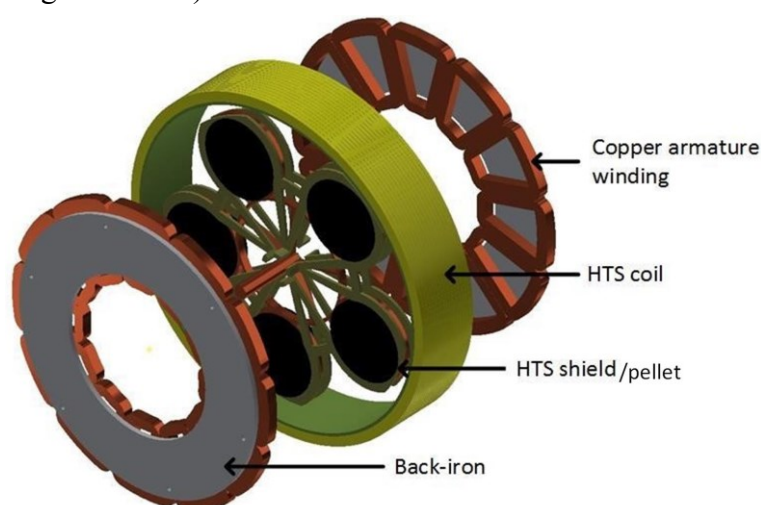


Fig. 1.19: View containing the active elements of the superconducting machine [63]

Baloch *et al.* present in [65] an axial flux dual stator flux modulating synchronous machine with a non-overlapped concentrated armature winding on the upper stator and field winding on the lower one (Fig. 1.20). This machine was compared to a radial flux machine where the armature and field windings are employed on a single stator. Compared to the radial flux machine, fill factor is less constraining due to the presence of 2 stators, current density of the proposed machine can be doubled, the rotor does not need back iron and the torque to volume ratio is higher. Comparing trapezoidal and sinusoidal rotor poles, it was concluded that the machine with trapezoidal shape rotor pole has the higher torque density (20.9 kNm/m³ for trapezoidal and 15.1 kNm/m³ for sinusoidal) but also the higher torque ripple (12% for trapezoidal and 8.5% for sinusoidal), on the other hand, the machine with the sinusoidal rotor poles had a lower cogging torque (7.8 N.m for sinusoidal and 13.8 N.m for trapezoidal) and torque ripple but also a lower torque density, so a compromise needs to be found. As for efficiency, the trapezoidal rotor pole gave a better machine efficiency than the sinusoidal pole (80.4% for trapezoidal and 75.5% for sinusoidal). It was also observed that the speed of the machine can be increased by adjusting the field current.

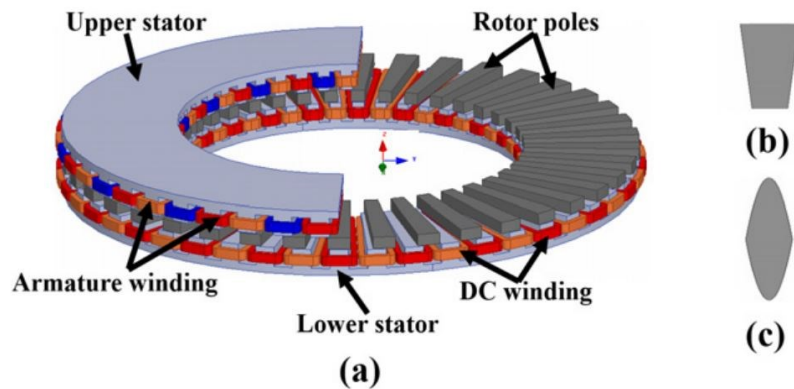


Fig. 1.20: (a) AFMSM topology (b) General rotor pole shape (c) Sinusoidal rotor pole shape [65]

Neethu *et al.* [66] propose a novel coreless single-sided axial flux motor with 12 layer non-overlapping, wave-type, distributed printed circuit board (PCB) winding for the stator and completely buried Halbach magnets in the rotor for high speed, low power application (Fig. 1.21). PCB technology is adopted for a uniform distribution in phase winding thus minimizing back-EMF harmonics. Protection of magnets against centrifugal forces and corrosive environment is assured using high strength, corrosion resistant material for rotor core. Analysis and optimization of the machine resulted in a design 96% efficient, developing an average torque of 0.02 N. at 30000 RPM.

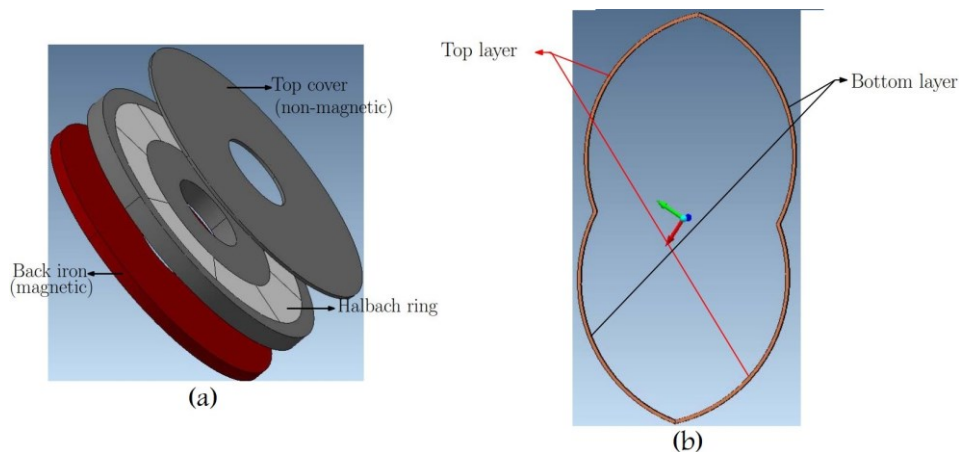


Fig. 1.21: Proposed machine in [66] (a) Exploded view of the Halbach rotor (b) Non-overlapping coils on PCB

In [67], a 1HP/1500RPM single rotor single stator axial-flux permanent-magnet synchronous motor with a novel line-starting capability using an induction cage is designed and analyzed (Fig. 1.22). The proposed design is compared with 3 commercial induction machines (of efficiency classes IE2, IE3 and IE4), 1 commercial line-start permanent magnet (LSPM) machine (IE4 efficiency class) and 1 line-start radial flux permanent magnet (RFPM) machine. Results show that the designed machine, at its rated power, has a higher efficiency than these 5 machines and a lower cost than the LSPM and the RFPM. Also, the rating of the machine could be increased by adopting a double stator or a double rotor configuration. On the other hand, the RFPM machine showed better dynamic performance than the designed axial flux one.

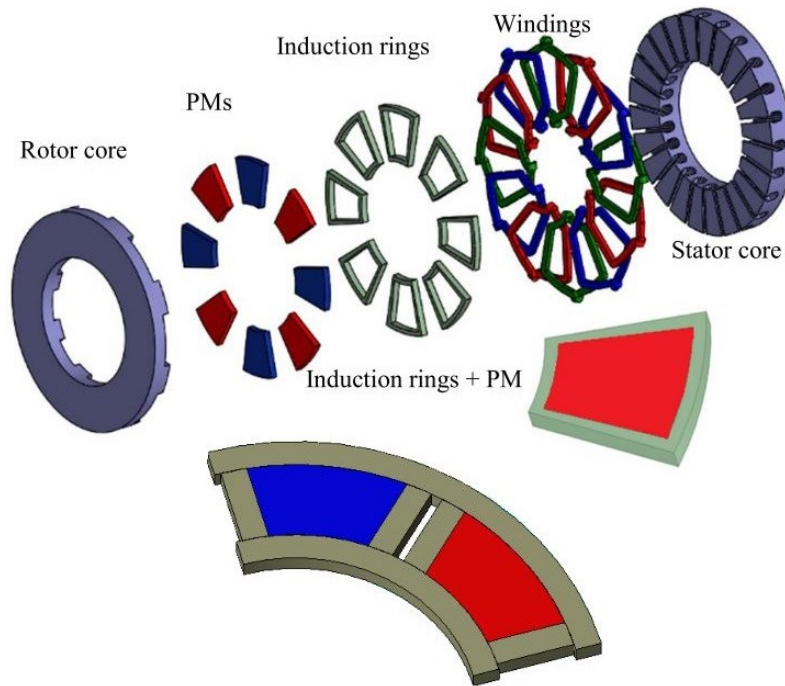


Fig. 1.22: Exploded view of the line-start AFPM motor [67]

In [68], the authors design and test a 300W/300RPM double rotor internal stator axial flux permanent magnet generator with coreless non overlapping concentrated windings (Fig. 1.22) using a 2-D analytic model, and an analytical formula for the winding factor. Air-gap magnetic fields, no-load back EMF, electromagnetic torque, and efficiency are calculated using this method. Response surface methodology was used to optimize machine parameters. The authors suggest that this method is suitable for all kinds of coreless concentrated winding structures. The proposed method was verified against 3D FEM and experimental results and shows good agreement. Results show that the efficiency of the built prototype is somewhere near 90%.

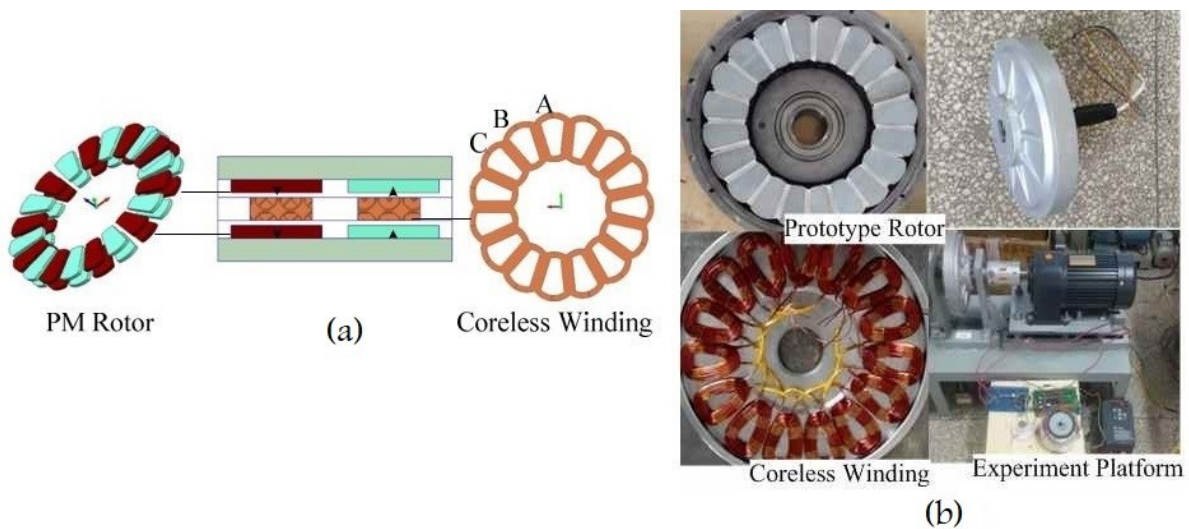


Fig. 1.23: (a) Machine design with coreless stator windings (b) Machine prototype and its main components

[68]

The authors in [69] optimize the volume of 2 internal stator twin external rotor AFPM machines for direct drive in-wheel motor of a solar-powered electric vehicle (Fig. 1.24). The first machine has a distributed winding at the stator while the second has a toroidal winding. Optimization was performed using a gradient-based method employed on a non-linear 2D equivalent model which couples a magnetostatic and a steady-state thermal model based on an isogeometric analysis (IGA) approach. The results were verified against 3D FEM for the torque calculation and 2D FEM for the coil temperature showing good agreement (<5% discrepancy for torque and 1% discrepancy for coil temperature). As a result, the machine with distributed winding has 24% higher power density than the toroidal winding machine, however the latter showcases 1.2% better efficiency (distributed has a power density of 3.17 W/cm³ at an efficiency of 96.08% and toroidal has a power density of 2.55 W/cm³ at an efficiency of 97.25%).

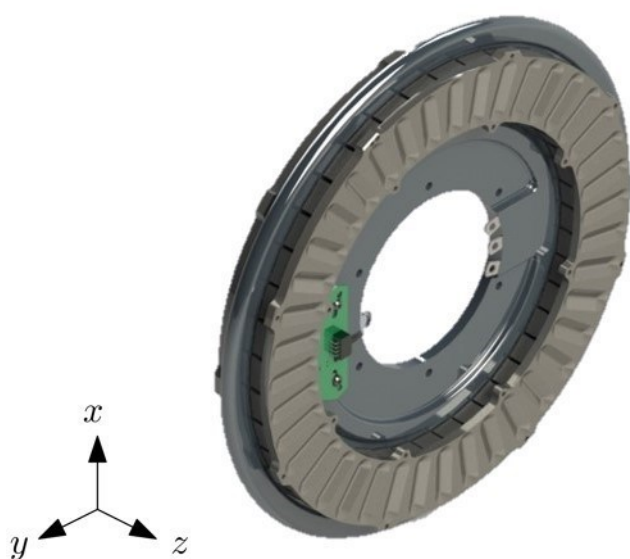


Fig. 1.24: Internal stator double external rotor AFPM machine topology [69]

Chai *et al.*[70] present the THD optimization of a two-layer spoke-type (TLST) axial flux interior permanent magnet (AFIPM) machine with flux barriers (Fig. 1.25b) which optimize the air gap flux density without changing the surface of the rotor. The proposed design is compared with a spoke type (ST) AFIPM (Fig. 1.25a) and optimization is based on a combination of a 2D magnetic equivalent circuit and an idealized and improved air gap flux density waveform (Fig. 1.25c). Results were compared to 2D FEM for THD calculation and the error on THD was 0.5%. Results show that both machines have a fundamental amplitude of air gap flux density of 1.08T, but the THD of the ST AFIPM is 16.6%; it is 9.2% lower for the TLST AFIPM machine. From 3D FEM simulations, it was observed that the THD on back-EMF is 7.5% for the ST AFIPM and 5.35% for the TLST AFIPM machine, thus confirming optimization effects on air gap flux density and stator iron losses indirectly.

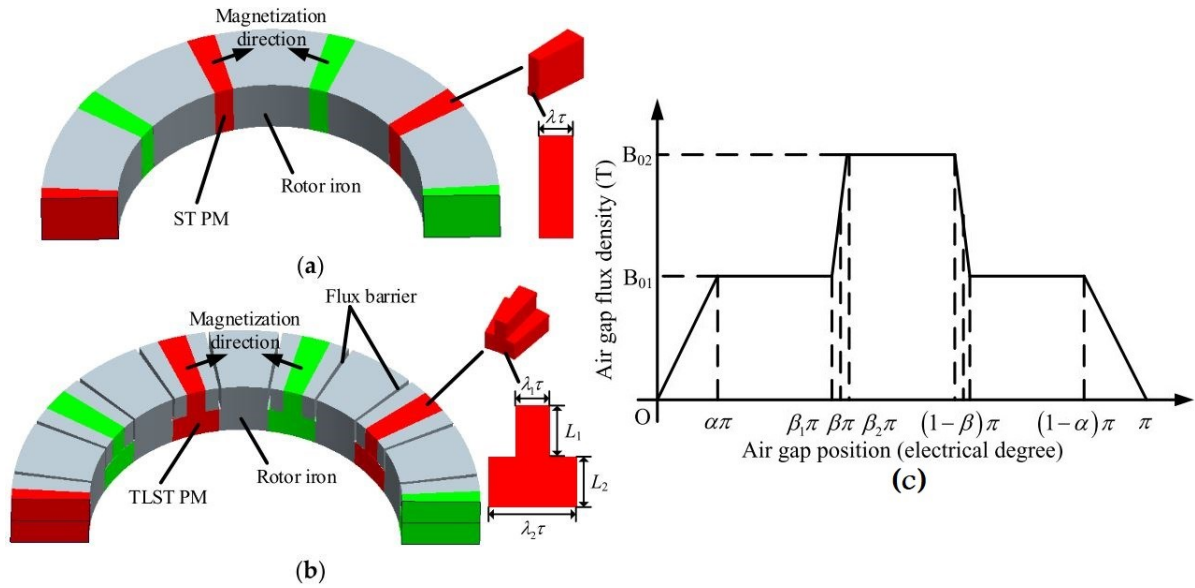


Fig. 1.25: Structure of the rotor (half side in axial direction): (a) rotor with spoke-type (ST) permanent magnets; (b) rotor with two-layer spoke-type (TLST) permanent magnets and flux barriers. (c) Improved air gap flux density waveform at no-load [70]

Rallabandi *et al.*[71] propose a novel structure called MAGNUS by combining a yokeless internal stator type NS arrangement (having small auxiliary teeth for permeance and flux modulation) with two external high polarity spoke-rotors, resulting in very high flux concentration (Fig. 1.26). The authors compare 2 stator structures: a YASA (yokeless and segmented armature) type stator with coils wound around the teeth, and another with Gramme ring windings. Results show that at 270 Nm/300RPM the MAGNUS machines has a higher torque density and can have half the losses of conventional YASA machines and hence achieve substantially higher efficiency.

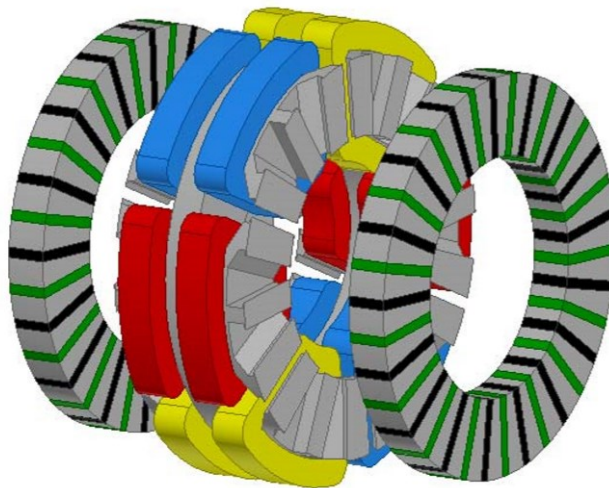


Fig. 1.26: Three dimensional model and an NN version of the MAGNUS topology employing a reduced number of concentrated coils in combination with a very large number of rotor poles [71]

Ishikawa *et al.* [72] propose a radial flux machine (Fig. 1.27c) and a hybrid flux machine (Fig. 1.27d) and compares them with an axial flux machine (Fig. 1.27b) and a

commercialized axial flux machine (Fig. 1.27a). Results show that the hybrid flux machine has a power density 9.4 times larger than that of the commercialized one. Also, efficiency-wise, the hybrid and radial generators have the same efficiency which is larger than the axial and commercialized generators (Fig. 1.28).

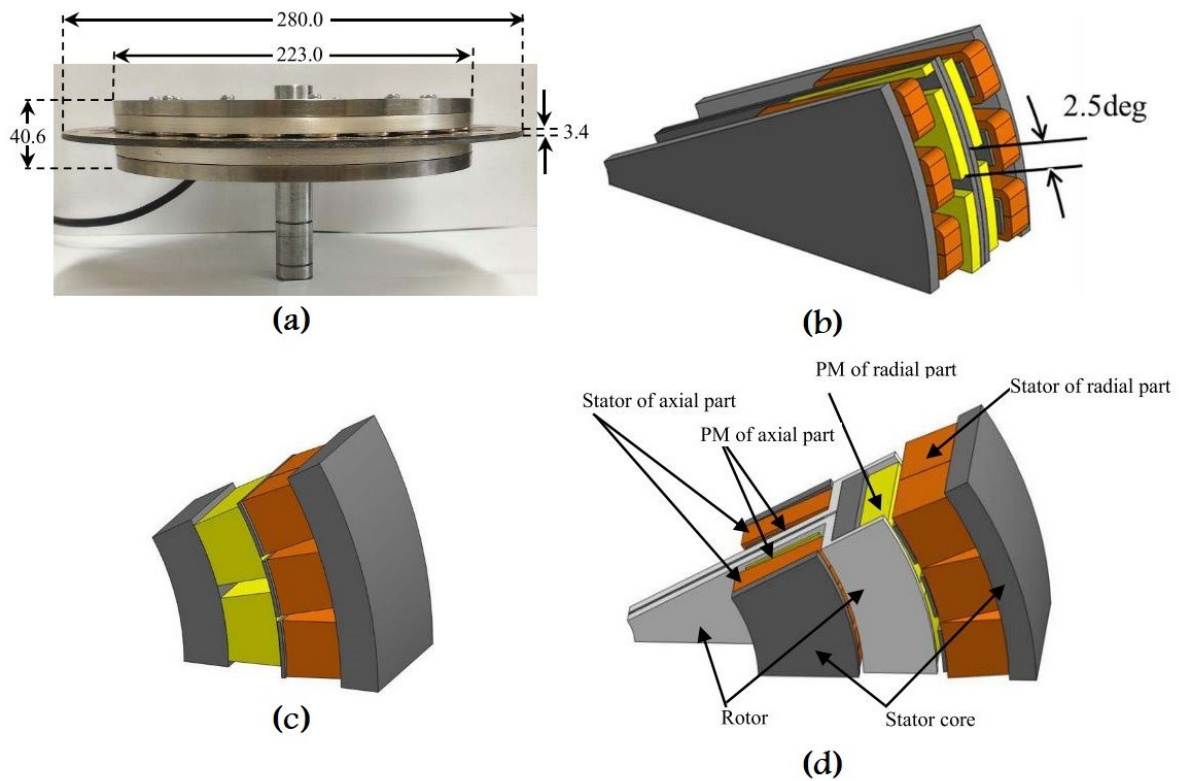


Fig. 1.27: (a) Commercialized generator (b) Designed axial-flux permanent magnet generator (c) Radial-flux permanent magnet generator (d) Proposed hybrid-flux PM generator

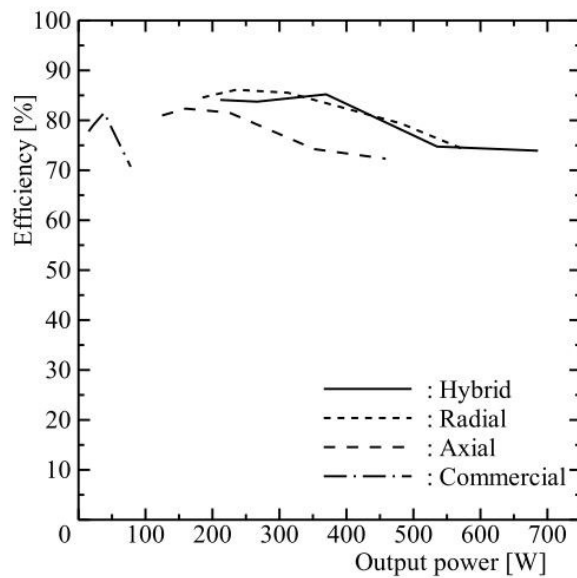


Fig. 1.28: Efficiency characteristics

The authors in [73] present a novel tapered-field brushless synchronous permanent magnet machine for high speed applications (Fig. 1.29) combining the benefits of classical structures while offering higher torque and ease of manufacturing from AMM (Amorphous magnetic material). It allows a larger air gap area for the same outer diameter but has a longer axial length. A prototype was constructed using 30 mm AMM ribbon which was cut with a precision waterjet cutter. The machine demonstrated an efficiency approaching 90% with a 0.7 mm air gap at 7000 RPM. This efficiency is maintained even at lower operating speeds.

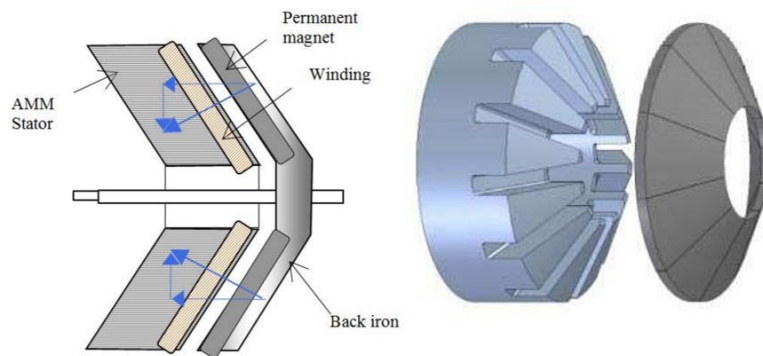


Fig. 1.29: Left: cross-sectional view of the novel AMM brushless permanent magnet motor topology. Right: 3-D view of the stator core with open slots and the rotor magnet structure [73]

In [74], the design of a novel double stator single rotor E-core axial flux machine (AFM) with flux concentrating ferrite magnets, and pole windings across each leg of an E-core stator is presented. This design results in better magnet utilization, higher torque density and ease of manufacturing due to its modular structure. The authors compare 5 machines (Fig. 1.30): the proposed E-core single-phase AFM, the proposed three-phase E-core AFM, a 6-4 radial flux surface mounted ferrite PM machine with concentrated windings, a 24-4 radial flux surface mounted ferrite PM synchronous machine (SMPMSM) with distributed windings and a radial flux SMPMSM with NdFeB magnets. Results show that the highest torque density was that of the E-core single-phase machine at almost 2-2.5 times that of ferrite RFMs. Also, the three-phase E-core AFM has a torque density 2 times higher than ferrite RFMs. These 2 machines had the smallest weight among the compared machines. Nevertheless, coil weight is higher (therefore copper loss is higher) for these 2 machines as well as core loss and thus efficiency is slightly lower. The power factor of the three-phase machine is higher than the single-phase one. The SMPM with distributed windings demonstrates the highest power factor.

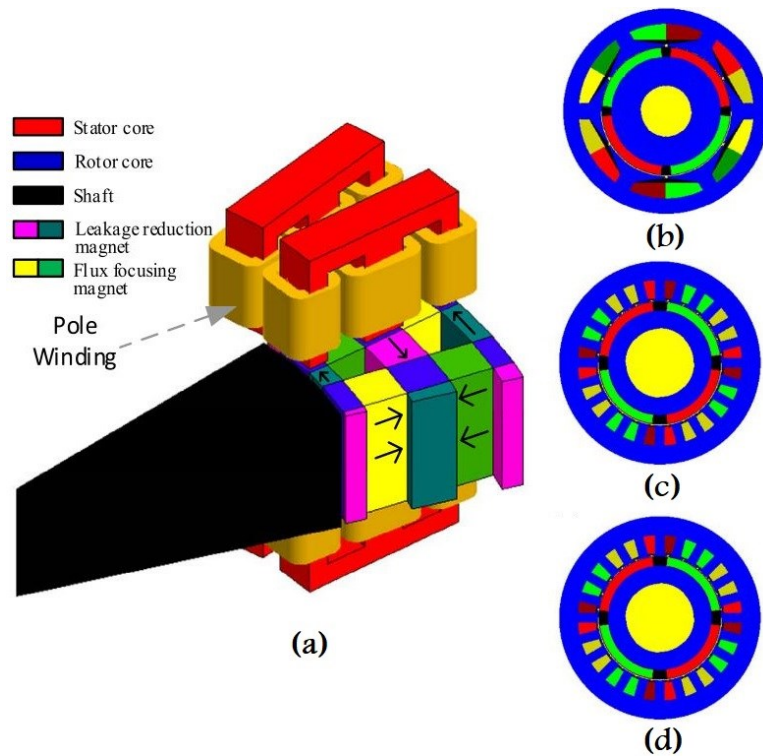


Fig. 1.30: (a) Isometric view of one pole of the proposed AFM (b) 6-4 Ferrite surface PMSM with concentrated winding (c) 24-4 Ferrite surface PMSM with distributed winding (d) 24-4 NdFeB surface PMSM with distributed winding [74]

The authors in [75] propose a novel dual stator axial flux spoke-type PM machine (Fig. 1.31). Its rotor has low cost ferrite inserted PM's in a spoke array. Its stators are shifted relative to each other by one stator tooth width. The coils are wound in a three phase group concentrated winding arrangement. The authors compare the designed machine to an identical structure but with the stators aligned. Compared to the aligned machine, results show an increase in magnetic flux density in one air gap of the proposed model as well as a reduction of cogging torque and torque ripple by 91.4% and 92% respectively. Back-EMF is more sinusoidal and has a higher RMS value contributing to a higher torque density and higher efficiency (2.49 Nm/kg 90.57% for the aligned machine and 2.73 Nm/kg 91.15% for the unaligned machine).

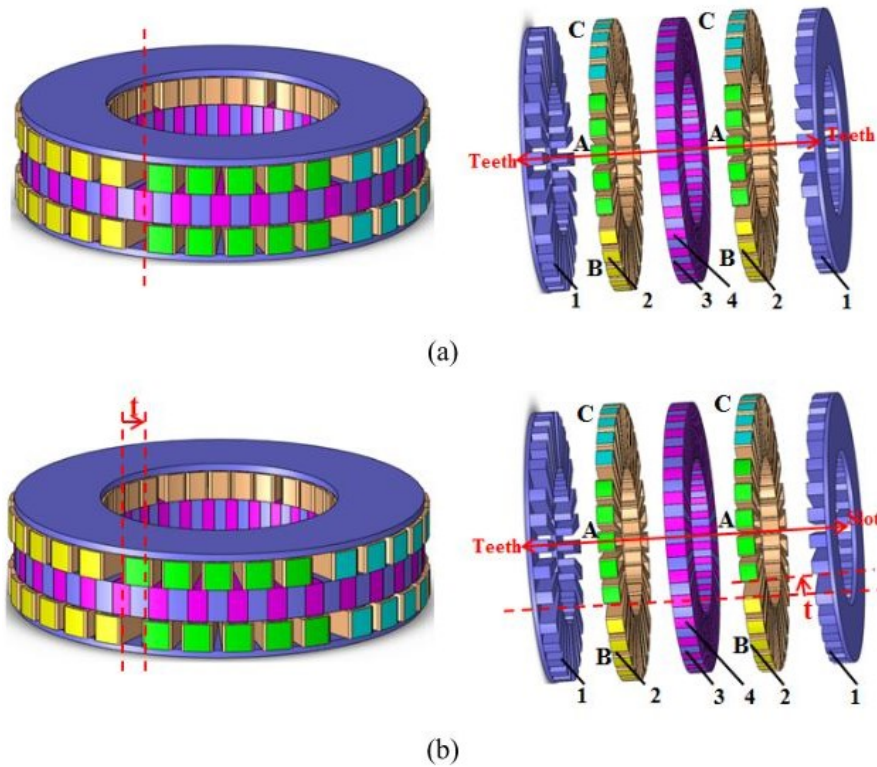


Fig. 1.31: Topologies of DSAFSPM Machines. (a) Basic model. (b) Proposed model. 1-Stator. 2-Phase-group winding. 3-Rotor pole. 4-Ferrite permanent magnet [75]

Magnax [76][77][78], now split into Traxial (focused on ground e-mobility) and Axial (focused on aircraft propulsion), manufactures axial flux machines and particularly yokeless dual rotor axial flux motors (Fig. 1.32) operating below 1200 Hz and equipped with a PT1000 temperature sensor. After years of research, the Belgian startup founded in 2015 started from the development of large generators for wind energy and shifted later on to smaller machines for electric vehicles. The company designs axial flux motors with reduced material use per kilowatt, a high torque-to-weight ratio, a short flux path, lower overall weight, lower iron losses and concentrated windings with rectangular-section copper wire (achieving a high fill factor) to minimize copper losses. Their design also accommodates a patented oil cooling system that can cool the windings directly and uniformly. Magnax develops motors adopting a design-for-manufacturing philosophy, making the production process cost-effective using standard automated processes and can be easily scaled for large series production.



Fig. 1.32: Magnax yokeless axial flux motor

YASA [79], now a wholly owned subsidiary of Mercedes-Benz, designed 2 variants of axial flux motors: the P400 motor series and the 750 motor. The P400 R e-motor provides a versatile range of torque-power combinations. It comes in a 305 mm diameter casing (IP67 enclosed), an axial length of 106.7 mm, is oil cooled and weighs 28.2 kg. It runs at 8000 RPM and develops a torque of 200 N.m (continuous) and 370 N.m (max at 450 A) and a power of 60 kW (continuous) and 160 kW (max at 750 V). Continuous ratings are given at coolant inlet $< 50^{\circ}\text{C}$ @20 ltrs/min and peak data at 60°C rotor, 60°C coolant inlet @20 ltrs/min and 60°C ambient. Another variant of the P400 series can provide a continuous power of 100 kW. Electrical performance of the P400 R motor are given in Fig. 1.33. The P400 C motor is lighter and has a shorter axial length than the P400 R at 24kg/80.4 mm and a peak power density of 6.7 kW/kg. Another variant of the YASA motor is the YASA 750 R (Fig. 1.34) offering 790 Nm (at 450 Arms) of peak torque, 200 kW (at 700 Vdc) and 100 kW (at 400 Vdc) of peak power, 400 Nm (at 40°C coolant) of continuous torque, up to 70 kW (at 3000 RPM/ 40°C coolant) of continuous power and a speed range of 0 – 3250 RPM with an axial length of 98mm and through-shaft mounting that may be stacked for increased torque and power. Its peak efficiency is $>95\%$, weighs 37 kg and has a peak power density >5 kW/kg. It has integrated position and temperature sensors and can be used in traction, generation and hydraulic replacement applications.

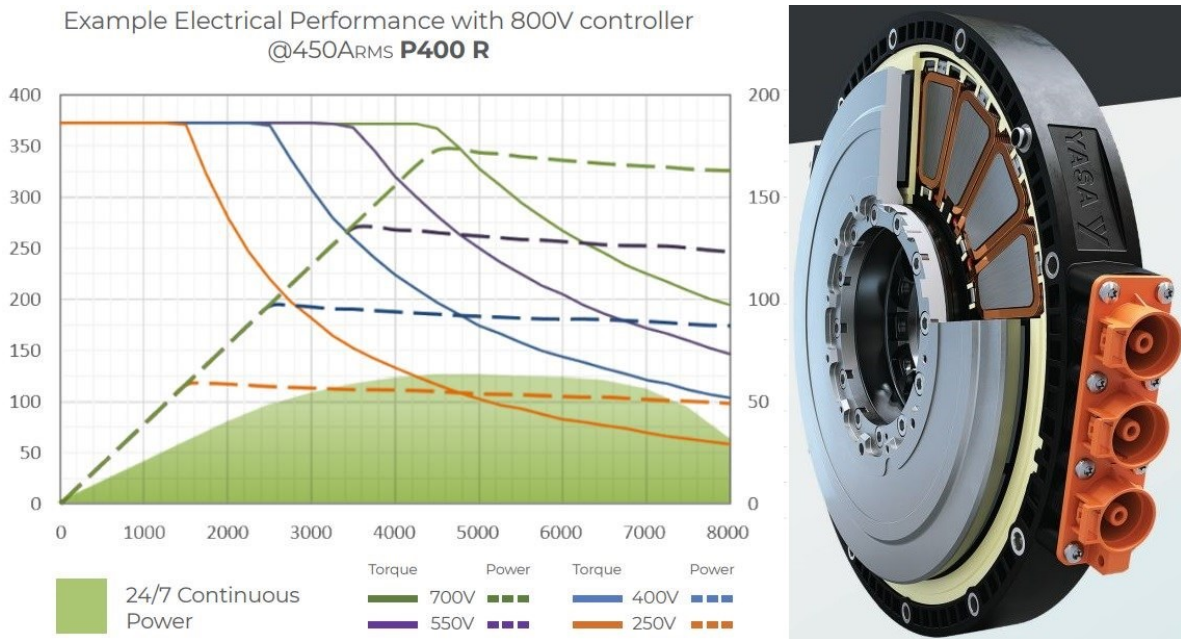


Fig. 1.33: Electrical Performance of P400 R motor with 800V controller @450ARMS [79]

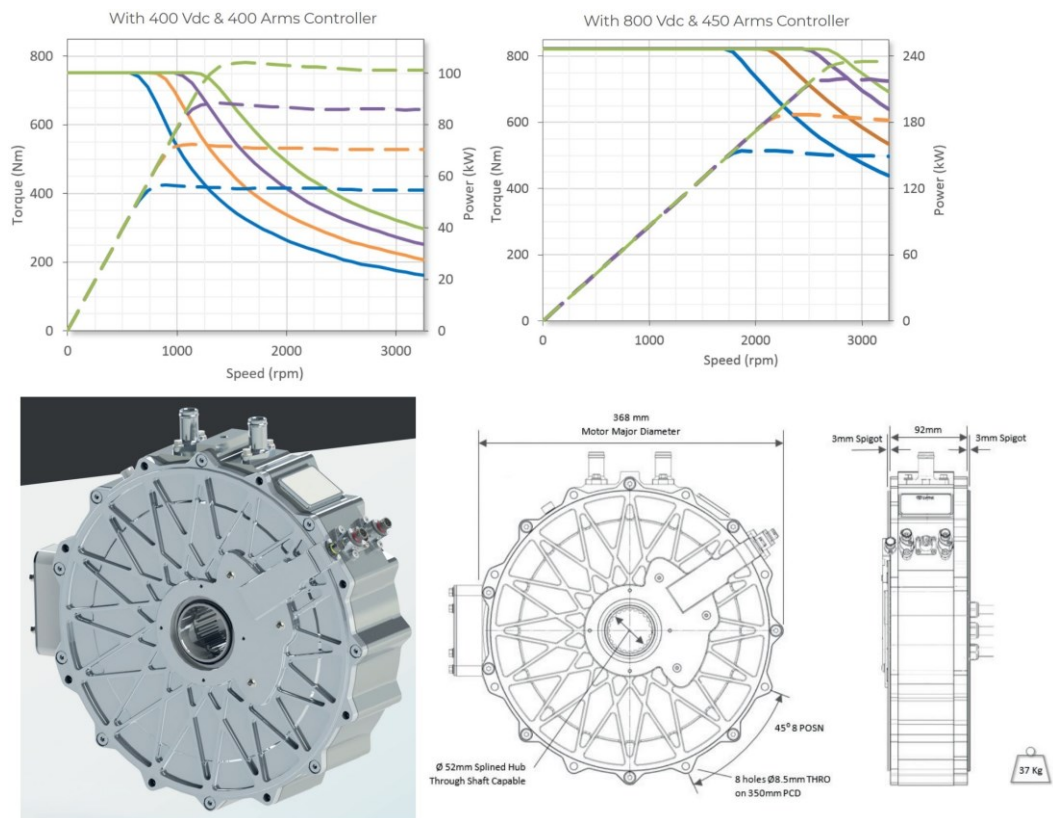


Fig. 1.34: YASA 750 structure and performance [79]

Turntide [80] (based in California) developed an axial flux switched reluctance motor with IoT capabilities (Fig. 1.35) that enables automated commissioning, remote monitoring, fault detection and control through Turntide's cloud mobile applications. Data from the motor controller, the cloud and third party systems is fed back to the Smart Motor System™ (patented by the company) to analyze the motors environment and determine its optimal speed

reducing energy consumption. The motor is used in the HVAC industry and costs around 2000\$. The motor adopts a concentrated winding configuration, spans a speed range of 200-1800 RPM, has a peak efficiency of 93.2% and exceeds 90% efficiency for fan array design points. It's around 15 cm in diameter and weighs under 45 kg. The efficiency torque curve of the motor for various speeds is given in Fig. 1.36.



Fig. 1.35: Turntide's TX switched reluctance axial flux motor

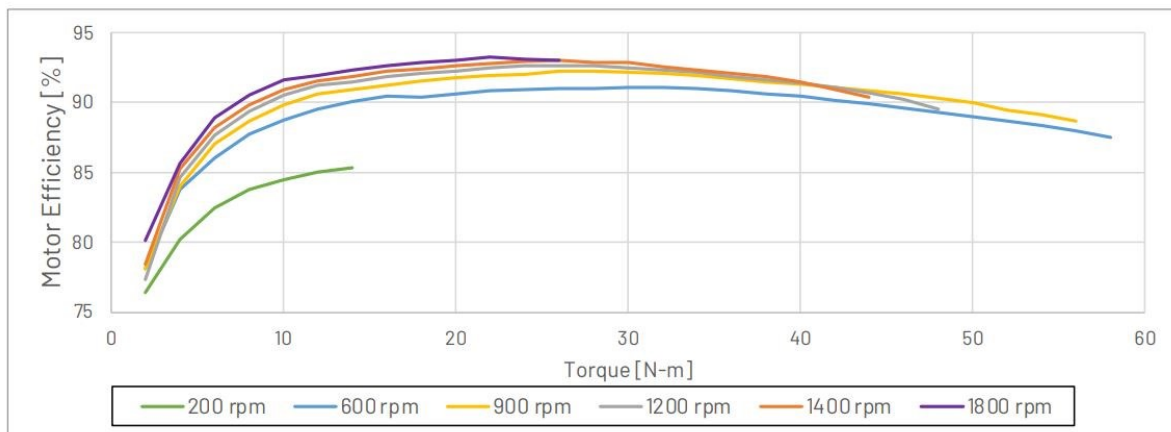


Fig. 1.36: Motor efficiency vs torque at various speeds

GREAH laboratory prototyped an axial flux surface mounted permanent magnet synchronous machine (in collaboration with Ragonot) and an axial flux switching machine (in collaboration with ERNEO); both being 3 phase machines. The 2 machines were designed, prototyped and enhanced along 3 theses [81][82][83]. The surface mounted PM machine is a 10 kW machine which has an internal radius of 135 mm, an external radius of 180 mm, 24 slots and 10 pole pairs; its magnets are made of NdFeB with a 1.1 T remanence each, its winding is of tooth type and it has a rated speed of 375 RPM. Fig. 1.37 and Fig. 1.38 illustrate

respectively the stator and rotor assembly process for the surface mounted PM machine. The flux switching machine (Fig. 1.39, Fig. 1.40, Fig. 1.41, Fig. 1.42 and Fig. 1.43) is also a 10kW/375 RPM machine. It has an internal radius of 133 mm, an external radius of 186 mm. It has 12 NdFeB magnets in its stator with a remanence of 1.2 T each. The rotor has 10 teeth and is made solely of a stack of ferromagnetic sheets.

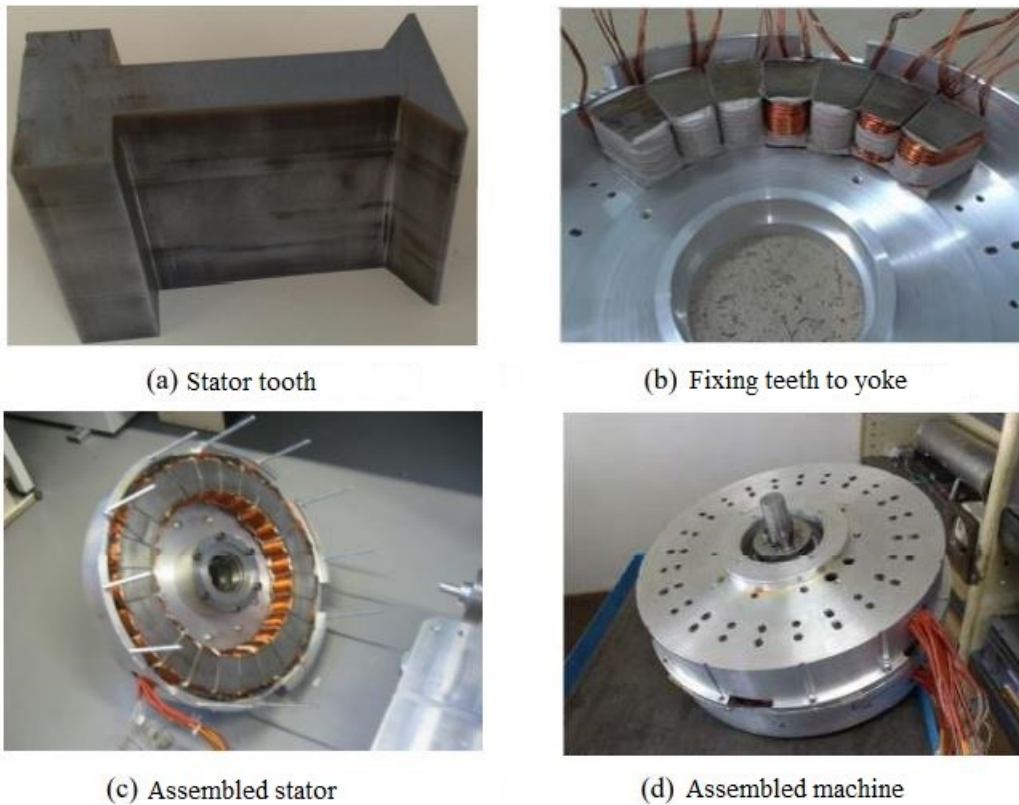


Fig. 1.37: Stator assembly process of the surface mounted PM machine

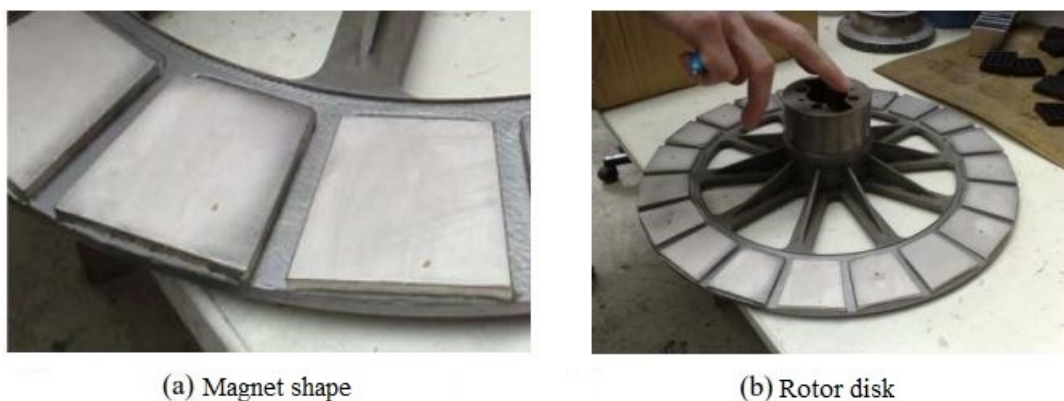


Fig. 1.38: Rotor assembly process of the surface mounted PM machine



Fig. 1.39: Stator of the flux switching machine without magnets



Fig. 1.40: Winding of the flux switching machine

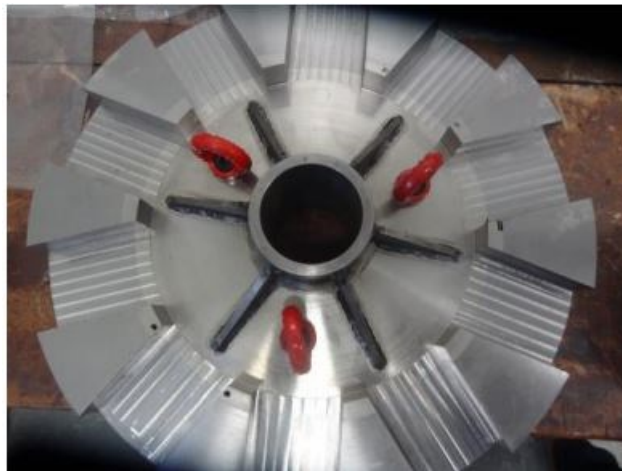


Fig. 1.41: Rotor of the flux switching machine

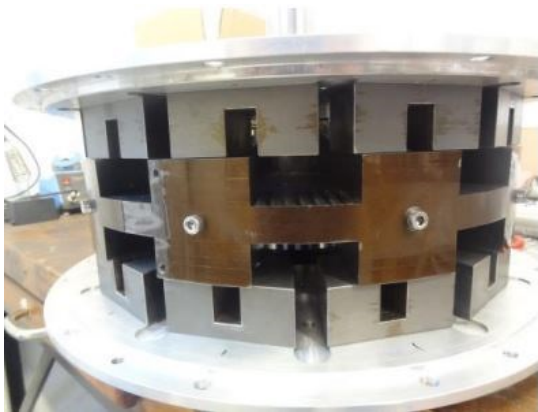


Fig. 1.42: Assembled flux switching machine

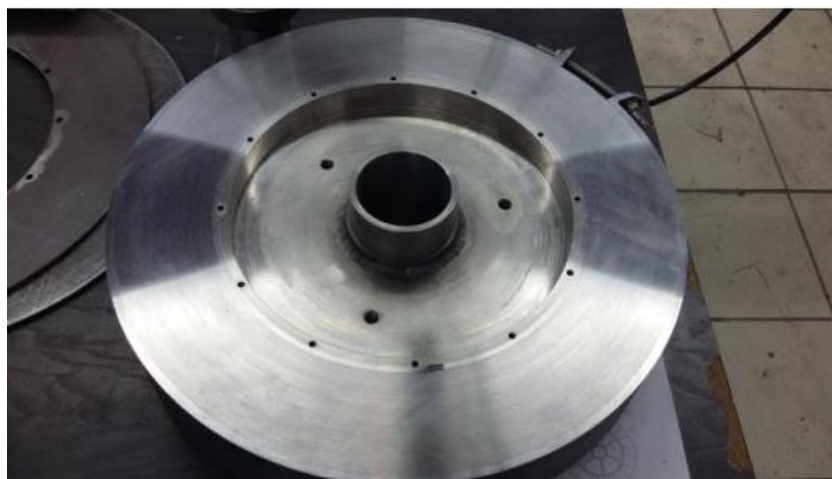


Fig. 1.43: Hub and shaft of the flux switching machine

VI. Materials used in Axial Flux Machines

The choice of materials to use in the fabrication of electrical machines is of great importance as it impacts the performance of the machine. Magnetic materials are classified as either soft or hard magnetic material according to their coercive force. A summary on

magnetic materials used in the manufacturing of axial flux machines is given below. In-depth information on materials can be found in reference [84].

1. Soft ferromagnetic materials

Soft magnetic materials are mainly classified into 3 categories: solid, laminated and powder material as indicated in Fig. 1.44. Tab. 1.5 lists main soft magnetic materials (Iron, Nickel and Cobalt) used in the fabrication of electrical machines. Alloys of these materials with other metals enhances their physical properties (mechanical resistance, electrical conductivity, magnetic saturation, permeability, etc.) and at the same time maintains their flux guiding capabilities. Common iron alloys are listed in Tab. 1.6.

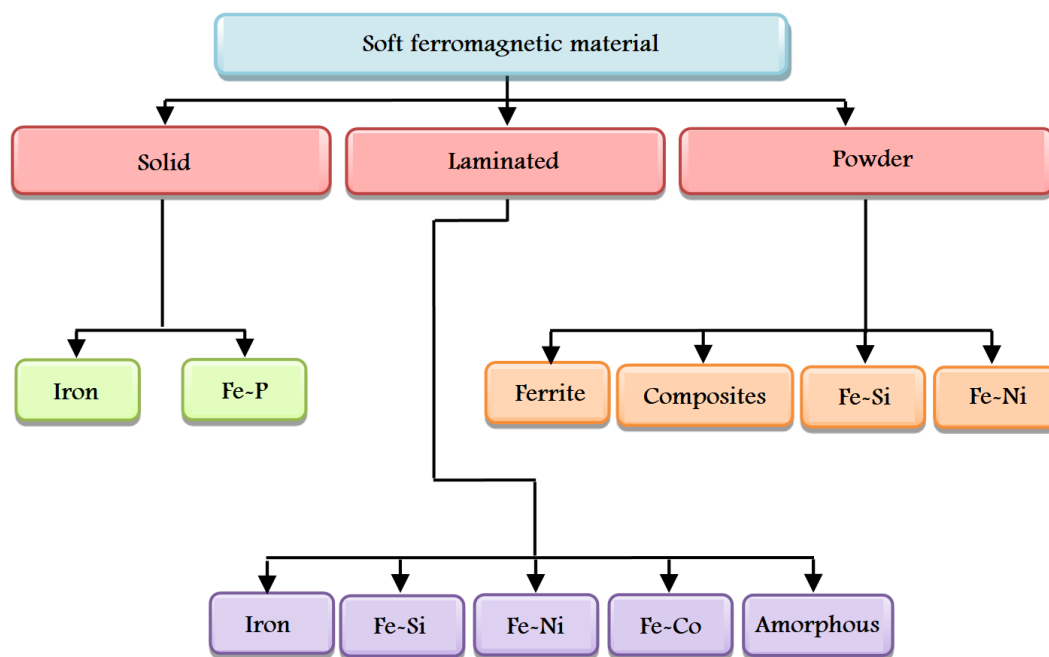


Fig. 1.44: Classification of main types of soft magnetic materials [85]

Tab. 1.5: Saturation flux density B_{sat} and Curie temperature T_c for the soft magnetic materials used in electrical machines [86]

Material	B_{sat} (T)	T_c (°C)
Iron (Fe)	2.15	770
Nickel (Ni)	0.6	360
Cobalt (Co)	1.79	1125

Tab. 1.6: Physical properties of common soft magnetic materials [87]

Material	Composition	B_s @800 A/m (T)	B_s @2500 A/m (T)	Resistivity ($\mu\Omega\text{cm}$)	Density (g/cm^3)	Thickness (mm)
Iron-Cobalt (CoFe)	49% Co, 49% Fe, 2% V	2.1	2.23	40	8.12	0.2-0.35
Iron-Nickel (NiFe)	40% Ni, 60% Fe	1.44	1.48	60	8.2	0.1-0.35
Iron-Silicon (SiFe) high content of Si	6.5% Si, Fe bal	1.29	1.4	82	7.49	0.1-0.2

Iron-Silicon (SiFe) Non oriented and fine	3% Si, 0.4% Al, Fe bal	1.15	1.63	52	7.65	0.1-0.27
Iron-Silicon (SiFe) Non oriented	1-3% Si, Fe bal		1.64	20-60	7.6-7.8	0.35-1
Soft Magnetic Composites (SMC)	<1% lubrication, Fe bal	0.71	1.22	20000	7.57	Solid

2. Ferromagnetic alloys

Sheeted SiFe alloy (93%-99% Fe) is the most commonly used material in the fabrication of electrical machines. Silicon increases mechanical stiffness and electrical resistivity of iron. Metals in small quantities are also present in that alloy: Si (up to 6.5%), Al (up to 1%) and Mn (up to 0.5%) [87]. Iron-based sheeted material undergo several successive rolling and annealing procedures in order to reduce its thickness and obtain sheets whose thickness is generally between 300 and 600 μm (more detail is available in Fig. 1.45) [88]. Fe-Co-V alloys (e.g Hiperco50HS, Hiperco50 and Hiperco27) can provide magnetic flux densities at saturation of about 1.6 T at 850°C [87]. At 50 Hz, the two most expensive materials CoFe and NiFe, are also the best in terms of magnetic flux density at saturation and iron losses. At higher frequencies (400 Hz), very thin and highly alloyed SiFe (6.5% Si) exhibits the lowest losses [89]. Silicon alloys (Fe-Si) reduce iron losses, cobalt (Fe-Co) alloys increase magnetic flux density and torque, nickel alloys (Fe-Ni) make it possible to considerably reduce internal magnetic anisotropies in order to obtain much softer alloys [82].

3. Soft magnetic composites (SMCs)

Among different soft magnetic materials, soft magnetic composites or SMCs have been successfully employed for applications requiring large air gaps or using permanent magnet excitations [83]. They consist of a powder of very small isolated iron particles pressed together on machine cores and they can guide 3D magnetic flux while having a high electrical resistivity, thus reducing eddy currents [87]. The downside is their relatively low permeability and flat B-H magnetization curve, leading to relatively low peak magnetic flux density values [90]. The main manufacturers of composite materials are TSC international (USA) and Höganäs (Sweden) and QMP (Canada) [82]. Fig. 1.46 illustrates a 220W wind generator developed by Khan *et al.* It is a 7 pole pair double stator internal rotor axial flux machine where the teeth were obtained by grinding SMC iron samples.

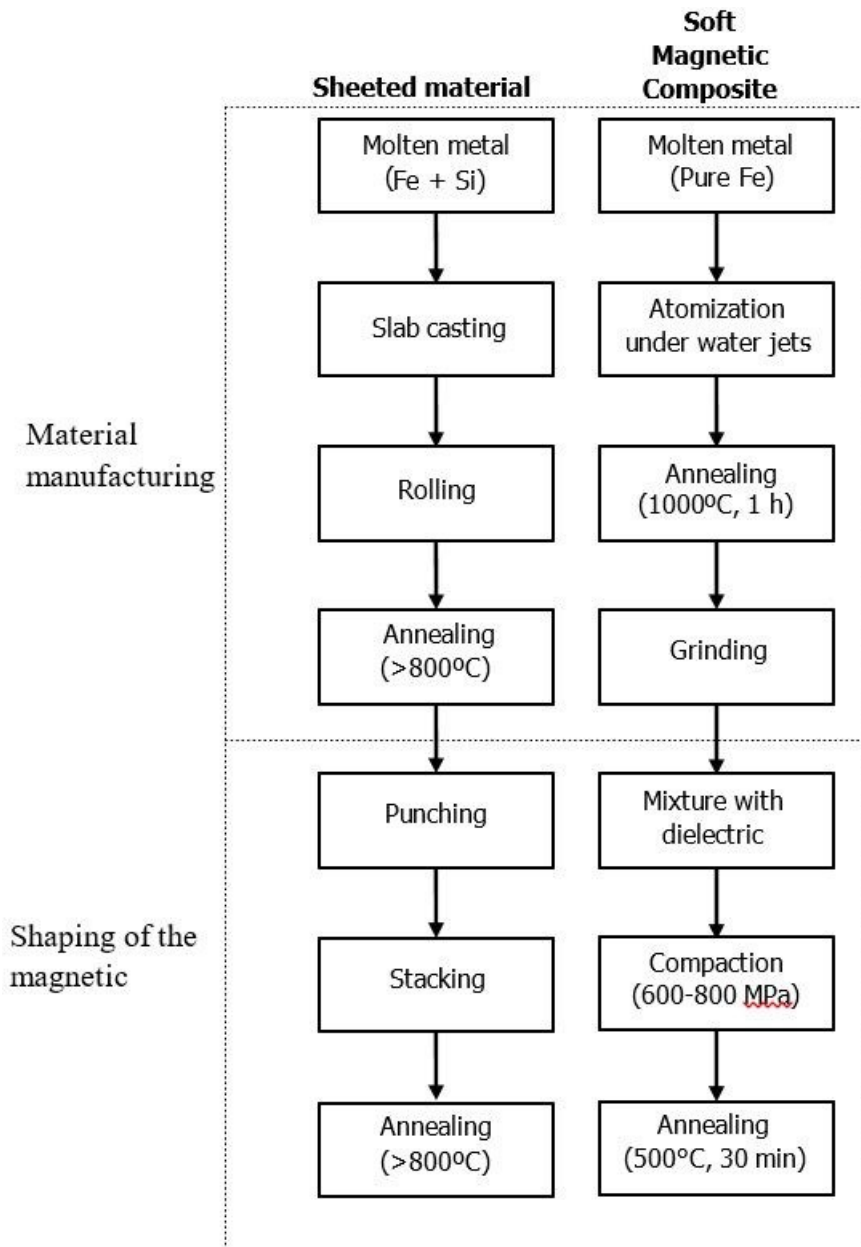


Fig. 1.45: Comparison of manufacturing processes of a magnetic circuit by sheet rolling and by powder metallurgy [85]

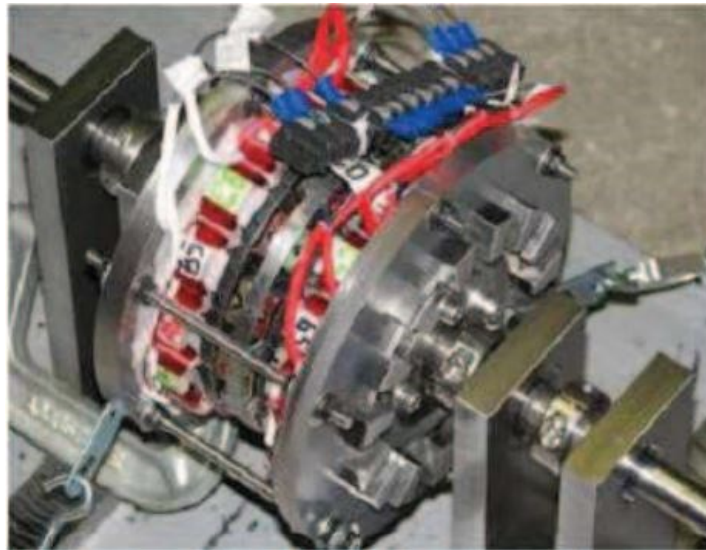


Fig. 1.46: Wind generator prototype with teeth made of SMC material

4. Hard magnetic materials

Hard magnetic materials (from which permanent magnets are manufactured) are characterized by their high coercive force which distinguishes them from soft magnetic materials, allowing them to conserve their magnetization even in the presence of a strong magnetic field. Several families of these materials are used in the manufacturing of electrical machines, namely ferrites, NdFeB, AlNiCo, SmCo and SmFe. The physical properties of these materials are summarized in Tab. 1.7. Rare earth NdFeB magnets can be found in applications such as aeronautics, permanent magnet machines, information technology, etc, Alnicos are used in applications such as metrology, Sm-Co for high temperature applications and ferrite magnets are found in almost all applications [82].

Tab. 1.7: Main physical properties of magnets proposed in [91]

	$B_r@25^\circ\text{C}$ (T)	$H_{cj}@25^\circ\text{C}$ (kA/m)	$\Delta H_{cj}/T$ (%/°C)	$\Delta B_r/T$ (%/°C)	$(BH)_{\text{max}}$ (kJ/m ³)	T max (°C)	Density (kg/m ³)	ρ ($\mu\Omega\cdot\text{m}$)	λ (W/m.K)	Price (€/kg) in 2009
Ferrites	0.3 à 0.4	290	+0.4	-0.2	20 à 35	250	5 000	10^{10}	2 to 5	2 to 5
NdFeB sintered	1 à 1.5	900 to 2000	-0.4	-0.1	190 to 440	140 to 200	7600	1.5	9 à 10	50 to 100
NdFeB bonded	0.5 to 0.7	600 to 1000	-0.4	-0.12	40 to 90	120 to 150	4000 to 6000	10 to 30	2 to 3	80 to 120
SmCo*	1 to 1.3	500 to 2000	-0.15 to -0.3	-0.03	280 to 380	350 to 550	8400	0.5 to 0.7	9 to 12	130 to 200

SmFe bonded	0.6 to 0.8	750 to 1000	-0.51	-0.06	70 to 110	180	/	/	/	/
-------------	------------	-------------	-------	-------	-----------	-----	---	---	---	---

5. Insulating materials

The quality of the electrical insulation system of electrical machines is an important factor that influence their reliability and performance. Three types of insulation exist: insulation against the housing, insulation between phases and insulation between coil turns. Electrical and mechanical stress is greater on the insulation against the housing than it is on the insulation between coil turns. Thus, it must be able to withstand the potential difference as well as have a greater thickness. Insulation between phases is thick compared to insulation between coil turns. In low voltage these two types of insulations are provided by organic insulation paper (Nomex, Mylar ...) characterized by good mechanical strength, withstands high temperatures and has a low thermal resistance facilitating evacuation of heat. On the other hand, the insulation between coil turns is the thinnest and therefore the most vulnerable to stress. Low voltage electrical machines are mostly wound in an unbalanced manner, so coil turns are subjected to different voltages. In the case where the first and last turns are adjacent, the insulation is subjected to the complete voltage of the coil. Insulations can be classified depending on the maximum temperature they can withstand and is given in the following table:

Tab. 1.8: Electrical insulation classes according to the maximum temperature

Class	Material	Maximum temperature
Y	Cotton fabric, paper and silk but not impregnated in a dielectric	90 °C
A	Cotton fabric, paper and silk impregnated in a dielectric	105 °C
E	Synthetic organic films	120 °C
B	Fiberglass, Mica, Bonded Asbestos Fibers	130 °C
F	Fiberglass, Mica, Bonded Asbestos Fibers impregnated in a dielectric	155 °C
H	Fiberglass, Mica, Bonded Asbestos Fibers combined with silicon addition and impregnation	180 °C
S	Films in polyamide enamel (Pyre-ML) or in polyamide (Kapton and Alconex GOLD)	240 °C

VII. Problems with Axial Flux Machines

1. Magnetic problems

a) Skewing

Magnet skewing and certain reduction techniques of cogging torque and losses can complicate manufacturing of axial flux machines. Several magnet skewing techniques exist: conventional skew, triangular skew, parallel-sided magnets, trapezoidal skew, round magnets (easy to manufacture [92]) and dual-skew magnets. These techniques are illustrated by

Fig. 1.47. To avoid magnet skewing, other techniques can be used but they give rise to other issues; e.g. the use of appropriate magnet pole-arc to pole-pitch ratio, which is around 0.7 for AFPM machines, reduces cogging torque but at the same time distorts back-EMF, reduces magnet flux, and, as a result, reduces the machine's average torque; magnet grouping increases torque ripple, and rotor displacement also reduces back-EMF and average torque [92].

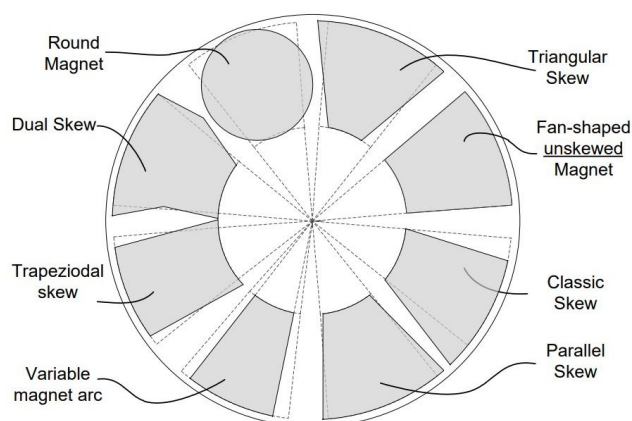


Fig. 1.47: Different skewing methods employed in AFPM designs [92]

Also, minimizing cogging torque through stator modifications (e.g. slot skewing) complicates manufacturing process and increases manufacturing cost, making them not common in such machines [92]. For machines with rolled laminated steel, skewing teeth to reduce cogging torque is even harder as this type of steel is hard to manufacture; even using SMCs is not a solution as they saturate at low flux density levels, limiting machine power density, also SMC stators along with rolled steel stators are subject to core losses at high speeds, so coreless motors are proposed [3].

b) Lamination

The manufacturing of stator laminated magnetic circuit is not necessarily an easy task because of the need to roll the steel sheets. Stacking sheets is simpler than rolling them, but techniques exist which consists in replacing the rolled stator by several plots of stacked sheets as in the case of radial flux machines. The authors in [93] and [94] fabricated toroidal slotless AFPM stators using tape-wound cores with thin gauge electrical steel, which does not require special manufacturing techniques. Slot cutting into tape-wound core was preformed in [95] for a 30kW/16000RPM axial flux machine using wire EDM technique, while in [96] slots were cut using machining which can introduce short circuits between lamination layers. Another, yet expensive, technique is winding stamped steel tape as performed by the authors in [97], but this not practical as specialized equipment is required for execution.

2. Thermal problems

a) End windings heat

Energy conversion from electricity to mechanical motion produces losses and consequently heat. The thermal aspect of axial flux machines has been always a complex issue, due to a lack of know-how in the subject. Heat dissipation is a major concern for motor

designers as it affects machine's performance, life-span and reliability. For radial flux machines, there is no space constraint on end windings on either sides of the stator. In these machines, end windings occupy the same volume to the right and left of the stator. On the other hand, axial flux machines cannot afford to exceed a certain volume at the inner radius as there is not much space, and the only way to overcome this is by increasing the inner radius to place the end windings. Thermally, high torque densities require a performing cooling system, so water cooling is commonly adopted in radial and axial flux permanent magnet machines (liquids have a higher thermal capacity than air), where for the latter, the water jacket or conduit is placed in the housing or in the end caps, but this configuration does not help evacuate heat from end windings. Potting material can be added around end windings or used to fill gaps between coils in slots [98], also a cooling pipe can be inserted between end windings [99] but this can cause space conflict. A liquid-cooled aluminum ring can be placed at the stator outer diameter [100] but this only suits single-stator double-rotor AFPM motors. Fins placed in slots can be used [101] but this may decrease slot fill factor. Machine designers often use epoxy resin to fill the region between end caps and end windings to enhance heat dissipation while protecting end windings and filling the gaps in slots [102]. In [103], a circumferential oil flow for a drum-wound machine is implemented where oil circulates over the outer surface of the end-windings. [104] proposes a novel direct oil cooling system for TORUS-type AFPM machines, where direct oil cooling of the outer end-windings is employed.

b) Insulation heat

As copper windings and stator cores generate the majority of losses, care should be taken when designing a cooling system to evacuate heat from these regions. It should be also noted that as the temperature increases, copper resistance increases thus reducing machine efficiency; also temperature increase reduces insulation lifetime [105]. Evacuation of heat from stator cores is relatively easy as they are highly conductive thermally. On the other hand, winding insulation makes heat dissipation a challenging task due to their small thermal conductivity, and as a result safety of insulation is not necessarily guaranteed.

c) Demagnetization

PM Remanance and intrinsic coercive force are highly affected by temperature, so this should be considered in the design process to avoid degradation of performance during operation, which can reduce torque and power rating of the machine as well as efficiency. This requires a highly effective cooling system which can reduce to a certain extent the demagnetization risk of magnets. A partially demagnetized machine loaded with a constant torque will turn in a viscous loop until stall [105]: demagnetization leads to higher current consumption, which leads to more copper losses, increasing the temperatures even more. Thus, performance and efficiency of a PM motor decreases with increase in temperature, which can also be caused by other materials (glue between PM and rotor iron) or structural composites.

d) Mechanical loss

Mechanical losses are a source of heat in axial flux machines. In [106] the machine's thermal behavior was greatly impacted by the excessive bearing loss, but aerodynamic effects had less pronounced effects due to fully enclosed and naturally cooled machine construction. But this type of construction is thermally challenging due to limitations in heat evacuation

from the rotor assembly due to low air flow/air movement. Also, integrating bearings within the stator assembly resulted in issues for the bearings, namely: an elevated operating temperature and difficulties setting and maintaining an appropriate bearing preload. Also windage losses for oil cooled machines is a very important aspect to manage at high speeds. In the design presented in [107] of a permanent magnet motor for a directly coupled pump, the machine was flooded with oil and operated at 20kRPM, this gave rise to high windage losses at the rotor surface, leading the authors to conclude that thermal management of the rotor is very important, especially when PMs exist. The authors also concluded that oil quantities need to be optimized and that a fin array requires proper design and analysis to avoid just adding an extra mass with no practical benefits.

3. Mechanical problems

a) Axial attraction force

There are problems specific to axial flux machines that have not been solved due to lack of experience and practice and that do not exist or have been partially solved for radial flux machines. One of the classic problems is the existence of the axial attraction force requiring that these machines (especially those with magnets) have a more rigid support structure than radial flux machines. A rotating disk does not exist in a radial flux machine, but in an axial flux machine it has an important mechanical role. The axial attraction force F_z can be calculated using the following equation:

$$F_z = \frac{B_g^2 S}{2\mu_0} \quad (1.3)$$

Where B_g is the average air gap flux density, S is the stator surface area and μ_0 is the permeability of free space. It is worth mentioning that the axial attraction force in a coreless AFPM machine is negligible [108]. Because of this axial attraction, special care must be taken when choosing shaft and bearings as well as when assembling the machine, which can be a complicated process and requires a preliminary mechanical study. For a machine without magnets, there are aspects that will appear only during operation and disappear when the machine is switched off, but with magnet machines the axial attraction problem is always there.

b) Centrifugal force

At high speeds, the mechanical integrity of the rotor in an AFPM machine becomes a serious issue [109]. It is much more difficult to design a high speed axial flux machine than it is to design a radial flux one due the centrifugal force exerted on the rotor of an axial flux machine. This force acts along the radius of rotation pulling the magnets outwards. The centrifugal force F_c experienced by a rotating body of mass m at a rotational speed ω and a rotational radius r with a tip speed $v = r\omega$ is given by:

$$F_c = m\omega v = mr\omega^2 \quad (1.4)$$

The above equation shows that the centrifugal force is proportional to the radius, so an obvious solution to reduce the centrifugal force is to reduce the radius of the rotor or the rotational speed. But it's not that straightforward, because reducing the radius will also reduce the torque faster as it is proportional to the radius cubed and this is totally contradictory with the objective of the machine:

$$T = \frac{\pi}{2}BA\lambda(1 - \lambda^2)R_o^3 \quad (1.5)$$

Where B is the magnetic loading, A is the electrical loading, λ is the inner to outer radius ratio, and R_o is the outer radius of the machine. As a result, when high speed is required, it is better to go with an RFPM design than with an AFPM one.

Another important aspect when designing a high-speed AFPM machine is the retainment ring that must be employed to hold the magnets in place, otherwise they could separate from the rotor due to the intense centrifugal force. The retainment ring must have specific properties [109]: high yield strength capability, large modulus of elasticity, acceptable elongation percentage, very low relative magnetic permeability, low magnetic saturation level, low mass density, acceptable material and manufacturing costs. The material used for a retainment ring is generally carbon fiber but due to several considerations it can be replaced by Maraging G125 material. Also centrifugal forces in high-speed applications make laminated sheets not suitable for the rotor structure since they can be a source of mechanical failure.

c) *Vibration*

Vibration of the rotor is also a concern in the design of axial flux machines. The natural rotor vibration frequency is given by [110]:

$$\omega_n = a_n \sqrt{\frac{EI}{\mu_l L^4}} \quad (1.6)$$

Where E is Young's modulus, I the rotor inertia, μ_l the mass per unit length, L the rotor length, and a_n is the numerical constant computed by Rayleigh method dependent on the problem boundaries. The computation of this quantity is important to detect the natural frequencies that, if reached by the rotor, vibration, resonance and subsequent rotor failure will occur. So, it is necessary to design the rotor in such a way that it pushes these natural frequencies away from its operating range avoiding vibration and resonance.

VIII. Problematic of the Thesis

The need to install more and more capacity of distributed wind energy where multi-GWhs are demanded, requires increasing the number of constructed generators, thus increasing the quantity of material used. This makes generator design a challenging task, especially when reduction of mass, size and down time is required while at the same time preserving a high power rating for the generator. These constraining specifications leads to

the adoption of relatively new topologies like axial flux machines due to their high power density, compactness and torque. Wind turbine applications require a low speed machine, and therefore more torque is required making it an objective in itself. With radial flux machines, the increase in torque is achieved by increasing the rotor radius or the machine active length. In the nacelle, the axial length can be limited and constrained, and we can have a little more margin in the radial direction. These constraints could favor the axial flux machine and lead to the contribution to the development of this solution. Also, the torque of an axial flux machine is proportional to the outer diameter cubed, this makes these machines exploitable in the radial direction, which is beneficial looking at the geometry and space constraints of the nacelle. Coupling of these machines with non-conventional gears such as magnetic gears while choosing a suitable gear ratio will achieve the required torque density of the generator-gear system. Magnetic gears are immune to mechanical failure, thus requiring little maintenance and no lubrication unlike their classical mechanical counterparts. The design of axial flux machines requires a specific procedure that, if applied, delivers a machine satisfying the specifications, and adequate tools that allows to pre-size the machine quickly to obtain the required performances before launching a 3D finite elements simulation to verify the obtained results and refine the design. The work done in this thesis serves these goals and contributes to the efforts made by GREAH for the past 20 years to research and develop axial flux machine designs.

IX. Conclusion

In this first chapter, a brief review on advances in axial flux machines has been presented. First, the different configurations of these machines have been described and their advantages and weaknesses have been elaborated. These different configurations, spanning from their simplest form the SSSR passing by the more complex DSSR and SSSR and finally arriving at the most complex MSMR configuration, have been compared and their application fields have been presented in order to make the choice of structure a simpler task on machine designers.

Then recent advances in the past 10 years of axial flux machine designs have been presented and their strong and weak points have been exposed, allowing a more in-depth in the field comprehension of actual design processes, giving designers an idea of existing designs so they can build on what's existing and avoid reinventing the wheel.

Afterwards, different materials used in the construction of axial flux machines were presented and categorized, also their magnetic and thermal characteristics were discussed. These materials are basically divided into soft and hard materials, but also ramify to different sub-groups e.g. solid, laminated and powder for soft material, and it is primordial to comprehend the differences between them as well as the applications suitable for every type of material as this effects greatly the performance of the machine.

Finally, the magnetic, thermal and mechanical problems have been addressed and the problematic has been stated.

References

- [1] H. Usman, J. Ikram, K. S. Alimgeer, M. Yousuf, S. S. H. Bukhari, and J.-S. Ro,

- “Analysis and Optimization of Axial Flux Permanent Magnet Machine for Cogging Torque Reduction,” *Mathematics*, vol. 9, no. 15, 2021, doi: 10.3390/math9151738.
- [2] C. C. Chan, “Axial-Field Electrical Machines - Design and Applications,” *IEEE Trans. Energy Convers.*, no. 2, 1987.
- [3] R. Huang, Z. Song, H. Zhao, and C. Liu, “Overview of Axial-Flux Machines and Modeling Methods,” *IEEE Trans. Transp. Electr.*, vol. 8, no. 2, pp. 2118–2132, 2022, doi: 10.1109/TTE.2022.3144594.
- [4] Z. Zhang, C. Wang, and W. Geng, “Design and Optimization of Halbach-Array PM Rotor for High-Speed Axial-Flux Permanent Magnet Machine With Ironless Stator,” *IEEE Trans. Ind. Electron.*, vol. 67, no. 9, pp. 7269–7279, 2020, doi: 10.1109/TIE.2019.2944033.
- [5] R. Tang, *Modern Permanent Magnet Machines: Theory and Design*. Beijing, China: China Machine Press, 2015.
- [6] F. Nishanth, J. Van Verdegheem, and E. L. Severson, “Recent Advances in Analysis and Design of Axial Flux Permanent Magnet Electric Machines,” 2021.
- [7] J. Chen, J. Zhu, and E. L. Severson, “Review of Bearingless Motor Technology for Significant Power Applications,” *IEEE Trans. Ind. Appl.*, vol. 56, no. 2, pp. 1377–1388, Mar. 2020, doi: 10.1109/TIA.2019.2963381.
- [8] S. Ueno and Y. Okada, “Characteristics and control of a bidirectional axial gap combined motor-bearing,” *IEEE/ASME Trans. Mechatronics*, vol. 5, no. 3, pp. 310–318, 2000, doi: 10.1109/3516.868923.
- [9] J. Asama, Y. Hamasaki, T. Oiwa, and A. Chiba, “Proposal and Analysis of a Novel Single-Drive Bearingless Motor,” *IEEE Trans. Ind. Electron.*, vol. 60, no. 1, pp. 129–138, Jan. 2013, doi: 10.1109/TIE.2012.2183840.
- [10] Q. D. Nguyen and S. Ueno, “Modeling and Control of Salient-Pole Permanent Magnet Axial-Gap Self-Bearing Motor,” *IEEE/ASME Trans. Mechatronics*, vol. 16, no. 3, pp. 518–526, Jun. 2011, doi: 10.1109/TMECH.2010.2045392.
- [11] S. Ueno and Y. Okada, “Characteristics of axial force and rotating torque and their control of permanent magnet type axial gap self-bearing motor,” *Electr. Eng. Japan*, vol. 132, no. 1, pp. 81–91, 2000.
- [12] J. Asama, D. Watanabe, T. Oiwa, and A. Chiba, “Development of a one-axis actively regulated bearingless motor with a repulsive type passive magnetic bearing,” in *2014 International Power Electronics Conference (IPEC-Hiroshima 2014 - ECCE ASIA)*, May 2014, pp. 988–993, doi: 10.1109/IPEC.2014.6869707.
- [13] J. Van Verdegheem, E. L. Severson, and B. Dehez, “Hybrid Active–Passive Actuation Approach of Passively Levitated Thrust Self-Bearing Machines,” *IEEE Trans. Ind. Appl.*, vol. 57, no. 6, pp. 7035–7045, Nov. 2021, doi: 10.1109/TIA.2021.3094179.
- [14] W.-S. Han, C.-W. Lee, and Y. Okada, “Design and control of a disk-type integrated motor-bearing system,” *IEEE/ASME Trans. Mechatronics*, vol. 7, no. 1, pp. 15–22, Mar. 2002, doi: 10.1109/3516.990883.
- [15] S.-H. Park and C.-W. Lee, “Lorentz force-type integrated motor-bearing system in dual rotor disk configuration,” *IEEE/ASME Trans. Mechatronics*, vol. 10, no. 6, pp. 618–625, Dec. 2005, doi: 10.1109/TMECH.2005.859825.
- [16] W. Geng and Z. Zhang, “Investigation of a New Ironless-Stator Self-Bearing Axial Flux Permanent Magnet Motor,” *IEEE Trans. Magn.*, vol. 52, no. 7, pp. 1–4, Jul. 2016, doi: 10.1109/TMAG.2016.2524649.

- [17] M. Sumino and S. Ueno, "Rotation test of a tilt controlling axial self-bearing motor with superconducting magnetic bearing," 2014.
- [18] S. Ueno, R. Iseki, and C. Jiang, "Stability of a tilt-controlling axial gap self-bearing motor with single-stator," *Mech. Eng. J.*, vol. 4, no. 4, pp. 16–00 337–16–00 337, 2017.
- [19] S. Ueno, K. Nakazawa, and C. Jiang, "Improvement of Stability of an Tilt-Controlling Axial Gap Self-bearing Motor with Single Stator," in *2019 12th Asian Control Conference (ASCC)*, Jun. 2019, pp. 1216–1221.
- [20] S. Ueno, T. Fukuura, and T. Van Toan, "A 5-dof active controlled disk type pm motor with cylindrical flux paths," 2014.
- [21] C. Jiang, K. Adnou, and S. Ueno, "5-degree of freedom active position control of an axial self-bearing motor with six concentrated stator windings," 2016.
- [22] M. Osa, T. Masuzawa, and E. Tatsumi, "5-dof control double stator motor for paediatric ventricular assist device," 2012.
- [23] M. Osa, T. Masuzawa, N. Omori, and E. Tatsumi, "Radial position active control of double stator axial gap self-bearing motor for paediatric vad," 2014.
- [24] N. Kurita, T. Ishikawa, N. Saito, T. Masuzawa, and D. L. Timms, "A Double-Sided Stator Type Axial Bearingless Motor Development for Total Artificial Heart," *IEEE Trans. Ind. Appl.*, vol. 55, no. 2, pp. 1516–1523, Mar. 2019, doi: 10.1109/TIA.2018.2884609.
- [25] Y. Wang, M. Chen, T. W. Ching, and K. T. Chau, "Design and Analysis of a New HTS Axial-Field Flux-Switching Machine," *IEEE Trans. Appl. Supercond.*, vol. 25, no. 3, pp. 1–5, Jun. 2015, doi: 10.1109/TASC.2014.2366465.
- [26] J. H. Kim, M. Liu, H. Ding, and B. Sarlioglu, "Comparison of dual structure axial flux-switching permanent magnet machines," in *2017 IEEE Energy Conversion Congress and Exposition (ECCE)*, Oct. 2017, pp. 328–333, doi: 10.1109/ECCE.2017.8095800.
- [27] J. H. Kim, Y. Li, and B. Sarlioglu, "Sizing, Analysis, and Verification of Axial Flux-Switching Permanent Magnet Machine," *IEEE Trans. Ind. Appl.*, vol. 55, no. 4, pp. 3512–3521, Jul. 2019, doi: 10.1109/TIA.2019.2905818.
- [28] H. Torkaman, A. Ghaheeri, and A. Keyhani, "Design of Rotor Excited Axial Flux-Switching Permanent Magnet Machine," *IEEE Trans. Energy Convers.*, vol. 33, no. 3, pp. 1175–1183, 2018, doi: 10.1109/TEC.2018.2807804.
- [29] J. H. Kim, Y. Li, E. Cetin, and B. Sarlioglu, "Influence of Rotor Tooth Shaping on Cogging Torque of Axial Flux-Switching Permanent Magnet Machine," *IEEE Trans. Ind. Appl.*, vol. 55, no. 2, pp. 1290–1298, Mar. 2019, doi: 10.1109/TIA.2018.2873530.
- [30] V. Rallabandi, N. Taran, D. M. Ionel, and I. G. Boldea, "Axial-flux PM synchronous machines with air-gap profiling and very high ratio of spoke rotor poles to stator concentrated coils," in *2017 IEEE International Electric Machines and Drives Conference (IEMDC)*, May 2017, pp. 1–7, doi: 10.1109/IEMDC.2017.8002371.
- [31] J. Ma *et al.*, "Optimal Design of an Axial-Flux Switched Reluctance Motor With Grain-Oriented Electrical Steel," *IEEE Trans. Ind. Appl.*, vol. 53, no. 6, pp. 5327–5337, Nov. 2017, doi: 10.1109/TIA.2017.2727438.
- [32] M. J. Kermanipour and B. Ganji, "Modification in Geometric Structure of Double-Sided Axial Flux Switched Reluctance Motor for Mitigating Torque Ripple," *Can. J. Electr. Comput. Eng.*, vol. 38, no. 4, pp. 318–322, 2015, doi: 10.1109/CJECE.2015.2465160.

- [33] J. S. Varga, "Magnetic and Dimensional Properties of Axial Induction Motors," *IEEE Trans. Energy Convers.*, vol. EC-1, no. 2, pp. 137–144, Jun. 1986, doi: 10.1109/TEC.1986.4765712.
- [34] B. Dianati, S. Kahourzade, and A. Mahmoudi, "Optimization of Axial-Flux Induction Motors for the Application of Electric Vehicles Considering Driving Cycles," *IEEE Trans. Energy Convers.*, vol. 35, no. 3, pp. 1522–1533, 2020, doi: 10.1109/TEC.2020.2976625.
- [35] J. Mei, C. H. T. Lee, and J. L. Kirtley, "Design of Axial Flux Induction Motor With Reduced Back Iron for Electric Vehicles," *IEEE Trans. Veh. Technol.*, vol. 69, no. 1, pp. 293–301, Jan. 2020, doi: 10.1109/TVT.2019.2954084.
- [36] A. Multi and I. Garniwa, "Design of slotted core Axial Flux Wound Rotor synchronous generator," in *2013 International Conference on QiR*, Jun. 2013, pp. 185–191, doi: 10.1109/QiR.2013.6632562.
- [37] H. Won, Y.-K. Hong, M. Choi, H. Yoon, S. Li, and T. Haskew, "Novel Efficiency-shifting Radial-Axial Hybrid Interior Permanent Magnet Synchronous Motor for Electric Vehicle," in *2020 IEEE Energy Conversion Congress and Exposition (ECCE)*, Oct. 2020, pp. 47–52, doi: 10.1109/ECCE44975.2020.9236145.
- [38] J. M. Seo, J.-S. Ro, S.-H. Rhyu, I.-S. Jung, and H.-K. Jung, "Novel Hybrid Radial and Axial Flux Permanent-Magnet Machine Using Integrated Windings for High-Power Density," *IEEE Trans. Magn.*, vol. 51, no. 3, pp. 1–4, Mar. 2015, doi: 10.1109/TMAG.2014.2344044.
- [39] L. Zhou, F. Guo, H. Wang, and B. Wang, "High-Torque Direct-Drive Machine with Combined Axial- and Radial-flux Out-runner Vernier Permanent Magnet Motor," in *2021 IEEE International Electric Machines & Drives Conference (IEMDC)*, May 2021, pp. 1–8, doi: 10.1109/IEMDC47953.2021.9449499.
- [40] R. Nasiri-Zarandi, M. Mirsalim, and A. Tenconi, "A Novel Hybrid Hysteresis Motor With Combined Radial and Axial Flux Rotors," *IEEE Trans. Ind. Electron.*, vol. 63, no. 3, pp. 1684–1693, Mar. 2016, doi: 10.1109/TIE.2015.2498142.
- [41] S. Kahourzade, A. Mahmoudi, H. W. Ping, and M. N. Uddin, "A comprehensive review of axial-flux permanent-magnet machines," *Can. J. Electr. Comput. Eng.*, vol. 37, no. 1, pp. 19–33, 2014, doi: 10.1109/CJECE.2014.2309322.
- [42] S. M. Mirimani, A. Vahedi, and F. Marignetti, "Effect of Inclined Static Eccentricity Fault in Single Stator-Single Rotor Axial Flux Permanent Magnet Machines," *IEEE Trans. Magn.*, vol. 48, no. 1, pp. 143–149, Jan. 2012, doi: 10.1109/TMAG.2011.2161876.
- [43] R. D. Chavan and V. N. Bapat, "The study of different topologies of Axial Flux Permanent Magnet generator," in *2016 International Conference on Automatic Control and Dynamic Optimization Techniques (ICACDOT)*, 2016, pp. 202–206, doi: 10.1109/ICACDOT.2016.7877579.
- [44] S. O. Ani, H. Polinder, and J. A. Ferreira, "Low cost axial flux PM generator for small wind turbines," in *2012 IEEE Energy Conversion Congress and Exposition (ECCE)*, 2012, pp. 2350–2357, doi: 10.1109/ECCE.2012.6342461.
- [45] H. Hakala, "Integration of motor and hoisting machine changes the elevator business," in *International conference on electrical machines*, 2000, vol. 3, pp. 1242–1245.
- [46] A. Shahbaz, K. Sahib, and S. S. H. Bukhari, "A Comprehensive Review on Axial Flux Machines and Its Applications," 2019.

- [47] A. Parviainen, M. Niemela, and J. Pyrhonen, "Modeling of axial flux permanent-magnet machines," *IEEE Trans. Ind. Appl.*, vol. 40, no. 5, pp. 1333–1340, 2004, doi: 10.1109/TIA.2004.834086.
- [48] M. Aydin, S. Huang, and T. A. Lipo, "Torque quality and comparison of internal and external rotor axial flux surface-magnet disc machines," in *IECON'01. 27th Annual Conference of the IEEE Industrial Electronics Society (Cat. No.37243)*, Nov. 2001, vol. 2, pp. 1428–1434 vol.2, doi: 10.1109/IECON.2001.975992.
- [49] T. Husain, B. Tekgun, Y. Sozer, and M. Hamdan, "Comparison of axial flux machine performance with different rotor and stator configurations," in *2017 IEEE International Electric Machines and Drives Conference (IEMDC)*, May 2017, pp. 1–8, doi: 10.1109/IEMDC.2017.8002354.
- [50] F. Locment, E. Semail, and F. Piriou, "Design and study of a multiphase axial-flux machine," *IEEE Trans. Magn.*, vol. 42, no. 4, pp. 1427–1430, Apr. 2006, doi: 10.1109/TMAG.2006.872418.
- [51] F. Caricchi, F. Crescimbeni, and E. Santini, "Basic principle and design criteria of axial-flux PM machines having counterrotating rotors," *IEEE Trans. Ind. Appl.*, vol. 31, no. 5, pp. 1062–1068, 1995, doi: 10.1109/28.464520.
- [52] E. F. I. Raj, M. Appadurai, E. F. I. Rani, and I. Jenish, "Finite-element design and analysis of switched reluctance motor for automobile applications," *Multiscale Multidiscip. Model. Exp. Des.*, pp. 1–11, 2022, doi: 10.1007/s41939-022-00119-8.
- [53] L. Qin, H. Yang, S. Fang, Z. Pan, Y. Meng, and H. Lin, "Investigation of Axial Field Switched Flux Memory Machine by a Combined Analytical Method," *IEEE Trans. Magn.*, vol. 9464, no. 1, pp. 6–10, 2022, doi: 10.1109/TMAG.2022.3149952.
- [54] A. M. Shaikh, U. Abdul Majeed, M. F. Shaikh, S. Ahmed, M. Bux, and K. Sahib, "Design and Analysis of Single Stack AFPM Machines with and without Air Gap between Rotor and Magnetic Poles," *Sir Syed Univ. Res. J. Eng. Technol.*, vol. 12, no. 1, 2022.
- [55] F. Ismagilov, V. Vavilov, I. Sayakhov, A. Zhrebtsov, R. Dadoyan, and A. Nurieva, "Comparative Analysis of Disk Type Electrical Machines Designs," in *2022 29th International Workshop on Electric Drives: Advances in Power Electronics for Electric Drives (IWED)*, 2022, pp. 1–4, doi: 10.1109/IWED54598.2022.9722593.
- [56] Y. Zhao, F. Lu, C. Fan, and J. Yang, "A Novel Axial-Flux Dual-Stator Toothless Permanent Magnet Machine for Flywheel Energy Storage," *Symmetry (Basel)*, vol. 14, no. 1, 2022, doi: 10.3390/sym14010061.
- [57] R. Tsunata, M. Takemoto, S. Ogasawara, T. Saito, and T. Ueno, "SMC Development Guidelines for Axial Flux PM Machines Employing Coreless Rotor Structure for Enhancing Efficiency Based on Experimental Results," *IEEE Trans. Ind. Appl.*, vol. 9994, no. c, pp. 1–1, 2022, doi: 10.1109/tia.2022.3154336.
- [58] A. Havel, M. Sobek, L. Stepanec, and J. Strossa, "Optimization of Permanent Magnet Parameters in Axial Flux Rotary Converter for HEV Drive," *Energies*, vol. 15, no. 3, 2022, doi: 10.3390/en15030724.
- [59] L. Jia, M. Lin, K. Lin, W. Le, and A. Yang, "Design and Analysis of Dual-Rotor Modular-Stator Hybrid-Excited Axial-Flux Permanent Magnet Vernier Machine," *Energies*, vol. 15, no. 4, Feb. 2022, doi: 10.3390/en15041458.
- [60] Y. Li, L. Huang, M. Chen, P. Tan, and M. Hu, "A Linear-Rotating Axial Flux Permanent Magnet Generator for Direct Drive Wave Energy Conversion," 2021, doi:

- 10.1109/LDIA49489.2021.9505815.
- [61] H. Zhou and D. Gerling, "A Novel Multi-Layer Structure for Axial Flux Machines," *IEEE Trans. Magn.*, vol. 57, no. 11, pp. 1–12, Nov. 2021, doi: 10.1109/TMAG.2021.3111497.
- [62] R. Huang, C. Liu, Z. Song, and H. Zhao, "Design and analysis of a novel axial-radial flux permanent magnet machine with Halbach-Array permanent magnets," *Energies*, vol. 14, no. 12, Jun. 2021, doi: 10.3390/en14123639.
- [63] A. Colle, T. Lubin, J. L  v  que, and J. Leveque, "Design of a Superconducting Machine and its Cooling System for an Aeronautics Application," *Aeronaut. Appl. Eur. Phys. J. Appl. Phys.*, vol. 93, no. 3, 2021, doi: 10.1051/epjap/2020200027.
- [64] A. Colle, T. Lubin, S. Ayat, O. Gosselin, and J. Leveque, "Test of a Flux Modulation Superconducting Machine for Aircraft," in *Journal of Physics: Conference Series*, Jul. 2020, vol. 1590, no. 1, doi: 10.1088/1742-6596/1590/1/012052.
- [65] N. Baloch, S. Khaliq, and B.-I. Kwon, "Design and analysis of an axial flux dual stator flux modulating synchronous reluctance machine," *Int. J. Appl. Electromagn. Mech.*, vol. 59, no. 3, pp. 785–796, 2019, doi: 10.3233/JAE-171040.
- [66] S. Neethu, S. P. Nikam, S. Singh, S. Pal, A. K. Wankhede, and B. G. Fernandes, "High-speed coreless axial-flux permanent-magnet motor with printed circuit board winding," *IEEE Trans. Ind. Appl.*, vol. 55, no. 2, pp. 1954–1962, Mar. 2019, doi: 10.1109/TIA.2018.2872155.
- [67] S. Kahourzade, A. Mahmoudi, R. Ravji, and W. L. Soong, "Line-Start Axial-Flux PM Motors: Introduction of a New Machine Topology," 2019.
- [68] Z. Jun, L. Shaolong, S. Dandan, H. Qiaoli, and L. Guanghai, "Magnetic Field Calculation and Multi-objective Optimization of Axial Flux Permanent Magnet Generator with Coreless Stator Windings," *J Electr Eng Technol*, vol. 13, no. 4, pp. 1586–1595, 2018, doi: 10.5370/JEET.2018.13.4.1586.
- [69] L. A. J. Friedrich, K. Bastiaens, B. L. J. Gysen, D. C. J. Krop, and E. A. Lomonova, "Design of an Axial-Flux Permanent Magnet Machine for a Solar-Powered Electric Vehicle," 2018.
- [70] F. Chai, Y. Bi, and Y. Pei, "Magnet shape optimization of two-layer spoke-type axial flux interior permanent magnet machines," *Energies*, vol. 11, no. 1, 2018, doi: 10.3390/en11010015.
- [71] V. Rallabandi, N. Taran, D. M. Ionel, and I. G. Boldea, "MAGNUS – An Ultra-high Specific Torque PMAxial Flux Type Motor with Flux Focusing and Modulation," 2017.
- [72] T. Ishikawa, S. Amada, K. Segawa, and N. Kurita, "Proposal of a Radial- and Axial-Flux Permanent-Magnet Synchronous Generator," *IEEE Trans. Magn.*, vol. 53, no. 6, Jun. 2017, doi: 10.1109/TMAG.2017.2665440.
- [73] N. Ertugrul, R. Hasegawa, W. L. Soong, J. Gayler, S. Kloeden, and S. Kahourzade, "A Novel Tapered Rotating Electrical Machine Topology Utilizing Cut Amorphous Magnetic Material," *IEEE Trans. Magn.*, vol. 51, no. 7, Jul. 2015, doi: 10.1109/TMAG.2015.2399867.
- [74] H. Tausif, S. Yilmaz, H. Iqbal, and M. Eduard, "Design of a Modular E-Core Flux Concentrating Axial Flux Machine," 2015.
- [75] W. Zhao, T. A. Lipo, and B.-I. Kwon, "Design and Analysis of a Novel Dual Stator Axial Flux Spoke-type Ferrite Permanent Magnet Machine," 2013.

- [76] “Magnax website.” <https://www.magnax.com/> (accessed May 11, 2022).
- [77] “Traxial website.” <https://www.traxial.com/> (accessed May 11, 2022).
- [78] “Axyal website.” <https://www.axyal.com/> (accessed May 11, 2022).
- [79] “YASA website.” <https://www.yasa.com/> (accessed May 12, 2022).
- [80] “Turntide website.” <https://turntide.com/> (accessed May 12, 2022).
- [81] N. Abdel Karim, “Optimisation multi-critères et multi-physique d’aérogénérateurs à aimants permanents à flux axial,” Université du Havre, 2008.
- [82] H. Tiegna, “Contribution à la modélisation analytique des machines synchrones à flux axial à aimants permanents à attaque directe en vue de leur dimensionnement. Application aux éoliennes,” Université Le Havre Normandie, 2013.
- [83] M. Dhifli, “Contribution au développement de structures discoïdes de machines électriques à aimants permanents à commutation de flux pour la l’éolien,” 2016.
- [84] F. Cardarelli, *Materials Handbook*, 2nd ed. Springer_Verlag London Limited, 2008.
- [85] C. Cyr, “Modélisation et Caractérisation des Matériaux Magnétiques Composites Doux utilisés dans les Machines Electriques,” Arts et Métiers ParisTech, 2007.
- [86] R. Hilzinger and W. Rodewald, *Magnetic materials: fundamentals, products, properties, applications*. Vacuumschmelze, 2013.
- [87] H. Ennassiri, “Analyse magnéto-vibroacoustique des machines synchrones discoïdes à commutation de flux dédiées aux véhiculx électriques hybrides,” Normandie Université, 2018.
- [88] J.-C. Bavay and J. Verdun, “Alliages fer-silicium,” *Tech. l’ingénieur*, vol. D2110 v1, 1991.
- [89] A. Krings, “Iron losses in electrical machines - Influence of material properties , manufacturing processes , and inverter operation,” KTH Royal Institute of Technology, 2014.
- [90] S. Kleen, W. Ehrfeld, F. Michel, M. Nienhaus, and H. D. St’olting, “Penny-motor, a family of novel ultraflat electromagnetic micromotors,” 2000.
- [91] J. Legranger, “Contribution à l’étude des machines brushless à haut rendement dans les applications de moteurs-générateurs embarqués,” Université de Technologie de Compiègne, 2009.
- [92] M. Aydin and M. Gulec, “Reduction of Cogging Torque in Double-Rotor Axial-Flux Permanent-Magnet Disk Motors: A Review of Cost-Effective Magnet-Skewing Techniques With Experimental Verification,” *IEEE Trans. Ind. Electron.*, vol. 61, no. 9, pp. 5025–5034, 2014, doi: 10.1109/TIE.2013.2276777.
- [93] M. Liben and D. C. Ludois, “Analytical Design and Experimental Testing of a Self-Cooled, Toroidally Wound Ring Motor With Integrated Propeller for Electric Rotorcraft,” *IEEE Trans. Ind. Appl.*, vol. 57, no. 3, pp. 2342–2353, May 2021, doi: 10.1109/TIA.2021.3058197.
- [94] A. Ghaheri, A. Mohammadi Ajamloo, H. Torkaman, and E. Afjei, “Design, modelling and optimisation of a slot-less axial flux permanent magnet generator for direct-drive wind turbine application,” *IET Electr. Power Appl.*, vol. 14, no. 8, pp. 1327–1338, 2020, doi: <https://doi.org/10.1049/iet-epa.2019.0385>.
- [95] F. Sahin, “Design and development of a high-speed axial-flux permanent-magnet machine,” Technische Universiteit Eindhoven, 2001.
- [96] Q. A. Shah Syed, V. Solovieva, and I. Hahn, “Magnetization Characteristics and Loss

- Measurements of the Axial Flux Permanent Magnet Motor's Stator," in *2019 IEEE International Electric Machines & Drives Conference (IEMDC)*, May 2019, pp. 1061–1066, doi: 10.1109/IEMDC.2019.8785080.
- [97] S. Sun, F. Jiang, T. Li, B. Xu, and K. Yang, "Comparison of A Multi-Stage Axial Flux Permanent Magnet Machine With Different Stator Core Materials," *IEEE Trans. Appl. Supercond.*, vol. 30, no. 4, pp. 1–6, Jun. 2020, doi: 10.1109/TASC.2020.2990761.
- [98] M. Polikarpova *et al.*, "Hybrid Cooling Method of Axial-Flux Permanent-Magnet Machines for Vehicle Applications," *IEEE Trans. Ind. Electron.*, vol. 62, no. 12, 2015.
- [99] V. Madonna, P. Giangrande, A. Walker, and M. Galea, "On the Effects of Advanced End-Winding Cooling on the Design and Performance of Electrical Machines," in *2018 XIII International Conference on Electrical Machines (ICEM)*, 2018, pp. 311–317, doi: 10.1109/ICELMACH.2018.8507170.
- [100] K. M. Rahman, N. R. Patel, T. G. Ward, J. M. Nagashima, F. Caricchi, and F. Crescimbeni, "Application of Direct-Drive Wheel Motor for Fuel Cell Electric and Hybrid Electric Vehicle Propulsion System," *IEEE Trans. Ind. Appl.*, vol. 42, no. 5, pp. 1185–1192, 2006, doi: 10.1109/TIA.2006.880886.
- [101] H. Vansompel, A. Hemeida, and P. Sergeant, "Stator heat extraction system for axial flux yokeless and segmented armature machines," in *2017 IEEE International Electric Machines and Drives Conference (IEMDC)*, May 2017, pp. 1–7, doi: 10.1109/IEMDC.2017.8001873.
- [102] Y. Bi, F. Chai, and L. Chen, "The Study of Cooling Enhancement in Axial Flux Permanent Magnet Motors for Electric Vehicles," *IEEE Trans. Ind. Appl.*, vol. 57, no. 5, pp. 4831–4839, 2021, doi: 10.1109/TIA.2021.3098251.
- [103] T. Woolmer, "Machine cooling systems," 20170012480A1, 2017.
- [104] F. Marcolini, G. De Donato, and F. Caricchi, "Direct Oil Cooling of End-Windings in Torus-Type Axial-Flux Permanent-Magnet Machines," in *2019 IEEE Energy Conversion Congress and Exposition (ECCE)*, 2019, pp. 5645–5651, doi: 10.1109/ECCE.2019.8912993.
- [105] R. Camilleri, T. Woolmer, A. Court, and M. D. McCulloch, "Investigation into the temperature profile of a liquid cooled YASA© AFPM machine," in *6th IET International Conference on Power Electronics, Machines and Drives (PEMD 2012)*, Mar. 2012, pp. 1–8, doi: 10.1049/cp.2012.0281.
- [106] R. Wrobel, G. Vainel, C. Copeland, T. Duda, D. Staton, and P. Mellor, "Investigation of mechanical loss and heat transfer in an axial-flux PM machine," in *2013 IEEE Energy Conversion Congress and Exposition*, 2013, pp. 4372–4379, doi: 10.1109/ECCE.2013.6647285.
- [107] Z. Xu *et al.*, "Thermal management of a permanent magnet motor for an directly coupled pump," in *2016 XXII International Conference on Electrical Machines (ICEM)*, 2016, pp. 2738–2744, doi: 10.1109/ICELMACH.2016.7732909.
- [108] N. S., S. P. Nikam, S. Pal, A. K. Wankhede, and B. G. Fernandes, "Performance Comparison Between PCB-Stator and Laminated-Core-Stator-Based Designs of Axial Flux Permanent Magnet Motors for High-Speed Low-Power Applications," *IEEE Trans. Ind. Electron.*, vol. 67, no. 7, pp. 5269–5277, Jul. 2020, doi: 10.1109/TIE.2019.2931503.
- [109] W. Fei, P. C. K. Luk, and T. S. El-Hasan, "Rotor Integrity Design for a High-Speed Modular Air-Cored Axial-Flux Permanent-Magnet Generator," *IEEE Trans. Ind.*

- Electron.*, vol. 58, no. 9, pp. 3848–3858, 2011, doi: 10.1109/TIE.2011.2106097.
- [110] J. D. Ede, Z. Q. Zhu, and D. Howe, “Rotor resonances of high-speed permanent-magnet brushless machines,” *IEEE Trans. Ind. Appl.*, vol. 38, no. 6, pp. 1542–1548, Nov. 2002, doi: 10.1109/TIA.2002.804765.

Chapter 2: Multiphysics Modelling of Axial Flux Machines

- 1. Introduction**
- 2. Analytical Magnetic Modelling Based on the Formal Solution of Maxwell's Equations**
- 3. Mesh Based Generated Reluctance Network (MBGRN) Modelling**
- 4. Lumped Parameter Thermal Modelling**
- 5. Magnetic Finite Element Method**
- 6. Mechanical Finite Element Method**
- 7. Conclusion**

I. Introduction

The design process of electrical machines require pre-sizing tools to quickly obtain a set of geometrical and physical parameters that will be used later on as inputs to more precise validation tools to fine tune the design and satisfy required specifications.

Pre-sizing tools include analytical models and lumped parameter models, and validation tools are based on the finite elements method.

Analytical models are based on the formal solution of Maxwell's equations and are machine specific, and lumped parameter models include reluctance network models and nodal thermal models and are based on an analogy with electrical circuits. Reluctance network models can be either expert models that are also machine specific or mesh based models that are independent of machine type.

Nodal thermal models model thermal behavior using nodal networks of conductances, capacitances and heat sources where each node has a temperature and heat is transferred from the node with the highest temperature to the node with lowest temperature.

The advantage of these pre-sizing models is the reduced computation time compared to finite element models, but this comes at the cost of precision.

The finite elements method is the most precise and widely used method to size an electrical machine electromagnetically, mechanically and thermally as it can mimic to a high extent the results obtained by experimental studies.

In this chapter, machine sizing tools were developed and explained starting from the analytical model based on the formal solution of Maxwell's equations in the different regions of an axial flux machine, then the mesh based generated reluctance network (MBGRN) method is explained, illustrating the concept of flux tube, model equations, modelling method of sources, numbering of blocks, boundary conditions, motion processing, modelling of non-linearities, computation of local and global quantities and the algorithm used to implement the method in MATLAB. After that, a 2D multi-slice version of the method is applied to a switched reluctance machine in both linear and non-linear magnetic material conditions to assess magnetic flux density and torque. The same process is then repeated with a quasi-3D version where the slices are connected by means of reluctances in the radial direction. The nodal thermal model is then explained illustrating heat transfer mechanisms and the solved heat equation. The finite element formulations used for electromagnetic and mechanical simulations are then presented; these include magneto-static and magneto-dynamic formulations for electromagnetic simulations and strong and weak formulations for mechanical simulations. The chapter ends with a conclusion that summarizes the whole work.

II. Analytical Modelling of Axial Flux Machines

1. Assumptions and solved equations

The SIMUMSAP tool used to pre-size the machine is based on an analytical model obtained by the exact 2D solution of the magnetic field. It is assumed that magnetic material relative permeability as well as their resistivity is infinite and permanent magnet permeability is equal to that of air, their resistivity infinite, and their remanence and axially oriented. Also, the volumic density of electrostatic charges is zero. The machine is divided into slices in the radial direction, then Maxwells equations are solved at mean radius for a given slice in the

different regions indicated by Fig. 2.1 by the separation of variables method. The contribution of the slices are summed up to obtain the values of global quantities. The regions in Fig. 2.1 are slots (I), slot opening (II), air gap (III) and magnets (IV). The method will be briefly exposed, more detail on the mathematical derivation of the method is available [1] and [2].

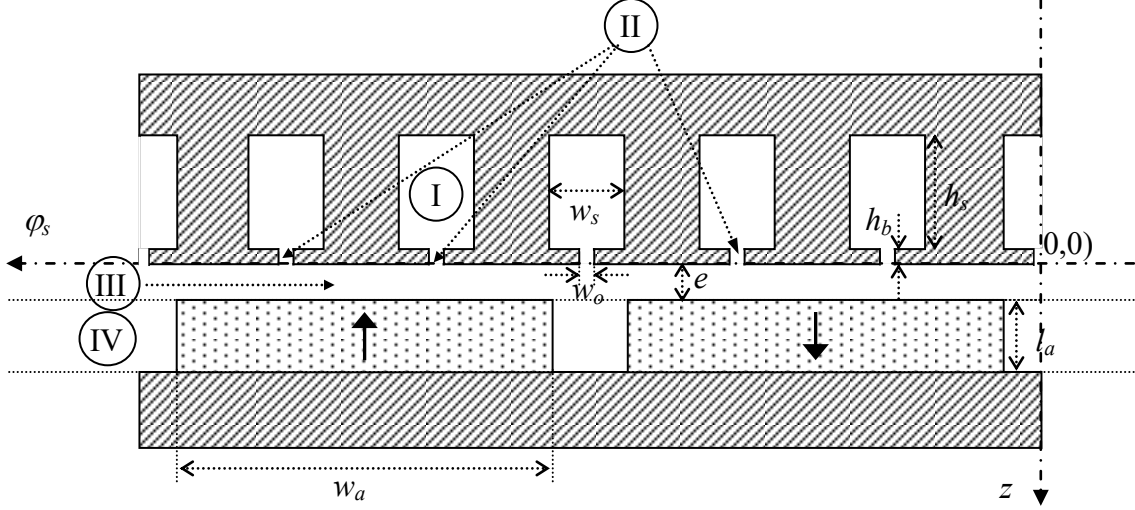


Fig. 2.1: Modeled pattern of the machine

The equation to be solved in the different regions is:

$$\Delta \vec{A} + \mu_0 \vec{J} + \mu_0 \vec{\nabla} \times \vec{M} = 0 \quad (2.1)$$

Where \vec{A} is the magnetic potential vector, \vec{J} is the current density and \vec{M} is the remanent magnetization.

The field vectors \vec{B} and \vec{H} , in the different regions, are coupled by:

$$\vec{B} = \begin{cases} \mu_0 \vec{H} & \text{in I, II and III} \\ \mu_0 (\vec{H} + \vec{M}) & \text{in IV} \end{cases} \quad (2.2)$$

As \vec{A} has a component only in the z-direction and by writing (2.49) in Cartesian coordinates, we obtain:

$$\begin{cases} \frac{1}{r^2} \frac{\partial^2 A}{\partial \varphi^2} + \frac{\partial^2 A}{\partial z^2} = -\mu_0 J & \text{in I} \\ \frac{1}{r^2} \frac{\partial^2 A}{\partial \varphi^2} + \frac{\partial^2 A}{\partial z^2} = 0 & \text{in II and III} \\ \frac{1}{r^2} \frac{\partial^2 A}{\partial \varphi^2} + \frac{\partial^2 A}{\partial z^2} = -\frac{1}{r} \frac{\partial B_r}{\partial \varphi} & \text{in IV} \end{cases} \quad (2.3)$$

In order for the remnant flux density in magnets to have the same form as that in regions III and IV, it is written as follows:

$$B_r(\varphi) = \sum_{k \neq 0} E_k^M \cos(k\lambda_p \varphi) + F_k^M \sin(k\lambda_p \varphi) \quad \text{Where } \lambda_p = \text{gcd}(N_s, p) \quad (2.4)$$

The boundary conditions required to solve the equations in each region are the following:

$$\begin{cases} B_z^{(1l)}(\varphi_{1l}, z) = 0 \\ B_z^{(1l)}(\varphi_{1l} + w_s, z) = 0 \\ B_\varphi^{(1l)}(\varphi, -h_b - h_s) = 0 \end{cases} \quad (2.5)$$

$$\begin{cases} B_z^{(2l)}(\varphi_{2l}, z) = 0 \\ B_z^{(2l)}(\varphi_{2l} + w_o, z) = 0 \end{cases} \quad (2.6)$$

$$B_\varphi^{(4)}(\varphi, l_a + e) = 0 \quad (2.7)$$

$$\varphi_{1l} = -\frac{w_s}{2} + l \frac{2\pi}{N_s} \quad \text{where} \quad l = 0..N_s - 1 \quad (2.8)$$

$$\varphi_{2l} = -\frac{w_o}{2} + l \frac{2\pi}{N_s} \quad \text{where} \quad l = 0..N_s - 1 \quad (2.9)$$

Where N_s is the total number of slots.

2. Solution in the different regions

Solving for the magnetic vector potential in the different regions and computing the normal and tangential components of the magnetic flux density we obtain:

a) Region I (slots): $-h_s - h_b \leq z \leq -h_b$

$$\begin{aligned} A^{(1l)} &= a_0^{(1l)} - \frac{\mu_0}{2} J^{(l)} (z + h_b + h_s)^2 \\ &+ \sum_{m \neq 0} \frac{r w_s}{m \pi} f_m^{(1l)} \frac{\cosh \left[\frac{m \pi}{r w_s} (z + h_b + h_s) \right]}{\cosh \left(\frac{m \pi (h_b + h_s)}{r w_s} \right)} \cos \left[\frac{m \pi}{w_s} (\varphi - \varphi_{1l}) \right] \end{aligned} \quad (2.10)$$

$$\begin{aligned} B_\varphi^{(1l)}(\varphi, z) &= -\mu_0 J^{(l)} (z + h_b + h_s) \\ &+ \sum_{m \neq 0} f_m^{(1l)} \frac{\sinh \left[\frac{m \pi}{r w_s} (z + h_b + h_s) \right]}{\cosh \left(\frac{m \pi}{r w_s} (h_b + h_s) \right)} \cos \left[\frac{m \pi}{w_s} (\varphi - \varphi_{1l}) \right] \end{aligned} \quad (2.11)$$

$$B_z^{(1l)}(\varphi, z) = \sum_{m \neq 0} f_m^{(1l)} \frac{\cosh\left[\frac{m\pi}{rw_s}(z + h_b + h_s)\right]}{\cosh\left(\frac{m\pi}{rw_s}(h_b + h_s)\right)} \sin\left[\frac{m\pi}{w_s}(\varphi - \varphi_{1l})\right] \quad (2.12)$$

b) Region II (slot opening): $-h_b \leq z \leq 0$

$$A^{(2l)} = a_0^{(2l)} - \mu_0 J^{(l)} h_s \frac{w_s}{w_o} z + \sum_{m \neq 0} \frac{rw_o}{m\pi} \left[C_m^{(2l)} \cosh\left(\frac{m\pi}{rw_o} z\right) + D_m^{(2l)} \sinh\left(\frac{m\pi}{rw_o} z\right) \right] \cdot \cos\left[\frac{m\pi}{w_o}(\varphi - \varphi_{2l})\right] \quad (2.13)$$

$$B_\varphi^{(2l)}(\varphi, z) = -\mu_0 J^{(l)} \frac{w_s}{w_o} h_s + \sum_{m \neq 0} \left[C_m^{(2l)} \sinh\left(\frac{m\pi}{rw_o} z\right) + D_m^{(2l)} \cosh\left(\frac{m\pi}{rw_o} z\right) \right] \cdot \cos\left[\frac{m\pi}{w_o}(\varphi - \varphi_{2l})\right] \quad (2.14)$$

$$B_z^{(2l)}(\varphi, z) = \sum_{m \neq 0} \left[C_m^{(2l)} \cosh\left(\frac{m\pi}{rw_o} z\right) + D_m^{(2l)} \sinh\left(\frac{m\pi}{rw_o} z\right) \right] \cdot \sin\left[\frac{m\pi}{w_o}(\varphi - \varphi_{2l})\right] \quad (2.15)$$

c) Region III (air gap): $0 \leq z \leq e$

$$A^{(3)}(\varphi, z) = a_0^{(3)} + \sum_{k \neq 0} \frac{r}{k\lambda_p} \left\{ \begin{array}{l} \left[C_k^{(3)} \operatorname{ch}\left(\frac{k\lambda_p z}{r}\right) + D_k^{(3)} \operatorname{sh}\left(\frac{k\lambda_p z}{r}\right) \right] \cos(k\lambda_p \varphi) \\ + \left[E_k^{(3)} \operatorname{ch}\left(\frac{k\lambda_p z}{r}\right) + F_k^{(3)} \operatorname{sh}\left(\frac{k\lambda_p z}{r}\right) \right] \sin(k\lambda_p \varphi) \end{array} \right\} \quad (2.16)$$

$$B_z^{(3)}(\varphi, z) = \sum_{k \neq 0} \left[\begin{array}{l} \left[C_k^{(3)} \operatorname{ch}\left(\frac{k\lambda_p z}{r}\right) + D_k^{(3)} \operatorname{sh}\left(\frac{k\lambda_p z}{r}\right) \right] \sin(k\lambda_p \varphi) \\ - \left[E_k^{(3)} \operatorname{ch}\left(\frac{k\lambda_p z}{r}\right) + F_k^{(3)} \operatorname{sh}\left(\frac{k\lambda_p z}{r}\right) \right] \cos(k\lambda_p \varphi) \end{array} \right] \quad (2.17)$$

$$B_\varphi^{(3)}(\varphi, z) = \sum_{k \neq 0} \left[\begin{array}{l} \left[C_k^{(3)} \operatorname{sh}\left(\frac{k\lambda_p z}{r}\right) + D_k^{(3)} \operatorname{ch}\left(\frac{k\lambda_p z}{r}\right) \right] \cos(k\lambda_p \varphi) \\ + \left[E_k^{(3)} \operatorname{sh}\left(\frac{k\lambda_p z}{r}\right) + F_k^{(3)} \operatorname{ch}\left(\frac{k\lambda_p z}{r}\right) \right] \sin(k\lambda_p \varphi) \end{array} \right] \quad (2.18)$$

d) Region IV (magnets): $e \leq z \leq e + l_a$

$$A^{(4)}(\varphi, z) = a_0^{(4)} + \sum_{k \neq 0} \frac{r}{k\lambda_p} \left\{ \left[C_k^{(4)} \left(\cosh\left(\frac{k\lambda_p z}{r}\right) - \tanh\left(\frac{k\lambda_p(l_a + e)}{r}\right) \sinh\left(\frac{k\lambda_p z}{r}\right) \right) + F_k^M \right] \cos(k\lambda_p \varphi) \right. \\ \left. + \left[E_k^{(4)} \left(\cosh\left(\frac{k\lambda_p z}{r}\right) - \tanh\left(\frac{k\lambda_p(l_a + e)}{r}\right) \sinh\left(\frac{k\lambda_p z}{r}\right) \right) - E_k^M \right] \sin(k\lambda_p \varphi) \right\} \quad (2.19)$$

$$B_z^{(4)}(\varphi, z) = \sum_{k \neq 0} \left[C_k^{(4)} \left(\cosh\left(\frac{k\lambda_p z}{r}\right) - \tanh\left(\frac{k\lambda_p(l_a + e)}{r}\right) \sinh\left(\frac{k\lambda_p z}{r}\right) \right) + F_k^M \right] \sin(k\lambda_p \varphi) \\ - \left[E_k^{(4)} \left(\cosh\left(\frac{k\lambda_p z}{r}\right) - \tanh\left(\frac{k\lambda_p(l_a + e)}{r}\right) \sinh\left(\frac{k\lambda_p z}{r}\right) \right) - E_k^M \right] \cos(k\lambda_p \varphi) \quad (2.20)$$

$$B_\varphi^{(4)}(\varphi, z) = \sum_{k \neq 0} \left[\sinh\left(\frac{k\lambda_p z}{r}\right) - \tanh\left(\frac{k\lambda_p(l_a + e)}{r}\right) \cosh\left(\frac{k\lambda_p z}{r}\right) \right] \left[C_k^{(4)} \cos(k\lambda_p \varphi) + E_k^{(4)} \sin(k\lambda_p \varphi) \right] \quad (2.21)$$

3. Continuity conditions

In order to determine the Fourier coefficients appearing in the above equations, the following continuity conditions are exploited:

d) From region I to region II

$$\begin{cases} B_\varphi^{(1l)}(\varphi, -h_b) = B_\varphi^{(2l)}(\varphi, -h_b) \\ B_z^{(1l)}(\varphi, -h_b) = B_z^{(2l)}(\varphi, -h_b) \end{cases} \quad \text{for} \quad \begin{cases} \varphi_{2l} \leq \varphi \leq \varphi_{2l} + w_o \\ l = 0..N_s - 1 \end{cases} \quad (2.22)$$

$$\begin{cases} B_\varphi^{(1l)}(\varphi, -h_b) = 0 \\ B_\varphi^{(1l)}(\varphi, -h_b) = B_\varphi^{(2l)}(\varphi, -h_b) \end{cases} \quad \text{for} \quad \begin{cases} \varphi \in [\varphi_{1l}; \varphi_{2l}] \cup [\varphi_{2l} + w_o; \varphi_{1l} + w_s] \\ \varphi \in [\varphi_{2l}; \varphi_{2l} + w_o], \quad l = 0..N_s - 1 \end{cases} \quad (2.23)$$

$$\begin{cases} B_z^{(1l)}(\varphi, -h_b) = B_z^{(1l)}(\varphi, -h_b) \\ B_z^{(1l)}(\varphi, -h_b) = B_z^{(2l)}(\varphi, -h_b) \end{cases} \quad \text{for} \quad \begin{cases} \varphi \in [\varphi_{1l}; \varphi_{2l}] \cup [\varphi_{2l} + w_o; \varphi_{1l} + w_s] \\ \varphi \in [\varphi_{2l}; \varphi_{2l} + w_o], \quad l = 0..N_s - 1 \end{cases} \quad (2.24)$$

e) From region II to region III

$$\begin{cases} B_\varphi^{(2l)}(\varphi, 0) = B_\varphi^{(3)}(\varphi, 0) \\ B_z^{(2l)}(\varphi, 0) = B_z^{(3)}(\varphi, 0) \end{cases} \quad \text{for} \quad \begin{cases} \varphi_{2l} \leq \varphi \leq \varphi_{2l} + w_o \\ l = 0..N_s - 1 \end{cases} \quad (2.25)$$

$$B_\varphi^{(3)}(\varphi, 0) = 0 \quad \text{for} \quad \varphi_{2l} + w_o \leq \varphi \leq \varphi_{2,l+1} \quad (2.26)$$

f) From region III to region IV

$$B_z^{(3)}(\varphi_s, e) = B_z^{(4)}(\varphi_r, e) \quad \text{and} \quad B_\varphi^{(3)}(\varphi_s, e) = B_\varphi^{(4)}(\varphi_r, e)$$

The angular positions of the rotor and stator coordinate systems are linked by the following equation:

$$\varphi_s = \varphi_r + \theta$$

where θ is the position of the rotor relative to the stator.

4. Determination of the vector potential constants

The determination of arbitrary constants of vector potential expressions in the different regions is based on the assumption of the nullity of the constant of region IV:

$$a_0^{(4)} = 0 \quad (2.27)$$

This choice leads to the nullity of the vector potential constant in region III due to the continuity of the vector potential at the boundary with region IV. :

$$a_0^{(3)} = 0 \quad (2.28)$$

Moreover, the continuity of the vector potential between region III and region II leads to the following:

$$A^{(2l)}(\varphi, 0) = A^{(3)}(\varphi, 0) \quad \text{for} \quad \varphi_{2l} < \varphi < \varphi_{2l} + w_o \quad \text{and} \quad l = 0..N_{sp} - 1 \quad (2.29)$$

Thus:

$$a_0^{(2l)} + \sum_{m \neq 0} \frac{r w_o}{m \pi} C_m^{(2l)} \cos \left[\frac{m \pi}{w_o} (\varphi - \varphi_{2l}) \right] = \sum_{k \neq 0} \frac{r}{k \lambda_p} \left\{ C_k^{(3)} \cos(k \lambda_p \varphi) + E_k^{(3)} \sin(k \lambda_p \varphi) \right\} \quad (2.30)$$

Integrating the previous equation along w_o makes it possible to write:

$$a_0^{(2l)} = \frac{1}{w_o} \int_{\varphi_{2l}}^{\varphi_{2l} + w_o} \left[\sum_{k \neq 0} \frac{r}{k \lambda_p} \left\{ C_k^{(3)} \cos(k \lambda_p \varphi) + E_k^{(3)} \sin(k \lambda_p \varphi) \right\} \right] d\varphi \quad (2.31)$$

After development, we obtain the constants of the vector potential in the slot openings:

$$a_0^{(2l)} = \frac{2r}{\lambda_p^2 w_o} \sum_{k \neq 0} \frac{1}{k^2} \left\{ C_k^{(3)} \cos \left(k \lambda_p l \frac{2\pi}{N_s} \right) + E_k^{(3)} \sin \left(k \lambda_p l \frac{2\pi}{N_s} \right) \right\} \sin \left(k \frac{\lambda_p w_o}{2} \right) \quad (2.32)$$

Similarly, the continuity of the vector potential at the boundary between the slot openings and slots makes it possible to write:

$$A^{(1l)}(\varphi, -h_b) = A^{(2l)}(\varphi, -h_b) \quad \text{for} \quad \varphi_{2l} < \varphi < \varphi_{2l} + w_o \quad \text{and} \quad l = 0..N_s - 1 \quad (2.33)$$

Thus:

$$a_0^{(1l)} - \mu_0 J^{(l)} h_s^2 + \sum_{m \neq 0} \frac{r w_s}{m \pi} f_m^{(1l)} \frac{\cosh\left[\frac{m \pi}{r w_s} h_s\right]}{\cosh\left(\frac{m \pi (h_b + h_s)}{r w_s}\right)} \cos\left[\frac{m \pi}{w_s} (\varphi - \varphi_{1l})\right] = \quad (2.34)$$

$$a_0^{(2l)} + \mu_0 J^{(l)} h_s h_b \frac{w_s}{w_o} + \sum_{m \neq 0} \frac{r w_o}{m \pi} \left[C_m^{(2l)} \cosh\left(\frac{m \pi}{r w_o} h_b\right) - D_m^{(2l)} \sinh\left(\frac{m \pi}{r w_o} h_b\right) \right] \cdot \cos\left[\frac{m \pi}{w_o} (\varphi - \varphi_{2l})\right]$$

The same integration as above allows to write:

$$a_0^{(1l)} - \mu_0 J^{(l)} h_s^2 = a_0^{(2l)} + \mu_0 J^{(l)} h_s h_b \frac{w_s}{w_o} + \frac{1}{w_o} \int_{\varphi_{2l}}^{\varphi_{2l} + w_o} \left[\sum_{m \neq 0} \frac{r w_s}{m \pi} f_m^{(1l)} \frac{\cosh\left(\frac{m \pi}{r w_s} h_s\right)}{\cosh\left(\frac{m \pi (h_b + h_s)}{r w_s}\right)} \cos\left[\frac{m \pi}{w_s} (\varphi - \varphi_{1l})\right] \right] d\varphi \quad (2.35)$$

After development, the expression determining the constants of the vector potential in the slots is obtained:

$$a_0^{(1l)} = a_0^{(2l)} + \mu_0 J^{(l)} h_s \left(h_s + h_b \frac{w_s}{w_o} \right) + \frac{2 r w_s^2}{\pi^2 w_o} \sum_{m \neq 0} \frac{1}{m^2} f_m^{(1l)} \frac{\cosh\left(\frac{m \pi}{r w_s} h_s\right)}{\cosh\left(\frac{m \pi (h_b + h_s)}{r w_s}\right)} \cos\left(\frac{m \pi}{2}\right) \sin\left(m \frac{\pi}{2} \frac{w_o}{w_s}\right) \quad (2.36)$$

5. Flux & EMF

The flux passing through a phase 'j' at no load is given by:

$$\begin{aligned} \phi_{Sj}(\theta) &= p N_{sp} \int_{R_i}^{R_o} \int_{\varphi_{s1}}^{\varphi_{s2}} B_z^{(3)}(\varphi_s, 0, \theta) r dr d\varphi_s \\ &= \frac{p(R_o^2 - R_i^2)}{2} \int_0^{2\pi/p} F_{Dj}^{(ph)}(\varphi_s) B_z^{(3)}(\varphi_s, 0, \theta) d\varphi_s \end{aligned} \quad (2.37)$$

where N_{sp} is the number of turns in series of the phase and $F_{Dj}^{(ph)}$ is the distribution function of phase 'j' that can be written in the following manner:

$$F_{Dj}^{(ph)} = E_{d0} + \sum_{k \neq 0} E_{dk} \cos(k \lambda_p \varphi_s) + F_{dk} \sin(k \lambda_p \varphi_s) \quad (2.38)$$

Replacing $B_z^{(3)}(\varphi_s, 0, \theta)$ by its expression in (61) and expanding the calculations, we arrive at the following expression for the flux of phase 'j':

$$\phi_{Sj}(\theta) = \frac{\pi(R_o^2 - R_i^2)}{2\lambda_p} \sum_{n \neq 0} (F_{dn} C_n^{(3)} - E_{dn} E_n^{(3)}) \quad (2.39)$$

The EMF is deduced taking the derivative of the no load phase flux:

$$e_j(t) = \frac{d\phi_{Sj}}{dt} = \Omega \frac{d\phi_{Sj}}{d\theta} \quad (2.40)$$

6. Electromagnetic torque

The Maxwell tensor method is used for the calculation of the electromagnetic torque on the surface of the permanent magnets. The expression of the electromagnetic force exerted on a given volume \mathcal{V} having a surface S surrounded by a medium of low relative permeability, is deduced from the expression of the Poynting vector expressing the exchange of electromagnetic power between this volume and the external environment:

$$\vec{F} = \int_{S(v)} \left(\mu_0 (\vec{H} \cdot \vec{n}_s) \vec{H} - \frac{1}{2} \mu_0 H^2 \vec{n}_s \right) dS \quad (2.41)$$

For an axial flux machine, the vector normal to the surface of volume \mathcal{V} and leaving this surface is written:

$$\vec{n}_s = -\vec{e}_z \quad \text{and} \quad \vec{H} = H_\varphi \vec{e}_\varphi + H_z \vec{e}_z \quad (2.42)$$

The surface density of electromagnetic force decomposes as follows in the cylindrical coordinate system:

$$d\vec{F} = dF_t \vec{e}_t + dF_n \vec{e}_n = - \left(\mu_0 H_z H_\varphi \vec{e}_\varphi + \frac{1}{2} \mu_0 (H_z^2 - H_\varphi^2) \vec{e}_z \right) dS \quad (2.43)$$

The torque exerted on the rotor is therefore written :

$$\vec{T} = \int \vec{r} \wedge d\vec{F} = - \left(\iint_S \mu_0 H_z H_\varphi r dS \right) \cdot \vec{e}_z + \left(\iint_S \frac{1}{2} \mu_0 (H_z^2 - H_\varphi^2) r dS \right) \cdot \vec{e}_\varphi \quad (2.44)$$

For the axial flux machine, only the axial component of the torque gives rise to the rotational movement of the rotor and it is written considering that the magnetic flux density is negligible on the lateral surface of the rotor as well as on its external base:

$$\vec{\Gamma}_{elm} = - \left(\frac{p(R_o^3 - R_i^3)}{3} \cdot \int_0^{2\pi/\lambda_p} \mu_0 H_z H_\varphi d\varphi \right) \cdot \vec{e}_z \quad (2.45)$$

The algebraic value of the electromechanical torque is therefore expressed as:

$$\Gamma_{elm} = - \frac{p(R_o^3 - R_i^3)}{3\mu_0} \cdot \int_0^{2\pi/\lambda_p} B_z^{(3)}(\varphi_s, e) B_\varphi^{(3)}(\varphi_s, e) d\varphi_s \quad (2.46)$$

By replacing the components of the magnetic flux density on the surface of the rotor by their expressions and developing the calculation of the integral, the following expression is obtained for the torque:

$$\Gamma_{elm} = -\frac{\pi(R_o^3 - R_i^3)}{3\mu_0} \times \sum_{n \neq 0} C_n^{(3)} F_n^{(3)} - D_n^{(3)} E_n^{(3)} \quad (2.47)$$

III. Mesh Based Generated Reluctance Network Method

Reluctance network models have been used as a design tool for electrical machines since the beginning of the last century. Despite the use of finite element analysis (FEA) powered by the rapid development of digital computers since the 1980's, reluctance networks (RN) remained part of design routines. This being mainly for their reasonable computation time vs. accuracy ratio [3].

RN methods are based on the analogy between magnetic and electric circuits with natural simplicity [4]. Consideration of magnetic saturation of ferromagnetic materials in reluctance networks is possible by linking material characteristics. This makes RNs extensively employed in designing and analyzing various types of electrical machines [5][6][7].

In scientific literature, RNs have remained a subject of research in recent years. Hane et al. presented in [8] the RN model of a three-phase-laminated-core variable inductor considering hysteresis. The authors in [9] developed a new RN based method with complementary distributed magneto-motive forces (MMF) in a fully meshed RN model with reluctance block elements. In [10], hybrid analytical models (HAM) are used to compute the magnetic field solution in constant permeability regions via an analytical formal solution, while the field in the slots and the ferromagnetic parts is evaluated through RN modeling.

Although the meshed RN method is relatively old and gives relatively good results, it is not yet widely spread in terms of design software tools compared to FEA [11]. Some computer-aided design software using RN modeling exist: Turbo-TCM [12] models small power alternators, RMXprt® [13] in the ANSYS® electromagnetic package features predefined topologies of stators and rotors, SPEED [14] combines analytical formulations with FEA and Reluctool® [15] based on lumped parameter magnetic equivalent circuits (MECs) requiring designer's expertise.

Modeling of axial flux machines requires considering 3D effects. One way to do this is by dividing the machine into several slices. Multislice FEA modeling for example can be used to evaluate torque in skewed machines [16]. Multislice hybrid modeling was used to estimate iron loss in axial flux permanent magnet machines [17].

1. Overview of the modelling approach

In this section, the different phases of the proposed method are presented detailing the automatically generated MBGRN algorithm.

a) Flux Tube

The RN method is based on partitioning the space where the magnetic field exists into flux tubes (Fig. 2.2) with prior knowledge of flux direction. A flux tube is a geometrical figure in which all lines of flux are perpendicular to its base and no lines of flux cut its sides. The bases of a flux tube - that contains no current - are equipotential planes. The ratio R of potential difference at both ends of the tube and the flux through it is a function of flux tube geometry and magnetic characteristics of the medium [18]:

$$R = \int_0^l \frac{dx}{c(x)A(x)} \quad (2.48)$$

where l is the total flux tube length, A is its cross-sectional area, and c is a function of material properties. For magnetic fields, R is defined as the reluctance and μ is the material's magnetic permeability.

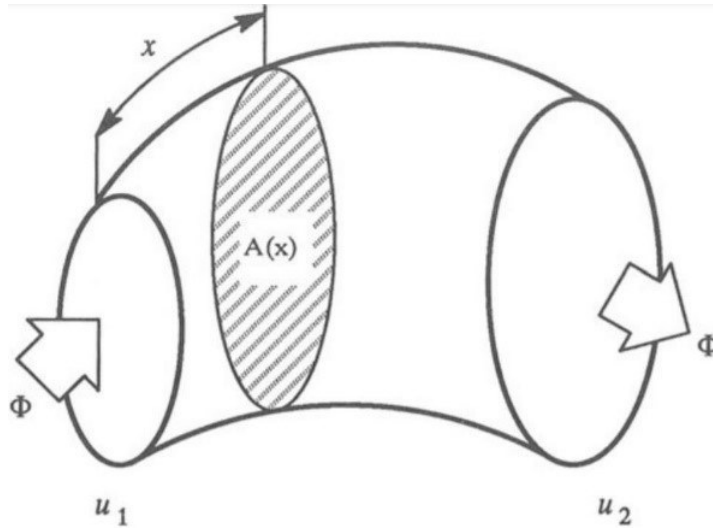


Fig. 2.2: Flux tube [18]

The Maxwell-Ampere equation in the tube is given by [19]:

$$\vec{\nabla} \times \vec{H} = \frac{\partial \vec{D}}{\partial t} + \vec{j} \quad (2.49)$$

Where \vec{H} is the magnetic field strength, \vec{D} the electric flux density and \vec{j} the current density.

In the stationary domain, where electromagnetic properties at low frequency are within the limits of a few tens of kilohertz, displacement current $\frac{\partial \vec{D}}{\partial t}$ is neglected [20]. Moreover, as we suppose that no current passes through the flux tube and therefore $\vec{j} = \vec{0}$, equation (2.49) becomes:

$$\vec{\nabla} \times \vec{H} = 0 \quad (2.50)$$

From (2.50) we deduce that \vec{H} can be written as a function of a scalar magnetic potential U :

$$\vec{H} = -\nabla U \quad (2.51)$$

U is in fact the magnetic scalar potential on either sides of the tube.

b) Model Equations

The conservation of flux allows applying Kirchhoff's current law to a flux tube. The sum of incoming fluxes to a node is equal to the sum of outgoing fluxes (Fig. 2.3). For a node i connected to n other nodes through branches which can contain reluctances and flux sources, we can write:

$$\Phi_{1i} + \Phi_{2i} + \Phi_{3i} + \dots + \Phi_{ji} = 0 \quad (2.52)$$

Φ_{ji} : represents the flux leaving node j and entering node i .

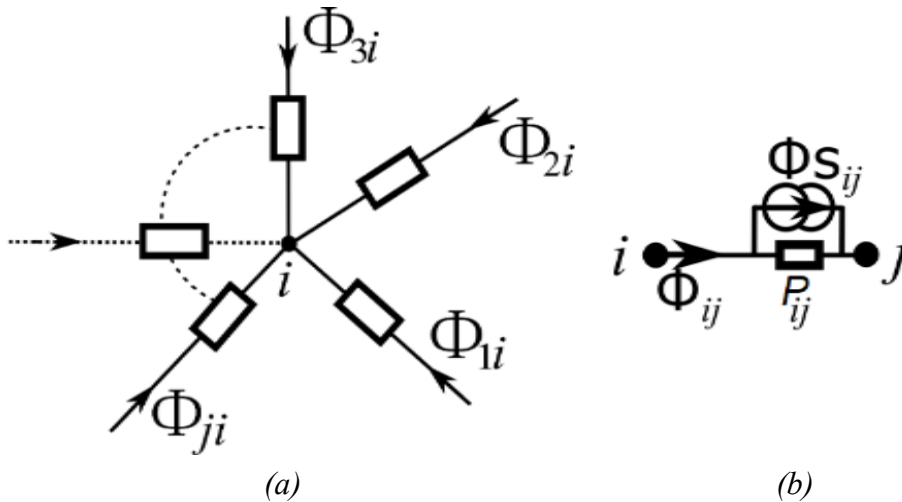


Fig. 2.3: (a) Permeance network (b) Permeance network branch with flux source [19]

The flux Φ_{ij} passing from node i to node j is:

$$\Phi_{ij} = (U_i - U_j)P_{ij} + \Phi_{Sij} \quad (2.53)$$

where

U_i and U_j are respectively the scalar potentials of nodes i and j .

P_{ij} is the value of the permeance linking nodes i and j .

$\Phi_{S_{ij}}$ is the flux source between nodes i and j .

From equations (2.52) and (2.53) we can obtain the equation where node i is linked to n other nodes:

$$\left(\sum_{\substack{k=1 \\ k \neq i}}^n P_{ki} \right) U_i - \sum_{\substack{k=1 \\ k \neq i}}^n P_{ki} U_k = \sum_{\substack{k=1 \\ k \neq i}}^n \Phi_{S_{ki}} \quad (2.54)$$

By writing the equations of all the nodes in the network, we obtain the following system of algebraic equations:

$$\begin{bmatrix} \sum_{k=2}^n P_{k1} & -P_{21} & \cdots & -P_{n1} \\ -P_{12} & \sum_{\substack{k=1 \\ k \neq 2}}^n P_{k2} & \cdots & -P_{n2} \\ \vdots & \vdots & \ddots & \vdots \\ -P_{1n} & -P_{2n} & \cdots & \sum_{k=1}^{n-1} P_{kn} \end{bmatrix} \begin{bmatrix} U_1 \\ U_2 \\ \vdots \\ U_n \end{bmatrix} = \begin{bmatrix} \sum_{k=2}^n \Phi_{S_{k1}} \\ \sum_{\substack{k=1 \\ k \neq 2}}^n \Phi_{S_{k2}} \\ \vdots \\ \sum_{k=1}^{n-1} \Phi_{S_{kn}} \end{bmatrix} \quad (2.55)$$

(2.55) can be written in matrix form as:

$$[P]_{n \times n} \times [U]_{n \times 1} = [\Phi_S]_{n \times 1} \quad (2.56)$$

With

$[P]$ permeance matrix.

$[U]$ vector of magnetic scalar potentials at the nodes.

$[\Phi_S]$ excitation vector (flux sources vector).

To solve the system, it is necessary to find the magnetic scalar potential at each node. But it is important to note here that the matrix system will have to be reconstructed for each magnetic state. It will be necessary to modify the sources vector $[\Phi_S]$ and the permeance matrix $[P]$ [19].

c) Modeling of Sources

- **Magnets:**

Magnets are modeled by a flux source in parallel with a reluctance (Fig. 2.4).

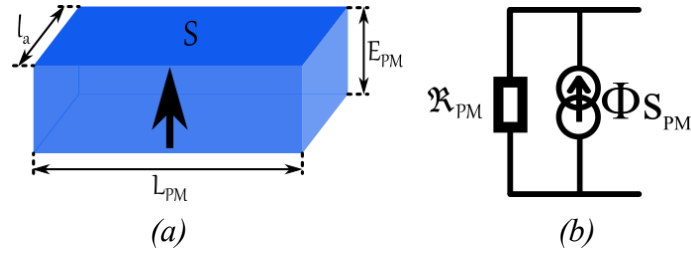


Fig. 2.4: RN model of a magnet [19]

The corresponding equations are the following:

$$R_{PM} = \frac{E_{PM}}{\mu_0 \mu_{r_{PM}} (L_{PM} l_a)} \quad (2.57)$$

$$\Phi_{S_{PM}} = B_r L_{PM} l_a \quad (2.58)$$

Where the following quantities correspond to the magnet: R_{PM} is its reluctance, $\Phi_{S_{PM}}$ its flux, L_{PM} its width, l_a its length, E_{PM} its thickness and B_r its remanence.

- **Coils:**

The modeling method of the coils is developed by the author in [19]. The magnetic sources are modeled by magneto motive sources distributed along the branches of the reluctance block elements. Fig. 2.5 illustrates an example of the MMF sources distribution due to coil currents. The total MMF generated by armature coils is distributed as MMF sources along the y -axis branches in the winding zone.

Total MMF according to position (along the x -axis) is the sum of the MMF created by each coil. The ratio (height of element block to height of coil zone) is used to weight the MMF sources on each branch of the block elements in the winding zone as shown in Fig. 2.5 and equation (2.59). ε_{tot} is the total MMF according to position and is calculated as in equation (2.60). x_i is the position of the central node of block element i . $\varepsilon_{i,y}$ is the MMF on the y -axis branch of block element i , E_h is the block element height, and Z_h is the zone height.

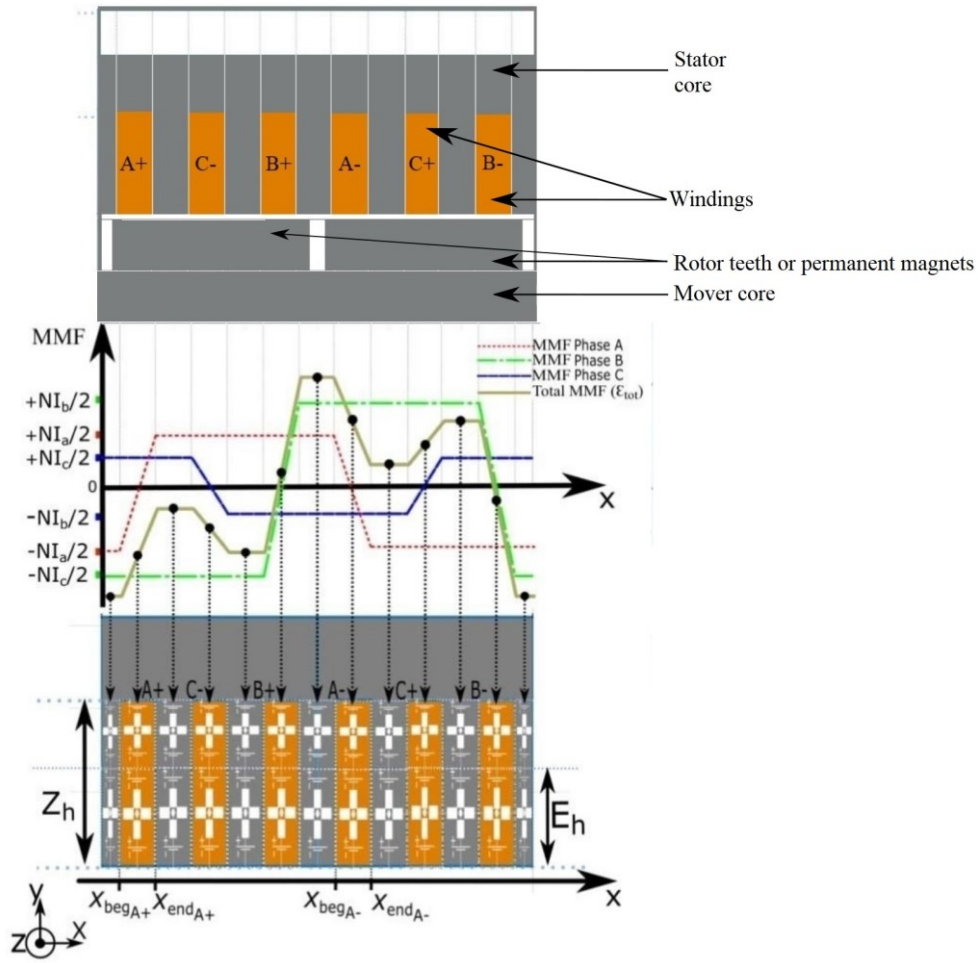


Fig. 2.5: MMF distribution [21]

$$\varepsilon_{i,y} = \frac{1}{2} \frac{E_h}{Z_h} \varepsilon_{tot}(x_i) \quad (2.59)$$

$$\varepsilon_{tot}(x) = \varepsilon_A(x) + \varepsilon_B(x) + \varepsilon_C(x) \quad (2.60)$$

where ε_A , ε_B , and ε_C are the MMFs due to coil current in each phase. They are calculated for each displacement step as shown in equation (2.61) for phase A. The same equation applies for phases B and C. N_s and I_A are, respectively, the number of turns per coil and phase current. $x_{beg_{A+}}$ and $x_{end_{A+}}$, are the x -axis coordinates (beginning and end) of the positive slot of phase A and $x_{beg_{A-}}$ and $x_{end_{A-}}$, the x -axis coordinates (beginning and end) of the negative slot of phase A.

$$\varepsilon_A(x) = \begin{cases} \frac{-N_S I_A}{2}, & \text{if } x < x_{beg_{A+}} \text{ or } x > x_{end_{A-}} \\ \left(\frac{N_S I_A}{x_{end_{A+}} - x_{beg_{A+}}} \right) x - \frac{N_S I_A}{2} \left(\frac{x_{end_{A+}} + x_{beg_{A+}}}{x_{end_{A+}} - x_{beg_{A+}}} \right), & \text{if } x_{beg_{A+}} < x < x_{end_{A+}} \\ \frac{+N_S I_A}{2}, & \text{if } x_{end_{A+}} < x < x_{beg_{A-}} \\ \left(\frac{-N_S I_A}{x_{end_{A-}} - x_{beg_{A-}}} \right) x + \frac{N_S I_A}{2} \left(\frac{x_{end_{A-}} + x_{beg_{A-}}}{x_{end_{A-}} - x_{beg_{A-}}} \right), & \text{if } x_{beg_{A-}} < x < x_{end_{A-}} \end{cases} \quad (2.61)$$

d) Numbering of Blocks

The shape of the magnetic matrix depends on the numbering sequence of nodes in the network. The numbers of neighboring k-nodes are as close as possible, similar to the numbering of the FE method illustrated by the example in Fig. 2.6 where the blocks are numbered starting from left to right and from down to up.

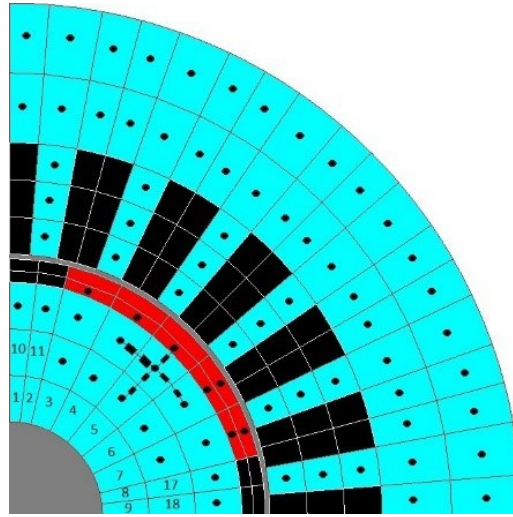


Fig. 2.6: Direction of numbering in FE method [20]

e) Boundary Conditions

The condition of tangent flux imposes a tangential flux at the edge of the model. Similarly a condition of normal flux imposes a tangential flux at the edge of the model. The conditions of periodicity and anti-periodicity impose the cyclicity of flux to reduce the model only to, respectively, a single pole or a pole pair.

Tangential Flux: A tangential flux condition is illustrated in Fig. 2.7. The elementary blocks of layers located at the edges of the model lose their vertical branches located near those edges [19].

Normal Flux: A normal flux condition is imposed in a reluctance network by simply setting the potential at peripheral nodes on the boundary to zero (Fig. 2.8). This translates in mathematical terms by the following ($1 < i < Nbr_{element_x}$):

$$P_{ii_normal} = P_{ii_tangential} + P_{i(i+Nbr_{element_x})} \quad (2.62)$$

Where

P_{ii_normal} is the new value of the diagonal elements of the permeance matrix $[P]$.

$P_{ii_tangential}$ is the value of the diagonal elements of the permeance matrix $[P]$ in case of tangential flux condition.

$Nbr_{element_x}$ is the number of elements located on the interface where the normal flux condition is applied.

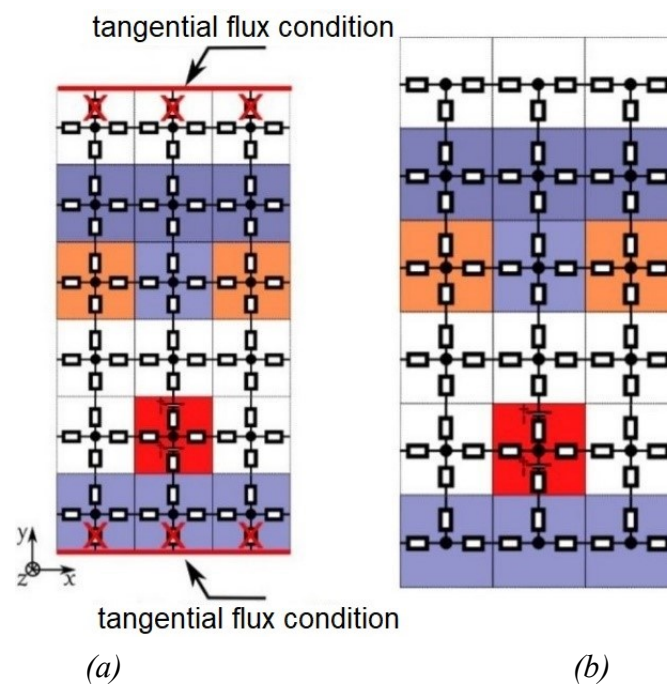


Fig. 2.7: Application of tangential flux conditions [19]

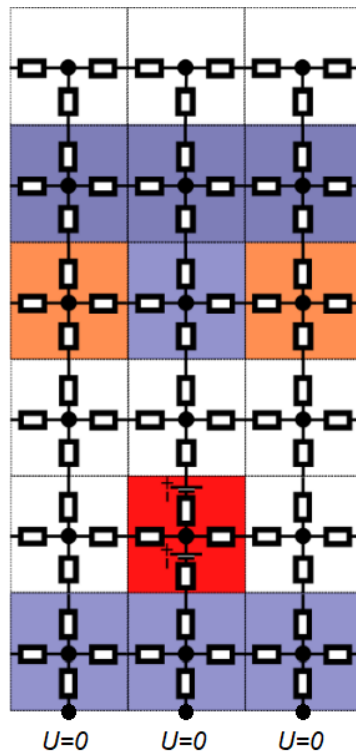


Fig. 2.8: Application of normal flux conditions [19]

Periodicity: The periodicity condition implies the connection of left and right border elements as illustrated in Fig. 2.9 to guide the flux leaving a border to re-enter through the other border.

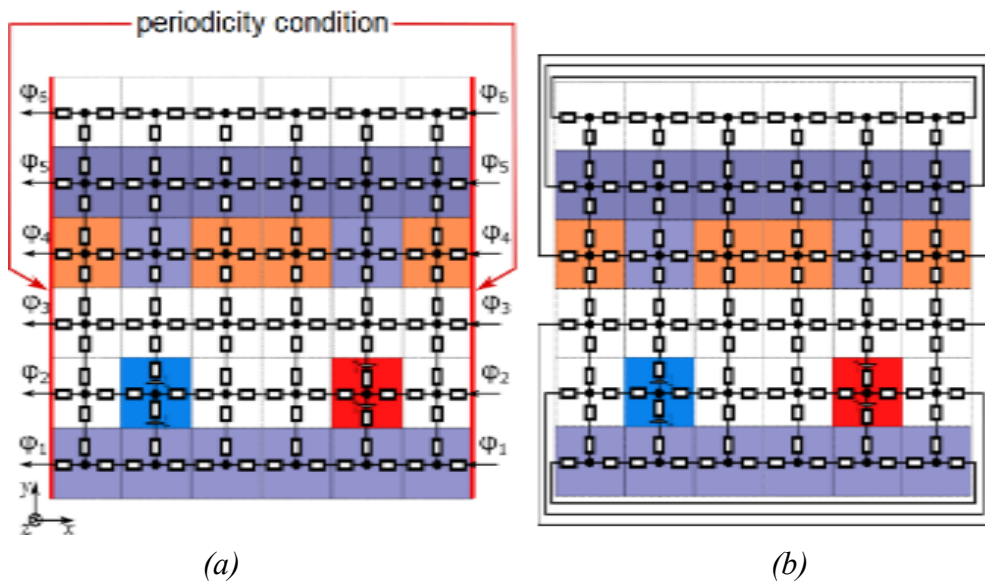


Fig. 2.9: Periodicity condition [19]

Anti-periodicity: The anti-periodicity condition is similar to the periodicity condition. It also translates by the connection of border elements (Fig. 2.10) with the only difference of changing the sign of the potential of the nodes on the border which can be expressed by the following equations (for nodes 1 and 3 as an example):

$$\varphi_{1,3} = \varphi_{3,1} \quad (2.63)$$

$$\frac{U_2 - U_1}{R_{1,2}} + \frac{U_4 - U_1}{R_{1,4}} + \frac{-U_3 - U_1}{R_{1,3}} = 0 \quad (2.64)$$

$$-(P_{1,2} + P_{1,3} + P_{1,4})U_1 + P_{1,2}U_2 - P_{1,3}U_3 + P_{1,4}U_4 = 0 \quad (2.65)$$

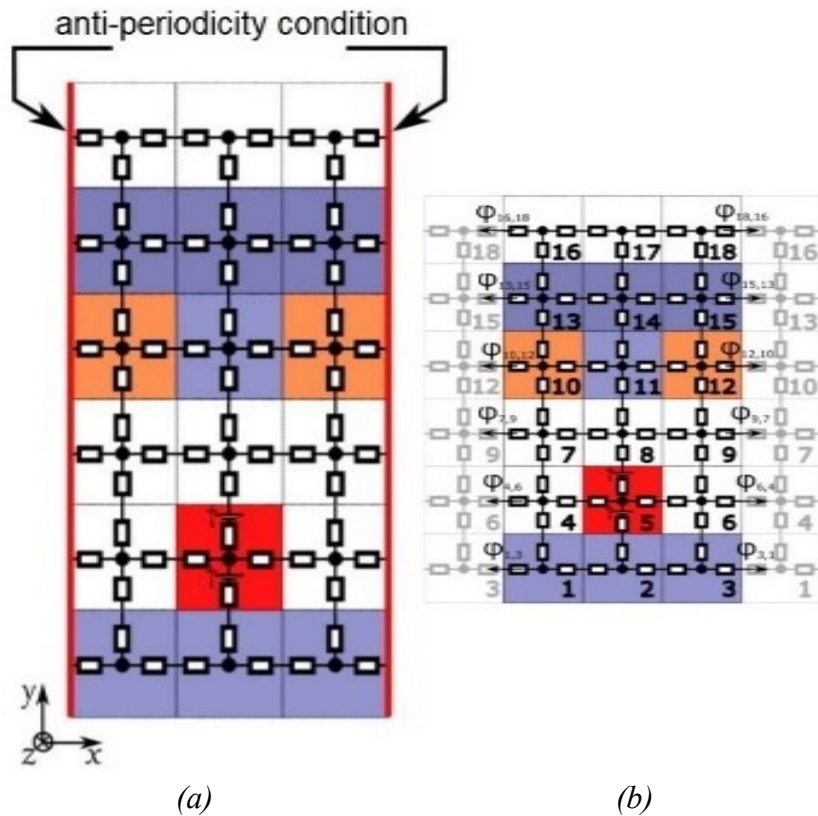


Fig. 2.10: Anti-periodicity condition [19]

f) Motion processing

The air gap is where conversion of electromagnetic energy takes place, so it is important to well model this part of the machine in order to obtain correct simulation results. To do this, different techniques can be used (analytical solution, conformal map, interpolation using finite element models ...).

One of the solutions to consider motion consists in re-meshing the airgap at each step [11]. Another solution is implemented in [22] through additional tangential reluctances in the air gap. Interpolation coupling is also used to connect the stator to the rotor, rendering motion processing independent of discretization [23][24]. The latter is the adopted solution on the model presented in this work.

In this technique, Lagrange interpolation is used to compute magnetic scalar potential of the nodes at the sliding surface (positioned at the middle of the air gap) and flux density of the branches of the reluctance block elements connected to the interface nodes. The nodes of the sliding surface are connected alternately to stator and rotor nodes allowing for independent meshes for both entities (Fig. 2.11).

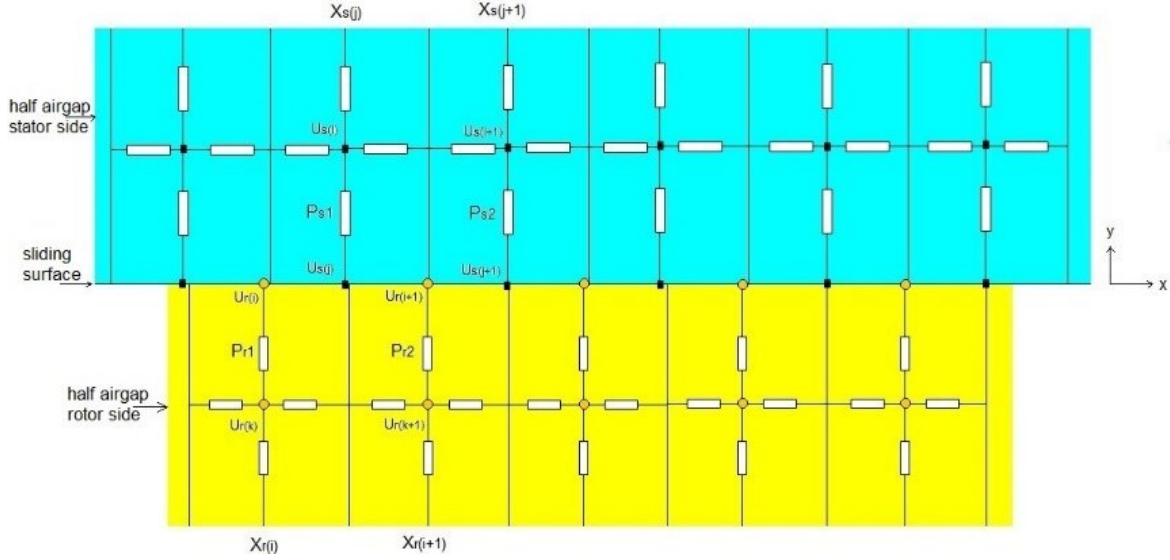


Fig. 2.11: Interpolation nodes and their connections [20]

The node equations at the sliding surface are obtained by interpolating the magnetic scalar potential and the magnetic flux density by a Lagrange polynomial of order N which is given by equations (2.66) and (2.67).

$$L_i(x) = \prod_{j=1; j \neq i}^N \frac{x - x_j}{x_i - x_j} \quad (2.66)$$

$$P_{N-1}(x) = \sum_{i=1}^N U_i L_i(x) \quad (2.67)$$

With x being the abscissa of the points of interpolation.

For a first order interpolation, the equation of magnetic scalar potential at rotor node $(i+1)$ is:

$$U_r^{(i+1)} = L_{r1} U_s^{(j)} + L_{r2} U_s^{(j+1)} \quad (2.68)$$

L_{r1} and L_{r2} are the interpolating Lagrange polynomials given by:

$$L_{r1} = \frac{x_r^{(i+1)} - x_s^{(j+1)}}{x_s^{(j)} - x_s^{(j+1)}} \text{ and } L_{r2} = \frac{x_r^{(i+1)} - x_s^{(j)}}{x_s^{(j+1)} - x_s^{(j)}} \quad (2.69)$$

The magnetic flux density of the branches linking the peripheral stator nodes (nodes at the sliding surface) with the central nodes of the blocks that forms the stator part of the airgap is given by interpolation of the magnetic flux density at rotor nodes and gives rise to the following equation for the magnetic potential (Permeances are shown in Fig. 2.11):

$$U_s^{(j)} = -\left(\frac{P_{r1} S_{s1}}{P_{s1} S_{r1}} L_{s1}\right) U_r^{(i)} - \left(\frac{P_{r2} S_{s1}}{P_{s1} S_{r2}} L_{s2}\right) U_r^{(i+1)} + \left(\frac{P_{r1} S_{s1}}{P_{s1} S_{r1}} L_{s1}\right) U_r^{(k)} + \left(\frac{P_{r2} S_{s1}}{P_{s1} S_{r2}} L_{s2}\right) U_r^{(k+1)} \quad (2.70)$$

$$\text{where } L_{s1} = \frac{x_s^{(j)} - x_r^{(j+1)}}{x_r^{(i)} - x_r^{(i+1)}} \text{ and } L_{s2} = \frac{x_s^{(j)} - x_r^{(i)}}{x_r^{(i+1)} - x_r^{(i)}} \quad (2.71)$$

g) Non-linear characteristic of ferromagnetic material

In electromagnetic actuator modeling, nonlinearity or magnetic saturation concerns the ferromagnetic parts. The relative magnetic permeability of ferromagnetic materials is a nonlinear function of the local magnetic field intensity H, so it depends directly on the spatial distribution of H. For isotropic materials, the relative permeability is the same in all directions for a given elementary volume. In this case, the relative magnetic permeability depends only on the strength of the H field and not on its spatial orientation. The magnetic characteristics of ferromagnetic materials is described by an analytical expression of the B(H) curve. There are several analytical expressions of this curve which can be used as approximations for curves obtained from experimental data.

In order to account for nonlinearities in solving the algebraic system given in equation (2.72) where A is a function of X and B is constant, either the fixed point or the Newton-Raphson method can be employed. These 2 methods use an iterative process to converge to the desired solution starting from an initial solution.

$$[A]. [X] = [B] \quad (2.72)$$

The fixed point method converts the above equation into an equation of the form:

$$[X]_{k+1} = [A([X]_k)]^{-1}. [B] \quad (2.73)$$

The elements of matrix $[A]_k$ depend on the value of the elements of vector $[X]_k$. To start the iterative process, an arbitrary value is assigned to the vector $[X]_0$, this value can be chosen as the solution of equation (2.72) in the linear case. The iterative process is stopped when the convergence criterion given by equation (2.74) is satisfied, or after a defined number of iterations.

$$\frac{\|[X]_{k+1} - [X]_k\|}{\|[X]_{k+1}\|} \leq \varepsilon \quad (2.74)$$

Where

$$\|[X]_{k+1}\| = \sqrt{x_1 + x_2 + \dots + x_n} \quad (2.75)$$

ε is the relative error and n is the number of elements of the X vector.

The Newton-Raphson method is based on finding the solution of an equation $f(x) = 0$ knowing its derivative $f'(x)$, so an approximate solution $x(k + 1)$ can be calculated using the tangent to the point $(x_k, f(x_k))$, of the curve of the function $f(x)$. The approximate solution is calculated as follows:

$$x_{k+1} = x_k - \frac{f(x_k)}{f'(x_k)} \quad (2.76)$$

For a function with multiple variables, the same procedure given by the above equation can be applied but with some modifications.

Let $[F]_k$ be the residual function at the k^{th} iteration:

$$[F]_k = [A]_k \cdot [X]_k - [B] \quad (2.77)$$

Knowing the partial derivatives of the function $[F]_k$ we can define the Jacobian matrix at iteration k as follows:

$$[J]_k = \begin{bmatrix} \frac{\partial F_1}{\partial x_1} & \frac{\partial F_1}{\partial x_2} & \dots & \frac{\partial F_1}{\partial x_{nn}} \\ \frac{\partial F_2}{\partial x_1} & \frac{\partial F_2}{\partial x_2} & \dots & \frac{\partial F_2}{\partial x_{nn}} \\ \vdots & \vdots & \ddots & \vdots \\ \frac{\partial F_{nn}}{\partial x_1} & \frac{\partial F_{nn}}{\partial x_2} & \dots & \frac{\partial F_{nn}}{\partial x_{nn}} \end{bmatrix} \quad (2.78)$$

The solution of the equation $[F]_k = 0$ is found by replacing equation (2.72) by an iterative equation that gives an approximate solution at iteration k :

$$[X]_{k+1} = [X]_k - [J]_k^{-1}([A]([X]_k) \cdot [X]_k - [B]) \quad (2.79)$$

The elements of the Jacobian matrix are computed as follows:

$$\begin{aligned}
J(i, j) &= \frac{\partial F_i}{\partial x_j} = \frac{\partial}{\partial x_j} \left(\sum_{l=1}^{nn} A(i, l)X(l) - B(i) \right) = \sum_{l=1}^{nn} \frac{\partial}{\partial x_j} (A(i, l)X(l)) \\
&= \sum_{l=1}^{nn} \frac{\partial A(i, l)}{\partial x_j} X(l) + \sum_{l=1}^{nn} A(i, l) \frac{\partial X(l)}{\partial x_j} = \sum_{l=1}^{nn} \frac{\partial A(i, l)}{\partial x_j} X(l) + A(i, j)
\end{aligned} \tag{2.80}$$

In our work, nonlinear magnetic characteristic of ferromagnetic material is accounted for by an iterative fixed point method. This method was chosen over the Newton-Raphson method because of the nodal approach adopted for the reluctance network, which makes application of the fixed point method more straightforward than Newton-Raphson where some modifications need to be made before it can be used. The implemented method solves (2.81) iteratively until convergence is reached. The magnetic scalar potential vector [U] is then obtained at magnetic equilibrium. In each iteration, the permeability of ferromagnetic reluctance elements is updated using (2.82) to (2.84). Where (2.84) is the analytical formula used for the non-linear μ -H characteristic. The Reluctances are then updated accordingly. The stopping criteria (ε) for the algorithm is depicted by (2.85).

$$[P][U] - [\Phi_S] = 0 \tag{2.81}$$

$$H_b = \frac{R_b \phi_b}{l_b} \tag{2.82}$$

$$H = \sqrt{\frac{1}{2} \sum_{b=1}^4 H_b^2} \tag{2.83}$$

$$\mu_r(H) = 1 + \left(\frac{2B_{sat}}{\pi\mu_0 H} \right) \tan^{-1} \left(\frac{\pi(\mu_{r0} - 1)\mu_0 H}{2B_{sat}} \right) \tag{2.84}$$

$$\left(\varepsilon = \sqrt{\frac{\sum_{i=1}^n (U_i^k - U_i^{k-1})^2}{\sum_{i=1}^n (U_i^k)^2}} \right) < 10^{-3} \tag{2.85}$$

Where H_e is the magnetic field in a reluctance block element.

H_b is the magnetic field of one branch inside the block. R_b , ϕ_b and l_b , are respectively the reluctance, magnetic flux and length of a branch. μ_r is the relative permeability of a block

B_{sat} is the magnetic flux density at saturation. μ_{r0} is the relative permeability at the origin. U_i^k is the potential at node i for iteration k . n is the total number of nodes. Details of method implementation can be found in the block diagram of Fig. 2.12.

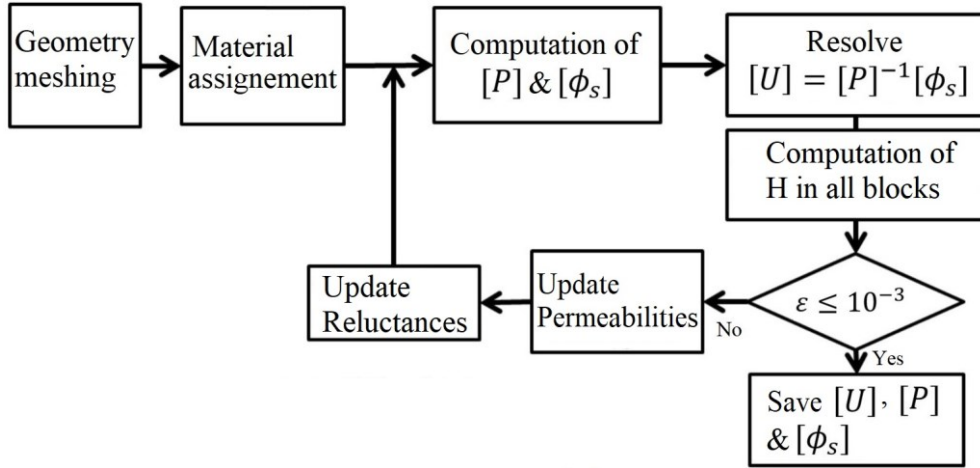


Fig. 2.12: Algorithm used for taking saturation into account

h) Local and global quantities computation

The magnetic flux density B at the connection between 2 nodes i and j is calculated by dividing the flux Φ_{ij} passing through the branch ij by the surface S normal to that branch:

$$B = \frac{\Phi_{ij}}{S} \quad (2.86)$$

The flux linkage per turn for each phase is calculated by summing the fluxes of the branches passing through the cross section of the coils that belong to that phase.

The self-inductance per phase is calculated by dividing the flux of the phase by the current passing through that phase.

The EMF per phase is calculated by deriving the flux-linkage with respect to time, or with respect to position and then multiplying by the speed.

The torque is calculated using Maxwell's stress tensor as the magnetic field value is known for all directions in a reluctance network. The Maxwell tensor (T) is given in a cartesian coordinate system in equation (2.87) where H_x , H_y and H_z are the components of the magnetic field H . The force is estimated by calculating the divergence of the Maxwell tensor as per (2.88). The torque is determined by the tangential component of the force using (2.89) and (2.90). H_t and B_n are the components, of the magnetic field and the magnetic flux density, respectively, tangential and normal to the estimation surface of the torque (Fig. 2.13).

$$T = \begin{bmatrix} H_x H_x - \frac{H^2}{2} & H_x H_y & H_x H_z \\ H_y H_z & H_y H_y - \frac{H^2}{2} & H_y H_z \\ H_z H_x & H_z H_y & H_z H_z - \frac{H^2}{2} \end{bmatrix} \quad (2.87)$$

$$\vec{F} = \vec{\nabla} \cdot T \quad (2.88)$$

$$F_t = \oiint H_t B_n dS \quad (2.89)$$

$$C_{em} = R \oiint H_t B_n dS \quad (2.90)$$

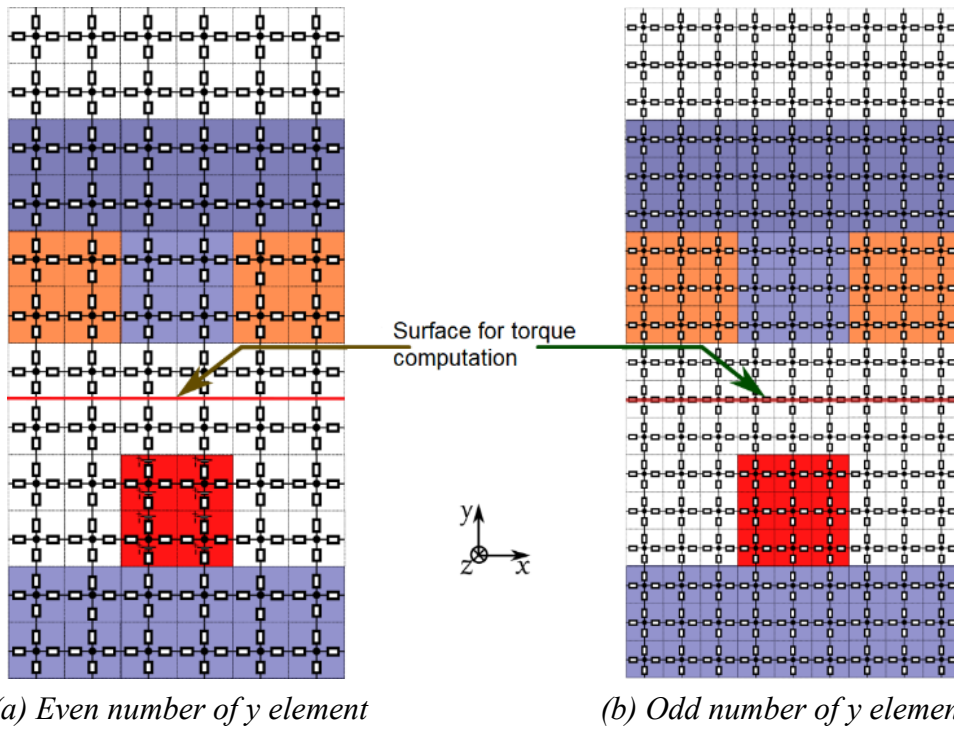
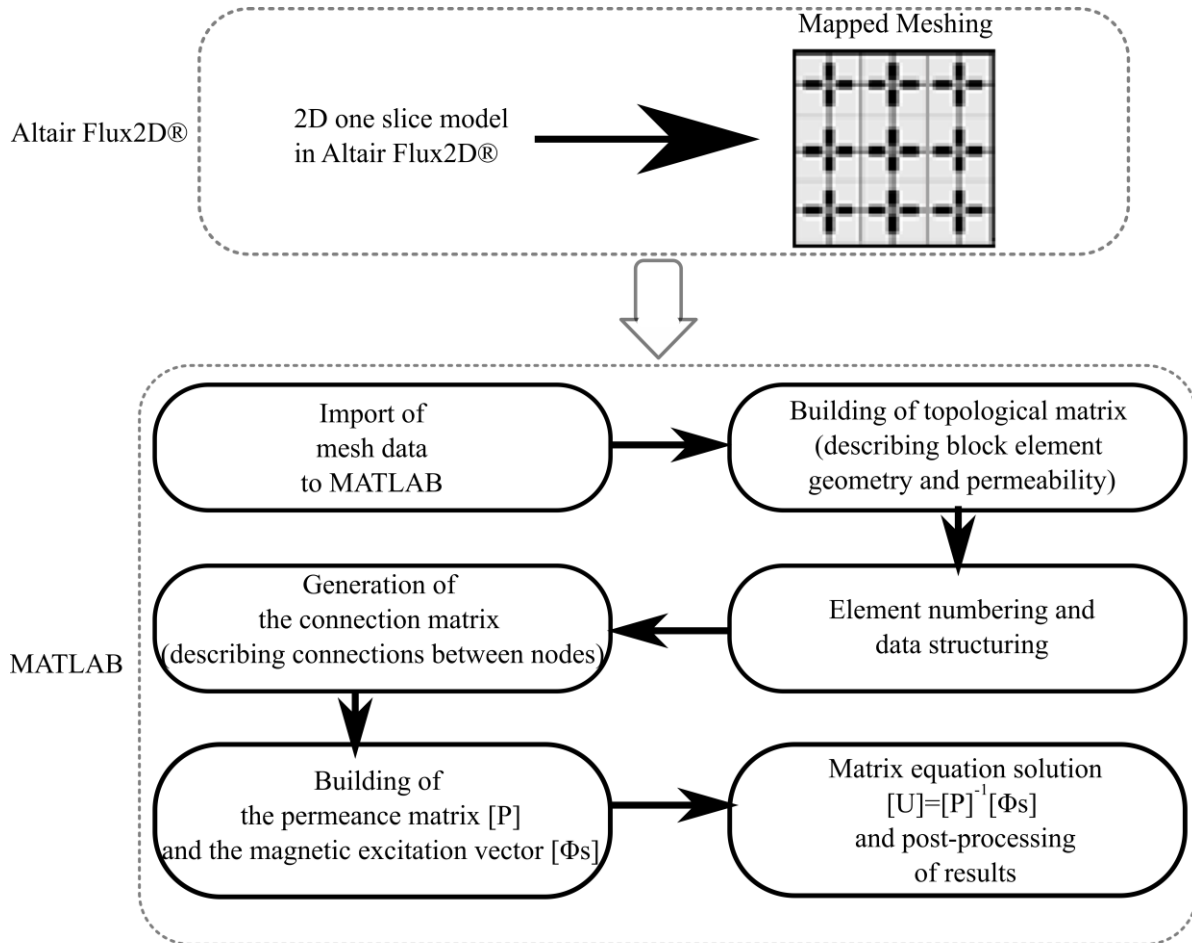


Fig. 2.13: Computation of torque using Maxwell tensor method in a meshed reluctance network [19]

i) Algorithm

The algorithm for generating the reluctance network is described in Fig. 2.14. The flow chart summarizes the automatic MBGRN approach adopted in this work and illustrates how the 2D MBGRN model is obtained for a given slice (subdivided into rectangular elements). The matrix system derived from the commercial FE software subdivisions is then formulated and solved for scalar magnetic potential at the central nodes of the reluctance block elements. Motion is taken into account using Lagrange first order interpolation for the peripheral nodes of the reluctance elements touching the sliding surface.



[P]: Permeance Matrix [U]: Magnetic scalar potential vector [ϕ_s]: Magnetic excitation vector

Fig. 2.14: Functional block diagram of the algorithm

The algorithm is detailed in the block diagram of Fig. 2.15 and consists in the following steps:

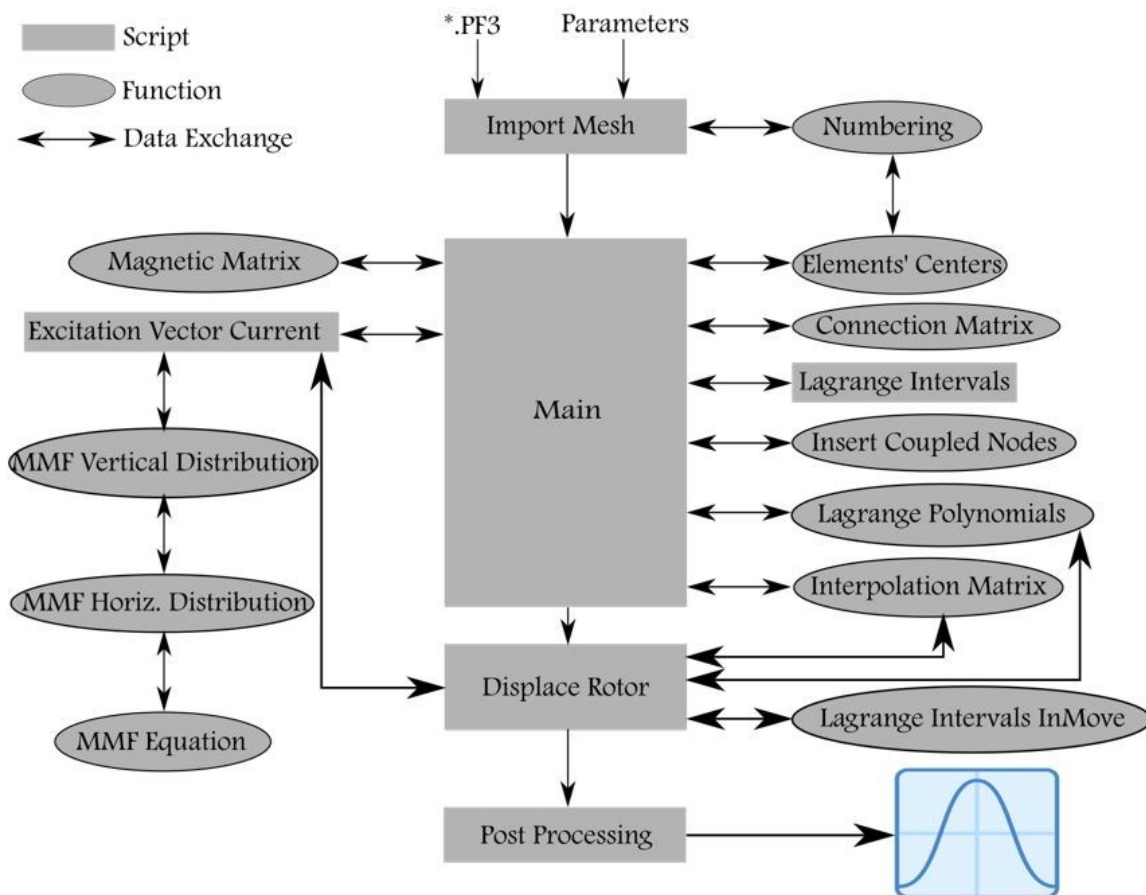


Fig. 2.15: Detailed block diagram of the proposed method

- **Meshing of structure**

The first step in reluctance network modeling is the construction of machine geometry.

To avoid implementing a modeler to construct the geometry, mesh it and number the elements of the mesh, we used instead the modeler of a commercial finite elements software where we create the geometry, mesh it using a mapped mesh and then store that mesh in a standard PF3 format. The PF3 format was chosen because it can be easily processed and it has been used before in previous works in the laboratory.

- **Importing mesh data and construction of the topological matrix**

The role of this part of the code is to read the data imported from the commercial finite elements software in the standard PF3 format which will be arranged in a table where we find the topological description of elements as well as their geometrical coordinates. From mesh data, we construct a matrix which contains information concerning the nodes as well as the coordinates of each element of the mesh.

Import Mesh: This script imports the mesh PF3 files of each region and creates a matrix containing-for each rectangular element-the numbers and coordinates of the 4 nodes that forms it; it also creates the vector of coordinates of the centers of gravity of each rectangular element and calculates the number of elements in the x and y directions.

The file that is first opened in mode read is the file containing the list of all face regions defined in the FE software followed by the numbers assigned to the nodes forming each rectangular block in the grid and finally the coordinates of these nodes.

After opening the file, the code stores its content in a variable *s*, searches *s* for the sentence “DESCRIPTEUR DE TOPOLOGIE DES ELEMENTS” to find the index at which it is located, then uses the function *importdata* to import all data located after that index and stores it in *topology.data* and the rest is stored in *topology.txtdata*. The data stored in *topology.data* actually represents—for each block—the numbers assigned to each node that forms it. Finally this data is stored in the variable *Mat_top*.

It is important to state here that the useful information in the *Mat_top* variable is located at even line numbers. Therefore only half of the lines are useful. This useful information is the numbers assigned to the nodes that forms each rectangular block (a block is formed by 8 nodes: 4 at its extremities and 1 node at the middle of each segment).

Then, the index at which the sentence “COORDONNEES DES NOEUDS” is located is first determined, then numerical data (representing node coordinates) located after it is stored in the variable *coord_nodes*. *coord_nodes* finally contains 4 columns (node number/node x coordinate/node y coordinate/node z coordinate). A shift in the x and y direction of the entire model is accounted for by the addition of values X and Y to *node x coordinate* and *node y coordinate* respectively.

Matrix *Mat_Coord_Elemt* is created with 4 columns (the 4 columns contain the numbers assigned to the 4 nodes that forms a block) and half the number of lines of *Mat_top*. The columns of *Mat_Coord_Elemt* are only 4 not 8 to account only for the nodes at the extremities of the block and not for those at the middle of each segment. In short, a line in *Mat_Coord_Elemt* matrix will contain the following information in the given order:

*node1/node2/node3/node4/0/node1_x/node1_y/node2_x/node2_y/
node3_x/node3_y/node4_x/node4_y.*

node1/node2/node3/node4 are the numbers assigned to the 4 nodes at the extremities of a block.

node1_x/node1_y/node2_x/node2_y/node3_x/node3_y/node4_x/node4_y are the corresponding coordinates

0 is a separator.

After creating *Mat_Coord_Elemt*, the center of gravity of each block is calculated using the function *Num_Elemt* (will be explained later on) and stored in the variable *barycentre*. This function also outputs a vector of same length as *barycentre*, called *classement*, its role is determining the order (number) of each center of gravity based on its x and y coordinates. This allows sorting of the matrix *Mat_Coord_Elemt* and the vector *barycentre* according to the following numbering scheme: “node numbers increase from left to right and from down to up”.

Finally, the number of elements in the x and y directions for the rotor are calculated (*Nbr_Elmt_x_Rt* and *Nbr_Elmt_y_Rt*). Firstly, *xref* and *yref* are calculated, they are the coordinates of the center of gravity having the lowest x and the lowest y among all centers, then by finding the number of elements having the same *xref* value, the number of elements in the y direction is determined, and by finding the number of elements having the same *yref* value, the number of elements in the x direction is determined. *Mat_top* is finally cleared to free memory.

- **Numbering and structuring of elements**

Each element of the reluctance network is assigned a number which identifies it, this number is then used when creating tables of geometrical and physical data.

Numbering: This function numbers the nodes according to the aforementioned scheme. It takes as input the matrix *Mat_Coord_Elemt* and outputs the vector *barycentre* of coordinates of the centers of gravity and the vector *classement* containing the number of the node in the network.

The x and y coordinates of the centers of gravity of the rectangular blocks are calculated by taking the average of the most distant abscissas and the most distant ordinates. The calculated coordinates are then stored in the last 2 columns of the *Mat_Coord_Elemt* matrix and in the *barycentre* vector.

The number of the center of gravity is determined. First a vector called *classement* with the same length as *Mat_Coord_Elemt* is created. Then the number of nodes for the different cases are calculated as shown in Fig. 2.16. The sum of the number of nodes located in the rectangles in the below figure gives the numbering of the node marked by an X; the node for which we seek the numbering.

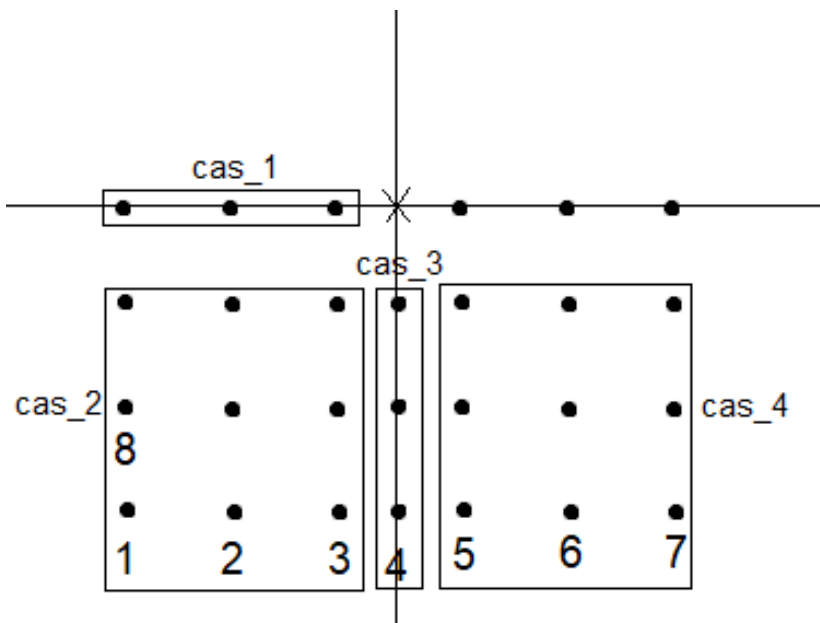


Fig. 2.16: Different cases for the computation of classement

Elements' Centers: The function takes as input the list of mesh file names *list*, the directory *rep* where they are located, a delimiter index *delimiterIn* and a header line index *headerlinesIn*. Its output is a vector *barycentre_Reg* of centers of gravity for each region, the list of region names *Regions* and the coordinates of the vertices of mesh elements *coord_nodes_Reg*. model shift upward or downward is taken into account by modification of coordinates of *coord_nodes_Reg*

- **Generation of the connection matrix**

This matrix is created based on the numbering scheme of blocks adopted in the commercial finite elements software. It contains information about all the connections of the reluctance network.

Connection Matrix: This function finds the connections between the nodes of the reluctance network and stores them in a matrix.

Fig. 2.17 shows an example of connections created with the function *connexion*.

1. For an off border node, the connections are organized as per the following vector:
lower node/left node/right node/upper node

2. For a right or left border node, the connections are organized as per the following vector:
vector:

lower node/right node/left node/upper node

3. In 1 and 2, *lower node* is replaced with *Inf* for nodes located in the lower strip

4. In 1 and 2 and for upper strip elements, the vector is shifted to the right, and *Inf* is inserted at the beginning.

Special case: For an interpolation node, the rules above do not apply, they are replaced by the following...

Each line in the connections matrix for an interpolation node looks like this:

central node/0/0/0

Where *central node* is the number of the center of gravity to which we connect the interpolation node using a reluctance.

Upper Strip	[Inf 7 11 12] 10	[Inf 8 10 12] 11	[Inf 9 10 11] 12
	[4 8 9 10] 7	[5 7 9 11] 8	[6 7 8 12] 9
	[1 5 6 7] 4	[2 4 6 8] 5	[3 4 5 9] 6
Lower Strip	[Inf 2 3 4] 1	[Inf 1 3 5] 2	[Inf 1 2 6] 3
	Left Border		Right Border

Fig. 2.17: Example showing the connections of each element with delimitation of regions

- **Construction of the magnetic matrix and the excitation vector**

From the connection matrix and the structure of elements, the algebraic system obtained by the model is assembled while taking into account the boundary and periodicity conditions.

Magnetic Matrix: This function creates the part of the system matrix related to the permeances. It takes as input the reluctances of a block in the x and y directions and the connections between nodes and calculates the permeances then constructs the aforementioned matrix.

Interpolation Matrix: This function creates the part of the system matrix related to interpolation coefficients. It implements the magnetic scalar potential interpolation equation by the first three sparse matrices (Mat_interp_1, Mat_interp_2, Mat_interp_3) and the magnetic flux density interpolation equation by the rest of the matrices (Mat_interp_4... Mat_interp_9). The final output is a sparse matrix computed by summing all aforementioned matrices.

Excitation Vector Current: This script computes the flux sources vector from the currents and turn numbers of the coils in the model. It first finds the abscissas of the beginning and end of the currents entering and leaving a slot for each phase along with the current value, turn number and winding direction. It also finds the abscissas of reluctance block vertices of the stator. It then builds the MMF distribution matrix Mat_Elements where each element is a structure representing a reluctance block. Each element contains the minimum and maximum values of x and y of the vertices of a block, with the block number, the MMF value in its right and left branches and the MMF value in its upper and lower branches. It then Creates the sparse matrix Sources that defines the MMF value between 2 nodes. It then computes the flux sources vector E. For every element the permeance in each branch is multiplied by the MMF in that branch to obtain the branch flux. The fluxes of all branches are then summed and the obtained value is stored in the corresponding position in E. For each reluctance block, the MMF value in its vertical branches (the MMF value is the same for upper and lower branches). The obtained vector is used later on in the code.

MMF Horiz. Distribution: This function computes the total MMF distribution function resulting from all phases for each x in the horizontal direction. It takes as inputs currents and coil turn numbers and puts out a vector of MMF's. In this code, the MMF's are computed directly at the centers of reluctance blocks to get rid of the interpolation to find the value at a center.

As shown in Fig. 2.18:

For the copper region inside a slot where there is current leaving, the MMF rises linearly from $-N*I/2$ to $N*I/2$ (N is the number of coil turns and I is the current passing through it).

For the copper region inside a slot where there is current entering, the MMF falls linearly from $N*I/2$ to $-N*I/2$.

Outside slots the MMF is constant at $N*I/2$ or $-N*I/2$ depending on the winding direction of the coil.

The equation of the MMF in a slot is computed using the function *Param_MMF_Lin*.

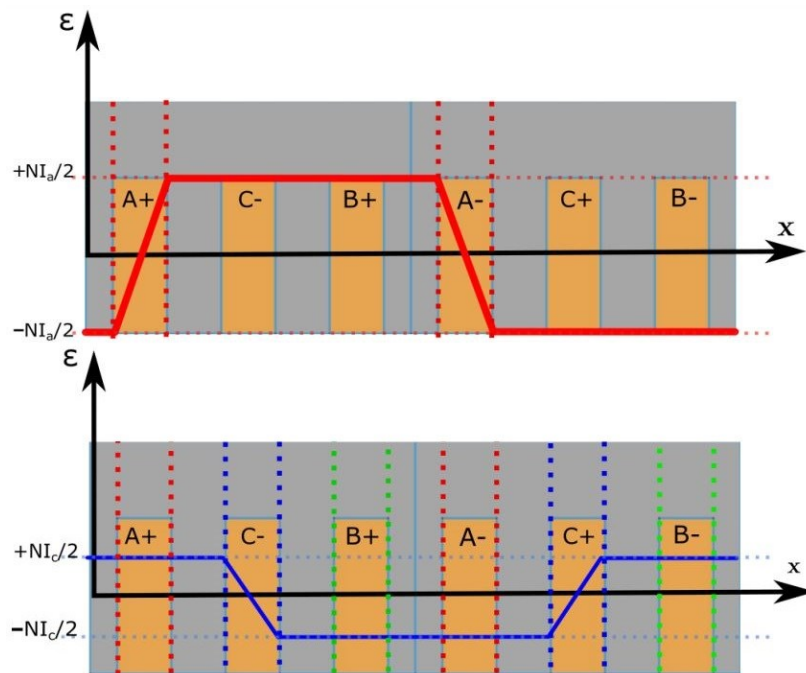


Fig. 2.18: MMF distribution function

MMF Vertical Distribution: This function computes the MMF distribution at the different levels in the y direction. It uses *MMF_distrib_standard* to compute, at each level, the MMF value in the upper and lower branch of a reluctance block, for all blocks at that level.

The MMF value $MMF(x, y)$ at a level y and at position x is calculated as:

$$MMF(x, y) = 0.5 * MMF(x) * MMF_factor(y)$$

$$MMF_factor(y) = elem_height(y) / zone_height$$

$MMF(x)$ is the value of the MMF in the vertical branches of a block whose center is located at position x . This block is located at the lowest y of the stator where there is a coil.

$MMF_factor(y)$ is a factor that varies with height.

$elem_height(y)$ is the height of a reluctance block at the chosen y .

$zone_height$ is the total height of the region where there are coils.

MMF Equation: This function computes the coefficients (a and b) of the MMF equation ($y = a * x + b$) at different positions in the slots. It takes as inputs the angles or abscissas of the start and end of the slot, the direction of winding represented by $+1$ or -1 and the MMF of the coil.

Main: The script's main function is to automatically construct the reluctance network then create the permeance matrix (which contains also information relative to interpolation) and the excitation vector. At the end the system is solved for the magnetic scalar potential.

After importing the mesh of each region, the function *Topologie* is called to create:

The vector *barycentre_Reg* of centers of gravity of every region.

The vector *Regions* which is a list of region names.

The vector *coord_nodes_Reg* of coordinates of vertices of mesh elements.

The vector *region* is then created; it states the region to which a center of gravity belongs. Dimensions of an element in the x, y and z direction are stored in *Dimensions*. The cross sectional areas in normal (y) and tangential (x) directions are stored in *Sections*. Relative permeability of elements is stored in *Permeability*. Reluctances in the x and y directions are stored in *reluct*. Magnet fluxes are stored in *flux_sources*. The variable *indice* is then calculated; it contains the number of the first node to be inserted to create the rotor air layer. The rotor air layer is followed by the rotor interpolation nodes followed by the stator interpolation nodes followed by the nodes used to create the stator air layer. The number of stator elements in the x and y directions is stored in *Nbr_Elmt_x_St* and *Nbr_Elmt_y_St* respectively. Connections between stator elements are stored in *Mat_connexion_St* and between rotor elements is stored in *Mat_connexion_Rt*. *Xst* and *Xrt* contain respectively the abscissas spanned by the stator and rotor mesh vertices. The intervals used in the Lagrange interpolation are computed using the script *interval_ind_lagrange*, then used by the function *polynome_interp_lagrange* to compute the Lagrange interpolating polynomials. Interpolating nodes are inserted at the sliding surface half way between the rotor and stator using the function *insert_coupled_nodes* and the connection matrix between all network nodes *Mat_connexion* is created. A tridiagonal matrix *Mag_Matrix* of permeances between nodes is created along with the matrix *Mat_interp* that contains the coefficients of the magnetic scalar potential of the central nodes of the rotor air and stator air layers, as well as the magnetic scalar potential of the interpolation nodes. The 2 matrices are added to form the final system matrix *Mag*. The excitation vector *E* is calculated from currents and magnets and the boundary conditions are set in our case to normal magnetic field by modification of *Mag*. Finally the system is solved for the magnetic scalar potential *X*.

- **Interpolation**

Lagrange Intervals: This script determines the intervals for the Lagrange interpolation at rotor and stator nodes. Its main outputs are 6 variables: *interval_st*, *interval_rt*, *xst*, *xrt*, *ind_St*, *ind_Rt*.

interval_st contains the stator interpolation intervals,

interval_rt contains the rotor interpolation intervals,

xst is the vector of abscissas of stator interpolation nodes,

xrt is the vector of abscissas of rotor interpolation nodes,

ind_St gives for each stator interpolation node, the index in *interval_rt* of the rotor interval to which it belongs,

ind_Rt gives for each rotor interpolation node, the index in *interval_st* of the stator interval to which it belongs.

Insert Coupled Nodes: This function inserts 2 layers of reluctance blocks between the rotor and the stator to model the air between them. One layer belongs to the rotor and the other belongs to the stator. It also inserts the interpolation nodes or coupling nodes between the rotor air and the stator air at what is called “the sliding surface” mid-way between the rotor and the stator.

Lagrange Polynomials: This function interpolates the value of a quantity at a rotor node between 2 stator nodes and vice-versa.

- **Motion processing**

Displace Rotor: This function moves the rotor and computes at each step the new interpolation matrix Mag_interp and the flux sources vector E . It then solves the system $Mag*X=E$ for the magnetic scalar potential X at each node in the network.

For each step the interpolation intervals are computed using the function $interval_ind_lagrange_move$, then the value of the lagrange interpolating polynomials at required nodes are calculated. Connections are then updated and the flux sources vector is calculated as well as the interpolation matrix and the system is solved for the potential.

Lagrange Intervals InMove: This function finds the list of stator interpolation intervals $interval_st$ and rotor interpolation intervals $interval_rt$. It also finds the number of the node at the lower bound and at the upper bound of the interval and stores them in $noueds_intervalle_st$ and $noueds_intervalle_rt$. It takes as inputs xst_delta the new abscissas of stator interpolation nodes, xrt the new abscissas of rotor interpolation nodes, $delta$ the movement step, nst the number of stator nodes out of rotor sight, nrt the number of rotor nodes out of stator sight and frt the indices of rotor interpolation nodes that moved beyond the higher x limit of the model.

- **Solution computation and results processing**

This is where the system is solved and the post-processing is performed. From the distribution of the magnetic scalar potential in the network, we compute local quantities and global quantities (magnetic flux density, torque, EMF, inductance ...).

Post Processing: This script calculates the electromagnetic force in the x direction at each step and the magnetic flux density in the air gap at initial position and then plots the resulting curves

2. Multi-slice MBGRN Modelling of Axial Flux Machines

a) *Studied machine*

The machine used to test the method, which is also illustrated in Fig. 2.19, is a 24-pole segmented rotor in a 3-phase, 36-slot per stator topology of an axial-field double stator switched reluctance machine (AFDSSRM). Its main geometrical parameters are presented in Fig. 2.20 and Tab. 2.1, its winding configuration which is fed by a 3 phase sine current, is presented in Fig. 2.21. The principle of the multi-slice model is presented in Fig. 2.19 (b) and Fig. 2.19 (c).

By taking into account a number of three-dimensional aspects of the machine, such as parallel side walls of the stator slots, it becomes possible to cut the machine, in the radial direction, in coaxial annular layers of constant thickness (see Fig. 2.19 b) and c). The AFSRM is divided into 3 annular slices in the radial direction as a first comparison. The 2D reluctance network of each slice is established at the average radius of said slice. The latter is cut following a cylindrical plane at its mean radius (Fig. 2.19 (c)). At last, the approach consists of meshing the studied domain in its entirety with reluctance block elements. The subdivision of the modeled domain is performed using the mapped meshing capabilities of a commercial

FE software. Equation (2.91) shows how the length of each slice ($L_{per}^{(i)}$) is determined. $r_{ext}^{(i)}$ and $r_{int}^{(i)}$ are respectively the external and internal radius of slice i , λ_p is the machine magnetic period and τ_p is the pole pitch.

$$L_{per}^{(i)} = \frac{r_{ext}^{(i)} - r_{int}^{(i)}}{2} \tau_p \quad (2.91)$$

$$\lambda_p = \text{gcd}(N_s, N_r) \quad (2.92)$$

$$\tau_p = \frac{2\pi}{\lambda_p} \quad (2.93)$$

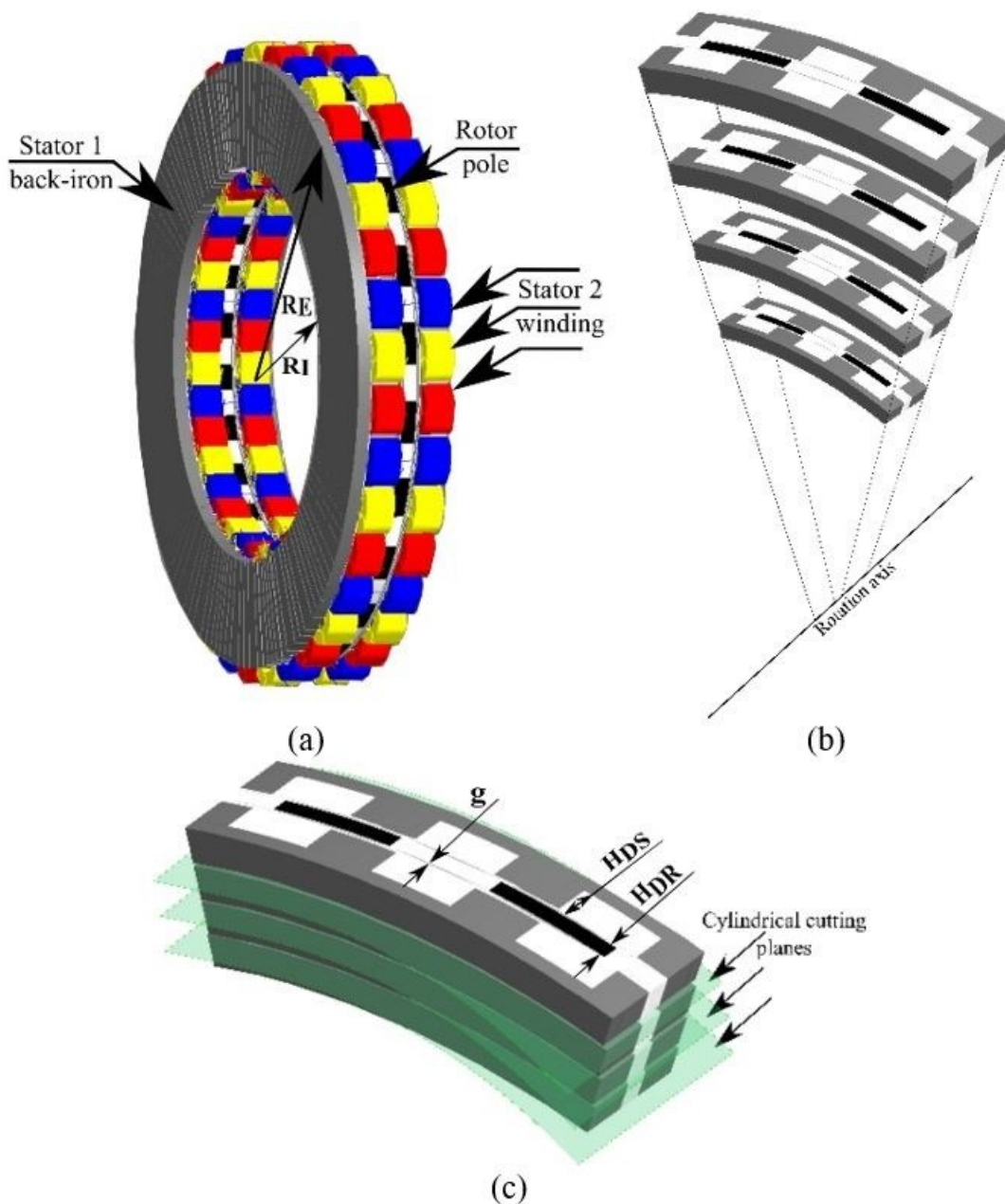


Fig. 2.19: Axial-field switched reluctance machine topology and multi-slice model principle

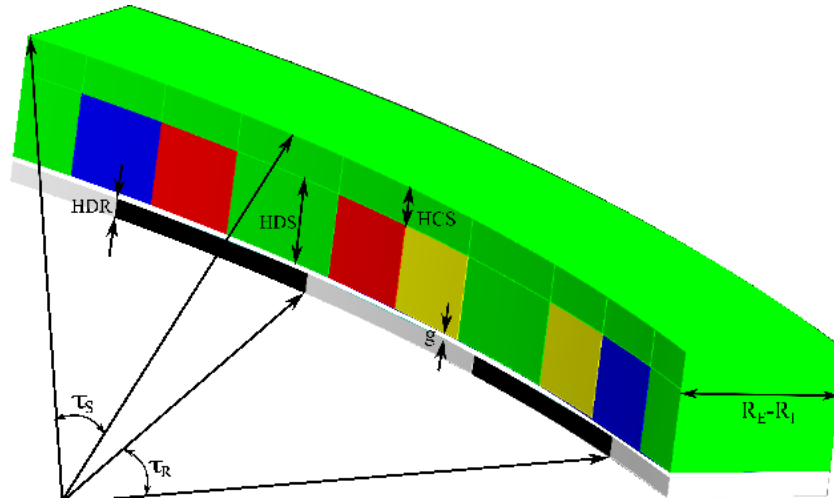


Fig. 2.20: Geometrical parameters illustrated on one magnetic pattern

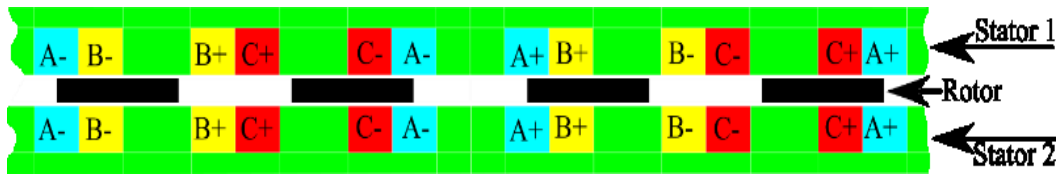


Fig. 2.21: Winding configuration of the machine

Tab. 2.1: Geometrical parameters of the studied AFSRM

Parameter		Value
External Radius	R_E	250 mm
Internal Radius	R_I	230 mm
Stator tooth height	H_{DS}	10 mm
Rotor tooth height	H_{DR}	5 mm
Airgap	g	0.5 mm
Stator tooth pitch	τ_S	10°
Rotor tooth pitch	τ_R	15°
Angle of repeating pattern	τ_P	30°
Rotor poles	N_R	24
Stator teeth	N_S	36 (per stator)
Magnetic pattern repetitions		12

The coils in the 3D model of the machine are supplied with the following currents:

$$I_a = I_m \sin(N_r \theta_r) \quad (2.94)$$

$$I_b = I_m \sin(N_r \theta_r - 120^\circ) \quad (2.95)$$

$$I_c = I_m \sin(N_r \theta_r + 120^\circ) \quad (2.96)$$

Where I_a, I_b, I_c are the currents in phases A, B and C respectively. I_m is the maximum current in a phase, set to 60A. N_r is the number of rotor teeth. θ_r is the rotor mechanical angle.

The coils in the 2D model of the machine are supplied with the following currents:

$$I_a^{(i)} = I_m \sin\left(\frac{360^\circ}{L_{per}^{(i)}} x_r\right) \quad (2.97)$$

$$I_b^{(i)} = I_m \sin\left(\frac{360^\circ}{L_{per}^{(i)}} x_r - 120^\circ\right) \quad (2.98)$$

$$I_c^{(i)} = I_m \sin\left(\frac{360^\circ}{L_{per}^{(i)}} x_r + 120^\circ\right) \quad (2.99)$$

Where $I_a^{(i)}, I_b^{(i)}, I_c^{(i)}$ are respectively the currents in phases A, B and C for slice i . x_r is the rotor position in the 2D plane.

b) Assessment and comparison of the multi-slice MBGRN with the full 3D FEA for the linear BH curve case

Magnetic flux density at the middle of the air gap and at mean radius was calculated with both models for a constant current of 30Amps injected in phase A with no current passing through the remaining windings. The results were also compared with the three-slice reluctance network model for the self-inductance of phase A. The total self-inductance is the sum of inductances of each slice. A fairly good agreement of the results can be observed for the magnetic flux density (Fig. 2.22). As for the self-inductance (Fig. 2.23), there is a slight shift of the value with respect to the 3D model. The maximum relative error is respectively around 19%, 26% and 9% for the normal component, tangential component and inductance. FEM takes 20 seconds of computation for 1 position whilst MBGRN takes 0.947 seconds.

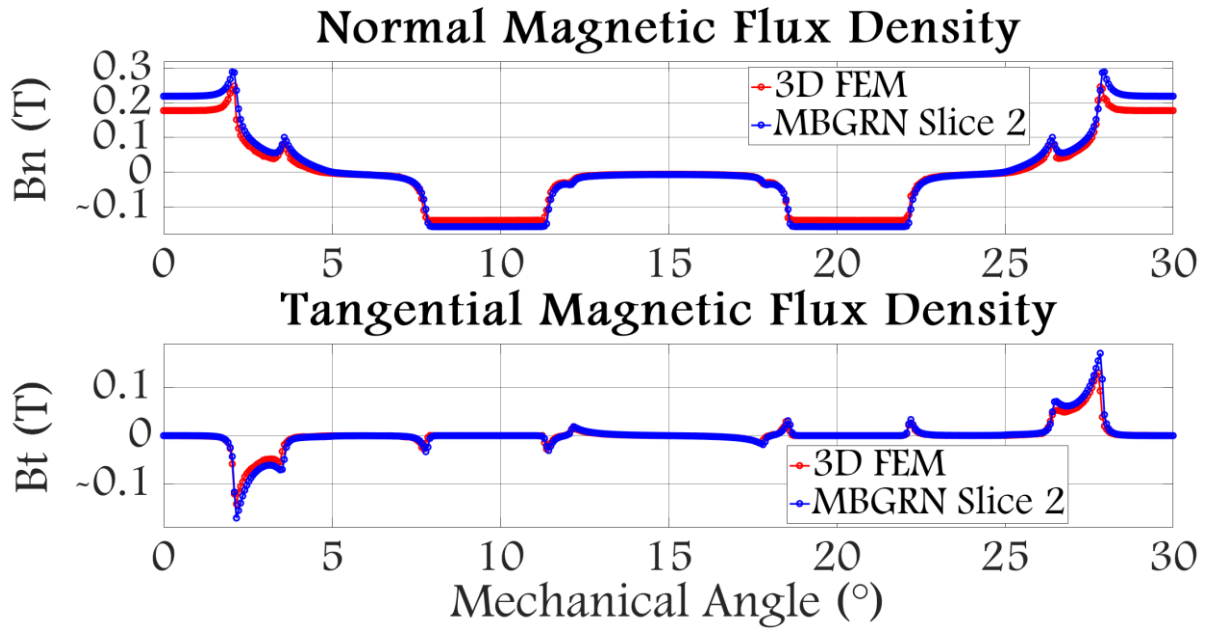


Fig. 2.22: Magnetic flux density in the middle of the air gap for both models

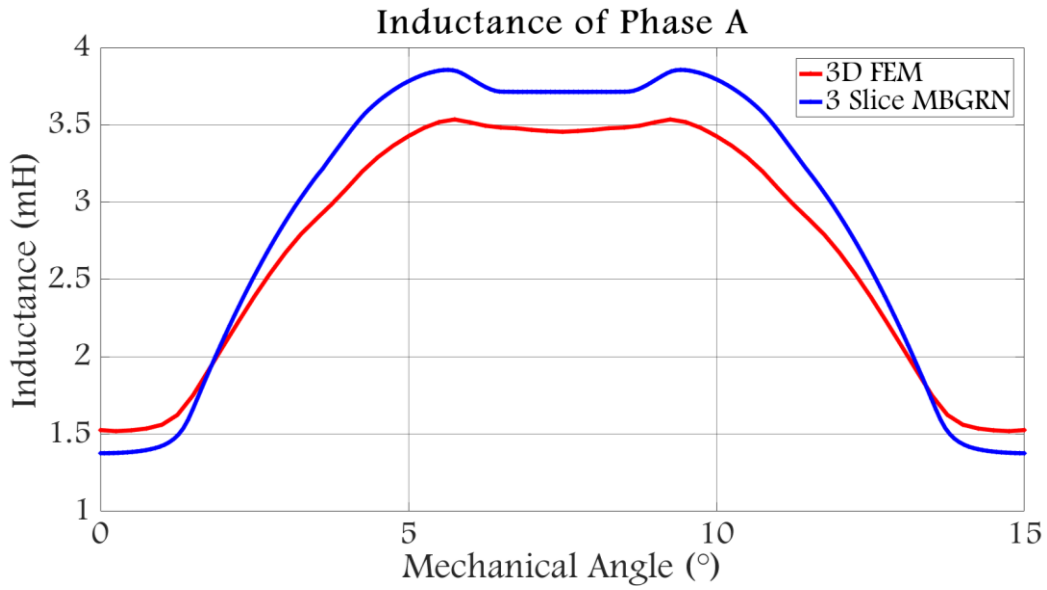


Fig. 2.23: Self-Inductance of phase A for both models

Magnetic flux density is computed using (2.100) to (2.106).

$$\phi_n(i) = (U_i - U_{i+m})/R_{i,i+m} \quad (2.100)$$

$$B_n(i) = \phi_n(i)/S_n(i) \quad (2.101)$$

$$\phi_{t1}(i) = \frac{U_i - U_{i+1}}{R_{i,i+1}} \text{ for } 1 \leq i \leq m - 1 \quad (2.102)$$

$$B_{t1}(i) = \phi_{t1}(i)/S_t(i) \quad (2.103)$$

$$\phi_{t2}(i) = \frac{U_{i-1} - U_i}{R_{i-1,i}} \text{ for } 2 \leq i \leq m \quad (2.104)$$

$$B_{t2}(i) = \phi_{t2}(i)/S_t(i) \quad (2.105)$$

$$B_t = (B_{t1} + B_{t2})/2 \quad (2.106)$$

Where ϕ_n is the flux in the air gap in the vertical direction, U_i is the potential at the interpolation node i at the middle of the air gap and U_{i+m} is the potential at the node $i + m$ right above node i . m is the number of stator elements in the horizontal direction for one layer. $R_{i,i+m}$ is the reluctance between nodes i and $i + m$. B_n is the normal component of the magnetic flux density in the middle of the air gap. S_n is the cross sectional area of a reluctance block in the vertical direction. ϕ_{t1}, ϕ_{t2} represent the flux in the middle of the air gap in the horizontal direction. B_{t1}, B_{t2} are the tangential component of the magnetic flux density in the middle of the airgap evaluated respectively at the right and left side of node i and B_t is the mean value of both.

The 2D thrust force for each slice is evaluated as in (2.107) and the 3D electromagnetic torque is computed as in (2.108).

$$F_i = 2 \frac{(r_{ext}^{(i)} - r_{int}^{(i)}) L_{per}^{(i)}}{\mu_0} \int_0^{L_{per}^{(i)}} B_t B_n d\phi \quad (2.107)$$

$$T = \lambda_p \sum_{i=1}^{N_{slices}} F_i r_{mean}^{(i)} \quad (2.108)$$

Where T is the electromagnetic torque, F_i is the force in the horizontal direction for slice i , $r_{ext}^{(i)} r_{mean}^{(i)}$ is the mean radius of slice i , N_{slices} is the number of slices.

Fig. 2.24 shows the current waveforms. Fig. 2.28 shows the normal and tangential components of the magnetic flux density in the middle of the air gap for MBGRN slice 2 and 3D FEM at mean radius. The comparison results for magnetic flux density, phase flux and torque are presented in Fig. 2.25 for slice 1, Fig. 2.26 for slice 2 and Fig. 2.27 for slice 3. Fig. 2.29 illustrates the comparison between electromagnetic torque obtained with the 3-slice MBGRN and 3D FEM. The accuracy of the method was evaluated by calculating the RMS error ϵ_{RMS} and the error on maximum values ϵ_{MAX} using (2.109) and (2.110).

$$\epsilon_{RMS} = \left(\frac{rms(y_{RN} - y_{FE})}{rms(y_{FE})} \right) \times 100 \quad (2.109)$$

$$\epsilon_{MAX} = \frac{|\max(y_{RN}) - \max(y_{FE})|}{\max(y_{FE})} \times 100 \quad (2.110)$$

Where y_{RN} and y_{FE} are respectively reluctance network model and finite element model computed quantities. Errors on the normal and tangential components of the magnetic flux density (MFD) as well as on electromagnetic torque are given in Tab. 2.2.

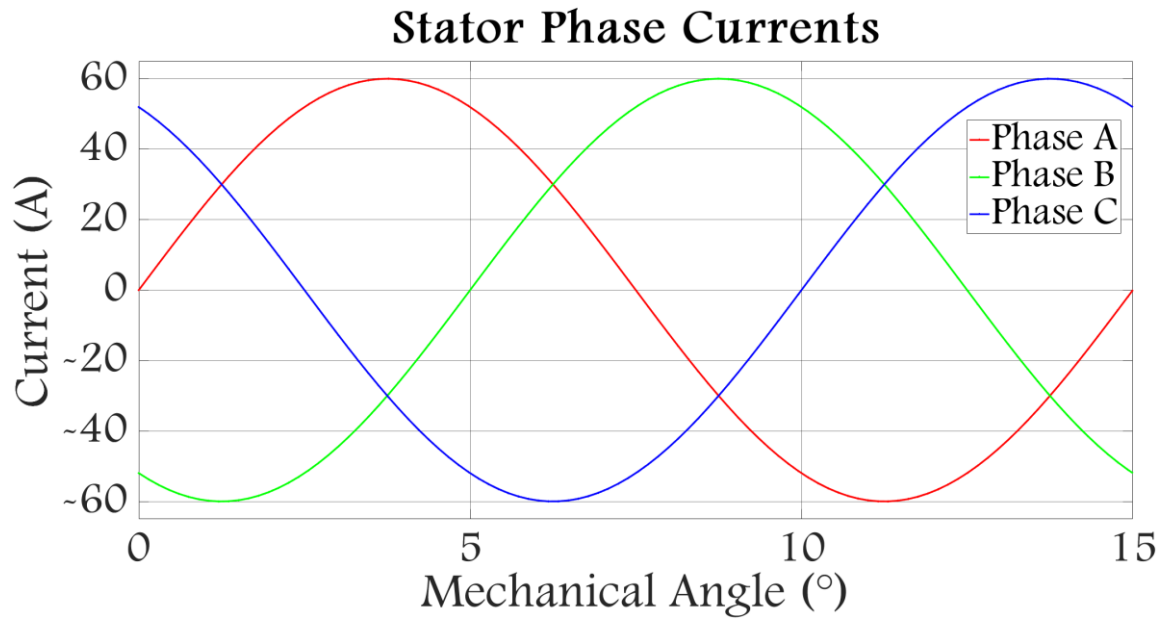
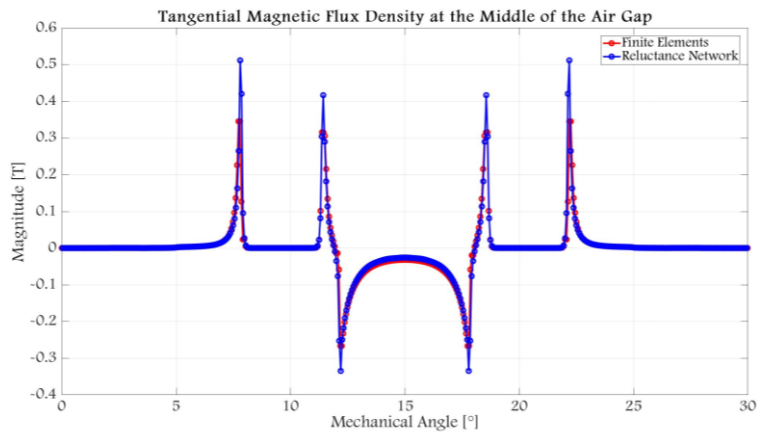
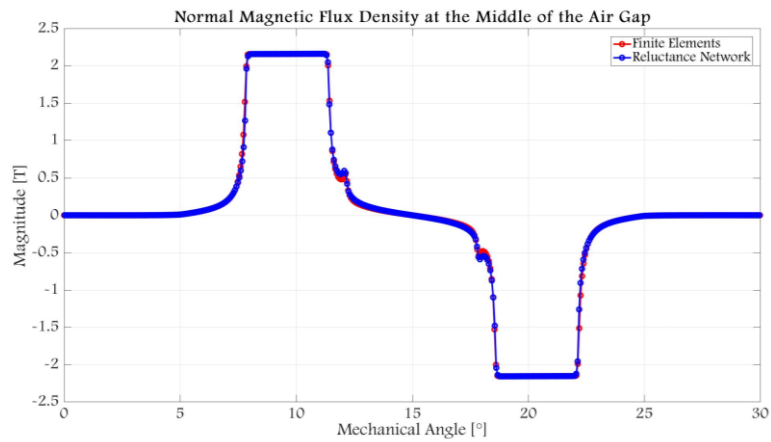
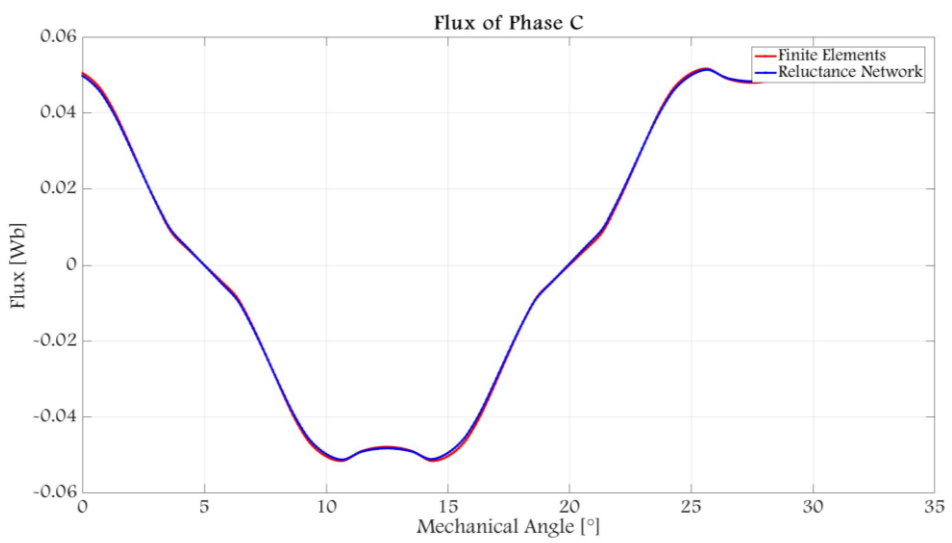
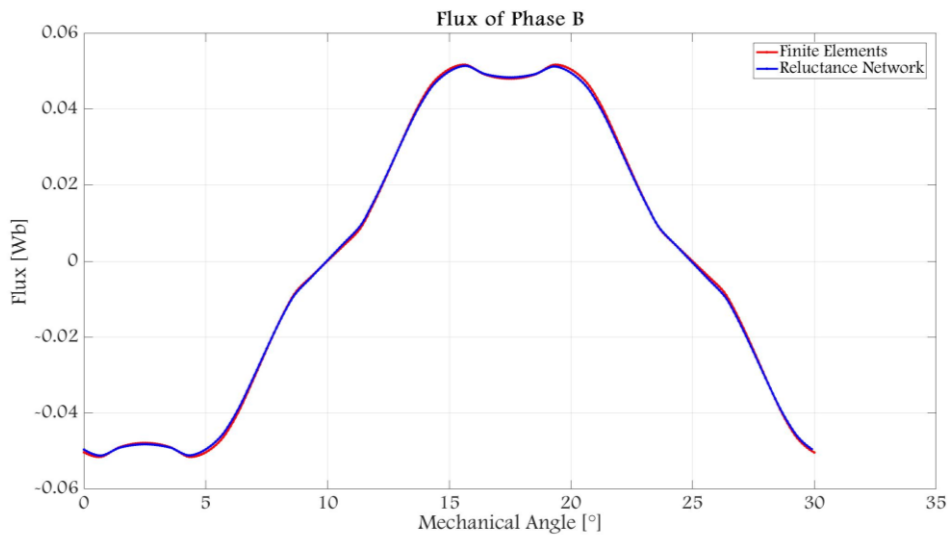
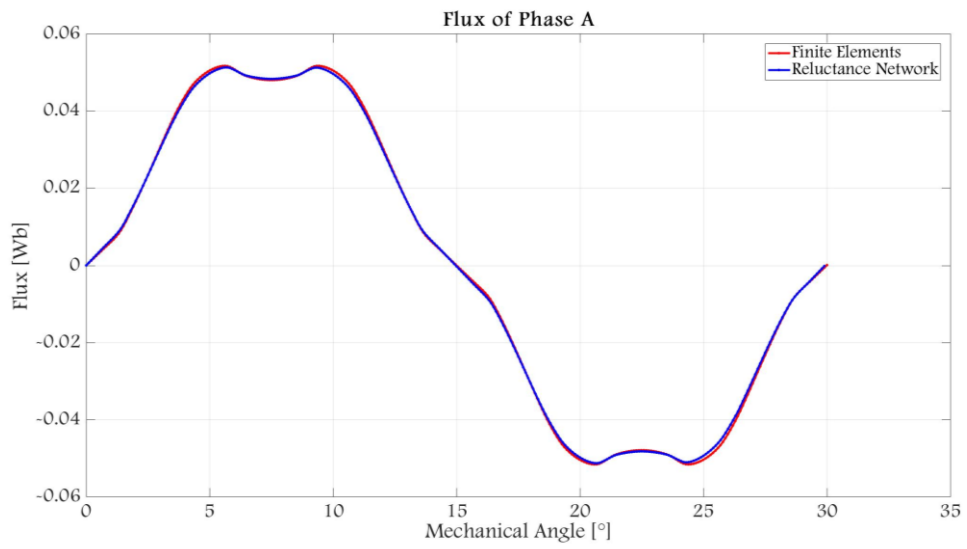


Fig. 2.24: Stator phase currents

Slice 1:





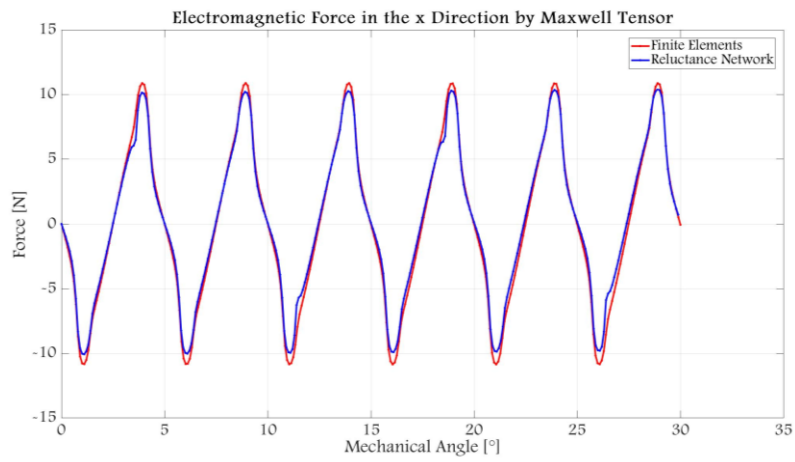
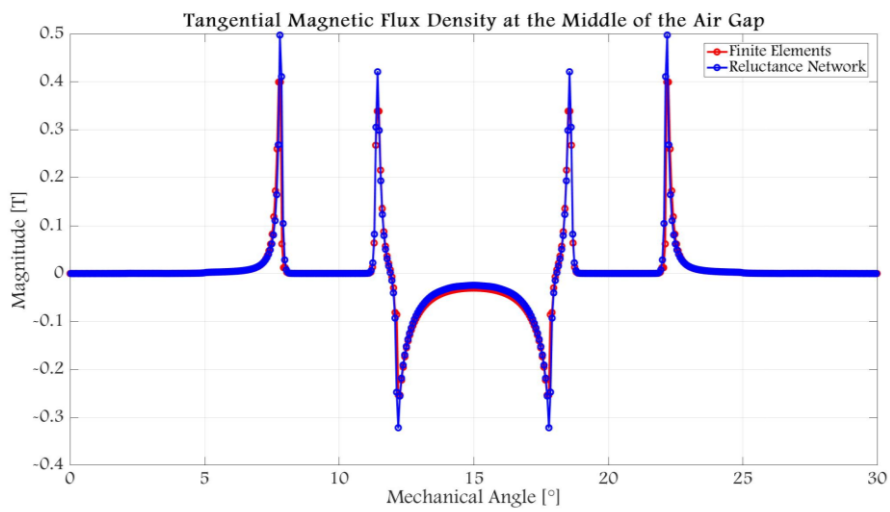
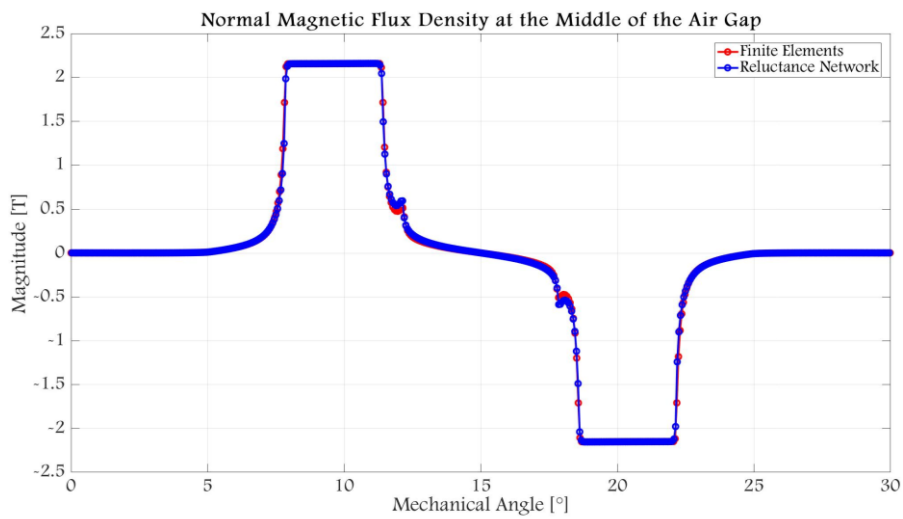
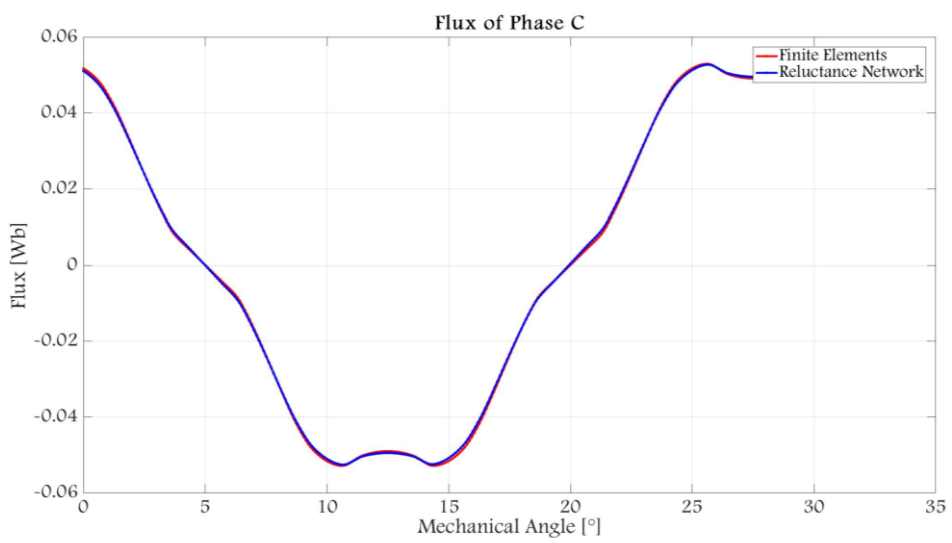
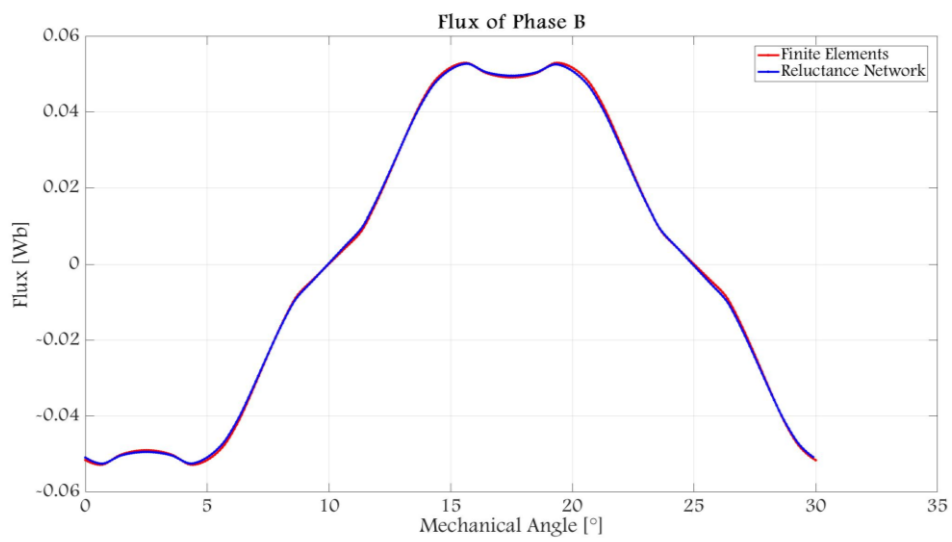
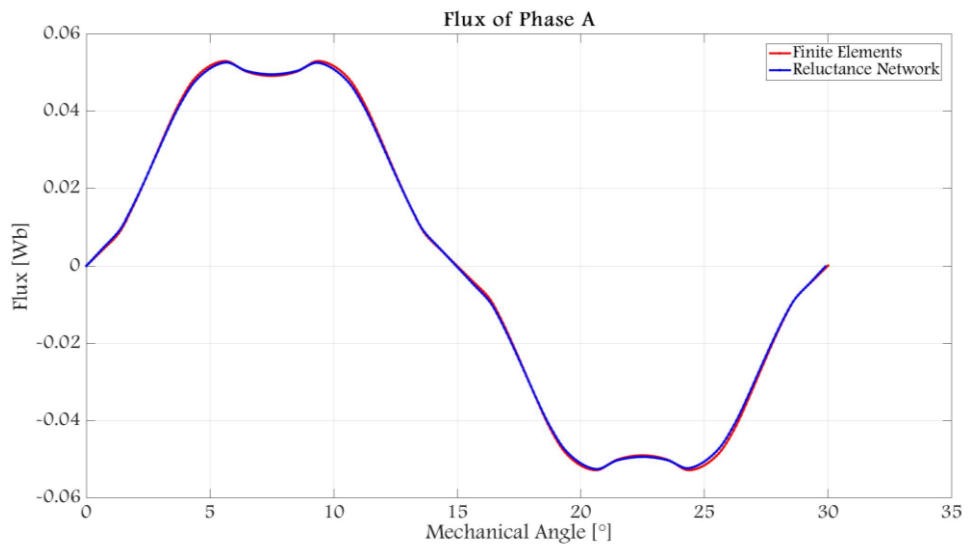


Fig. 2.25: Comparison between 2D reluctance network (slice 1) and 2D finite elements for magnetic flux density, phase flux and torque

Slice 2:





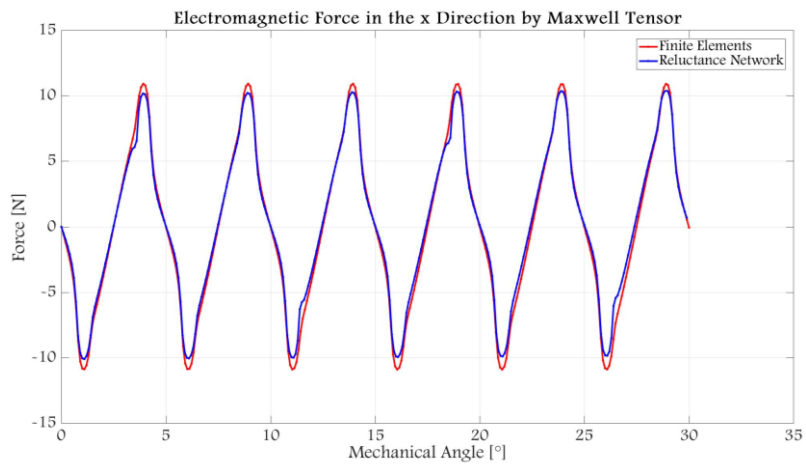
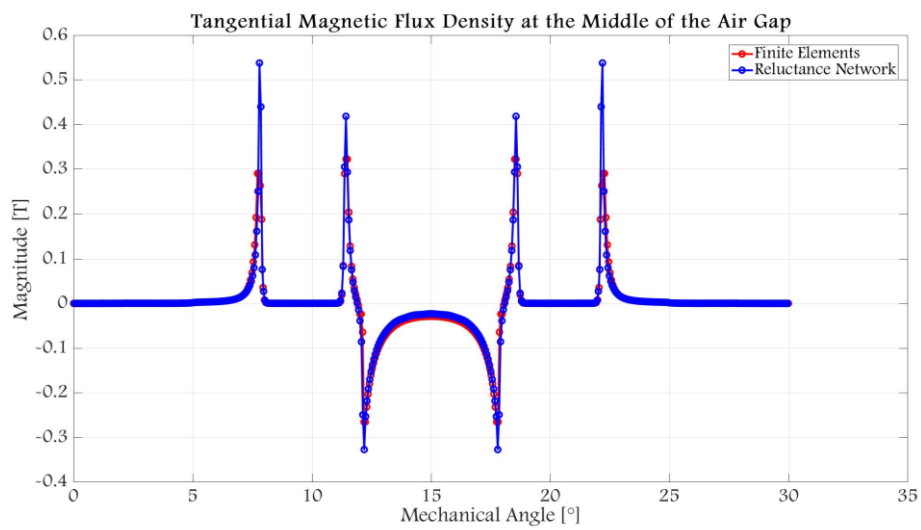
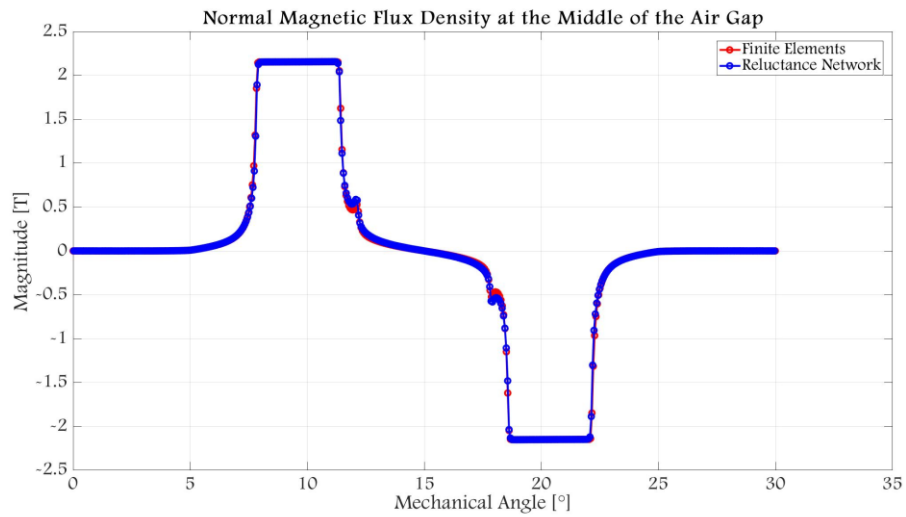
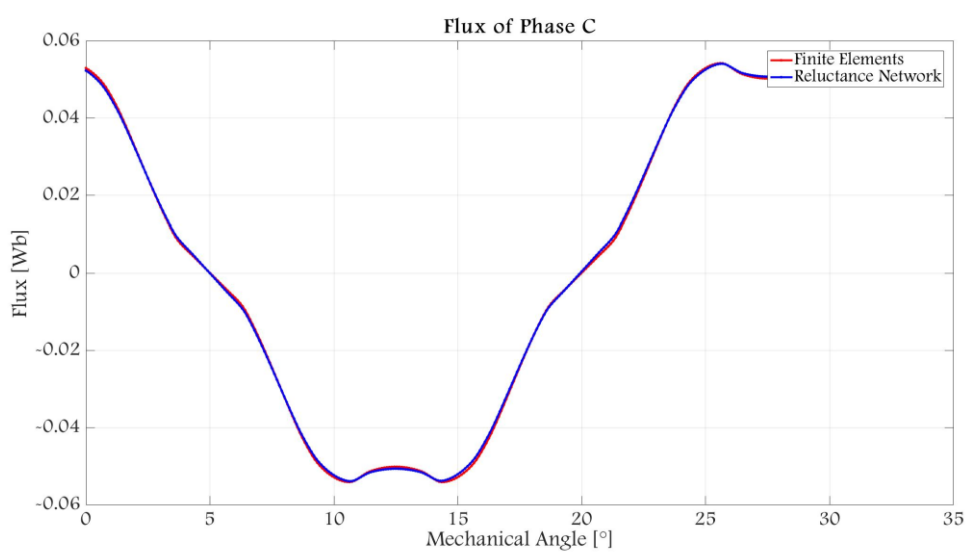
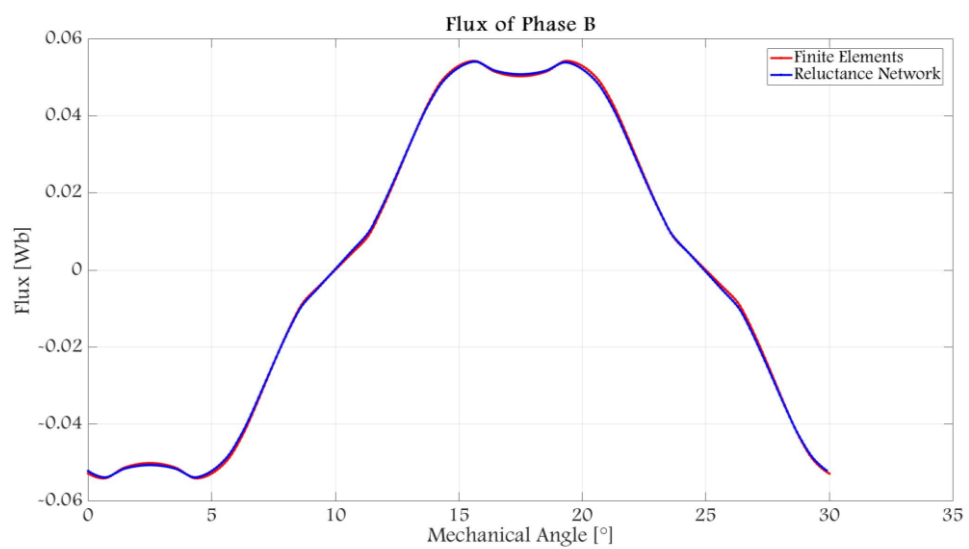
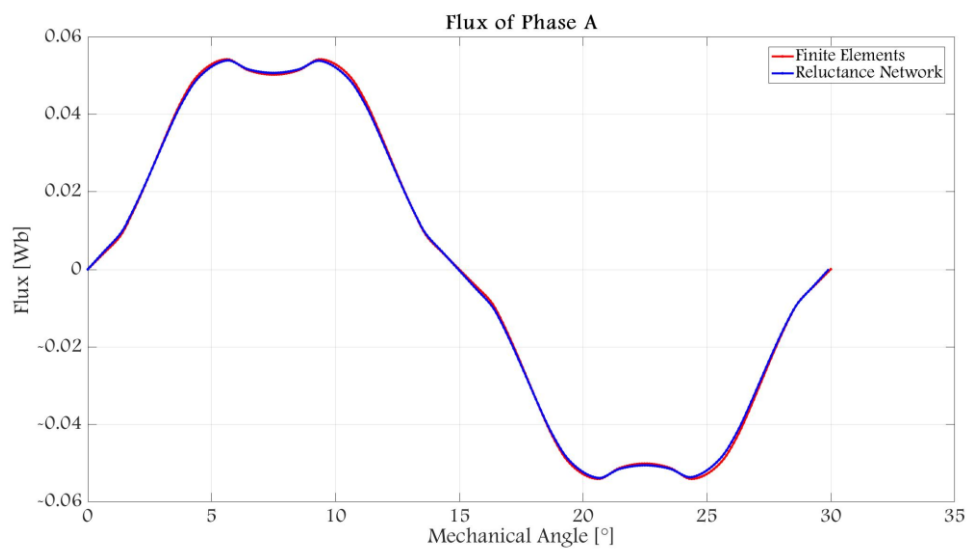


Fig. 2.26: Comparison between 2D reluctance network (slice 2) and 2D finite elements for magnetic flux density, phase flux and torque

Slice 3:





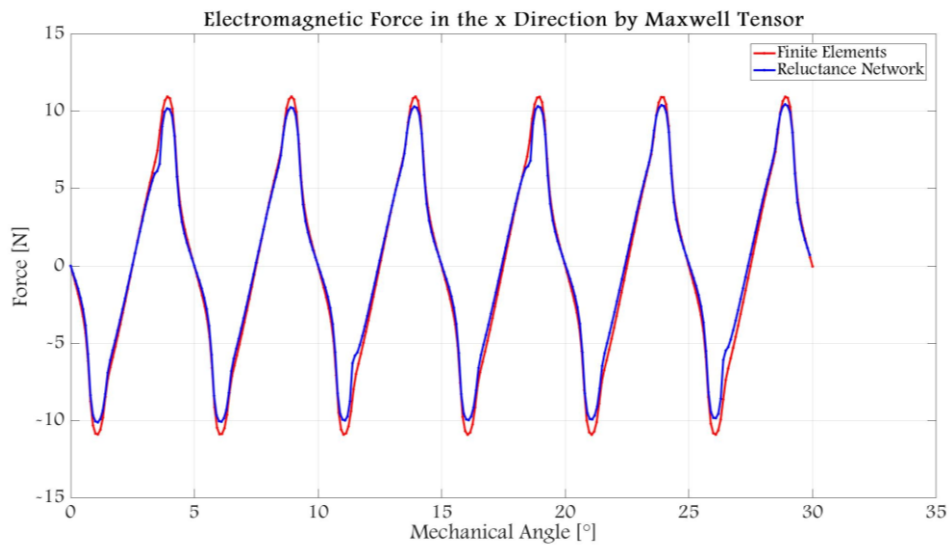


Fig. 2.27: Comparison between 2D reluctance network (slice 3) and 2D finite elements for magnetic flux density, phase flux and torque

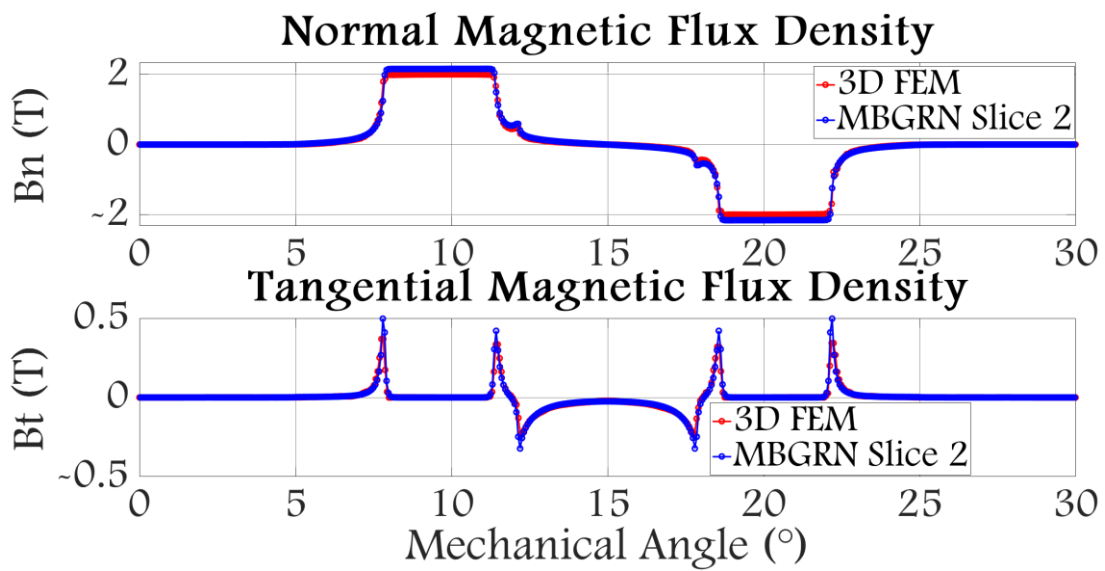


Fig. 2.28: Normal and tangential magnetic flux density in the middle of the air gap at $x=0$ for both models

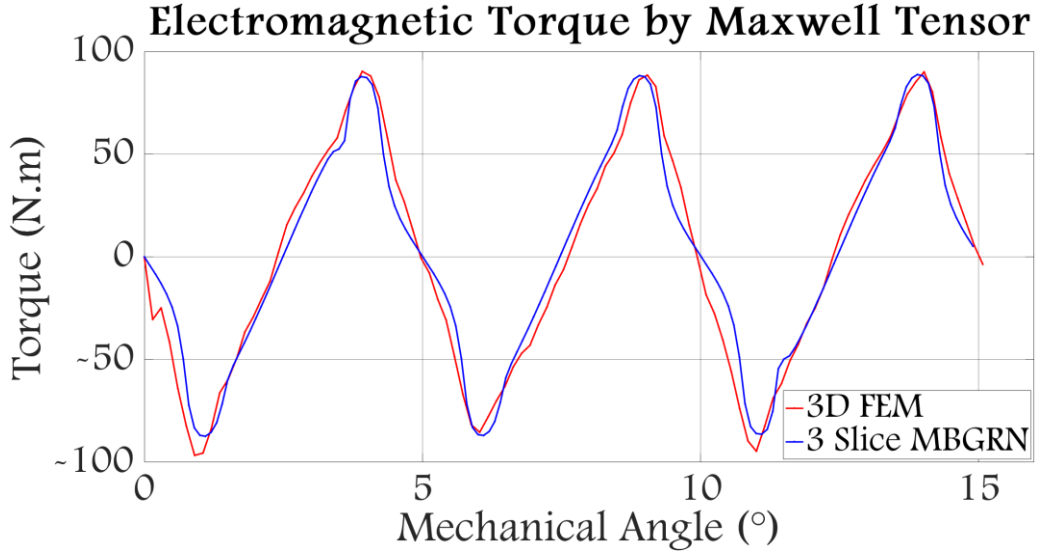


Fig. 2.29: Electromagnetic torque for both models

Tab. 2.2: Errors on important quantities for the proposed method

Quantity	ϵ_{RMS} (%)	ϵ_{MAX} (%)
Normal MFD	8.83	6.88
Tangential MFD	28.33	34.74
Torque	19.06	2.29

Computation time for the proposed method in comparison with 3D FEM was assessed on a computer with a 3.50 GHz Intel(R) Xeon(R) CPU E5-1620 v4 and 64 GB of RAM. MBGRN model is carried out in the four following steps: set-up machine parameters and phase currents, import mesh, construction of system matrix, resolve system at each rotor position. Computation time and speed factor for one rotor position were evaluated as in (2.111) and (2.112) and is illustrated in Tab. 2.3.

$$t_{MBGRN}^{total} = \sum_{i=1}^{N_{slices}} t_{MBGRN}^{(i)} \quad (2.111)$$

$$Speed\ factor = \frac{t_{3DFEM}}{t_{MBGRN}^{total}} \quad (2.112)$$

$t_{MBGRN}^{(i)}$ and t_{3DFEM} are respectively the total MBGRN computation time for slice i and FEM computation time. t_{MBGRN}^{total} is the total computation time for all MBGRN slices.

Tab. 2.3: Computation time comparison between both methods

Method	Computation time
Multislice MBGRN	46.90 s
3D FEM	429 s

Speed factor	9.15
--------------	------

In an attempt to improve the accuracy of the method, 2 additional cases were considered increasing the number of slices used to compute torque. First, the machine was divided into 5 slices and the 2D reluctance network model was generated and solved for each slice then the contributions of all 5 slices were aggregated to obtain the electromagnetic torque. The same process was repeated with the machine divide into 7 slices in the radial direction. An odd number of slices was chosen to always obtain a slice located at the mean radius of the machine, to be able to compare magnetic flux density at mean radius between FEM and RN. Results show that there was no actual improvement in torque accuracy with the increase of number of subdivisions from 3 to 5 to 7 and this can be seen by the following figures. So, it was decided to limit the number of slices to 3, as this was the least number of slices that gave the best accuracy in the shortest amount of time.

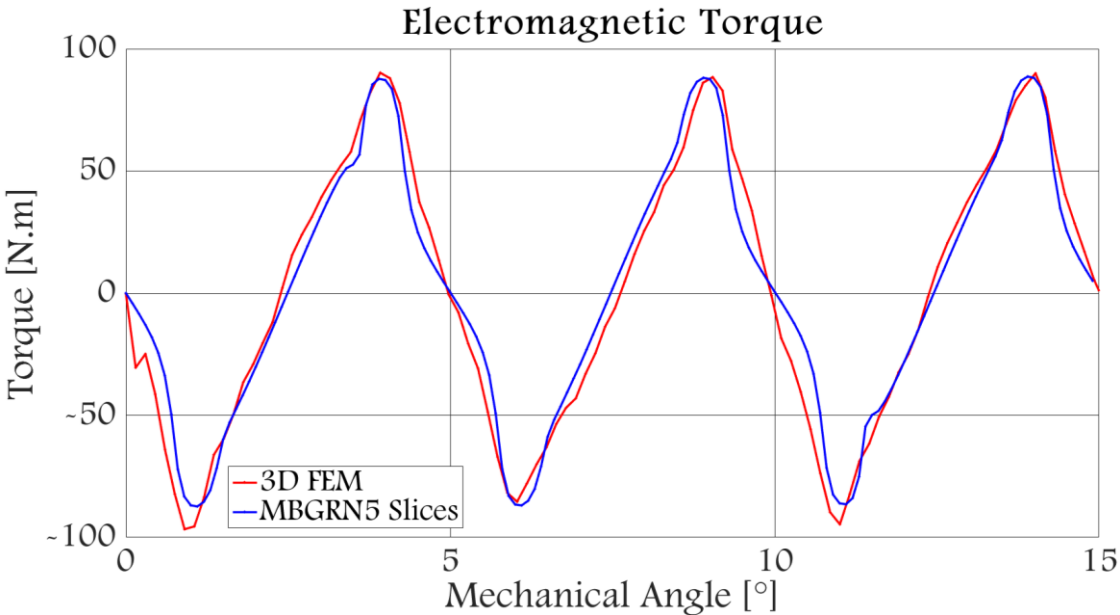


Fig. 2.30: Electromagnetic torque comparison between both models for 5 slices

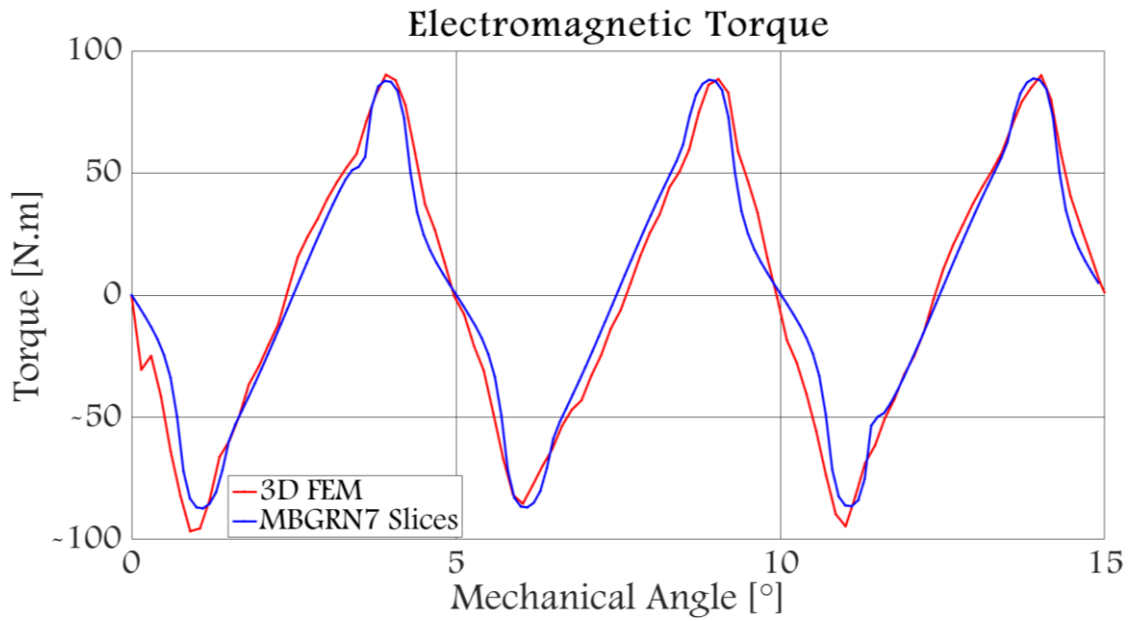


Fig. 2.31: Electromagnetic torque comparison between both models for 7 slices

As the results did not change much when adding additional slices, the radial component of air gap magnetic flux density was plotted for 1 rotor position sweeping the machine in the radial and circumferential directions. As can be seen by the below figure the radial component does not change much with the radius and has a low magnitude compared to the normal and tangential components; and this explains why the torque did not change much when adding additional slices.

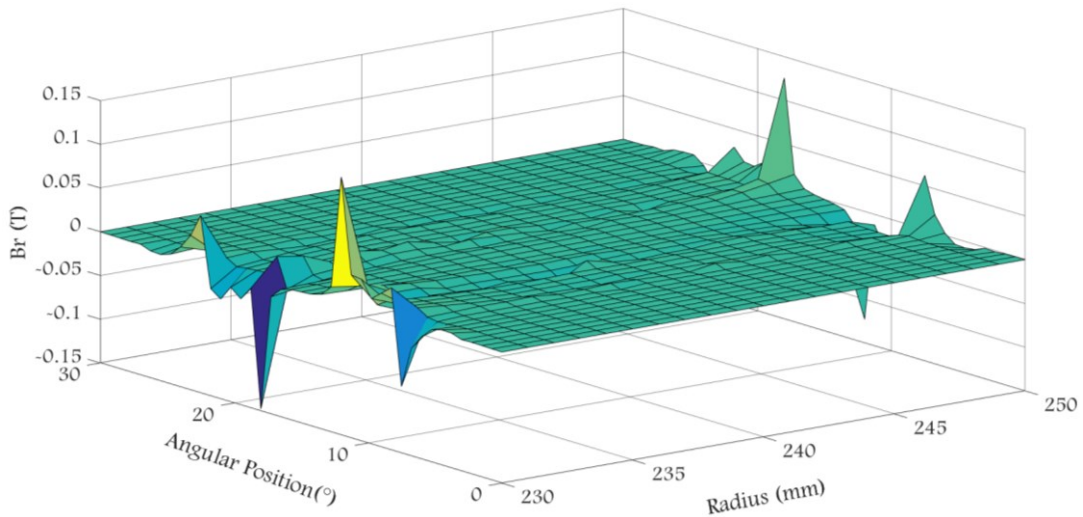


Fig. 2.32: Radial component of air gap magnetic flux density as a function of radius and angle

c) Non-linear BH curve case

B_{sat} is the magnetic flux density at saturation set equal to 1.99 T. μ_{r0} is the relative permeability at the origin, set equal to 3500. $U_i^k U_i$ is the potential at node i for iteration k . n is the total number of nodes. Fig. 2.33 and Fig. 2.34 show respectively the obtained normal and tangential magnetic flux densities in the middle of the air gap, and electromagnetic torque.

Tab. 2.4 shows the corresponding errors and Tab. 2.5 shows computation time comparison in seconds between both models.

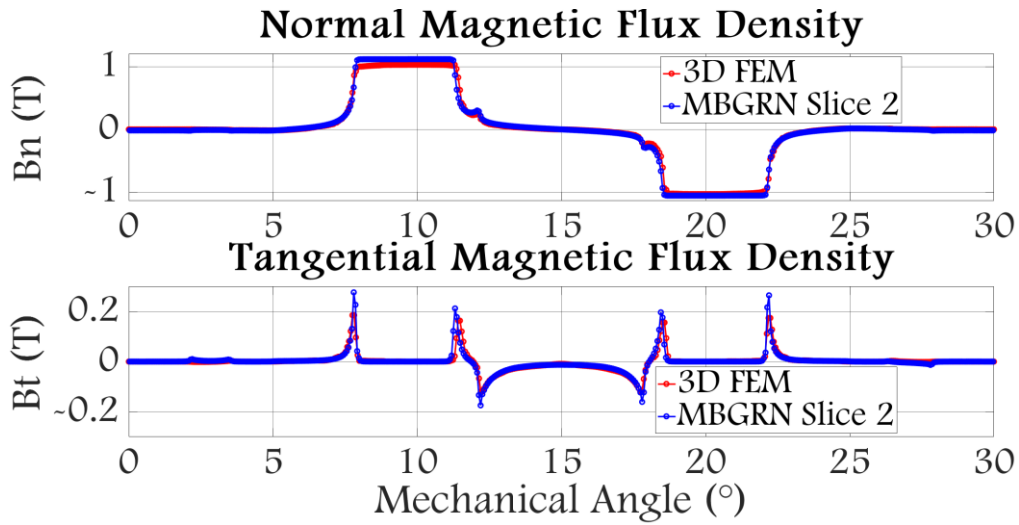


Fig. 2.33: Normal and tangential magnetic flux density in the middle of the air gap at $x=0$ for both models incorporating saturation

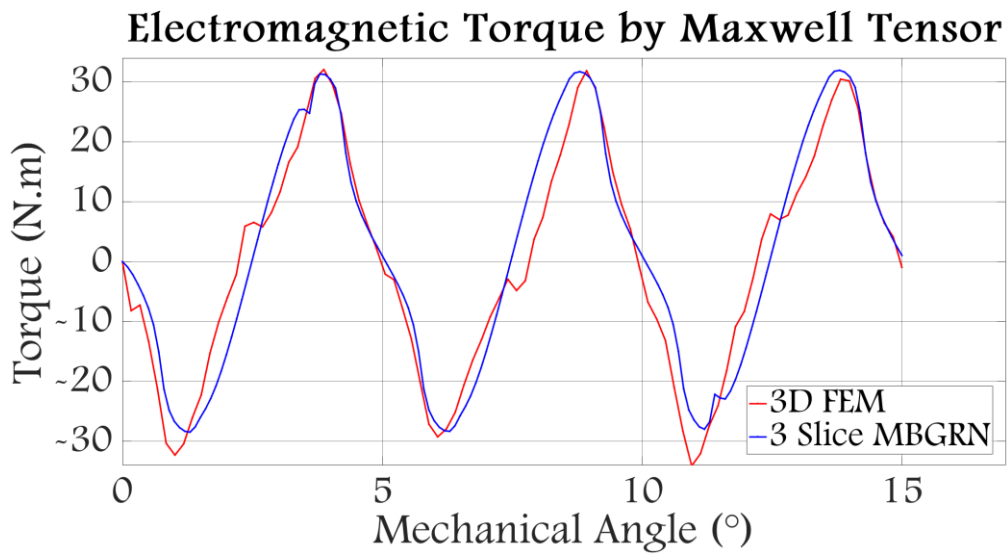


Fig. 2.34: Electromagnetic torque for both models incorporating saturation

Tab. 2.4: Errors on important quantities for the proposed method

Quantity	ϵ_{RMS} (%)	ϵ_{MAX} (%)
Normal MFD	9.86	8.62
Tangential MFD	49.14	49.36
Torque	29.12	0.58

Tab. 2.5: Computation time comparison between both methods

Method	Computation time (s)
Multi-slice MBGRN	54.0675
3D FEM	1644.53
Speed factor	30.42

d) Application of the method on a surface mounted PM machine

In this section, we will try to extend the method to be applied on an axial flux surface mounted PM machine (Fig. 2.35). The geometric parameters of the machine are given in Tab. 2.6. The machine is cut into 5 slices of same thickness in the radial direction and the 2D reluctance network is established at the mean radius of each slice. A simulation was performed at one position at no load and in linear magnetic material conditions to evaluate the magnetic flux density at the middle of the air gap for both 3D finite elements model and the multi-slice reluctance network model at the mid-slice (slice 3). Fig. 2.36 shows a comparison between both models for the normal component of the magnetic flux density and Fig. 2.37 shows a comparison between both models for the tangential component of the magnetic flux density.

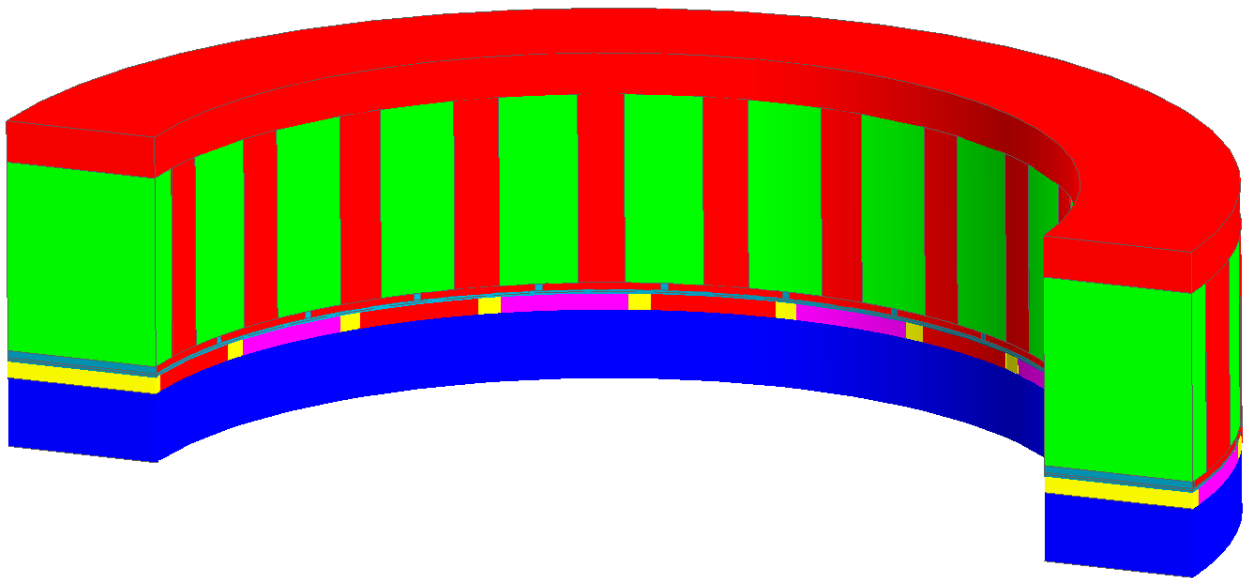


Fig. 2.35: Modeled half of the studied axial flux surface mounted PM machine

Tab. 2.6: Geometrical parameters of the studied machine

Parameter	Value
External Radius	180 mm
Internal Radius	135 mm
Slots/poles	24/20
Magnet remanence	1.2 T
Airgap	1.2 mm
Polar arc coefficient	0.85

Slot height	55 mm
Magnet thickness	4.7 mm
Angle of repeating pattern	180°
Magnetic pattern repetitions	2

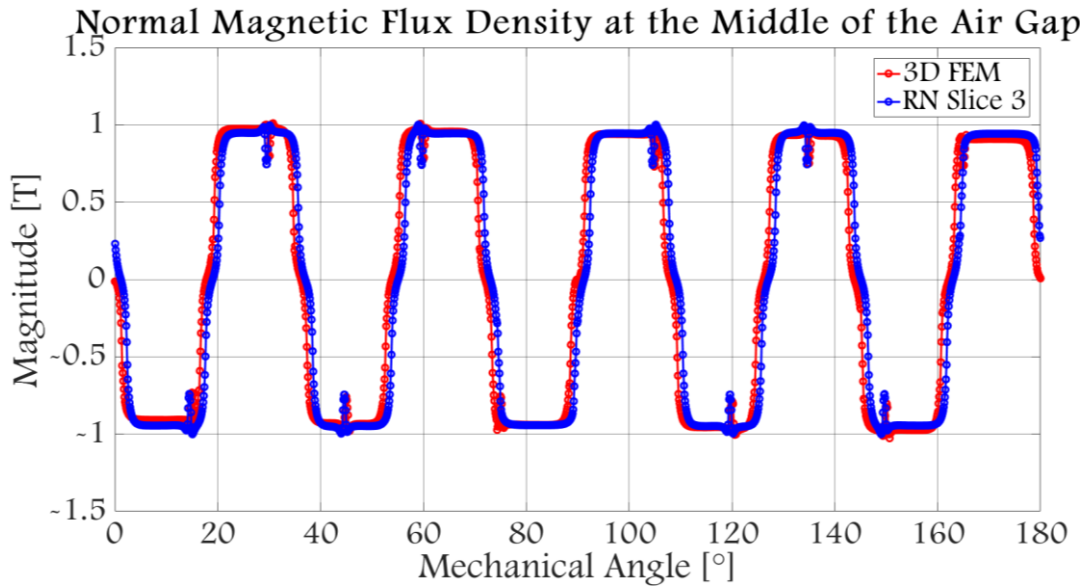


Fig. 2.36: Normal component of the magnetic flux density at the middle of the air gap at $x=0$ for both models

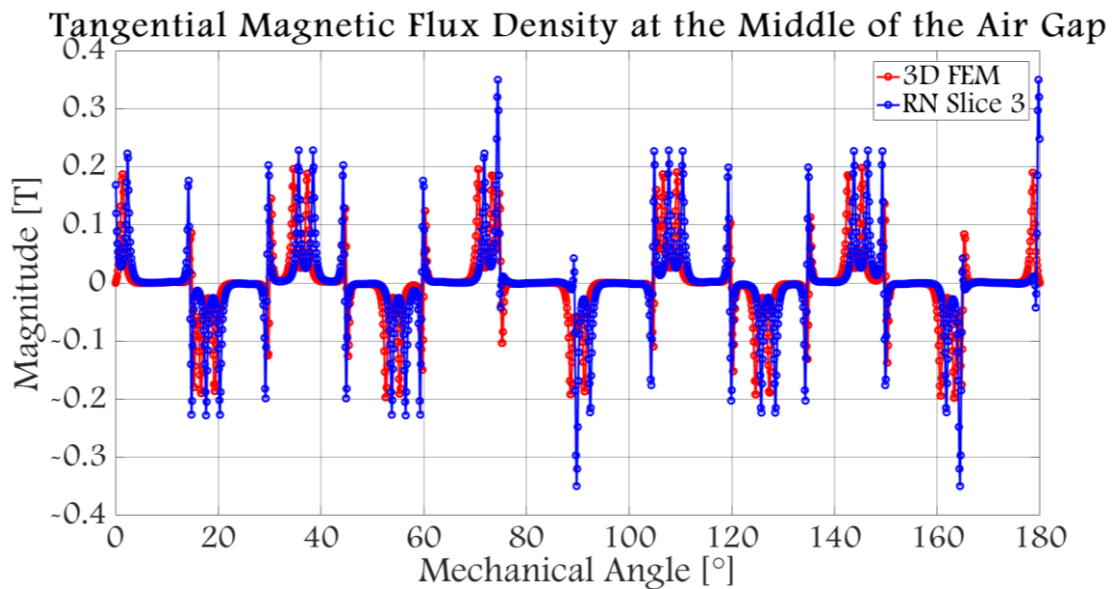


Fig. 2.37: Tangential component of the magnetic flux density at the middle of the air gap at $x=0$ for both models

3. Quasi-3D Reluctance Network

a) Algorithm

The algorithm for generating the reluctance network is the same as for the 2D multi-slice case with the difference that after constructing the magnetic matrix and the excitation vector of all slices of the model and before solving the system, the slices are connected with reluctances in 3rd direction (Fig. 2.38) and the overall system matrix and excitation vector are created, as depicted in the following matrices (for 3 slices as an example):

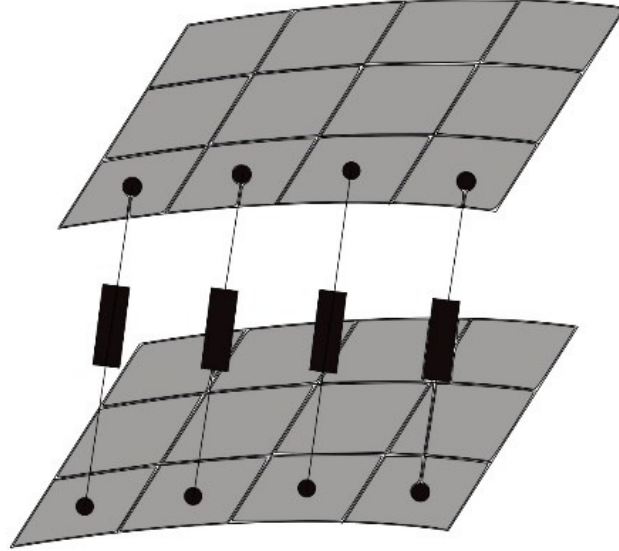


Fig. 2.38: Connection of slices by reluctances

$$P_{ij} = \begin{cases} [Mag_i]_{(n_\varphi \times n_z)} & \text{if } i = j \\ [M_{ij}]_{(n_\varphi \times n_z)} & \text{if } i = j + 1 \text{ or } j = i + 1 \\ [0]_{(n_\varphi \times n_z)} & \text{elsewhere} \end{cases} \quad (2.113)$$

$$M_{ij} = \begin{bmatrix} P_{ri-j}^1 & \dots & 0 \\ \vdots & \ddots & \vdots \\ 0 & \dots & P_{ri-j}^m \end{bmatrix} \quad (2.114)$$

$$\varphi_s = \begin{bmatrix} [\varphi_{s1}] \\ \vdots \\ [\varphi_{sN_c}] \end{bmatrix} \quad (2.115)$$

$$P_{ri-j}^k = \frac{\mu_0 \mu_r^k \theta^k L_a}{\log\left(\frac{R_j}{R_i}\right)} \quad (2.116)$$

P 's diagonal elements are then modified using:

$$P_{kk}^{new} = P_{kk}^{old} - P_{ri-j}^k \quad (2.117)$$

Where $1 \leq i \leq N_c$, $1 \leq j \leq N_c$ and $1 \leq k \leq m$. N_c is the number of slices in the radial direction. m is the number of permeances in the radial direction between slices i and j . n_φ and n_z are respectively the number of elements in the circumferential and axial direction in a slice. Mag_i is the permeance matrix of slice i ; it is constructed from the values of permeances linking each node in the slice to its neighboring nodes. $[0]$ is a zero element matrix. P_{ij} are the elements of the overall magnetic matrix P of the system. $[\varphi_{s1}] \dots [\varphi_{sN_c}]$ are the flux sources vectors for each slice respectively. φ_s is the overall flux sources vector for the whole

system. P_{ri-j}^k are the permeances inserted between slices i and j in the radial direction (the connection between 2 slices is illustrated in Fig. 2.38). μ_0 is the permeability of free space. μ_r^k is the relative permeability of reluctance block k . θ^k is the opening angle of reluctance block k . L_a is the depth of a slice. R_i is the radius at which is located slice i . $P_{kk}^{old}, P_{kk}^{new}$ are respectively the new and current value of the diagonal elements of P . M_{ij} and $[0]$ are inserted in a way to make the overall permeance matrix square.

b) Studied Machine

The studied machine is the same AFDSSRM described above and supplied with the same current as above for the 2D and 3D models.

c) Error computation

To quantify observed error better than in the 2D multi-slice case (especially for the tangential component of magnetic flux density), the accuracy of the method was evaluated this time by calculating the error ε_{MEAN}^{MFD} on MFD and $\varepsilon_{MEAN}^{Torque}$ on torque. Each error metric was chosen because it best reflects the errors observed in the curves (y_{RN} and y_{FE} are respectively the vectors containing the values of the quantity calculated using the reluctance network model and the finite element model):

$$\varepsilon_{MEAN}^{MFD} = \frac{\text{mean}(|y_{RN}| - |y_{FE}|)}{\text{mean}|y_{FE}|} \times 100 \quad (2.118)$$

$$\varepsilon_{MEAN}^{Torque} = \frac{|\text{mean}(y_{RN} - y_{FE})|}{\text{mean}|y_{FE}|} \times 100 \quad (2.119)$$

d) Linear BH curve conditions

The currents injected in the coils of the 3 phases are the same as in the 2D case. Fig. 2.39 shows the normal and tangential components of the magnetic flux density (MFD) in the middle of the air gap for slice 2 obtained with the Q3DRN and compared with the one obtained by the 3D FEM at mean radius. Fig. 2.40 illustrates the comparison between electromagnetic torque obtained with the 3 slices of the Q3DRN and that obtained with 3D FEM.

Errors on the normal and tangential components of the MFD as well as on electromagnetic torque for the Q3DRN method compared with full 3D FEM are given in Tab. 2.7 with the corresponding computation time. Computation time was assessed for one rotor position on a computer with a 3.50 GHz Intel® Xeon® CPU E5-1620 v4 and 32 GB of RAM. It was calculated for the last 2 steps of the algorithm without post-processing. The steps are 1) set-up machine parameters and phase currents; 2) import mesh; 3) construction of system matrix; 4) creation of overall system matrix and corresponding flux sources vector and system solving.

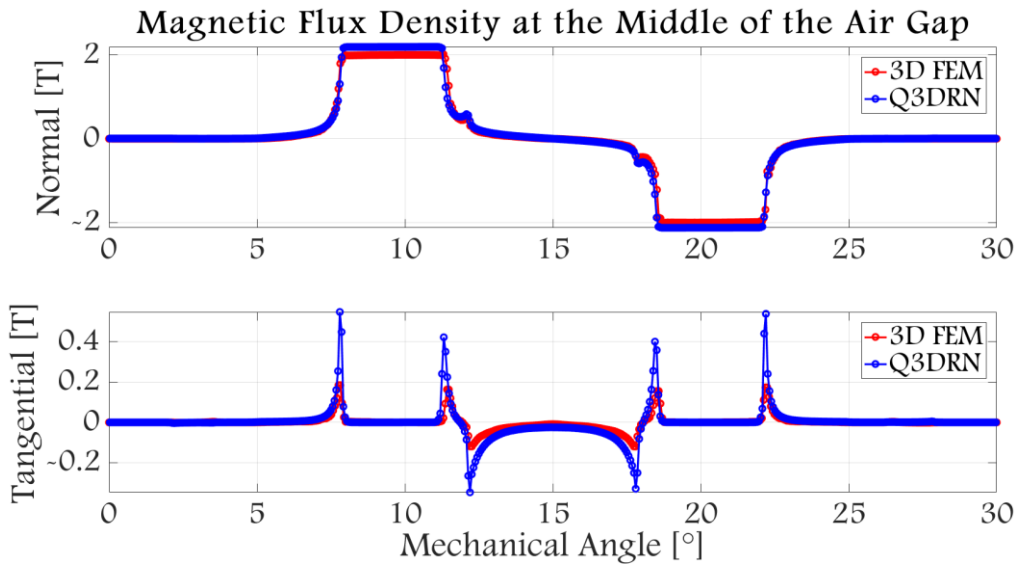


Fig. 2.39: Normal and tangential magnetic flux density in the middle of the air gap at $x=0$ for both models in linear conditions

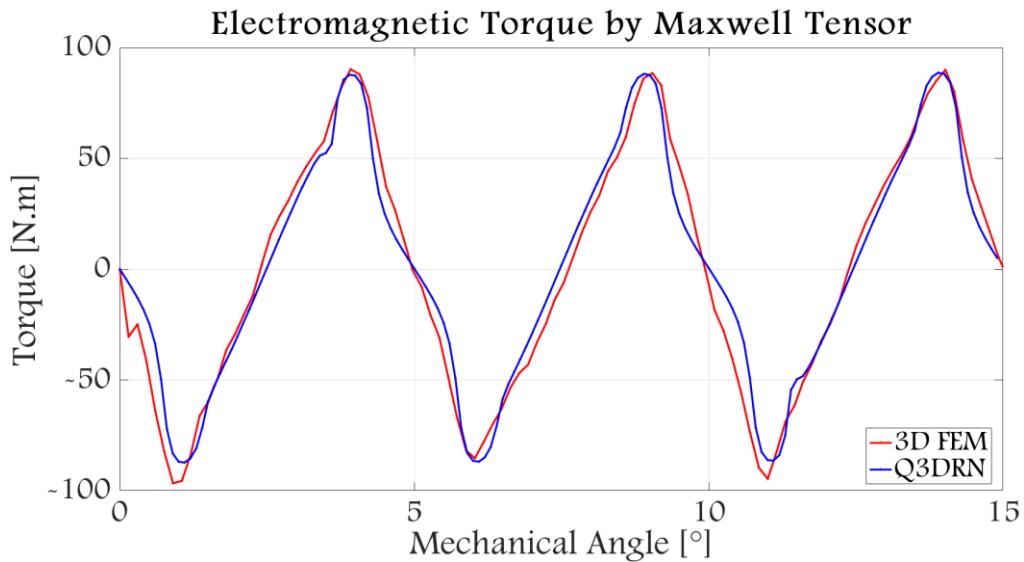


Fig. 2.40: Electromagnetic torque for both models in linear conditions

Tab. 2.7: Precision and computation time for the proposed method

Quantity	Error (%)	Method	Computation time
Normal MFD	8.92	Q3DRN	39.75 s
Tangential MFD	6.5	3D FEM	429 s
Torque	2.48	t_{FE}/t_{RN}	10.79

e) Nonlinear BH curve case

Fig. 2.41 shows the normal and tangential magnetic flux densities in the middle of the air gap at mean radius. Fig. 2.42 illustrates the electromagnetic torque. Tab. 2.8 shows the

errors on magnetic flux densities and torque and compares computation time for 1 resolution between Q3DRN and full 3D FEM.

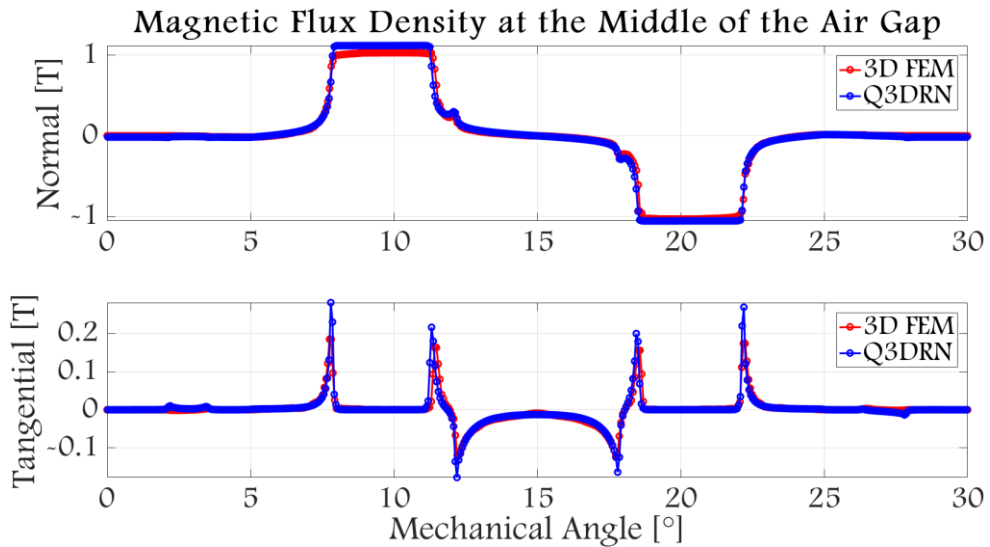


Fig. 2.41: Normal and tangential magnetic flux density in the middle of the air gap at $x=0$ for both models in nonlinear conditions

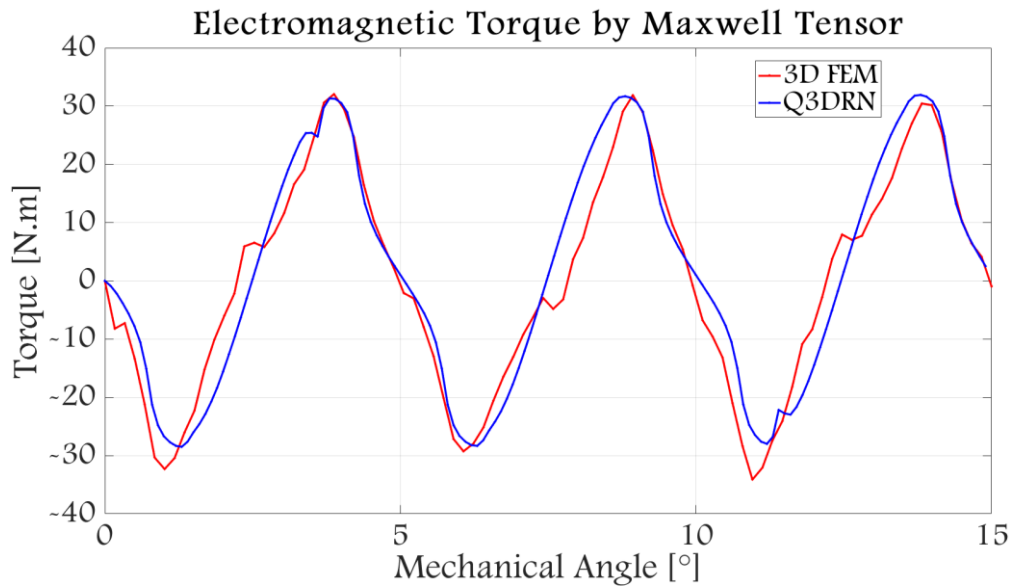


Fig. 2.42: Electromagnetic torque for both models in nonlinear conditions

Tab. 2.8: Precision and computation time for the proposed method

Quantity	Error (%)	Method	Computation time
Normal MFD	7.93	Q3DRN	51.99 s
Tangential MFD	6.42	3D FEM	1178 s
Torque	7.64	t_{FE}/t_{RN}	22.66

f) Q3DRN model validity evaluation by parameter variation

To verify the robustness of the proposed method, a parametric study by geometric parameter variation was conducted. The study consisted of varying the rotor to stator tooth width ratio $K_t = w_r/w_s$ by fixing the stator's tooth width and varying the rotors (w_r is the rotor tooth width and w_s is the stator tooth width); the reluctance network is then regenerated and the obtained system is solved. The tooth width ratio before any modification is 1.8, so 2 ratios were chosen: 1.5 (a ratio decrease) and 2.1 (a ratio increase), then electromagnetic torque was computed for each case and compared with full 3D FEM in linear and nonlinear BH curve conditions (Fig. 2.43). Torque characteristic for different K_t s using RN is presented in Fig. 2.44. Precision and computation time are reported in Tab. 2.9.

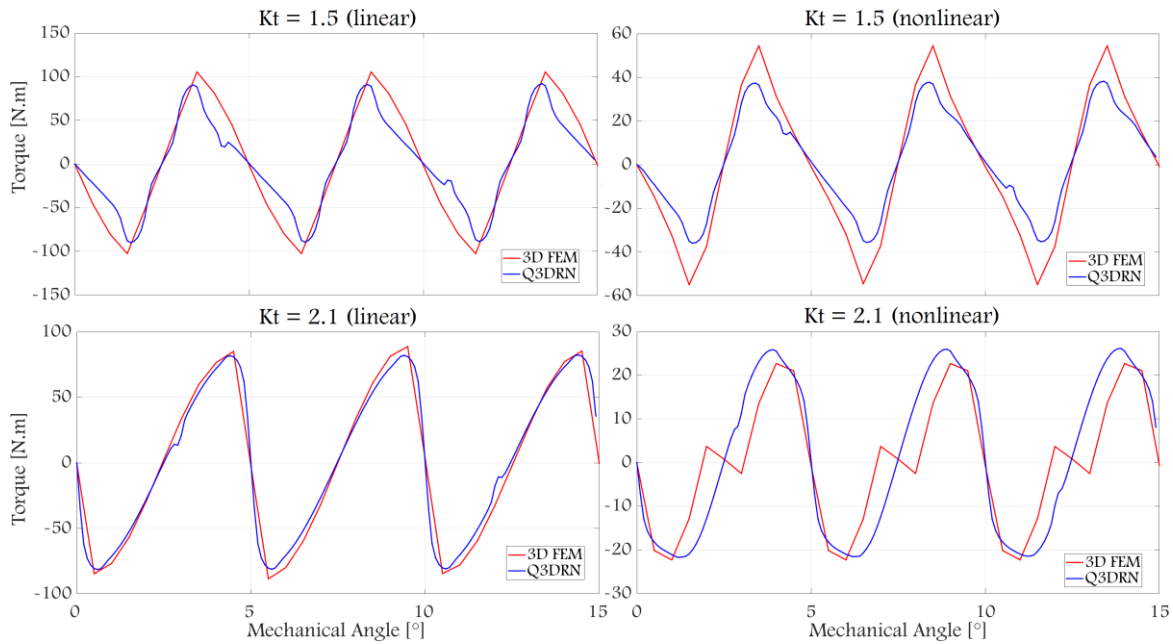


Fig. 2.43: Electromagnetic torque for $K_t=1.5$ and 2.1 in linear and nonlinear BH curve conditions

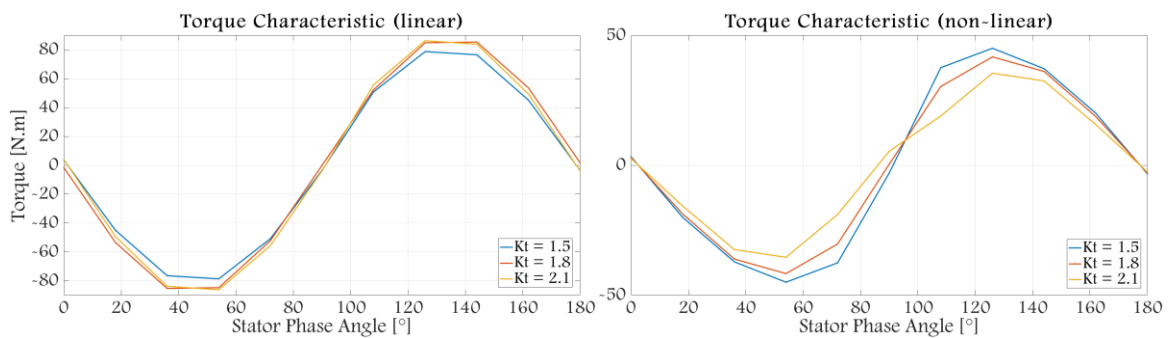


Fig. 2.44: Electromagnetic torque characteristic for different K_t s

Tab. 2.9: Precision on torque computation and computation time (sec/resolution) comparison for the different tooth width ratios

Ratio	Iron Permeability	Error (%)	Q3DRN	3D FEM	t_{FE}/t_{RN}
1.5	Linear	0.53	35.77	300	8.39
1.5	Non-Linear	5.64	51.43	545	10.6
1.8	Linear	2.48	39.75	429	10.79
1.8	Non-Linear	7.64	51.99	1178	22.65

2.1	Linear	1.4	30.83	244	7.91
2.1	Non-Linear	6.735	47.05	841	17.87

IV. Magnetic Finite Element Method [25][19][26]

1. Maxwell's equations

The basic building blocks of the finite elements method are Maxwell's equations. These partial differential equations link local quantities such as magnetic flux density and magnetic field intensity to space and time variables and depict the global behavior of the modeled physical system. To completely characterize the modeled system 3 equations are added that are relative to the medium in which electromagnetic phenomena takes place to obtain the following system of 7 equations:

$$\vec{\nabla} \times \vec{E} = -\frac{\partial \vec{B}}{\partial t} \quad (2.120)$$

$$\vec{\nabla} \times \vec{H} = \frac{\partial \vec{D}}{\partial t} + \vec{j} \quad (2.121)$$

$$\vec{\nabla} \cdot \vec{B} = 0 \quad (2.122)$$

$$\vec{\nabla} \cdot \vec{D} = \rho \quad (2.123)$$

$$\vec{B} = \mu \vec{H} + \vec{B}_r \quad (2.124)$$

$$\vec{D} = \epsilon \vec{E} \quad (2.125)$$

$$\vec{j} = \sigma \vec{E} \quad (2.126)$$

Where	$\vec{B}(T)$	magnetic flux density,
	$\vec{B}_r(T)$	remnant magnetic flux density in magnets,
	$\vec{D}(C/m^2)$	electrical flux density,
	$\vec{E}(V/m)$	electric field,
	$\vec{H}(A/m)$	magnetic field,
	$\vec{j}(A/m^2)$	current density,
	$t(s)$	time,
	$\epsilon(F/m)$	permittivity,
	$\mu(H/m)$	permeability,
	$\rho(C/m^3)$	charge density,
	$\sigma(S/m)$	conductivity.

In electrical engineering, the displacement currents $\frac{\partial \vec{D}}{\partial t}$ can be neglected in equation (2.121) due to the low frequency involved; the equations are thus decoupled, allowing us to study magnetic and electric fields separately.

2. Magneto-static Formulations [27][28]

In magneto-statics, the equations to be solved are the following, and they are solved on a domain D whose boundary is decomposed into 2 complementary parts Γ_h and Γ_b :

$$\vec{\nabla} \times \vec{H} = \vec{J}_0 \quad (2.127)$$

$$\vec{\nabla} \cdot \vec{B} = 0 \quad (2.128)$$

The equation describing material behavior is added to the above equations:

$$\vec{B} = \mu \vec{H} \quad (2.129)$$

Boundary conditions are imposed on Γ_h and Γ_b :

$$\vec{H} \wedge \vec{n}|_{\Gamma_h} = 0 \quad (2.130)$$

$$\vec{B} \cdot \vec{n}|_{\Gamma_b} = 0 \quad (2.131)$$

a) Magnetic scalar formulation φ

In order to introduce the scalar potential formulation, we define a source field \vec{H}_S such that its rotational satisfies:

$$\vec{\nabla} \times \vec{H}_S = \vec{J}_0 \quad (2.132)$$

For the source field, we set as a boundary condition on Γ_h :

$$\vec{H}_S \wedge \vec{n}|_{\Gamma_h} = 0 \quad (2.133)$$

By grouping equations (2.127) and (2.132), we can write:

$$\vec{\nabla} \times (\vec{H} - \vec{H}_S) = 0 \quad (2.134)$$

This makes it possible to introduce the magnetic scalar potential φ such that:

$$\vec{H} = \vec{H}_S - \nabla \varphi \quad (2.135)$$

To obtain a unique solution for the magnetic scalar potential, a homogenous boundary conditions is imposed on the boundary Γ_h :

$$\varphi|_{\Gamma_h} = 0 \quad (2.136)$$

By combining equation (2.134) with the behavior law (2.129) and equation (2.128), we obtain the scalar potential formulation of a magneto-static problem:

$$\vec{\nabla} \cdot \mu (\vec{H}_S - \nabla \varphi) = 0 \quad (2.137)$$

b) Magnetic vector formulation \vec{A}

Since flux density \vec{B} has zero divergence, there exists is a vector potential \vec{A} such that:

$$\vec{B} = \vec{\nabla} \times \vec{A} \quad (2.138)$$

In order to obtain a unique solution, a gauge condition is imposed on \vec{A} (i.e $\vec{\nabla} \cdot \vec{A} = 0$). Also, a boundary condition is set for \vec{A} on Γ_b such that:

$$\vec{A} \wedge \vec{n}|_{\Gamma_b} = 0 \quad (2.139)$$

By grouping equations (2.127) and (2.138) with the behavior law (2.129), the formulation in magnetic vector potential is written as:

$$\vec{\nabla} \times \frac{1}{\mu} \vec{\nabla} \times \vec{A} = \vec{j}_0 \quad (2.140)$$

3. Magneto-dynamic Formulations [29][28]

In magneto-dynamics, we have to solve equations (2.141) and (2.142) below with the behavior laws in a conductive domain Dc where induced currents appear.

$$\vec{\nabla} \times \vec{E} = -\frac{\partial \vec{B}}{\partial t} \quad (2.141)$$

$$\vec{\nabla} \times \vec{H} = \vec{j} \quad (2.142)$$

The equation describing the behavior of a conducting material is added to the above equations:

$$\vec{j} = \sigma \vec{E} \quad (2.143)$$

The boundary of Dc is decomposed into 2 complementary parts Γ_e and Γ_h on which boundary conditions are imposed for \vec{E} and \vec{H} :

$$\vec{E} \wedge \vec{n}|_{\Gamma_e} = 0 \quad (2.144)$$

$$\vec{H} \wedge \vec{n}|_{\Gamma_h} = 0 \quad (2.145)$$

For simplification, it is assumed that the source term is external to the domain Dc and the equations to be solved only on the domain Dc are presented. It is then explained how to make the coupling between the equations of magneto-dynamics on Dc and those of magneto-statics defined on D - Dc. Two formulations can then be introduced:

a) A-V formulation

The first formulation is the A-V formulation combining the magnetic vector potential A and the electric scalar potential V.

By replacing in equation (2.141) the magnetic flux density by its given expression in (2.138), we can write:

$$\vec{\nabla} \times \left(\vec{E} + \frac{\partial \vec{A}}{\partial t} \right) = 0 \quad (2.146)$$

which leads to the following relation by introducing the scalar potential:

$$\vec{E} = -\left(\frac{\partial \vec{A}}{\partial t} + \vec{\nabla} V \right) \quad (2.147)$$

By combining (2.147), (2.138) and (2.142) with the material behavior laws (2.129) and (2.126), we obtain:

$$\vec{\nabla} \times \frac{1}{\mu} \vec{\nabla} \times \vec{A} = -\sigma \left(\frac{\partial \vec{A}}{\partial t} + \vec{\nabla} V \right) \quad (2.148)$$

b) T-φ formulation

The second formulation is the T- φ formulation which combines the electric vector potential T and the magnetic scalar potential φ.

As $\vec{\nabla} \cdot \vec{J} = 0$, we can write the current density \vec{J} as a function of an electric vector potential \vec{T} in the form:

$$\vec{J} = \vec{\nabla} \times \vec{T} \quad (2.149)$$

By replacing in the domain Dc the current density in equation (2.142) by its expression as a function of the vector potential T (2.149) we obtain:

$$\vec{\nabla} \times (\vec{H} - \vec{T}) = 0 \quad (2.150)$$

This expression gives rise to the magnetic scalar potential φ:

$$\vec{H} = \vec{T} - \vec{\nabla} \phi \quad (2.151)$$

Grouping (2.141) and (2.151) with the behavior laws, we can write the magnetic formulation in potentials in the Dc domain in the following form:

$$\vec{\nabla} \times \frac{1}{\sigma} \vec{\nabla} \times \vec{T} = -\frac{\partial}{\partial t} \left(\mu (\vec{T} - \vec{\nabla} \phi) \right) \quad (2.152)$$

V. Thermal Model

1. Heat Transfer Mechanisms

In the following is a brief overview of the thermal modelling approach, for a more in-depth look the reader is referred to [30][31][32][33].

Heat transfer takes places mainly by means of 3 mechanisms: conduction, convection and radiation.

a) Conduction

Thermal conduction is the transfer of a heat quantity by direct interaction, under the influence of a temperature gradient, within a medium or between media in direct physical contact without material flow. This can be expressed using Fourier's law by:

$$\frac{dQ}{dt} = [\lambda] dS \cdot \vec{\nabla} T \cdot \vec{n} \quad (2.153)$$

Where

$\frac{dQ}{dt}$ is the heat exchange power in W

$[\lambda]$ is the thermal conductivity tensor in the principal directions of the material

dS is the exchange surface perpendicular to the flux (YZ) in m²

$\vec{\nabla} T \cdot \vec{n}$ is the scalar product of the temperature gradient by the vector normal to dS in K/m

b) Convection

Thermal convection is the transfer of heat by a moving fluid (gas or liquid). It can be natural, like in the case of outer yokes of a machine in the absence of external ventilation, or forced when heat transfer is generated by an action other than the natural presence of temperature gradients. Convection is always associated with heat conduction. Heat transfers that pass through a fluid/solid interface can be expressed using Newton's formula:

$$\frac{dQ}{dt} = hS(T_F - T_S) \quad (2.154)$$

Where

h is the convective heat transfer coefficient in W/m^2K which depends on geometry and flow type

S is the exchange surface in m^2

$(T_F - T_S)$ is the difference of mean temperature between the fluid and the surface of the object in contact with the fluid

c) Radiation

Thermal radiation is the electromagnetic radiation emitted or absorbed by a body, which depends only on its thermodynamic temperature and the cleanliness of its surface. In an electrical motor or generator, radiant heat exchange can take place between the air gap surfaces and the rotor and stator surfaces, or between the outer surfaces and the surrounding medium.

2. Methods of Thermal Modelling

Several methods are used to study the thermal properties of electrical machines. Numerical methods such as the nodal finite element method or the computational fluid dynamics (CFD) method are commonly used. Numerical methods are certainly useful for optimizing designs and validating the behavior of the product before manufacturing, but they are difficult to adapt to pre-sizing. The experimental method helps in the validation of numerical methods and remains the reference. However, it requires the conducting tests on a real prototype. Semi-analytical methods such as the thermal resistance network method make it possible to reduce the time spent on pre-sizing while maintaining an acceptable accuracy. The thermal network method or nodal method or lumped parameter method is used for thermal modeling of electrical machines and is based on the generation of a network of thermal resistances which has a certain analogy with the electrical circuit and the magnetic reluctance circuit. The thermal semi-analytical method is advantageous for determining the thermal behavior of particularly critical areas. For example, permanent magnets which may be inaccessible to experimental measurement if they are buried. The work presented uses an analytical method, the lumped parameter method, which derives from Kirchhoff's theory and takes into account the paths traveled by heat.

3. Lumped Parameter Method

In order to study the thermal behavior of the machine, we chose a lumped parameter thermal model as it is widely used. The particular model that we used was developed by Guillaume VEREZ [34] at GREAH and integrated into the SIMUMSAP tool. It's a nodal network of thermal resistances, thermal capacitances and heat sources, where the temperature is computed at each node. To construct this network, the machine geometry is subdivided into

small volumes that are considered to be homogeneous and isotherm, then the different elements of the network are computed for each volume. Fig. 2.45 shows the connection between the different volumes of the machine.

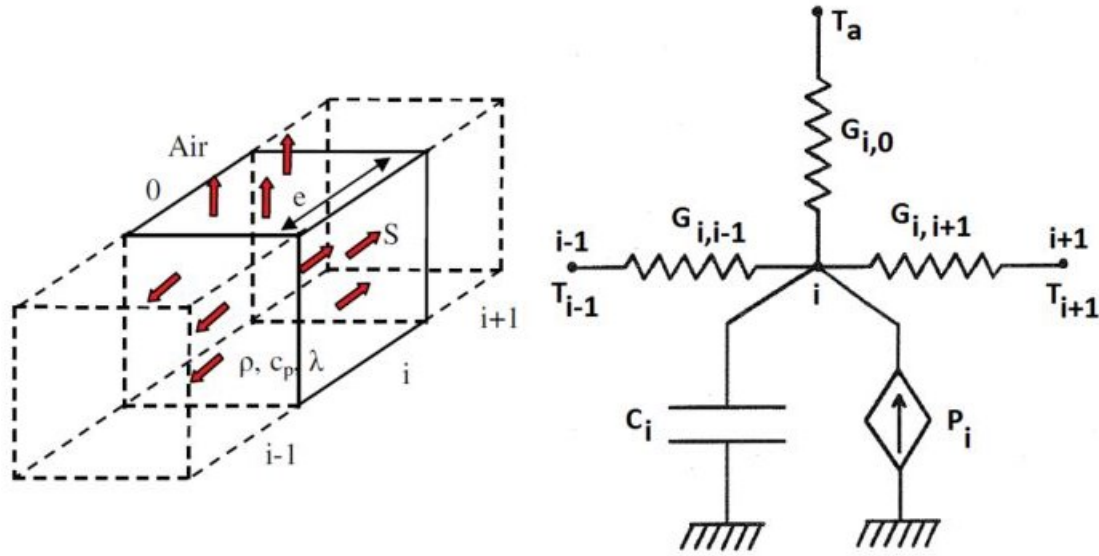


Fig. 2.45: Conductance network for each node [35]

Starting from the heat equation (2.155), and integrating it on the volume i gives (2.156). As there is little temperature difference inside the motor frame and its surfaces' emissivity is low, radiation can be neglected [36]. But if it is necessary to take it into account, a 10% increase in convection coefficient is possible for little radiation [37]. These reflections yields equation (2.157) for a finite number of volumes n which can be written in matrix form as (2.158).

$$\rho c \frac{dT}{dt} d\tau + \nabla \Phi d\tau = p d\tau \quad (2.155)$$

$$C_i \frac{dT_i}{dt} = \Phi_{conduction} + \Phi_{mass\ transfer} + \Phi_{convection} + \Phi_{radiation} + P_i \quad (2.156)$$

$$C_i \frac{dT_i}{dt} = \sum_{j=1}^n G_{ij}(T_j - T_i) + G_{i,ext}(T_i - T_a) + P_i \quad (2.157)$$

$$[C][\dot{T}] = -[G][T] + [L]T_a + [P] \quad (2.158)$$

Where $\rho c \frac{dT}{dt} d\tau$ is the rate of change of the energy stored in the volume element $d\tau$. ρ is the density and c the specific heat capacity. $\nabla \Phi d\tau$ is the flux outgoing $d\tau$, and p heat production density produced in this volume. G_{ij} is the thermal conductance (W/K) of volume i which defines exchange between volume i and j . C_i is the heat capacity (J/K) of volume i . T_i is the temperature (K) of volume i . $G_{i,ext}$ is the thermal conductance of volume i towards air. T_a is air temperature. $[G](n \times n)$ is the thermal conductance matrix, $[C](n \times n)$ is the heat capacity matrix, $[T]$ is the temperature vector ($n \times 1$), $[P](n \times 1)$ is the dissipated power matrix and $[L](n \times 1)$ gathers $G_{i,ext}$ terms.

VI. Mechanical Finite Element Method [38][39][40]

The structural system is discretized by a set of appropriate finite elements interconnected at points called nodes. Nodes will have nodal displacements or degrees of freedom which may include translations or rotations. When the nodes displace, they drag the elements along in a certain manner. In other words, displacements of any points in the element are interpolated from the nodal displacements.

In structural mechanics the deformation and stresses are calculated for structural objects that are subject to loads (body and surface forces, thermal loads, etc.). Stresses are the internal forces in a structure that are reactions to the load that is applied to the structure, whereas strain is a measure of the deformation. The constitutive relation describes how stress and strain relate to each other. For linear elasticity Hooke's law, $\sigma = E\varepsilon$, describes the relation, where σ is the stress, ε is the strain and E is Young's modulus.

1. Strong formulation

In stress analysis, a rectilinear coordinate system is the most convenient to develop the mathematical theory. A Cartesian coordinate system of origin O and axes Ox , Oy , and Oz is adopted here as it is often used in the finite element method. For an elementary volume δV , the total stress is broken down into normal and shear stress. The normal stress is perpendicular to the volume and is either in the x or y or z direction and is denoted in the following by σ_{xx} , σ_{yy} and σ_{zz} . The shear stress is tangential to the volume and is denoted in the following by σ_{xy} , σ_{yx} , σ_{xz} , σ_{zx} , σ_{yz} and σ_{zy} . Finally the stress tensor can be defined by:

$$\sigma = \begin{bmatrix} \sigma_{xx} & \sigma_{xy} & \sigma_{xz} \\ \sigma_{yx} & \sigma_{yy} & \sigma_{yz} \\ \sigma_{zx} & \sigma_{zy} & \sigma_{zz} \end{bmatrix} \quad (2.159)$$

We can define the stress equilibrium by the following equation reflecting the spatial variation of the stress when the body is at rest (static structural analysis):

$$\tilde{\nabla}^T \sigma + b = 0 \quad (2.160)$$

Where $\tilde{\nabla}^T$ is a differential operator and is given by $\tilde{\nabla}^T = \begin{bmatrix} \frac{\partial}{\partial x} \\ \frac{\partial}{\partial y} \\ \frac{\partial}{\partial z} \end{bmatrix}^T$ and b is the body force

acting on the structure. Body forces are often zero but if their orders of magnitude are similar to those of external forces, they have to be included in the equation.

For a displacement u , the strain kinematic relation defining the relationship between strain and displacement is as follows:

$$\epsilon = \tilde{\nabla}^T u \quad (2.161)$$

The boundary conditions are defined by one of the following equations, where t is the traction vector and is u a prescribed displacement on the surface of the structure:

$$\begin{cases} t = S_n = h & \text{on } S_h \\ u = g & \text{on } S_g \end{cases} \quad (2.162)$$

2. Weak formulation

In order to obtain the weak formulation, the strong formulation is multiplied with a weight function v and integrated over the volume; (2.160) thus yields the following condition:

$$\int_V v \tilde{\nabla}^T \sigma dV + \int_V v b dV = 0 \quad (2.163)$$

Green's theorem is used along with the boundary condition in (2.162) to obtain the equation for the weak formulation of stress equilibrium which is the following:

$$\int_V (\tilde{\nabla} v)^T \sigma dV = \int_V v^T t dS + \int_V v^T b dV \quad (2.164)$$

Finite element software uses the weak formulation in mechanical simulation to approximate the continuous displacement vector u based on the following equation:

$$u = Na \quad (2.165)$$

Where

N is a shape function matrix

a is the nodal displacement vector

The weight function v can be approximated by the following equation if the same approach is adopted (c is defined as an arbitrary vector):

$$v = Nc \quad (2.166)$$

Based on the above equation, the following expression can be obtained:

$$\int_V (\tilde{\nabla} N)^T \sigma dV = \int_V N^T t dS + \int_V N^T b dV \quad (2.167)$$

Using the strain-displacement relationship given in equation (2.161) and the constitutive relation (2.168) linking stress and strain by the constitutive matrix D ,

$$\sigma = D\epsilon \quad (2.168)$$

the final formulation used in finite element modelling of bodies in structural mechanics is obtained:

$$Ka = f \quad (2.169)$$

Where K is the linear stiffness matrix, and is given by the following integral:

$$K = \int_V (\tilde{\nabla} N)^T D (\tilde{\nabla} N) dV \quad (2.170)$$

and f is the force vector grouping body forces, boundary conditions and initial strain.

Finally, the system of equations that is solved in commercial FE software is that of equation (2.169) and the obtained solution a represents an approximation of the displacement vector u .

VII. Conclusion

In this chapter, different tools used for electrical machine sizing were presented and explained.

First, the 2D multi-slice analytical model based on the formal solution of Maxwell's equations in the different regions of an axial flux machine is developed. In this model, the solution for the magnetic vector potential as well as the magnetic flux density in the different regions of a 2D slice are obtained; these local quantities were then used to obtain global quantities such as flux, EMF and torque.

Then, an alternative method for sizing electrical machines was presented with a good compromise between precision and computation time relative to finite elements. The method, which is based on a reluctance network model, was applied on an axial flux machine. But as the method is generic it can be applied to all types of machines including radial flux ones. A demonstration of method capabilities was illustrated for a use case of a double stator single rotor switched reluctance axial flux machine.

The method was assessed by error and computation time measurement in linear and non-linear BH curve conditions for normal and tangential magnetic flux density in the air gap and total electromagnetic torque produced.

First, a 2D multislice reluctance network model was constructed and solved to find local and global variables. Results show a fairly good agreement between the proposed model and the full 3D-FEA model. The presented method also showed a gain in computation time relative to 3D-FEA, which makes it suitable for parameter optimization and electromagnetic performance analysis in early design stages of electrical machines.

Then, the model was improved by connecting the slices with reluctances in the third direction to take into account the variation of magnetic flux density from slice to slice in the radial direction. Once again results showed good concordance with 3D FEM for magnetic flux density and torque.

Towards the end of the chapter, the lumped parameter thermal model is presented showcasing the different heat transfer mechanisms i.e. conduction, convection and radiation with their corresponding heat transfer equations; then, the different thermal modelling approaches such as numerical models (nodal finite elements, CFD...) and semi analytical models (lumped parameter...) were presented and the choice of the model was justified. This was followed by an explanation of the lumped parameter thermal model and the solved heat equation.

The finite elements method used to electromagnetically size electrical machines was explained starting by Maxwell's equations that are used to obtain the formulations for magneto-static and magneto-dynamic simulations. Then, the formulations used in each type of simulation were detailed. These formulations being magnetic scalar and magnetic vector formulations for magneto-static simulations and A-V and T- φ formulations for magneto-dynamic simulations.

Finally, the finite elements method used to mechanically size electrical machines was briefly explained for both strong and weak formulations, illustrating the solved equation by mechanical FE software to obtain the approximate value of displacement in a material.

References

- [1] H. Tiegna, A. Bellara, Y. Amara, and G. Barakat, "Analytical Modeling of the Open-

- Circuit Magnetic Field in Axial Flux Permanent-Magnet Machines With Semi-Closed Slots,” *IEEE Trans. Magn.*, vol. 48, no. 3, pp. 1212–1226, Mar. 2012, doi: 10.1109/TMAG.2011.2171979.
- [2] J. Azzouzi, G. Barakat, and B. Dakyo, “Quasi-3-D analytical modeling of the magnetic field of an axial flux permanent-magnet synchronous machine,” *IEEE Trans. Energy Convers.*, vol. 20, no. 4, pp. 746–752, Dec. 2005, doi: 10.1109/TEC.2005.845538.
- [3] J. Perho, “Reluctance Network for Analysing Induction Machines,” 2002.
- [4] H. W. Derbas, J. M. Williams, A. C. Koenig, and S. D. Pekarek, “A Comparison of Nodal- and Mesh-Based Magnetic Equivalent Circuit Models,” *IEEE Trans. Energy Convers.*, vol. 24, no. 2, pp. 388–396, Jun. 2009, doi: 10.1109/TEC.2008.2002037.
- [5] D. Elloumi, A. Ibalá, R. Rebhi, and A. Masmoudi, “Lumped Circuit Accounting for the Rotor Motion Dedicated to the Investigation of the Time-Varying Features of Claw Pole Topologies,” *IEEE Trans. Magn.*, vol. 51, no. 5, pp. 1–8, May 2015, doi: 10.1109/TMAG.2015.2405896.
- [6] S. Wu, X. Zhao, X. Li, P. C. K. Luk, and Z. Jiao, “Preliminary Design and Optimization of Toroidally Wound Limited Angle Servo Motor Based on a Generalized Magnetic Circuit Model,” *IEEE Trans. Magn.*, vol. 52, no. 9, pp. 1–9, 2016, doi: 10.1109/TMAG.2016.2559441.
- [7] X. Lu, K. L. V. Iyer, K. Mukherjee, and N. C. Kar, “Development of a Novel Magnetic Circuit Model for Design of Premium Efficiency Three-Phase Line Start Permanent Magnet Machines With Improved Starting Performance,” *IEEE Trans. Magn.*, vol. 49, no. 7, pp. 3965–3968, Jul. 2013, doi: 10.1109/TMAG.2013.2242869.
- [8] Y. Hane, K. Nakamura, T. Ohinata, and K. Arimatsu, “Reluctance Network Model of Three-Phase-Laminated-Core Variable Inductor Considering Magnetic Hysteresis Behavior,” *IEEE Trans. Magn.*, vol. 55, no. 7, pp. 1–6, Jul. 2019, doi: 10.1109/TMAG.2019.2900527.
- [9] H. Xie, G. Krebs, M. H. Hassan, M. Zhang, C. Marchand, and Z. Ren, “A New Reluctance Network-Based Method With Complementary Distributed Magnetomotive Forces,” *IEEE Trans. Magn.*, vol. 55, no. 6, pp. 1–5, Jun. 2019, doi: 10.1109/TMAG.2019.2909407.
- [10] S. Ouagued, A. A. Diriye, Y. Amara, and G. Barakat, “Mesh relaxation effect on results quality /computation time ratio of a hybrid semi-numerical model,” in *2016 Eleventh International Conference on Ecological Vehicles and Renewable Energies (EVER)*, Apr. 2016, pp. 1–5, doi: 10.1109/EVER.2016.7476411.
- [11] H. Nguyen-Xuan, H. Dogan, S. Perez, L. Gerbaud, L. Garbuio, and F. Wurtz, “Efficient Reluctance Network Formulation for Electrical Machine Design Using Optimization,” *IEEE Trans. Magn.*, vol. 50, no. 2, pp. 869–872, Feb. 2014, doi: 10.1109/TMAG.2013.2282407.
- [12] D. Petrichenko, “Calculation and Simulation of Turbogenerators Using Permeance Network. Optimization Application.,” Ecole Centrale de Lille, 2007.
- [13] ANSYS, “Electromagnetics Suite.” Canonsburg, PA, USA, 2015.
- [14] T. J. E. Miller, M. McGilp, and A. Wearing, “Motor design optimisation using SPEED CAD software,” in *IEE Seminar on Practical Electromagnetic Design Synthesis (Ref. No. 1999/014)*, Feb. 1999, pp. 2/1-2/5, doi: 10.1049/ic:19990050.
- [15] B. du Peloux, L. Gerbaud, F. Wurtz, V. Leconte, and F. Dorschner, “Automatic generation of sizing static models based on reluctance networks for the optimization of

- electromagnetic devices,” *IEEE Trans. Magn.*, vol. 42, no. 4, pp. 715–718, Apr. 2006, doi: 10.1109/TMAG.2006.872010.
- [16] H. De Gersem and L. A. M. D’Angelo, “Modeling Skew by Single- and Multi-Slice 2-D Machine Models,” *IEEE Trans. Magn.*, vol. 57, no. 6, pp. 1–4, Jun. 2021, doi: 10.1109/TMAG.2021.3065901.
- [17] A. A. Diriye, S. Ouagued, Y. Amara, G. Barakat, and H. Tiegna, “Iron loss estimation in axial field PM machines using a quasi-3D hybrid analytical model,” in *2016 Eleventh International Conference on Ecological Vehicles and Renewable Energies (EVER)*, Apr. 2016, pp. 1–6, doi: 10.1109/EVER.2016.7476422.
- [18] V. Ostović, *Dynamics of Saturated Electrical Machines*. Springer-Verlag: New York, 1989.
- [19] S. Asfirane, “Développement d’un outil de génération automatique des réseaux de réductances pour la modélisation de dispositifs électromécaniques,” Université Paris Saclay (COMUE), 2019.
- [20] Y. Laoubi, “Modélisation des machines électriques par les réseaux de perméances génériques. Cas des machines à flux axial,” Université du Havre, 2017.
- [21] S. Asfirane, S. Hlioui, Y. Amara, O. De La Barriere, G. Barakat, and M. Gabsi, “Global Quantities Computation Using Mesh-Based Generated Reluctance Networks,” *IEEE Trans. Magn.*, vol. 54, no. 11, 2018, doi: 10.1109/TMAG.2018.2829155.
- [22] R. Benlamine, T. Hamiti, F. Vangraefschèpe, F. Dubas, and D. Lhotellier, “Modeling of a coaxial magnetic gear equipped with surface mounted PMs using nonlinear adaptive magnetic equivalent circuits,” in *2016 XXII International Conference on Electrical Machines (ICEM)*, 2016, pp. 1888–1894, doi: 10.1109/ICELMACH.2016.7732781.
- [23] M. A. Benhamida, H. Ennassiri, Y. Amara, G. Barakat, and N. Debbah, “Study of switching flux permanent magnet machines using interpolation based reluctance network model,” in *2016 International Conference on Electrical Sciences and Technologies in Maghreb (CISTEM)*, Oct. 2016, pp. 1–7, doi: 10.1109/CISTEM.2016.8066809.
- [24] S. Asfirane *et al.*, “Scalar Magnetic Potential Interpolation for Non-Conformal Meshing in Mesh-Based Generated Reluctance Networks,” *IEEE Trans. Magn.*, vol. 55, no. 7, pp. 1–8, Jul. 2019, doi: 10.1109/TMAG.2019.2899820.
- [25] G. Barakat, “Modélisation tridimensionnelle d’une machine synchrone rapide à griffes par la méthode des éléments finis,” Institut National Polytechnique de Grenoble (INPG), 1995.
- [26] SABONNADIÈRE Jean-Claude and COULOMB Jean-Louis, “Calcul des champs électromagnétiques.” *Techniques de l’Ingénieur*.
- [27] P. Dular and F. Piriou, “Static Formulations: Electrostatic, Electrokinetic, Magnetostatics,” in *The Finite Element Method for Electromagnetic Modeling*, John Wiley & Sons, Ltd, 2008, pp. 69–116.
- [28] S. Clénet and F. Piriou, “Calcul du champ électromagnétique en basses fréquences - Modèles numériques par éléments finis,” *Convers. l’énergie électrique*, 2008.
- [29] Z. Ren and F. Bouillault, “Magnetodynamic Formulations,” in *The Finite Element Method for Electromagnetic Modeling*, John Wiley & Sons, Ltd, 2008, pp. 117–137.
- [30] Z.-Q. Zhu and D. Liang, “Perspective of Thermal Analysis and Management for Permanent Magnet Machines, with Particular Reference to Hotspot Temperatures,”

- Energies*, vol. 15, no. 21, 2022, doi: 10.3390/en15218189.
- [31] D. A. Howey, “Thermal design of air-cooled axial flux permanent magnet machines,” 2010.
 - [32] C. H. Lim *et al.*, “2-D lumped-parameter thermal modelling of axial flux permanent magnet generators,” in *2008 18th International Conference on Electrical Machines*, 2008, pp. 1–6, doi: 10.1109/ICELMACH.2008.4799880.
 - [33] N. Rostami, M. R. Feyzi, J. Pyrhonen, A. Parviainen, and M. Niemela, “Lumped-Parameter Thermal Model for Axial Flux Permanent Magnet Machines,” *IEEE Trans. Magn.*, vol. 49, no. 3, pp. 1178–1184, Mar. 2013, doi: 10.1109/TMAG.2012.2210051.
 - [34] G. Verez, H. Tiegna, G. Barakat, and G. Hoblos, “Analytical thermal modelling of axial flux permanent magnet synchronous machines,” in *2012 XXth International Conference on Electrical Machines*, 2012, pp. 2799–2805, doi: 10.1109/ICEIMach.2012.6350283.
 - [35] J. Azzouzi, “Contribution à la modélisation et à l’optimisation des machines synchrones à aimants permanents à flux axial. Application au cas de l’aérogénérateur,” Université du Havre, 2007.
 - [36] A. Parviainen, “Design of axial-flux permanent-magnet low-speed machines and performance comparison between radial-flux and axial-flux machines,” Lappeeranta University of Technology, 2005.
 - [37] M. Broussely, “Réduction de modèles thermiques par la théorie des réseaux, application à la surveillance d’une machine asynchrone par couplage d’un modèle thermique réduit avec un schéma équivalent électrique,” 2000.
 - [38] A. Hedlund, “Effective Finite Element Analysis Workflow for Structural Mechanics,” no. 15020. 2015.
 - [39] GP Nikishkov, “Introduction to the Finite Element Method,” *Univ. Aizu*.
 - [40] J. T. Mottram and C. T. Shaw, *Using Finite Elements in Mechanical Design*. McGraw-Hill, 1996.

Chapter 3: Design of an Axial Flux Machine for Low Power Wind Turbine Applications

- 1. Introduction**
- 2. 3D Character of Axial Flux Machines**
- 3. Magnetic Study**
- 4. End Winding Inductance**
- 5. PM Eddy Current Loss**
- 6. Thermal Study of the Designed Machine**
- 7. Mechanical Study of the Designed Machine**
- 8. Performance Summary**
- 9. Conclusion**

I. Introduction

In the first chapter, different configurations and designs of axial flux machines were investigated to help inspire the design of our own machine and determine a starting point from which the machine can be modified according to specifications.

To design electrical machines, the classical way to go is to model and test the performances of the design using finite elements analysis with the help of commercial softwares available on the market. But as it is well known now, this method consumes long periods of computation time so it is not suitable for rapid machine pre-sizing. A workaround for this problem is to use an analytical model -when available- for the machine under study which is derived from the formal solution of Maxwell's equations. Fortunately, analytical models have been developed in the past at GREAH laboratory (Groupe de Recherche en Electrotechnique et Automatique du Havre) and have been implemented under the MATLAB® environment in an analysis and sizing tool for electrical machines called SIMUMSAP (SIMUlation analytique de Machines Synchrones à Aimants Permanents). This tool stems essentially from thesis' carried out within GREAH by Azzouzi [1], Abdel-Karim [2], Mahyob [3], Bellara [4], Tiegna [5] and Verez [6].

In this chapter, first, the 3D aspect of axial flux machines is presented, then the design methodology is presented justifying the choice of the topology, the winding configuration and electrical and geometrical parameters, and the adopted design is simulated using a commercial finite elements software environment in order to determine electromagnetic performance indicators (magnetic flux density, total electromagnetic torque, cogging torque, EMF, electromagnetic power, efficiency...). Towards the end, thermal and mechanical aspects of the machine are presented and machine performance indicators are summarized followed by a conclusion to wrap up the work done in this chapter.

II. 3D Aspect of Axial Flux Machines

Due to their inherent 3D geometry, axial flux machines have 3D effects in their active part and at the radial ends that must be taken into account during modeling. These effects can be classified into 3D effects and edge effects and are distinguishable for some structures, but in most cases they are not. 3D effects are topological variations in the direction perpendicular to the modeling plane for a given position of the moving part relative to the fixed part. As a result, using an analytical design method or 2D finite element analysis (FEA) -which are usually applied at mean machine radius- does not generally yield sufficiently accurate computation results.

This 3D aspect can be taken into account by using the 3D finite elements method. However, 3D FEA requires even more computational time when it comes to high-power axial flux machines, as these machines involve larger and larger diameters and exponentially high number of nodes, and thus FEA is more suitable and preferable during the refining phases of the design.

The modelling of axial-flux PM machines is constrained by a speed-accuracy compromise. In case of laminations in the radial direction, the shortcoming of the model in terms of accuracy may be considered to be irrelevant in most of the design cases due to the orientation of the laminations, but if the iron parts are designed to saturate, the effects caused by the 3D flux should be examined too.

It should be noted also that if the flux density significantly differs at the outer and inner radii of the machine, part of the flux flows also diagonally in the magnetic circuit.

With all that being said, we can state that in most cases all methods which are not 3D or quasi-3D cannot give satisfactory results for axial flux machines. Reluctance networks offer the possibility of 3D modelling, but finite elements method is well established in that area, not only it can provide accurate results (if the correct meshing strategy is adopted) but also it can adapt to any geometry, giving it the upper hand on other methods for 3D simulation. It is possible to obtain coherent results using 2D simulations for machines with large diameters due to their characteristics and their fairly simple structure, which is constrained by the limitations of the fabrication process, this allows reluctance network based methods to model these machines and obtain results with satisfactory accuracy.

III. Magnetic Study

1. Pre-sizing and Parametric Sweep Analysis using the Analytical Model

In this part, we present the sizing of an axial flux synchronous generator with permanent magnets for a 30 kW wind turbine. The generator is coupled to the turbine by means of a magnetic gear; therefore to reduce the size of the generator achieving the required power with a reasonable gear ratio, a nominal rotational speed of 2000 RPM was chosen. In order not to exceed an output voltage frequency of 400 Hz (for inverter considerations), it is necessary that the number of pole pairs is less than 12. In order to reduce the cogging torque, several techniques are possible such as magnet inclination or slot inclination or a fractional number of slots per pole. The latter technique seems to be the least difficult to implement. Also, Joule losses in stator coils are an important source of loss among all losses for wind turbine-type operation.

All these reasons led us to choose a fractional number of slots per pole with a tooth winding (tooth winding was chosen to reduce the end winding lengths and subsequently reduce the Joule losses at the stator). Thus, the cogging torque can be reduced and the end windings are shorter, which makes it possible to reduce the radial footprint of the winding and reduce the joule stator losses. Finally, a combination of 10 pole pairs and 24 slots was chosen thus obtaining a number of slots per pole of 1.2: this combination allows to have a fundamental cogging torque of rank 120 (lcm of 20 and 24), which is far away from the fundamental of the total torque, and an operating frequency of less than 400 Hz with a reasonable number of slots given the internal radius of the machine and therefore the size of the end windings at the internal radius. The air gap was chosen as 1.2 mm based on other similar designs.

The following simulation study is therefore intended to present the performance of the prototype sized with SIMUMSAP (a tool developed by GREAH Laboratory based on the formal resolution of Maxwell's equations) and a commercial finite elements software. During the various calculations, we adopt the hypothesis that the median plane of the rotor is a plane of symmetry (the machine can be split into two independent single air gap machines).

The geometry of the studied machine is illustrated in Fig. 3.5. It has 10 pole pairs and 24 slots in order to obtain an output voltage frequency below 400 Hz and to reduce the cogging torque. Similarly, to reduce Joule losses in the windings and thus increase efficiency, the machine winding is of tooth type, with each slot being occupied by two sides of coils superimposed in the slot to compensate the leakage flux at the bottom of the slot. The coils are arranged in a series configuration (4 coils in each phase) and they are composed of 9 turns

each, with a fill factor of 0.4 and are fed with a current density of 3.5 A/mm². There is 2 end winding planes and the phase windings of the first stator are connected in parallel with the windings of the second stator. Also the phases in each stator are connected in a star configuration. For reasons of mechanical resistance of the rotor in the presence of magnetic attraction forces between the disks, we opted for a stator-rotor-stator structure, the rotor being, in this case, subjected to two attraction forces of opposite directions that cancel out if the rotor is perfectly centered between the two stator disks. The two stators are therefore identical and arranged on either side of the rotor disc carrying the permanent magnets on each of its two faces. These magnets, whose remanence is axial, can have magnetizations of opposite directions from one side of the rotor to the other or of the same direction.

In the first case, the magnet flux returns to each of the two stators following a circumferential path in the rotor yoke which gives us two independent single air-gap machines.

In the second case, the flux axially passes through the rotor magnetic circuit and passes from one stator to another. The median plane of the rotor is an antisymmetry plane. This second arrangement makes it possible to reduce the thickness of the rotor magnetic circuit or even to eliminate it. However, the mechanical stresses that the rotor is expected to undergo during operation slightly distance this possibility. In addition to the bending stresses that apply to the rotor disc (the perfect centering cannot exist for these small machines), torsional stresses with circumferential directions deform the rotor disc. Mechanical reinforcements are therefore required and can be provided, for example, by the presence of a steel disc whose thickness is to be determined according to the desired rigidity.

In order to choose the most suitable internal and external radius as well as the depth of the stator slots, a parametric sweep analysis was performed using the analytical model in linear BH curve conditions. The input parameters for this study were the internal radius R_i , the external radius R_e and the slot height H_s ; the outputs were the torque, the total active weight and the torque mass density. In this study, the machine was divided into 10 slices as the slots are straight and the tooth pitch vary as a function of machine radius (the tooth width is larger at the external radius than it is at the internal radius and the tooth cross section is trapezoidal). To perform this study, the magnets were chosen to obtain a magnetic flux density of 0.8 T in the air gap at no load, and thus a flux density of around 1.2 T in a tooth at no load and around 1.6 T when the machine is loaded. Then, we choose a slot width that allows to insert the stator windings in the slots, and then we vary the slot height. The results obtained are given in Fig. 3.1, Fig. 3.2, Fig. 3.3 and Fig. 3.4. Fig. 3.1 illustrates the torque variation as a function of internal and external radius, Fig. 3.2 shows the total active weight variation as a function of internal and external radius, torque mass density variation as a function of machine radii is presented in Fig. 3.3, Fig. 3.4 presents torque mass density variation as a function of stator slot height maintaining the internal radius at a value of 110 mm and the external radius at 180 mm.

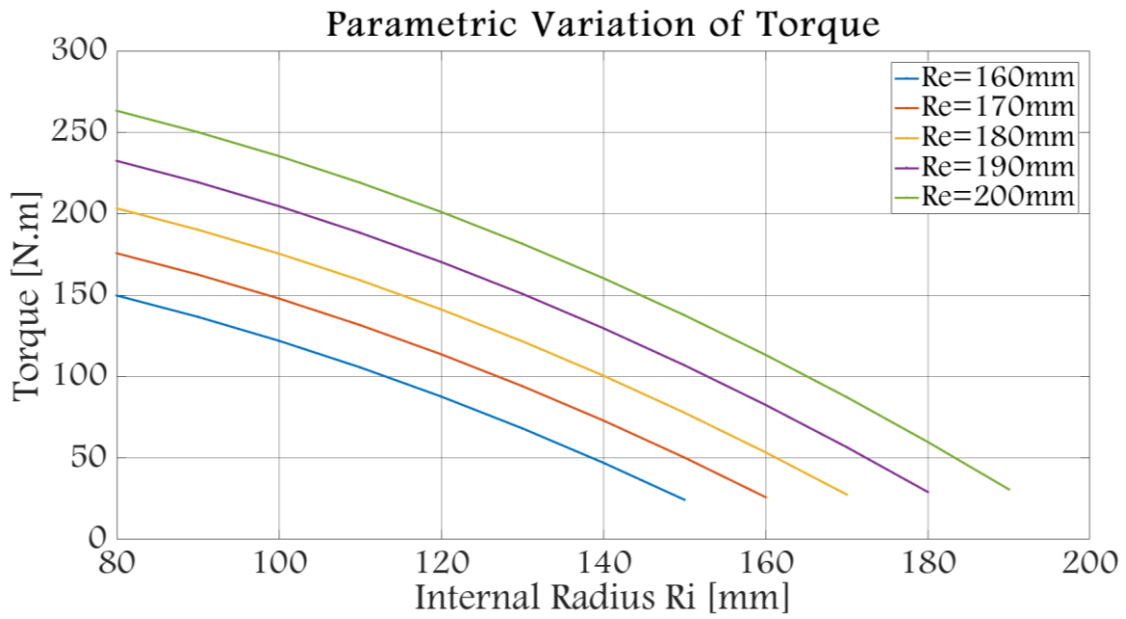


Fig. 3.1: Torque as a function of external radius Re and internal radius Ri

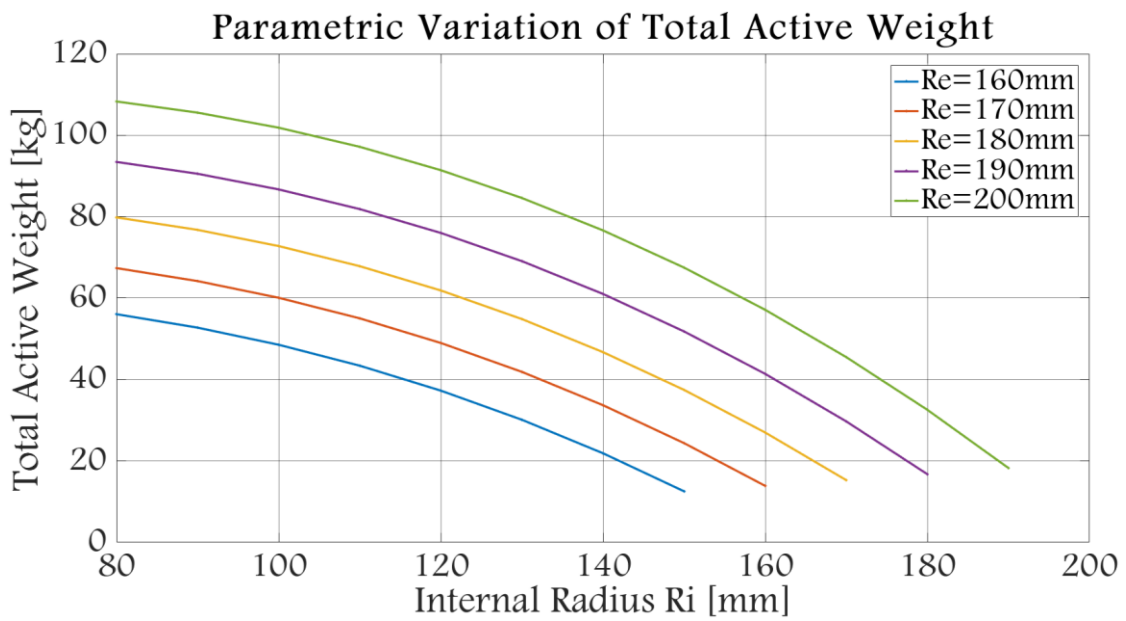


Fig. 3.2: Total active weight as a function of external radius Re and internal radius Ri

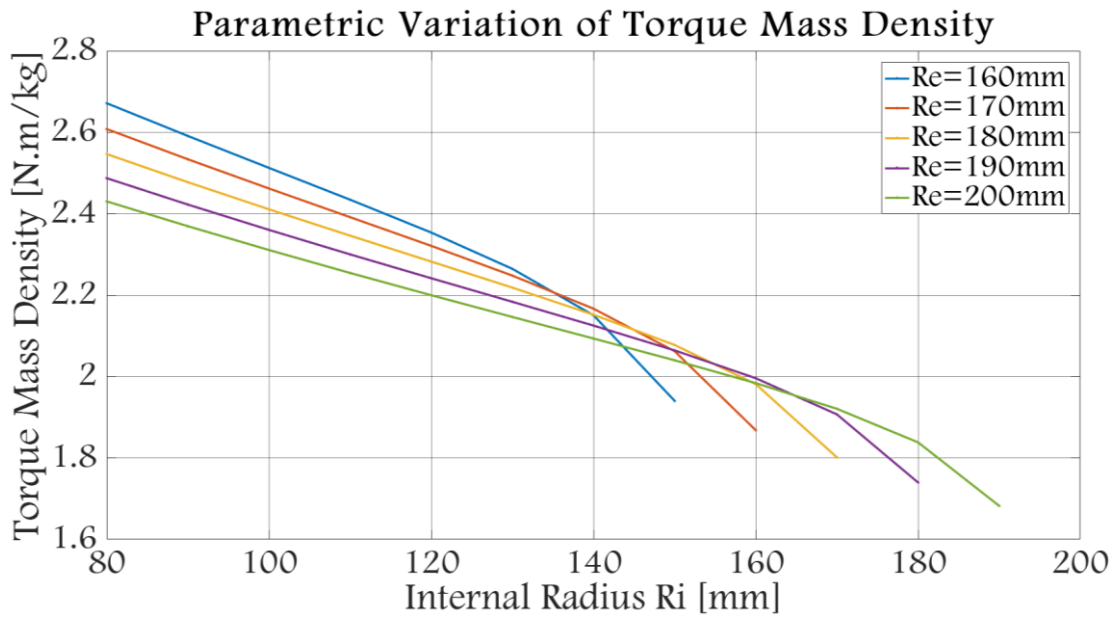


Fig. 3.3: Torque mass density as a function of external radius R_e and internal radius R_i

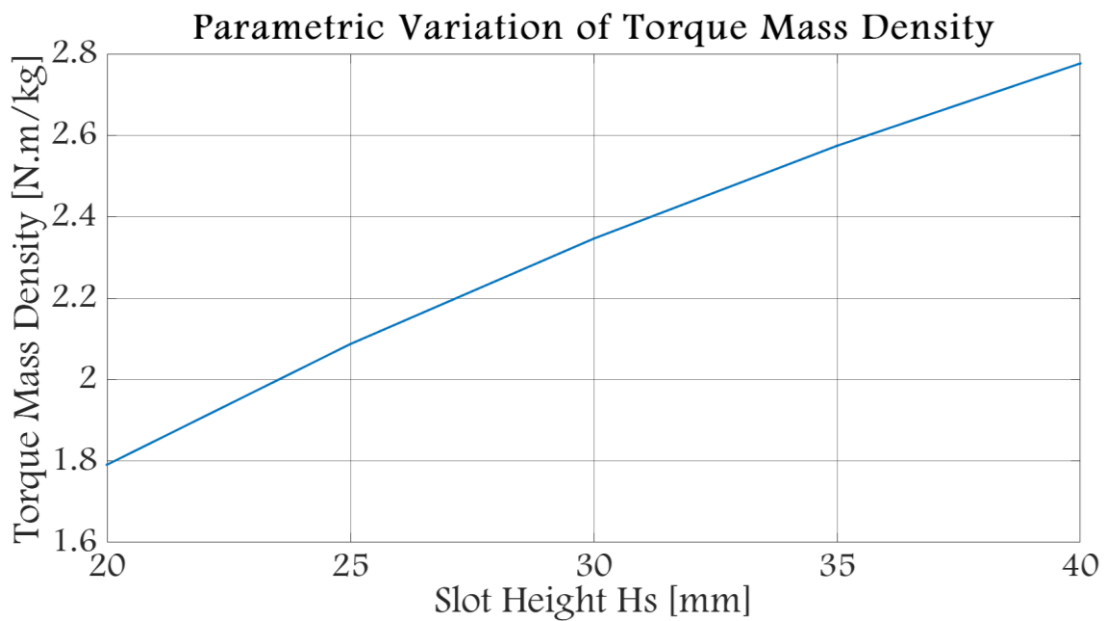


Fig. 3.4: Torque mass density as a function of stator slot height

Fig. 3.6 and Tab. 3.1 show the main geometric parameters of this machine with an internal radius of $R_i = 110$ mm and an external radius of $R_e = 180$ mm which makes a radial excursion of 70 mm and satisfies the ratio of 0.6 which gives the highest torque. The distribution of the coils in the slots is shown in Fig. 3.7. Permanent magnets are Neodymium-Iron-Boron (NdFeB) mounted on both rotor surfaces. Their remanence is 1.21 T.

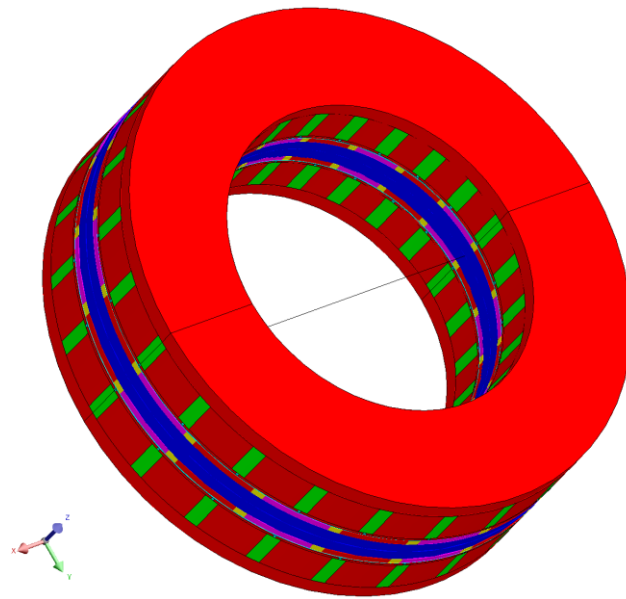


Fig. 3.5: 3D view of the machine

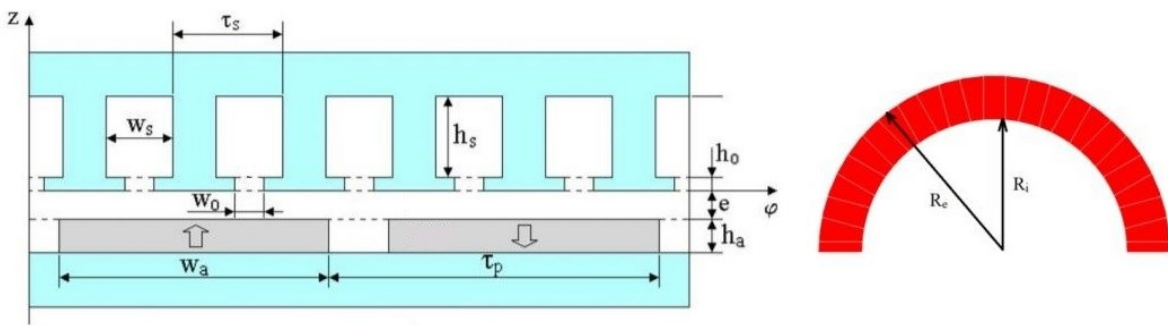


Fig. 3.6: The geometrical parameters of the machine

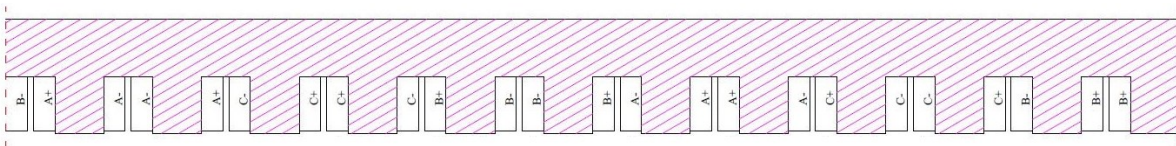


Fig. 3.7: Winding configuration

Tab. 3.1: Dimensional Characteristics of the machine

Parameter	Value
External Radius (R_e)	180 mm
Internal Radius (R_i)	110 mm
Number of Stator Slots	24
Number of Magnets	20
Slot Width (w_s)	10 mm
Slot Height (h_s)	30 mm
Slot Opening Height (h_0)	2 mm
Slot Opening Width (w_0)	2 mm
Magnet Opening (w_a)	15.3°

Magnet Thickness (ha)	4.7 mm
Magnet Spacing	2.7°
Stator Yoke Thickness	12 mm
Rotor Yoke Thickness	20 mm
Air Gap Length (e)	1.2 mm
Rotation Speed	2000

The high speed at which the machine is destined to spin is inadequate with the low speed of a 30kW wind turbine of 100 RPM max, therefore it's required to integrate a gear to adapt the speed of the turbine to the design speed of the generator. A mechanical gear creates serious reliability and maintenance issues so it cannot be adopted especially for offshore wind turbines where it is challenging to access the turbine. An alternative to mechanical gears are magnetic gears that use contactless speed conversion avoiding the wear and tear associated with their mechanical counterparts, thus increasing overall system efficiency. As the designed machine is of an axial flux nature, the magnetic gear to be coupled with it is chosen to be of the same axial flux topology. An axial flux magnetic gear is composed of a low speed rotor (LSR), a high speed rotor (HSR) and a modulator (Fig. 3.8). The modulator converts the magnetic field generated by one rotor to a magnetic field in the air gap of the other rotor. Assuming the low speed rotor has p_l pole pairs, the high speed rotor has p_h pole pairs and the modulator has n_p pole pieces, the following condition is satisfied by the magnetic gear:

$$n_p = p_l + p_h \quad (3.1)$$

The angular velocity of the low speed rotor ω_l can be written in function of the angular velocity of the high speed rotor ω_h and the modulator ω_m by:

$$\omega_l = \frac{p_h}{p_h - n_p} \omega_h + \frac{n_p}{n_p - p_h} \omega_m \quad (3.2)$$

Assuming the modulator is fixed ($\omega_m = 0$), the gear ratio can be expressed by:

$$G_r = \frac{\omega_h}{\omega_l} = \frac{p_l}{p_h} \quad (3.3)$$

The following relationships can be established between the torque of the LSR T_l , the torque of the HSR T_h and the torque of the modulator T_m :

$$T_l + T_h + T_m = 0 \quad (3.4)$$

$$\frac{T_l}{T_h} = \frac{\omega_h}{\omega_l} \quad (3.5)$$

The design of the magnetic gear will not be addressed in this work, but details on the design procedure can be found in [7] and [8].

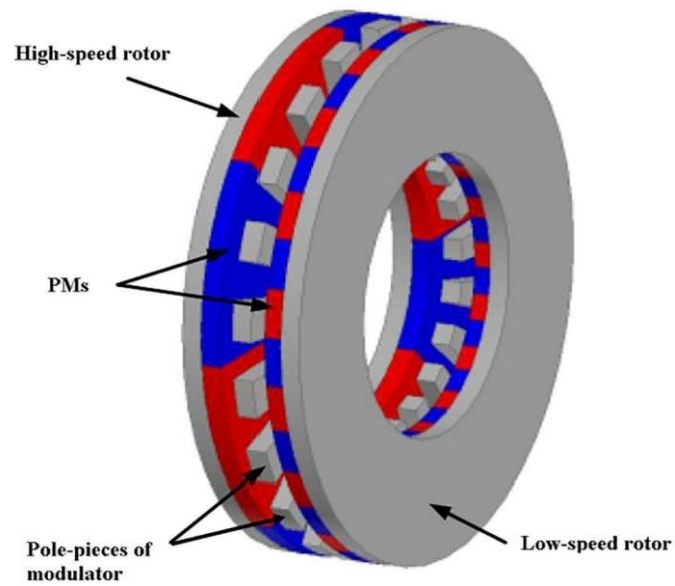


Fig. 3.8: Axial flux magnetic gear [8]

2. Validation of the Final Design Using Finite Elements

Local and global quantities are calculated using a commercial finite elements software in nonlinear BH curve conditions where the iron is of the type M270-35A. The quantities that will be presented in the following are magnetic flux densities, torques, EMF, axial attraction forces, power, and losses. The machine is meshed using tetrahedral elements as shown in the following figures.

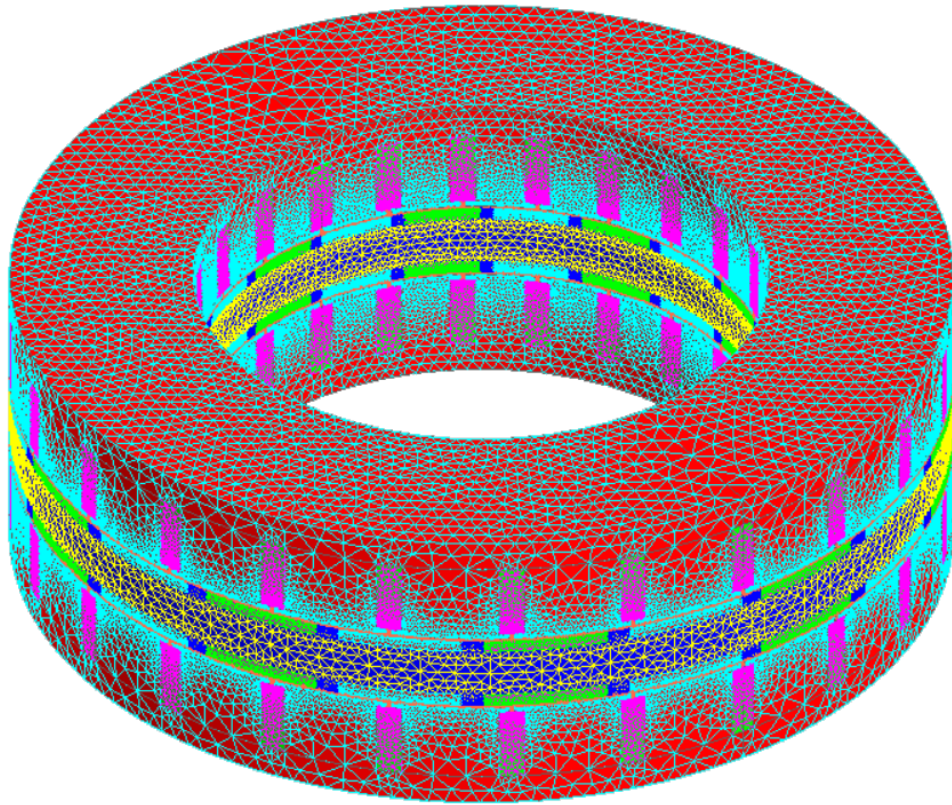


Fig. 3.9: Meshing of the whole machine

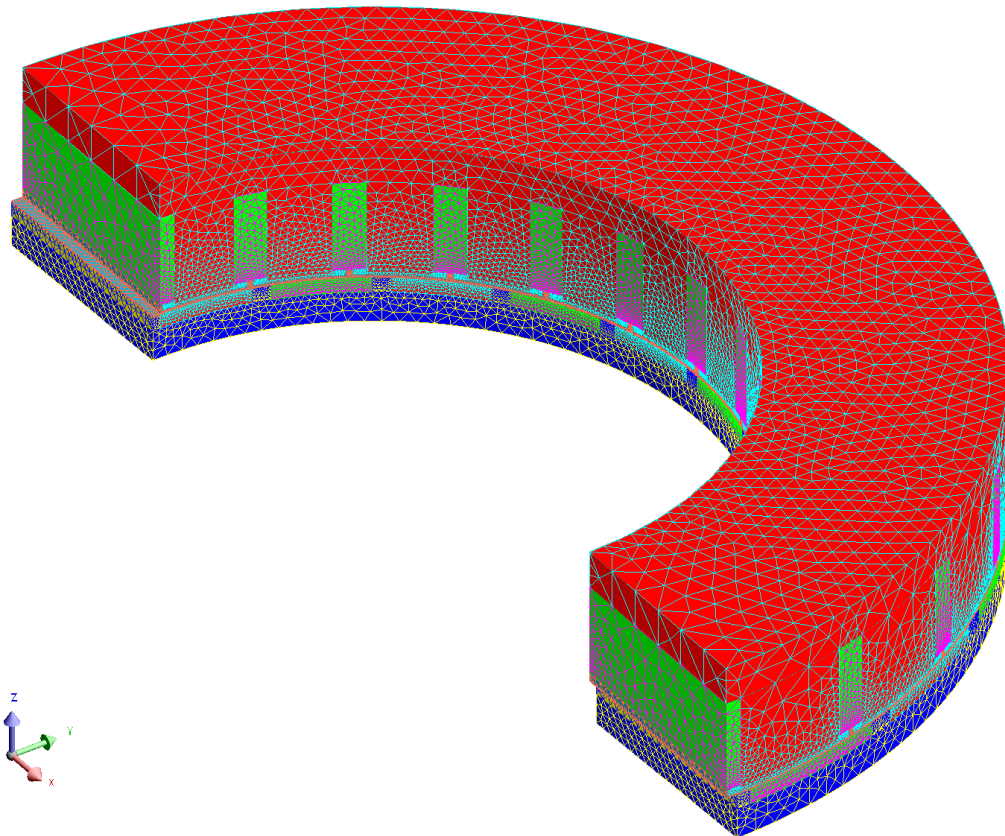


Fig. 3.10: Meshing of the modeled part

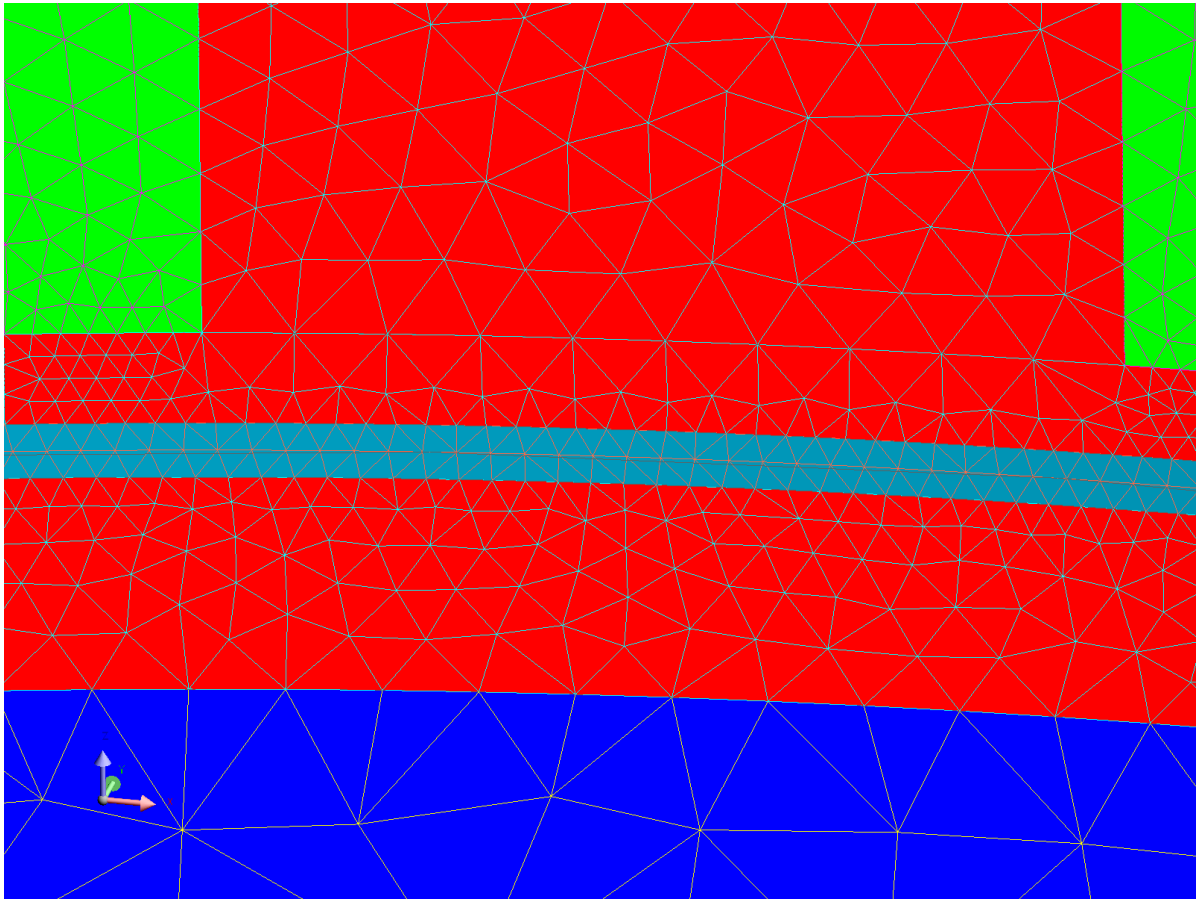


Fig. 3.11: Zoom on the air gap region mesh

a) Magnetic Flux Density

The results obtained with FLUX at no load in the magnets and in the middle of the air gap at mean radius, for normal and tangential components of magnetic flux density, are presented in Fig. 3.12 through Fig. 3.15, and at load in Fig. 3.16 through Fig. 3.19. Results are given for a rotor position relative to the stator of 0° and for a magnet remanence of 1.21 T.

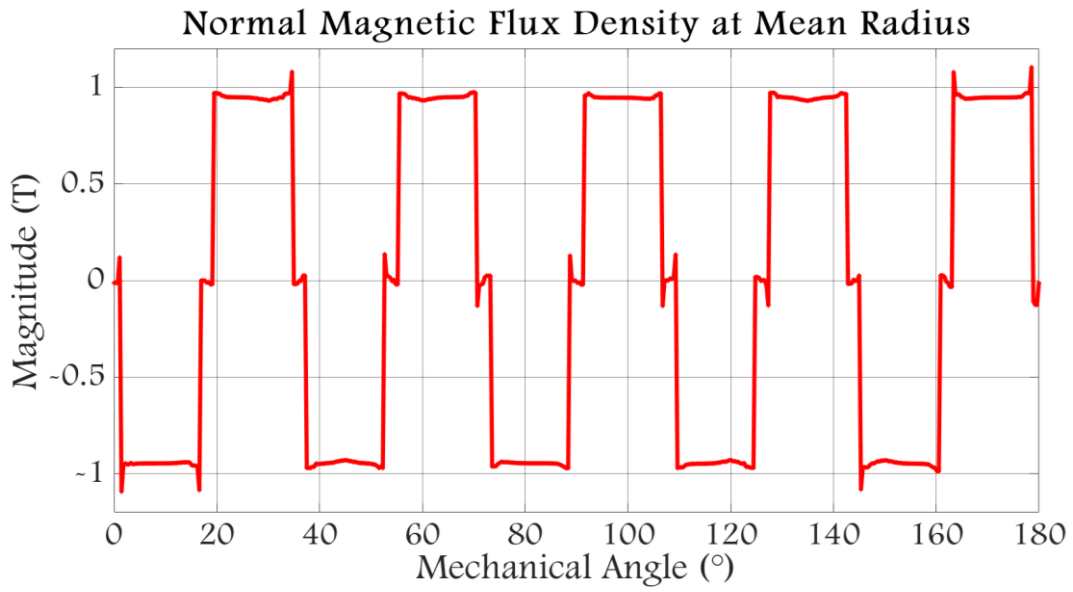


Fig. 3.12: Magnetic flux density in the magnets at no load (normal component)

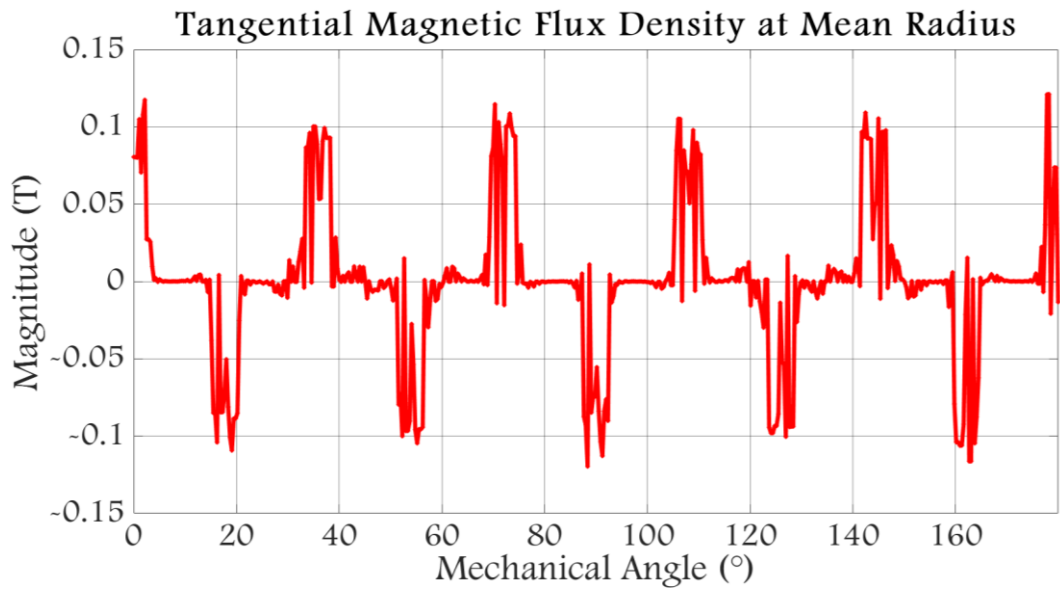


Fig. 3.13: Magnetic flux density in the magnets at no load (tangential component)

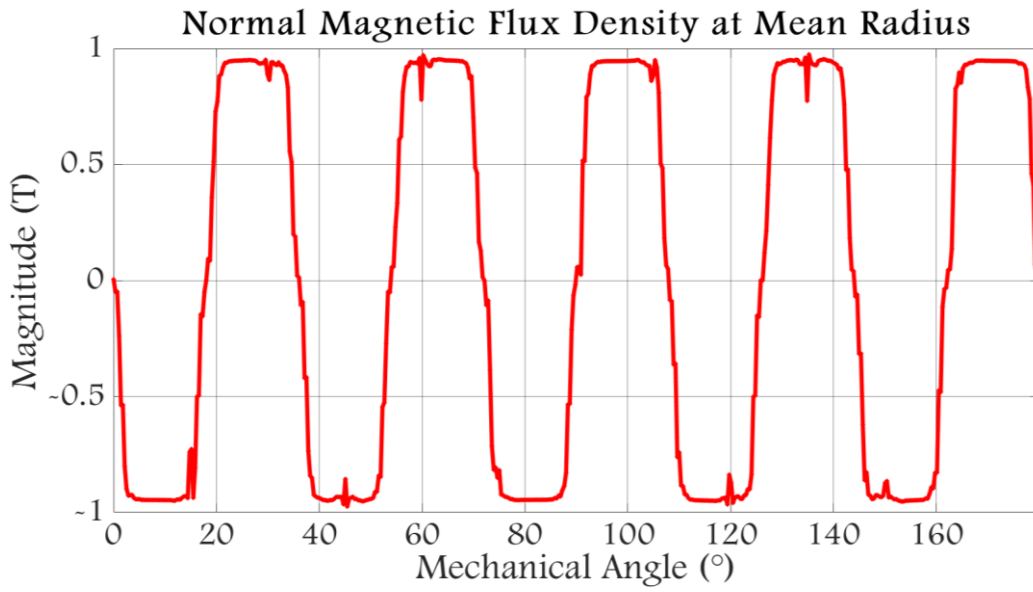


Fig. 3.14: Magnetic flux density in the air gap at no load (normal component)

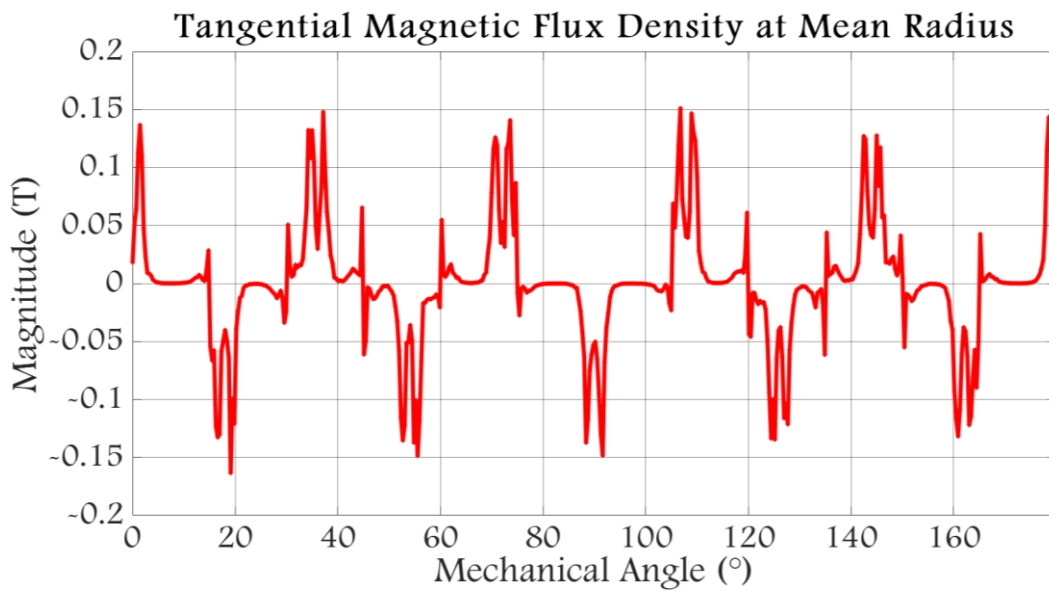


Fig. 3.15: Magnetic flux density in the air gap at no load (tangential component)

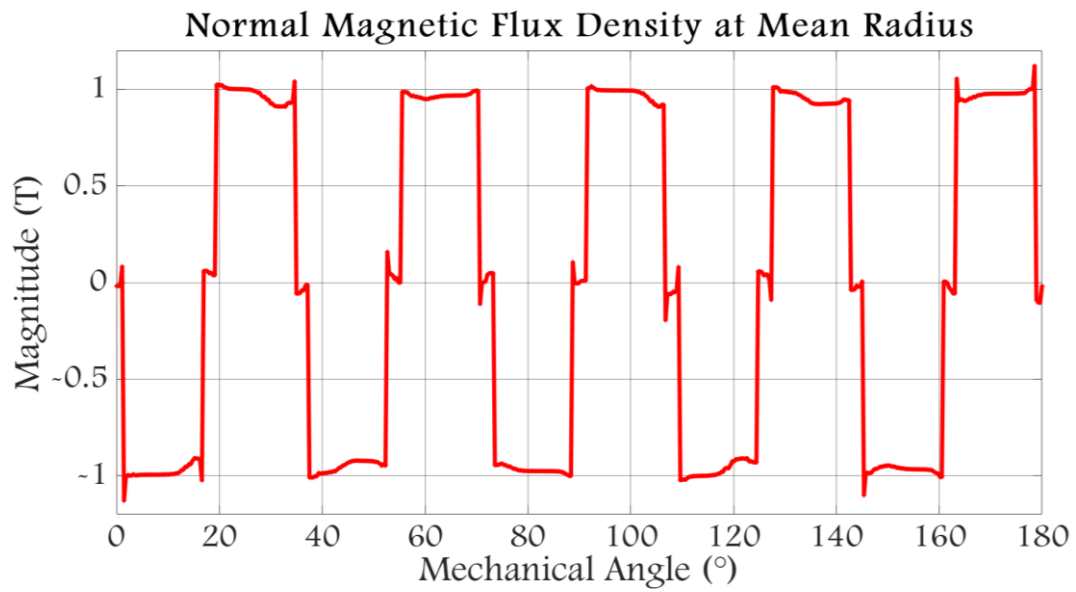


Fig. 3.16: Magnetic flux density in the magnets at load (normal component)

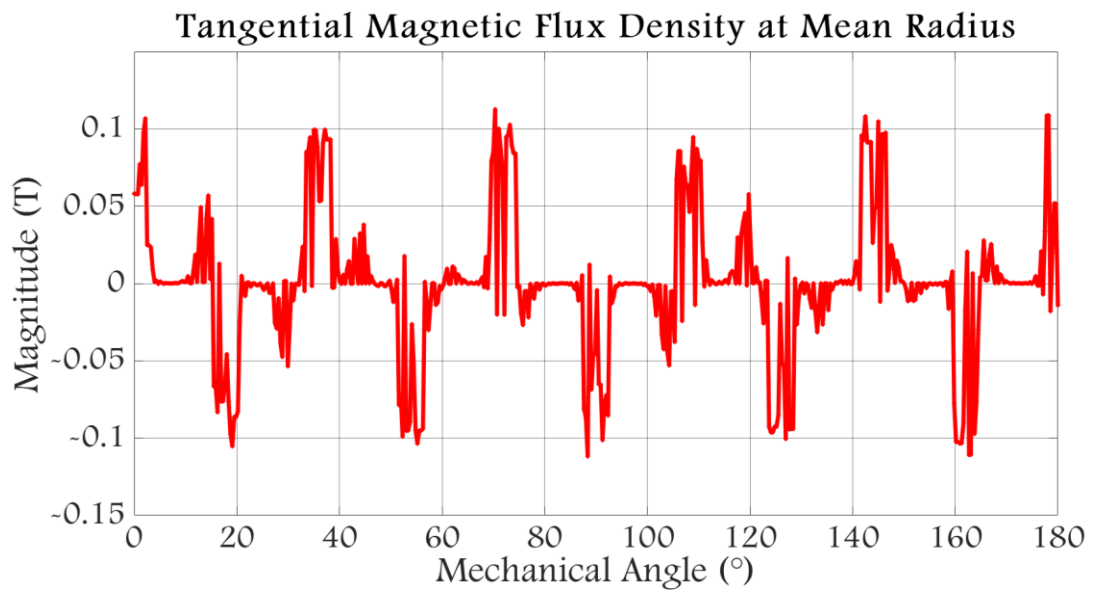


Fig. 3.17: Magnetic flux density in the magnets at load (tangential component)

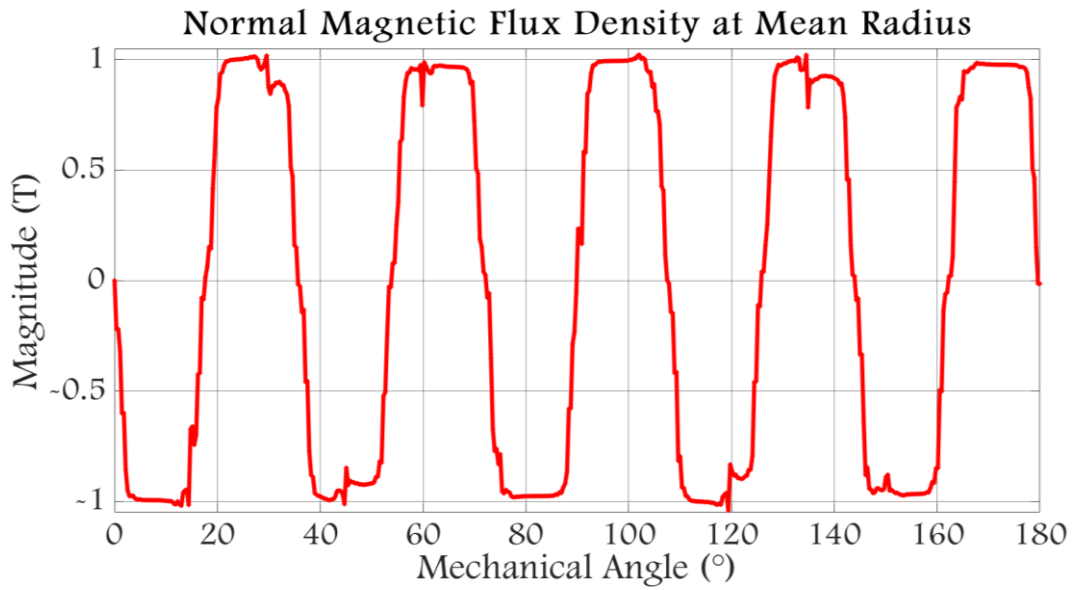


Fig. 3.18: Magnetic flux density in the air gap at load (normal component)

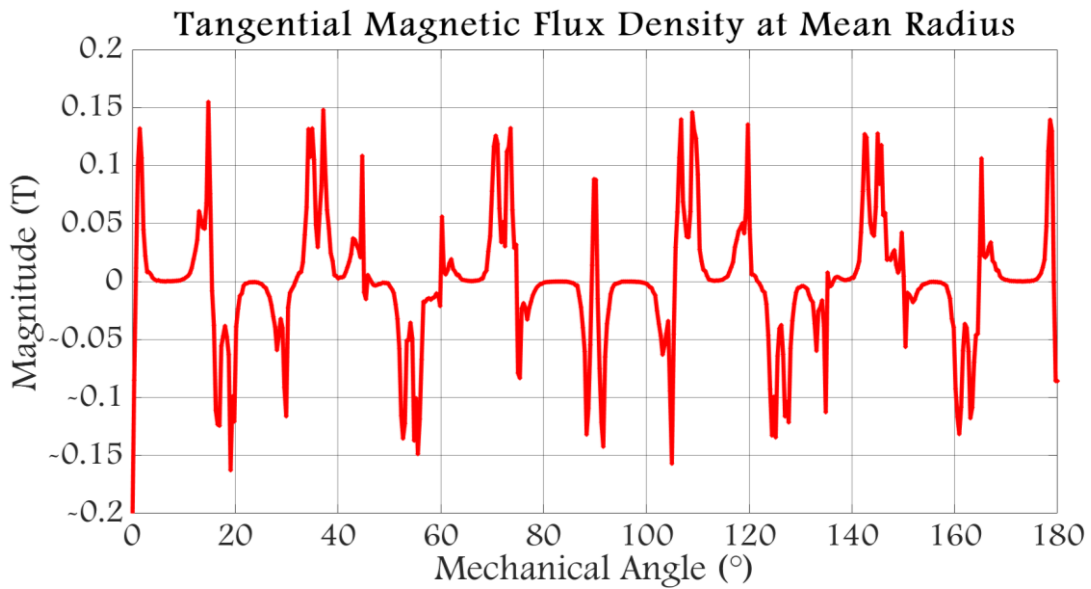


Fig. 3.19: Magnetic flux density in the air gap at load (tangential component)

b) Joule Losses

A current density of 3.5 A/mm^2 was chosen for the simulation. So, the imposed current in the windings is calculated as follows:

Let S_{slot} be the vertical cross section of a slot, h_s its height and w_s its width. So we have:

$$S_{slot} = h_s \times w_s = 30 \times 10 = 300 \text{ mm}^2 \quad (3.6)$$

Let S_{cu} be the total cross-sectional area of copper in a slot conductor. It follows:

$$S_{cu} = k_f \times S_{slot} = 0.4 \times 300 = 120 \text{ mm}^2 \quad (3.7)$$

The cross-sectional area of a conductor S_{cond} is then:

$$S_{cond} = \frac{S_{cu}}{n_{turns/coil} \times n_{coils/slot}} = \frac{120}{9 \times 2} = 6.67 \text{ mm}^2 \quad (3.8)$$

And thus the maximum current I_{max} passing through a coil turn is:

$$I_{rms} = J_{rms} \times S_{cond} = 3.5 \times 6.67 = 23.34 \text{ A} \quad (3.9)$$

Where:

J_{rms} is the RMS value of the current density in a slot

k_f the fill factor of the coils

$n_{turns/coil}$ the number of turns of a coil

$n_{coils/slot}$ the number of coils occupying a slot

The length of a coil L_{coil} is computed as follows:

$$L_{coil} = n_{turns/coil} \times (2(R_e - R_i) + 2\pi k_w \alpha_s R_i + \alpha_t (R_e + R_i)) = 2.27 \text{ m} \quad (3.10)$$

$$\alpha_t = \frac{2\pi}{N_s} - \alpha_s = 0.262 \text{ rad} \quad (3.11)$$

$$\alpha_s = 2 \sin^{-1} \left(\frac{w_s}{2R_i} \right) = 0.0909 \text{ rad} \quad (3.12)$$

Where:

R_i is the machine internal radius

R_e the machine external radius

k_w the winding factor (considered equal to 1)

α_s the opening angle of the stator slots

α_t the opening angle of the stator teeth

N_s the number of slots

The resistance R_s of a phase winding is computed as follows:

$$R_s = n_{coils/phase} \times \rho_{cu} \frac{L_{coil}}{S_{cond}} = 24.5 \text{ m}\Omega \quad (3.13)$$

Where:

$n_{coils/phase}$ is the number of coils in series per phase

ρ_{cu} the resistivity of copper

Finally the Joule losses are computed using the following formula:

$$\Delta P_J = n_{stators} \times n_{phases} \times n_{windings/phase} \times R_s I_{rms}^2 = 160.28 W \quad (3.14)$$

Where:

$n_{stators}$ is the number of stators (2 in our case)

n_{phases} the number of phases (3 in our case)

$n_{windings/phase}$ the number of windings in parallel for 1 phase (2 in our case)

c) Iron Losses

Iron losses are estimated either by modeling hysteresis and eddy current losses or by a posteriori calculation where hysteresis is not introduced in the B(H) curve. The first approach models hysteresis within the B(H) curve. It is a question of integrating the B(H) function into the direct resolution of the problem. Whereas, in the second approach, hysteresis is not taken into account in direct resolution as it does not fundamentally change the flux distribution in the device. For example, Preisach's model is essentially based on the representation of hysteresis phenomena by considering sheets at the microscopic scale. Another numerical model, the loss surface (LS) model, makes it possible to obtain losses locally from the derivative of magnetic flux density. This model developed by Cester [9], was improved by Chevalier [10] who separated the representation of $H\left(B, \frac{dB}{dt}\right)$, into a static part and the a dynamic one [5].

In this method the estimation of magnetic losses is done a posteriori using a model of dynamic hysteresis. A material is characterized in this model by a surface $H\left(B, \frac{dB}{dt}\right)$ (as shown in Fig. 3.20) determined experimentally using an Epstein type device for magnetic measurements in medium frequency. An analytical model then determines the magnetic field intensity H(t) from the magnetic flux density B(t), thus reconstructing the hysteresis cycle. B(H) curves like the ones shown in Fig. 3.21 are obtained allowing for precise computation of iron losses.

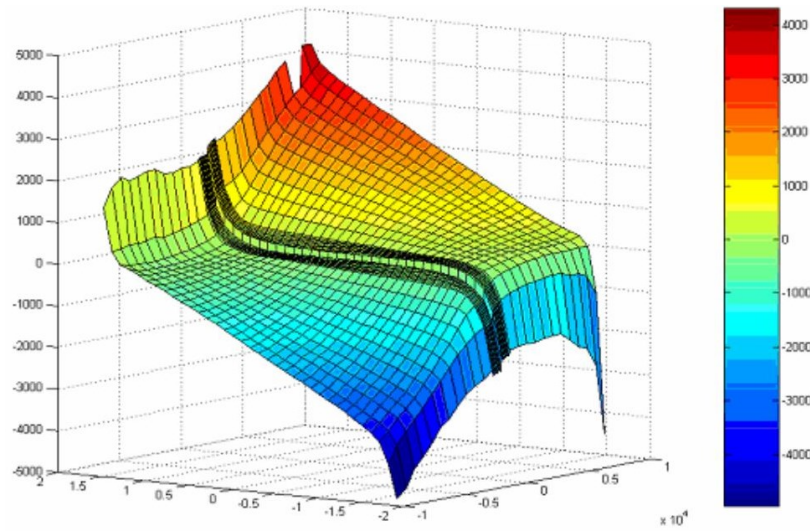


Fig. 3.20: An example of a $H \left(B, \frac{dB}{dt} \right)$ surface [11]

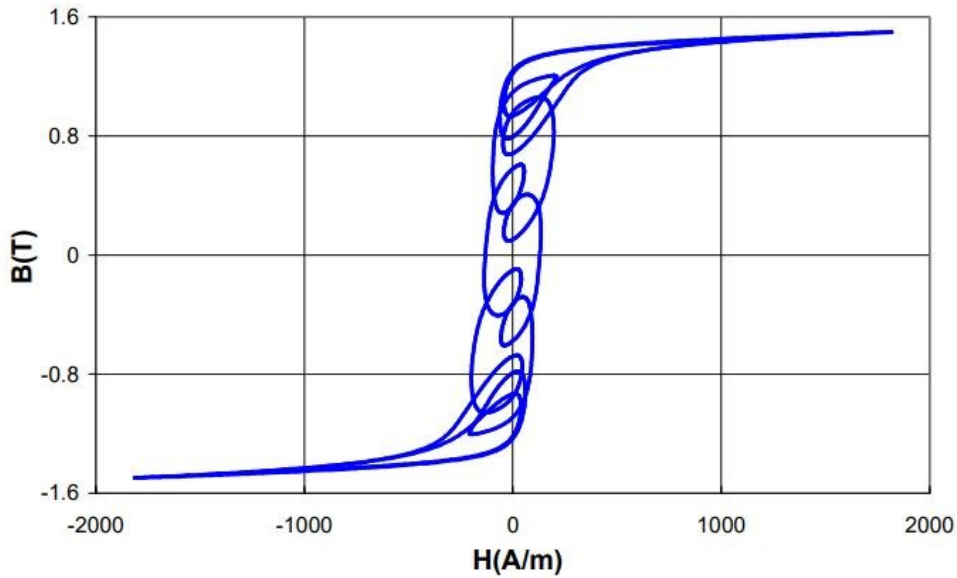


Fig. 3.21: Example of B(H) curve of M330-35A steel [11]

Most analytical models for calculating iron losses are based on Bertotti's model and others on Steinmetz's model. Amara proposed in [12] a technique for estimating iron losses based on the coupling of analytical models with a reluctance network using Bertotti's empirical method [13].

Bertotti's model decomposes iron losses into 3 parts: hysteresis losses, classical losses and excess losses, these being proportional to the frequency f , to f^2 and to $f^{\frac{3}{2}}$ respectively.

In a situation where magnetic potential, magnetic field and magnetic flux density are supposed to have a non-sinusoidal variation with time, iron losses are obtained using Bertotti's model by the following expression:

$$P_v = k_h f B_m^2 + \frac{\pi \sigma d^2 f^2}{6} \int_{2\pi} \left(\frac{dB_m}{d\theta_e} \right)^2 d\theta_e + \sqrt{2\pi} k_{ex} f^{\frac{3}{2}} \int_{2\pi} \left| \frac{dB_m}{d\theta_e} \right|^{\frac{3}{2}} d\theta_e \quad (3.15)$$

Thus the average power dissipated in a volumetric region is:

$$P_{mean} = \iiint_{region} P_v dv \quad (3.16)$$

In the case of a sinusoidal variation the expression becomes:

$$\Delta P_F = k_h f B_m^2 + k_{ed} (f B_m)^2 + k_{ex} (f B_m)^{\frac{3}{2}} \quad (3.17)$$

Where:

k_h is the hysteresis coefficient

k_{ed} the eddy current coefficient

k_{ex} the excess loss coefficient

σ is the material conductivity

d is the thickness of the sheet

f frequency of stator magnetic flux density

B_m maximum value of magnetic flux density in the ferromagnetic part

Hysteresis losses, transformed into heat, represent the power required for the alternative cyclic magnetization of iron. They are directly related to the irreversible evolution of the crystal structure of the material constituting the sheets. The organization of matter in Weiss domain is modified under the effect of variation in intensity and / or direction of the magnetic field. The losses generated are thus proportional to the air of the hysteresis cycle, to the number of magnetization cycles and are independent of sheet thickness.

Eddy current losses are due to the creation of electromagnetic forces induced in iron, themselves due to alternative cyclic magnetization. These forces give rise to currents that form in the mass of iron in planes normal to the direction of flux.

The calculation of excess losses makes it possible to correct the value given to dynamic losses, often attributed only to eddy current losses.

Many authors have used analytical models for the prediction of electromagnetic losses [12][14][15][16] for radial flow machines with permanent magnets. For axial flux machines, finite element, analytical or semi-analytical methods are used for the prediction of iron losses. In [17], losses in the iron core and permanent magnets caused by spatial harmonics and time harmonics are analyzed with the 3D finite element method in an axial flux machine for flywheel application. The calculation of losses in axial flux machines with fractional slots is discussed in references [18] and [19]. In [18] an analytical method is used while in [19] a semi-analytical method is used for the calculation of eddy current losses in the rotor [19].

In this work, the estimation of iron losses was performed using an LS model already implemented in a commercial finite elements software. In this software, LS model is defined for different lamination nuances; these are: M270-35A, M330-35A, M330-65A, M400-50A, M600-50A, M600-65A, M800-50A, M800-65A. Simulation was performed using a magneto-transient formulation where both stator and rotor irons were assigned a M270-35A iron and the currents shown in section VIII were injected in the coils. This simulation was followed by

a posteriori iron loss computation in the stator iron region and in the rotor iron region. The mean value of stator iron losses was found to be 690.56 W and that of rotor iron losses 6.6 W.

d) Flux & EMF

The fluxes and EMFs at no load for the three phases have a waveform that is close to a trapezoid with a maximum value of 157 mWb for the flux and 281.6 V (233.97 Vrms) for the EMF (the EMF is plotted for the nominal rotational speed of 2000 rpm). The phase flux and the EMF are shown in Fig. 3.22 and Fig. 3.23 below, respectively.

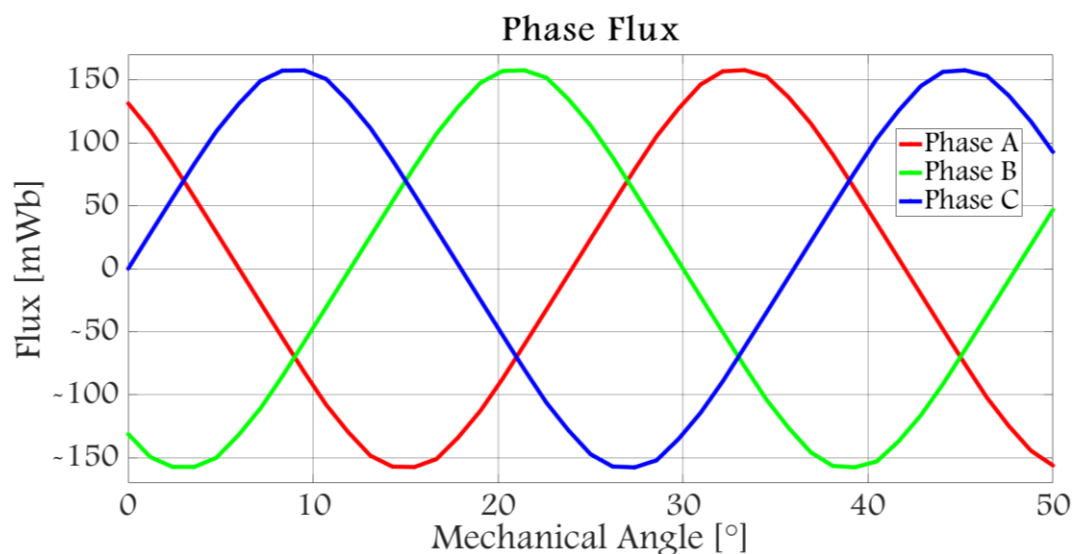


Fig. 3.22: Flux per phase

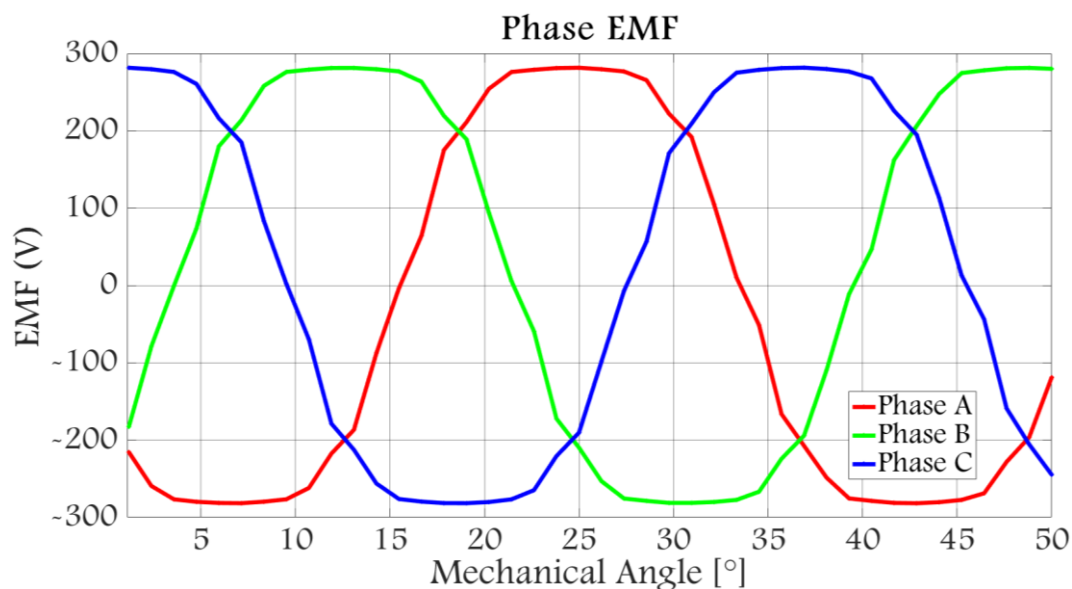


Fig. 3.23: EMF per phase

e) Electromagnetic torque & power

The total torque is obtained by Maxwell stress tensor. The total torque is mainly due to the interaction between the permanent magnets' field and the field due to the stator

excitation. The total torque shown in Fig. 3.25 corresponds to the average torque for different rotor positions with the stator current always in phase with the stator EMF. As the permanent magnets are surface mounted, the machine has no saliency and the maximum torque is obtained for rotor and stator fields in quadrature.

The electromagnetic power is calculated for a speed of 2000 RPM (Fig. 3.26). Therefore, it has the same waveform as the total torque. The electrical power delivered by the machine is equal to the electromagnetic power minus the losses (mechanical losses, iron losses, Joule losses, etc.).

A 3D mageto-transient simulation was performed with currents shown in section VIII injected in the coils and in nonlinear permeability conditions in order to obtain the mean value of the torque and power of the machine. The obtained results show that torque fluctuates between a value of 151.02 N.m and a value of 154.15 N.m with a mean value of 152.32 N.m (Fig. 3.24), and thus has a torque ripple of 2.05% which is a low value of ripple for this kind of machine.

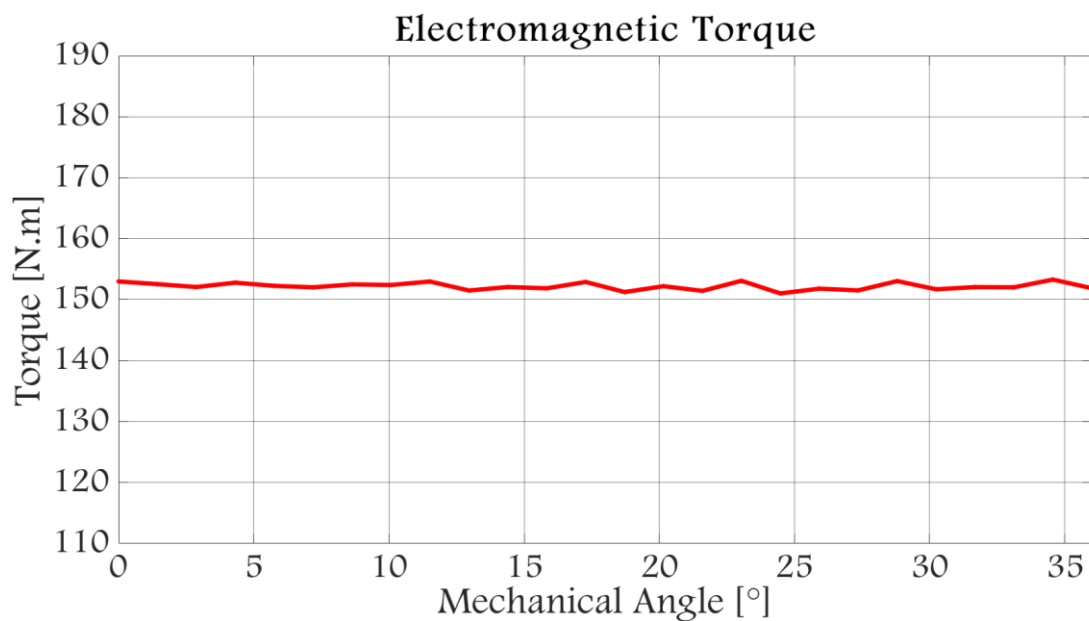


Fig. 3.24: Instantaneous torque

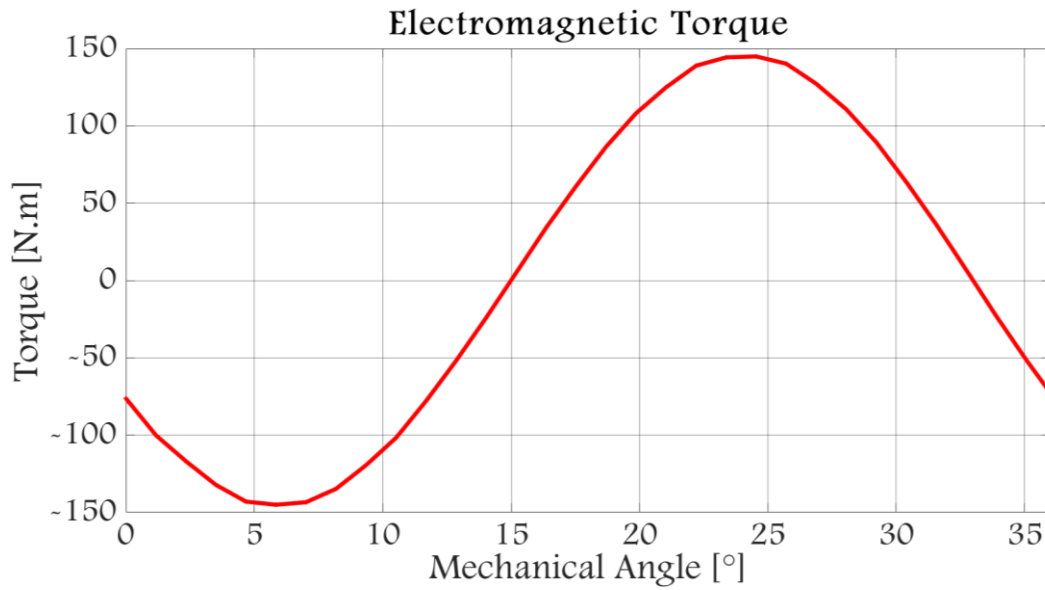


Fig. 3.25: Torque characteristic for different rotor positions

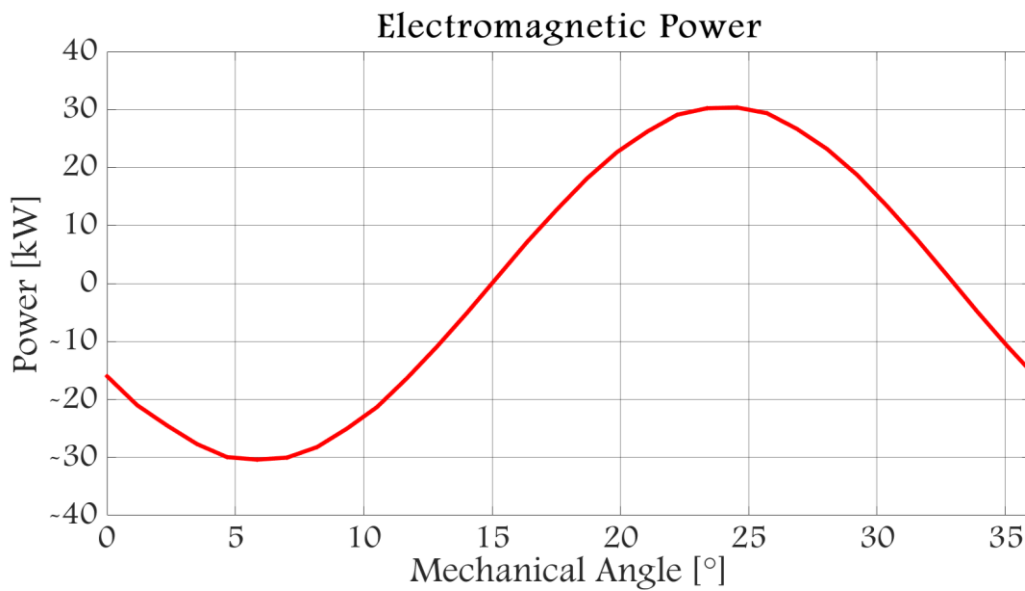


Fig. 3.26: Electromagnetic power

f) Cogging torque

Cogging torque is one of the major concerns in PM machines as it is a main source of torque and speed fluctuations. It is caused by the interaction between magnet flux and stator reluctance variations (due to slotting), or caused by airgap reluctance variation. Its average value must be zero and it's computed with no stator excitation in the coils. In mathematical terms, it can be expressed by the following equation [20]:

$$T_{cog} = -\frac{1}{2} \phi_{gap} \frac{d\mathfrak{R}}{d\theta} \quad (3.18)$$

Where:

ϕ_{gap} the magnetic flux crossing each airgap

\mathfrak{R} the stator reluctance.

Thus, by reducing air gap flux or stator reluctance variation, cogging torque is reduced. Practically, it is not wise to reduce air gap flux as this will degrade the machine's performance. On the other hand, reducing stator reluctance variation is a viable solution to reduce cogging torque. In general, reduction of cogging torque can be achieved by either harmonic current injection or by shaping or skewing the magnets, displacing magnets and rotors, optimizing the magnet pole-arc, or employing a fractional number of slots.

The cogging torque for the designed machine is obtained by Maxwell stress tensor. The cogging torque (Fig. 3.27) was computed using an analytical model and is of a few N.m (maximum value of 1.41 N.m) as a result of the chosen slot-pole combination. It has a period of 3° ($360^\circ/\text{LCM}(10, 24)$).

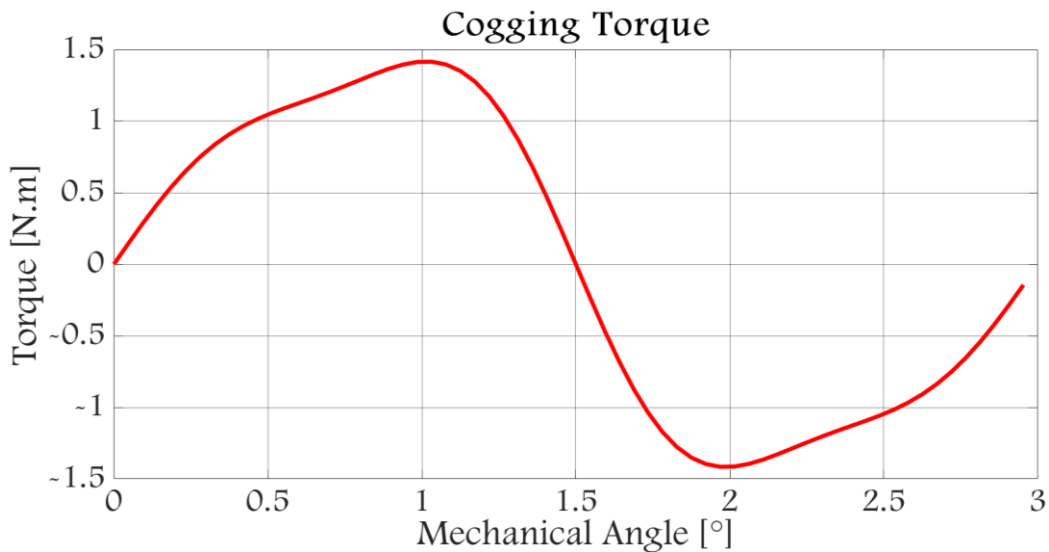


Fig. 3.27: Cogging torque using the analytical model

An attempt to compute the cogging torque using finite elements in linear BH curve conditions yielded the curve shown in Fig. 3.28. The computation was performed using second order mesh elements with a total of 1196034 nodes. As can be seen, the quality of the curve is not as high as that obtained with the analytical model (apart from the difference in magnitude). This is mostly caused by the tangential component of the magnetic flux density (Fig. 3.29). To overcome this, additional layers of mesh elements have to be added inside the air gap; but this increases the computation time and requires additional resources.

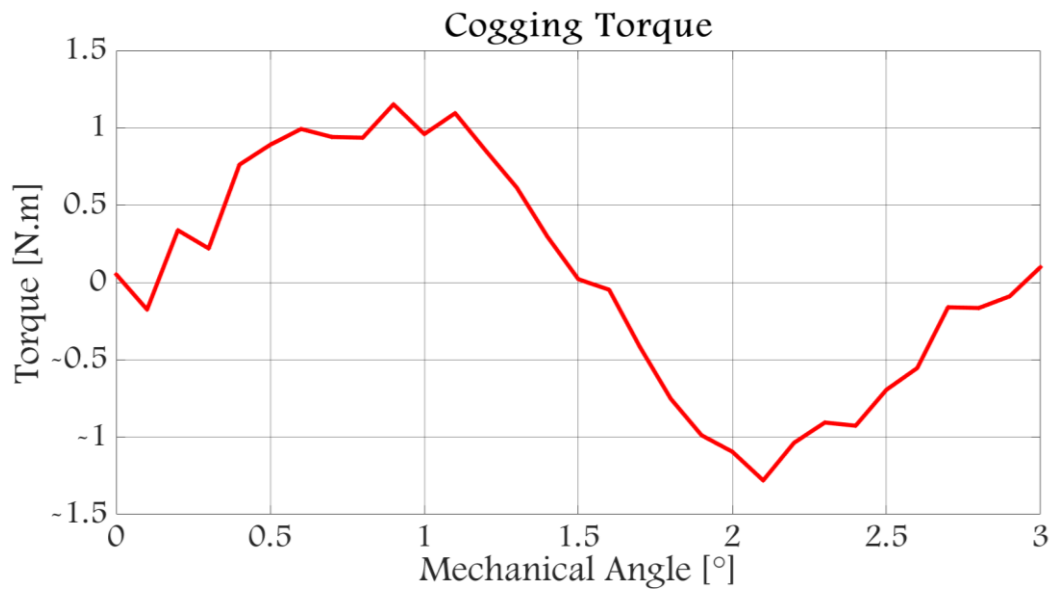


Fig. 3.28: Cogging torque using the finite element model

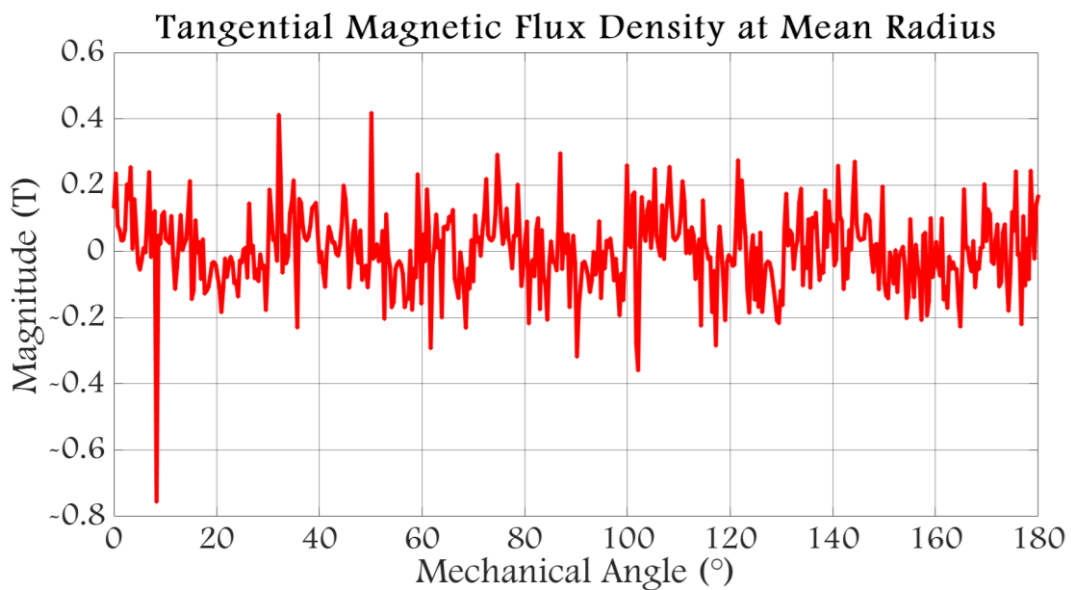


Fig. 3.29: Tangential magnetic flux density in the middle of the air gap at 1.5° rotor position

g) Attraction forces

The axial attraction forces acting on a disk at no load and at load are shown respectively in Fig. 3.30. The mean value of the axial attraction force on one side of the rotor disk at no load is 17.26 kN, which corresponds to the equivalent of the weight of 1.76 tons. The casing holding a stator disc must be mechanically designed to withstand this force for the stator-rotor-stator structure.

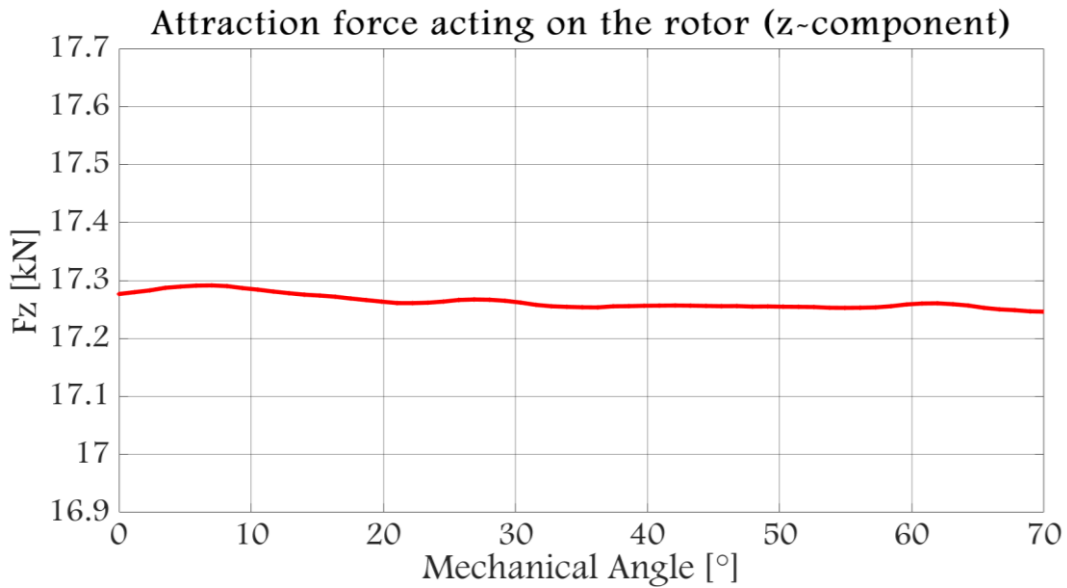


Fig. 3.30: Attraction force at no load

IV. End Winding Inductance

Many methods were employed for the computation of end winding inductance and they were proposed for radial flux machines and linear machines. Most of the time, the end winding is fully encapsulated in air, and the end-coil shape is circular or semicircular. This can be seen in the analytical approximation used in [21], and the analytical approach in [22]. In [21], Laplace's equation is solved for the magnetic vector potential in the end-winding region, then the magnetic flux density is calculated and the inductance is deduced from the flux linkage.

[23] develops an equation for calculating the end winding inductance for concentrated modular winding configurations, supposing an oval shape for the coils. [24] proposes the use of the method of images for the calculation of the end-winding inductance. In [25], the authors model the end coil as a set of serially connected straight filaments taking the influence of the iron core into account using the method of images.

[26] compares the accuracy of two analytical methods (one of which is proposed by the authors) and two FE based methods for five different non-overlap winding PM wind generators. It is shown that ignoring the effect of the laminated core in the calculation of the end-winding inductance yields non valid results. Also the proposed method gave consistently good results compared with the 3-D FE analysis.

Computation of end-winding inductance with a 2D FE model is proposed in [27], where some permeable machine structure components can be taken into account. To compute end-winding inductance accurately, 3D finite element analysis must be performed as shown in [28] and [29]. In [29], the end winding inductance is deduced from the stored magnetic energy calculated by a 3-D time-harmonic finite element analysis. A 3D FE model of the end-winding region and a small part of the lamination stack is used in [30] to compute the end winding inductance. Some methods compute the end winding inductance by first computing the per-phase inductance using 3D finite elements, then subtract from it the per-phase inductance obtained by a 2D finite elements model.

The end winding inductance can also be calculated by first determining the total phase flux using 3D finite elements in nonlinear permeability conditions and then subtracting the flux in the air gap to obtain the leakage flux. Assuming that the contribution of the slots to the leakage flux can be neglected, we can obtain the end winding inductance by simply dividing the value of the leakage flux by the current crossing the end windings.

V. PM Eddy Current Loss

PM Eddy current losses were not considered in this work, but the different methods found in literature to compute them will be presented. The benchmark method used to compute eddy current losses is the magneto-transient finite element method, but it is time consuming, for example the full transient 3D FE model used in [31] took about 5 days to obtain the solution. It is worth mentioning that Eddy currents can cause demagnetization of magnets [31]. Segmentation of magnets can be employed to reduce the effects of eddy-currents [32], but [33] argue that reducing eddy currents is not necessarily achieved by increasing the number of segments as can be seen in Fig. 3.31. Curve A is related to relatively small-frequency eddy-currents and curves B and B' to high-frequency eddy currents. As eddy-current frequency increases, the loss behavior changes from that of curve B to that of curve B', meaning that the loss peak is reached for a finer magnet segmentation. Analytical and semi-analytical methods have been developed to compute these curves without going through time consuming transient 3D FEA as can be found in [16][31][34][35][36][37][38][39][40][41], where different simplifying assumptions are considered and eddy-current reaction field is taken into account.

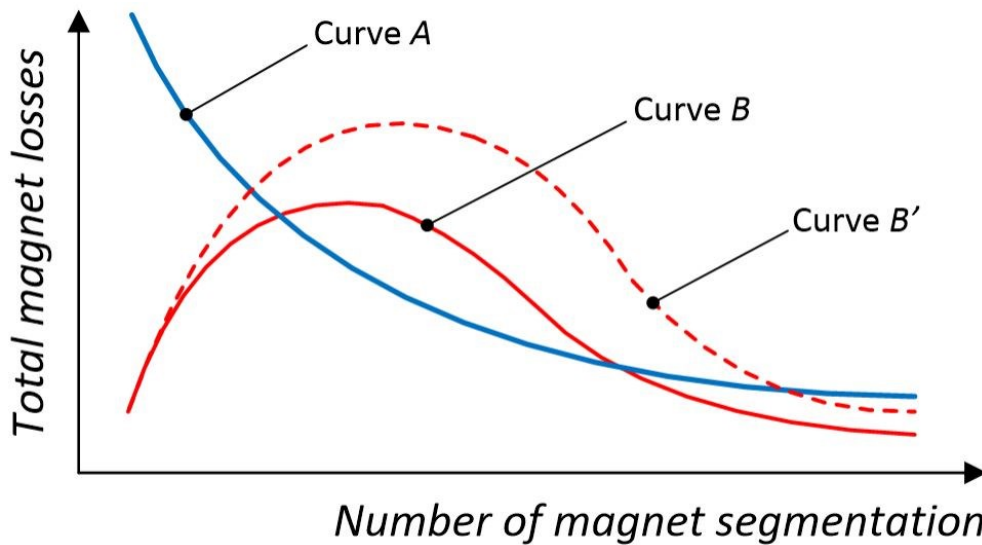


Fig. 3.31: Qualitative curves describing magnet loss variation as a function of magnet segmentation [33]

In [31] the authors present an analytical solution of the eddy currents in the permanent magnets (PMs) in the Axial Flux Permanent Magnet Synchronous Machine (AFPMSM) coupling Maxwell's equations solution for the flux density in the axial direction at the surface of PMs and electric circuit network, taking into account the effect of armature field and slots. The method is adapted from the method proposed in [42] for radial PM machines. PMs are modeled by a network of resistances and inductances. The inductances are added to describe the skin effect and the armature field effect on the total losses in the PM and can be removed for low speed applications or when no armature reaction is considered. The authors divide the

machine into several slices in the axial direction. Then the field solution is reconstructed and applied on a simple geometry of one PM in the 2D FE model. The authors compared their method with finite elements achieving sufficiently accurate results with more than 200 times reduction in computation time.

In [14] and [43], the authors develop a power loss formula based on obtaining the current sheet distribution formula in the space. The magnetic vector potential is then deduced using Maxwell's equations neglecting slotting and skin effect.

[44] introduced simple mathematical formulations for eddy-current loss calculations due to time harmonics in the stator current neglecting slotting and skin effect as well as spatial distribution of this field on the surface of the PM.

In [45] and [46], the flux density in PMs is computed using a Magnetic Equivalent Circuit (MEC). The eddy current losses were calculated in the post processing phase by assuming a certain resistance limited path for the current (assumed to be frequency independent) and neglecting skin effect.

Simpler techniques were proposed in [47] to compute no load losses due to the slotting effect. The method uses carter coefficient and the permeance function developed in [48] to calculate the flux density on the surface of the PM assuming the resistance path to be constant.

[39] proposes an analytical and FE model for radial flux machines which includes the effect of axial and circumferential magnet segmentation and the effect of the reaction field. It's a quasi-3D analytical approach which assumes that the magnetic field inside magnets is purely oriented along one direction and does not vary along that direction; accordingly, the eddy currents are supposed to flow parallel to the plane perpendicular to that direction

In [49] a purely numerical method is proposed that uses a radial 2D FEM solver and an axial 2D FEM solver to determine eddy current paths and losses in magnets. The method is 6 times faster compared with a transient 3D solver

In [50] the authors propose a semi-analytical method which combines a reduced set of magnetostatic solutions for the flux density distribution with a new analytical formulation for eddy-current losses in the permanent magnets assuming purely resistive eddy current paths. The method employed in [51] is relatively the same with the difference that the field distribution obtained by magneto-static 3D FEA is processed through a finite-difference algorithm.

[41] proposes an analytical method based on the generalized 3D image theory for accurate prediction of 3-D eddy current distributions and the corresponding loss in the rotor magnets of permanent magnet machines. The method assumes fictitious current densities outside the magnet domain assuring that eddy currents do not cross magnet faces anywhere, therefore not having to impose specific boundary conditions to the field solution. Validation of the method was done through a 3-D time-stepped transient finite-element analysis that showed a huge reduction in computation time, where the proposed method took about 10 s for computing 3-D eddy current loss in contrast to more than 24 h for the 3-D FEA.

A 3D finite element magneto-transient simulation with the magnets assigned a resistivity of $1.5 \times 10^{-6} \Omega \cdot m$ was then performed with the currents shown below injected in the coils, where I_a , I_b and I_c are the currents in the phases a,b and c respectively, $I_m \approx 33A$ is the maximum current, $\omega = 120000 \text{ }^\circ/s = 2094.4 \text{ rad/s}$ is the electrical angular speed

and ψ is the phase angle between EMF and current that yields the highest mean torque value. The meshing of a magnet for the computation of eddy current loss is given in Fig. 3.32.

$$\begin{cases} I_a = I_m \cos(\omega t - \psi) \\ I_b = I_m \cos(\omega t - 120^\circ - \psi) \\ I_c = I_m \cos(\omega t + 120^\circ - \psi) \end{cases} \quad (3.19)$$

$$\delta = \frac{1}{\sqrt{\sigma \mu \pi f}} \quad (3.20)$$

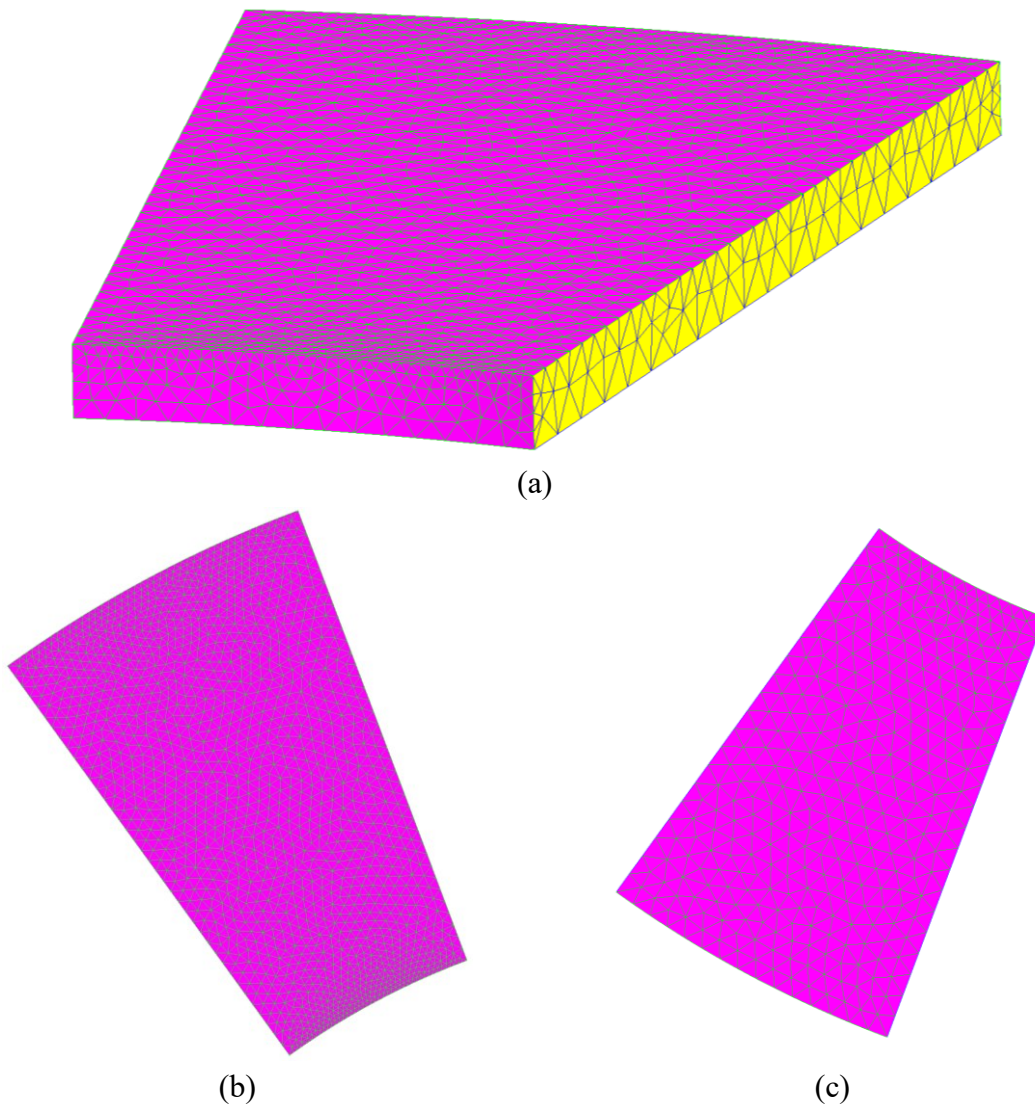


Fig. 3.32: Meshing of a magnet; (a) perspective, (b) top view, (c) bottom view

The distribution of eddy current density in PMs is shown in Fig. 3.33. It can be noted that eddy currents flow in loops within the volume of the PMs (the current density has two components in the local reference frame of the PMs). The mean value of these eddy current losses is equal to 52.72 W. It is worth mentioning that the skin depth for the 3rd, 5th and 7th

harmonic are respectively 19.48, 15.1 and 12.76 mm which exceeds the thickness of 4.7 mm of the magnets. These values were calculated using the above equation taking $\sigma = 0.667 \times 10^6 \text{ S/m}$ as conductivity of magnets and permeability μ that of air and the frequency $f = nf_1 = n \times 333.33 \text{ Hz}$ where n is the harmonic number and f_1 is the fundamental electrical frequency. On the other hand, looking at Fig. 3.34 and Fig. 3.35, which show the eddy current paths at the inner and outer radius respectively, it can be seen that the eddy currents are tangent to the magnets at both radii.

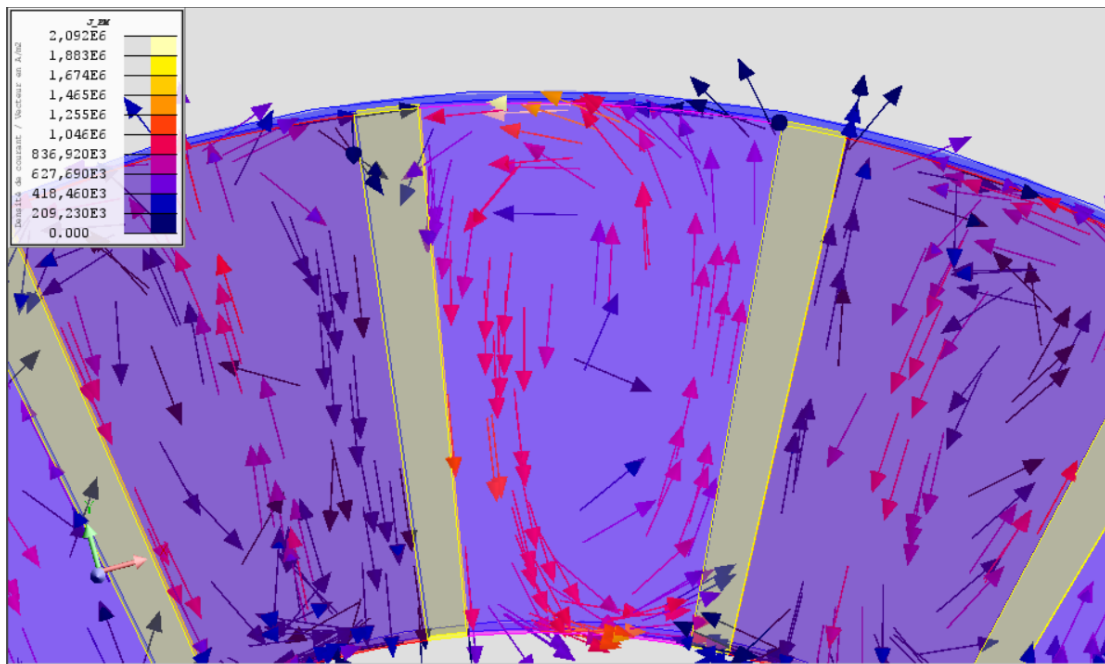


Fig. 3.33: Eddy current density in the magnets

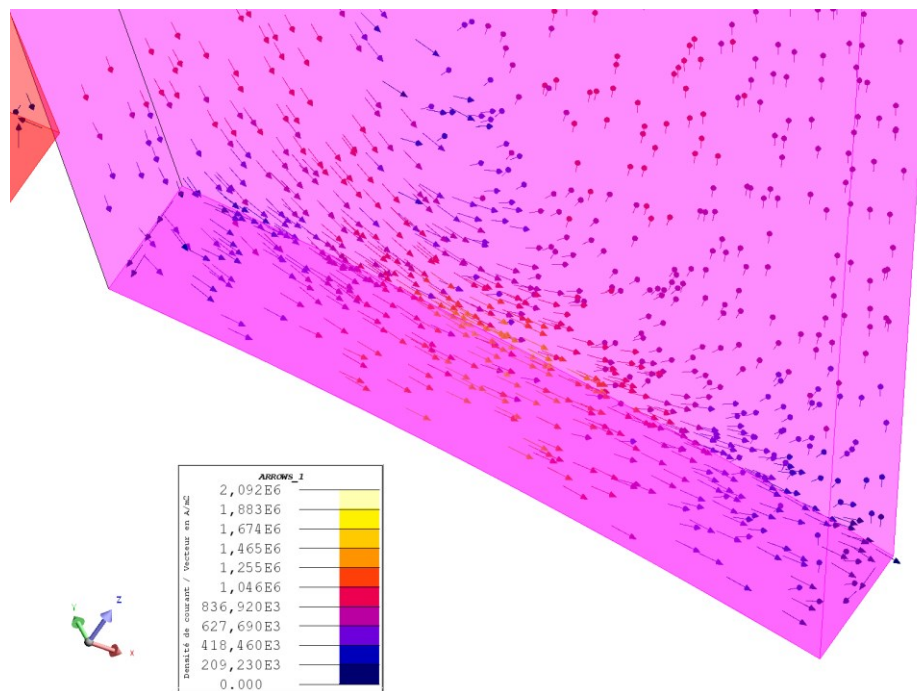


Fig. 3.34: Density of eddy currents in magnets at the inner radius

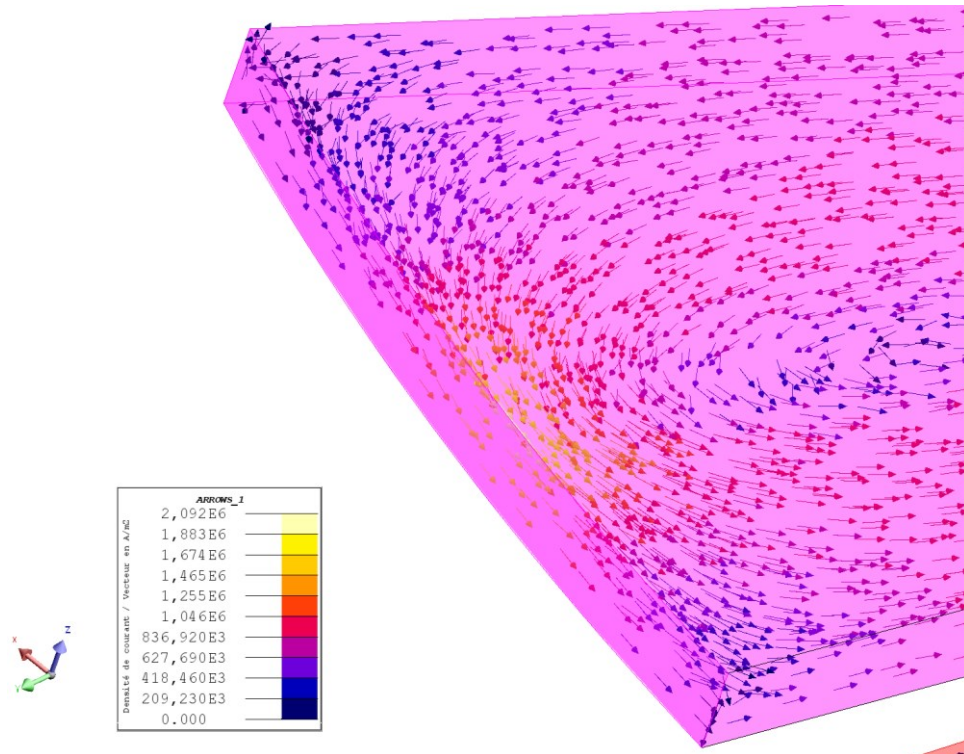


Fig. 3.35: Density of eddy currents in magnets at the outer radius

The machine can deviate from its rated speed, either it will run at a speed below its rated speed thus reducing the electrical frequency at its output, either it will run at a speed exceeding its rated speed thus increasing the electrical frequency at its output. This implies a change in PM Eddy current loss as it is frequency dependent. In order to study the impact of frequency change on the losses in magnets, several magneto-dynamic simulations were performed for different speed and thus for different frequencies and the mean value of PM Eddy current loss in magnets was recorded. The results are given in Tab. 3.2 and Fig. 3.36. As can be seen in the below figure, the PM Eddy current loss increases with the increase of frequency from 200 to 500 Hz.

Tab. 3.2: PM Eddy current loss for different frequencies and speeds

Rotation Speed (RPM)	1200	1500	2000	2500	3000
Electrical Frequency (Hz)	200	250	333.33	416.67	500
PM Eddy Current Loss (W)	22.45	33.45	52.72	84.16	111.99

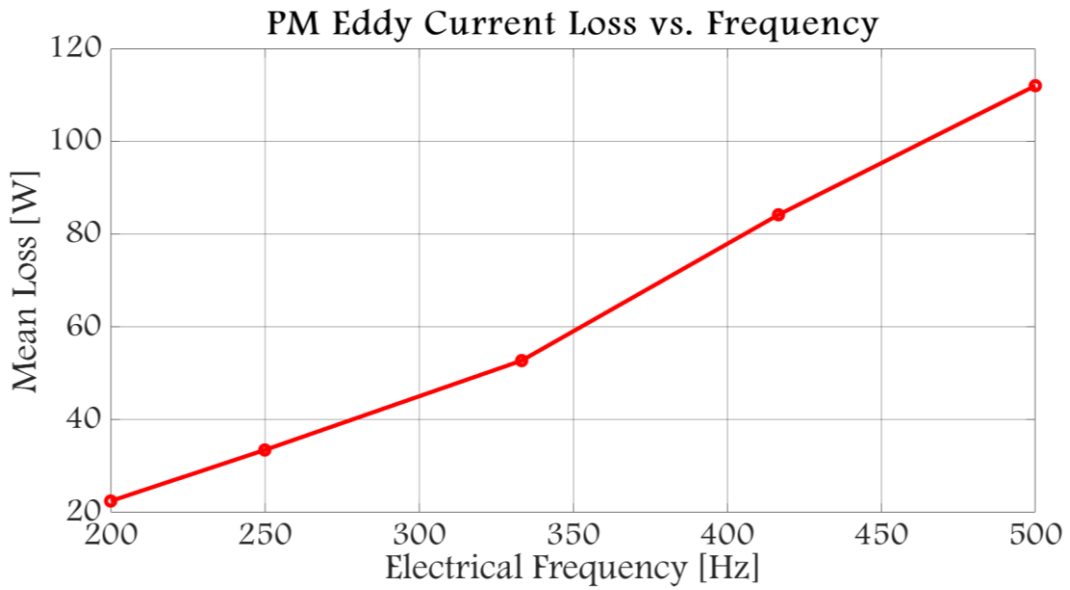


Fig. 3.36: PM Eddy current loss variation as a function of frequency

For the magnetic flux density, it can be seen by Fig. 3.37 and Fig. 3.38 below that the impact of eddy currents on both normal and tangential components inside the air gap is not high and the amplitudes do not vary much as compared with the case where the PM eddy currents are not taken into account (Fig. 3.18 and Fig. 3.19), this allows to compute the induced eddy currents in the magnets independently from the magnetic flux density inside the air gap.

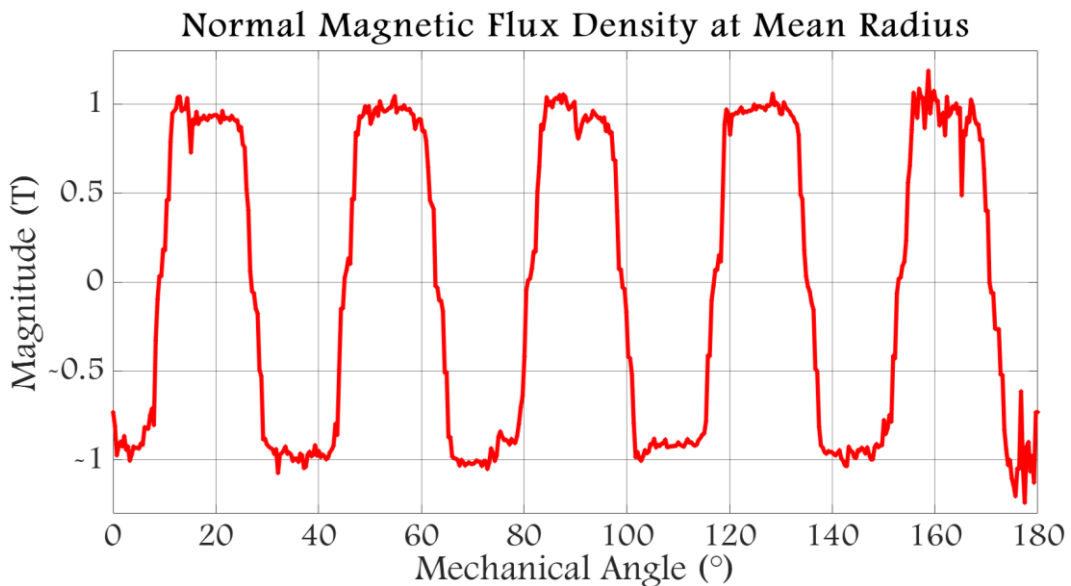


Fig. 3.37: Impact of PM eddy currents on air gap magnetic flux density (normal component)

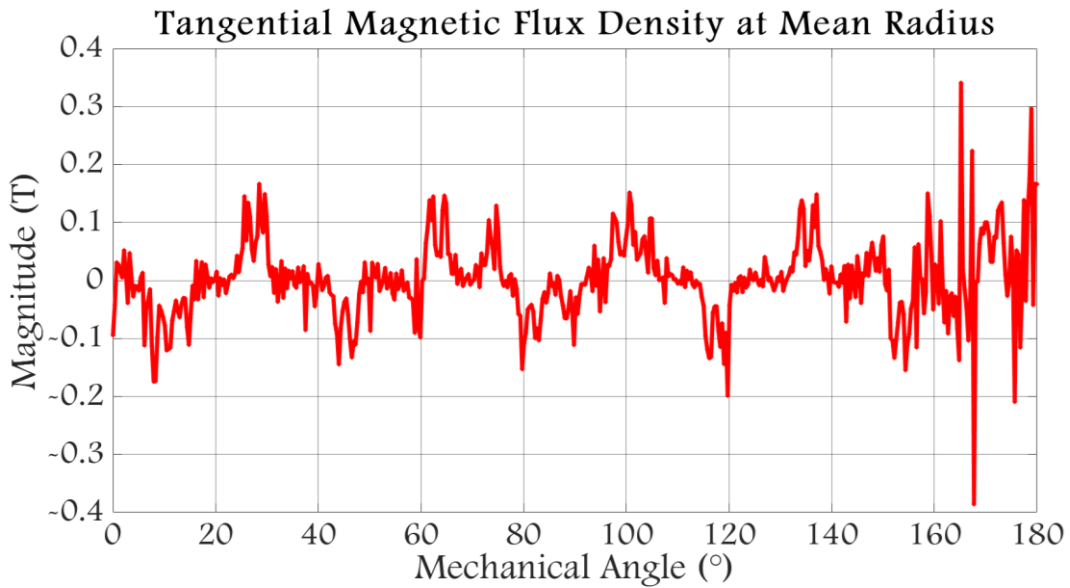


Fig. 3.38: Impact of PM eddy currents on air gap magnetic flux density (tangential component)

VI. Thermal Study of the Designed Machine

The thermal study is conducted by setting the thermal conductivities to the values given in Tab. 3.3 and the thicknesses to the values given in Tab. 3.4. Ventilation is considered with a mean convective exchange coefficient between bearing support plates and outside air of $h_{bearing}^{air} = 50 \text{ W/m}^2 \cdot \text{K}$.

In this model, heat transfer by radiation is not considered. Also, eddy current losses in magnets as well as iron losses in the rotor magnetic circuit are neglected. Despite the fact that the flux axially passes through the rotor, we have maintained a magnetic circuit for the rotor for mechanical considerations. The geometry is considered ideal and the carter is considered smooth without fins. The thermal calculation presented in this section is carried out for a nominal operating point. Steady-state temperatures for permanent magnets (95°C) and copper (102°C) are below temperatures that can cause irreversible performance deterioration.

Tab. 3.3: Thermal conductivities of the different regions

Region	Value
Stator sheets (axial direction)	9
Stator sheets (radial direction)	42
Insulation	0.2
Coils (axial direction)	0.72
Coils (radial direction)	195
Air	0.0262
Aluminum	237
Magnets	9
Fiberglass	1.2
Bearing	38.9

Tab. 3.4: Thicknesses of different machine elements

Element	Value (mm)
Insulation sheet (axial direction)	1
Fiberglass	0.5
Bearing	20
Carter	10

The temperature levels in different regions in steady state are given in Tab. 3.5. Fig. 3.39 represents the different regions where these temperature are calculated.

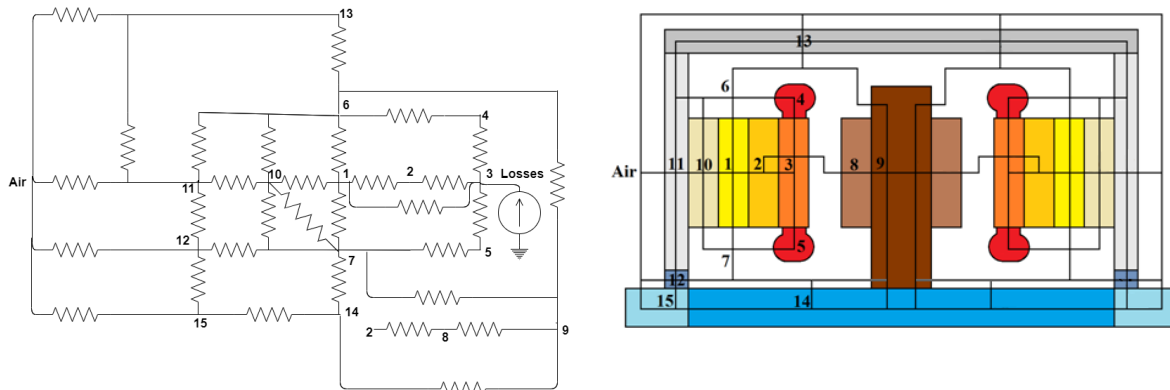


Fig. 3.39: Thermal nodal network

Tab. 3.5: Temperatures in the different regions

Parameter	Region	Value (°C)
T1	Stator sheets	78
T2	Stator teeth	99
T3	Copper in slots	102
T4	External end winding	86
T5	Internal end winding	104
T6	External air gap	83
T7	Internal air gap	98
T8	Magnets	95
T9	Rotor sheets	95
T10	Stator fixing plate	78
T11	Stator bearing support	77
T12	Stator side bearing	87
T13	Carter	77
T14	Shaft inside the machine	95
T15	Shaft outside the machine	87

VII. Mechanical Study of the Designed Machine

1. Deflection of the Rotor Disk

The axial thickness of the rotor must fulfill two constraints: magnetic and mechanical. The first is the law of conservation of flux, and the second guarantees minimum deflection of the disks.

When a machine with magnets in the rotor is assembled, care should be taken because of the attraction and repulsion forces between the stator and rotor disks. These forces can be estimated by:

$$F = \alpha_m S_{ag} B_{ag}^2 / 2\mu_0 \quad (3.21)$$

Where α_m is the polar arc coefficient, S_{ag} is the active air gap surface and B_{ag} is the mean magnetic flux density in the air gap.

So, when mounting a stator against a rotor with magnets, the deflection Δe encountered by the rotor disks should be avoided. This deflection can be estimated by the equation proposed by Young in [52], which theoretically should not exceed 10% of the air gap length and imposes a minimal axial thickness on the rotor disks.

In order to estimate the deflection of the rotor disk, a mechanical simulation using ANSYS Mechanical finite elements software is conducted. The simulation takes as input the axial attraction force at no load acting on each side of the rotor which is then distributed as pressure on the magnets of the corresponding side as to create a tensile stress on the rotor normal to each side. An aluminum hub is inserted in the internal diameter of the rotor to transmit torque to the shaft and also to increase the rigidity of the structure. The shaft is considered having a diameter of 32 mm and replaced by a fixed support boundary condition. All contacts are considered bonded and the structure is meshed with 5mm tetrahedral elements. Fig. 3.40 illustrates the rotor structure and its mesh.

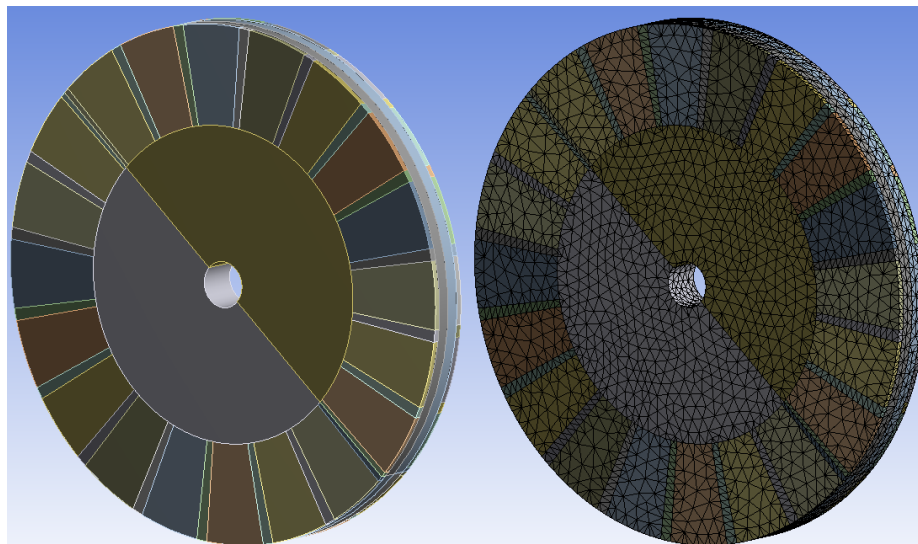


Fig. 3.40: The studied structure and its mesh

The mechanical properties of the different elements of the structure are listed in the following table:

Tab. 3.6: Mechanical properties used in the simulation

Element	Young modulus (MPa)	Poisson's ratio	Density (kg/m ³)
Rotor yoke	200000	0.3	7600
Magnets	150000	0.24	7600
Hub	72000	0.32	2700

The simulation was performed considering a decentering of 20% relative to the air gap length which is 1.2 mm, this yields an air gap of 1.44 mm on one side of the rotor and 0.96 mm on the other side. The mean axial attraction force on each side is 17200 N for the 1.44 mm side and 20557 N on the 0.96 mm side. This data was fed to the ANSYS simulation model and results can be visualized in Fig. 3.41.

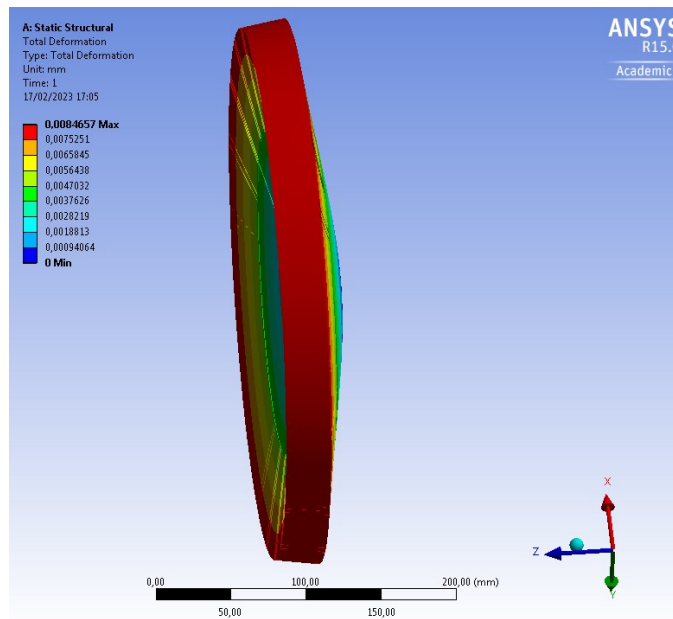


Fig. 3.41: Deflection of the rotor disk to axial attraction force

2. Mechanical Loss

Mechanical losses include losses resulting from all types of friction due to machine rotation. They appear in the form of heat or kinetic energy transferred to a fluid (air for example). These include mechanical losses caused by friction in bearings, aerodynamic losses due to air friction at the air gap and ventilation losses necessary to allow air circulation for cooling the machine.

Losses due to friction in bearings can be calculated by:

$$P_{friction} = \frac{3\omega}{100\pi} k_{fr} (M_{rotor} + M_{shaft}) \quad (3.22)$$

Where M_{rotor} and M_{shaft} are the rotor and shaft masses respectively and k_{fr} is a constant between 1 and 3 m^2/s^2 .

Aerodynamical losses are computed by:

$$P_{aero} = \frac{1}{2} C_f \rho (2\pi\omega)^3 (R_e^5 - D_{shaft}^5) \quad (3.23)$$

Where ρ, ω, R_e and D_{shaft} are respectively the specific coolant density (water in general), the rotation speed (in rad/s), the machine's external radius and the shaft diameter.

C_f is the coefficient of a turbulent flow, and can be calculated as follows:

$$C_f = \frac{3.87}{\sqrt{Re_{yn}}} \quad (3.24)$$

Re_{yn} is the Reynolds number which is a function of the rotation speed (μ is the fluid dynamic viscosity):

$$Re_{yn} = 2\pi\omega\rho^2 R_e^2 / \mu \quad (3.25)$$

In order to compute mechanical losses, we first need to calculate $\omega = 2\pi N/60$, with N the speed of the rotor in RPM, which yields 209.44 rad/s. Then we estimate the value of k_{fr} to be $2 \text{ m}^2/\text{s}^2$ and the mass of the shaft to be 1 Kg. The mass of the rotor yoke and permanent magnets is calculated based on their volume and density which yields a total mass of the rotor of 8.82 Kg. If we suppose the machine to be air cooled then the dynamic viscosity is that of air and it is $\mu = 1.8 \times 10^{-5} \text{ Kg/m.s}$ and its specific density is $\rho = 1.2 \text{ Kg/m}^3$ at 1 atm and 20°C. The diameter of the shaft is estimated at 32 mm. Plugging all these values in the above equations we obtain a value of $P_{friction} = 39.29 \text{ W}$ for the losses due to friction in bearings and a value of $P_{aero} = 541.3 \text{ W}$ for the aerodynamical losses.

VIII. Performance Summary

Main indicators of the machine's performance are summarized in Tab. 3.7. The efficiency is computed taking into account Joule, iron and mechanical losses:

$$\eta = \frac{P_{em}}{P_{em} + \Delta P_J + \Delta P_F + \Delta P_{PM} + \Delta P_M} \times 100 \quad (3.26)$$

$$P_{em} = T_{em} \times \omega_m \quad (3.27)$$

$$\omega_m = \frac{2\pi N}{60} \quad (3.28)$$

Where:

P_{em} mean electromagnetic power

T_{em} mean electromagnetic torque

N rotation speed of the rotor in RPM

ω_m rotational speed of the rotor in rad/s

ΔP_{PM} Eddy current loss in PMs

ΔP_M total mechanical loss

Tab. 3.7: Machine's performances

Parameter	Value
Mean power	31.683 kW
Mean torque	152.32 N.m
Rotation speed	2000 RPM
Efficiency	95.51%
Torque ripple	2.05%
Phase resistance	24.5m Ω
Stator phase cyclic inductance	0.56 mH
Stator RMS phase current	23.34 A
RMS phase EMF	233.97 V
Line to line voltage	405.25 V
Stator Joule loss	160.28 W
Stator iron loss	690.56 W
Rotor iron loss	6.6 W
PM Eddy current loss	52.72 W
Friction loss (Bearings)	39.29 W
Aerodynamical loss	541.3 W
PM weight	3.82 kg
Rotor iron weight	5 kg
Stator iron weight	27.61 kg

Copper weight	5.41 kg
Active part weight	41.84 kg

IX. Conclusion

In this chapter, the 3D aspect of flux in axial flux machines was first presented explaining the need for a 3D model to take into account the end effects and provide more accurate results, justifying the use of 3D finite elements in the sizing and performance assessment of the design

The design of a 30 kW/2000RPM axial flux permanent magnet synchronous machine was then presented with the design steps explained and its performances evaluated in nonlinear permeability conditions using commercial finite elements software. The design shows good performance as it has an efficiency of 95% providing the required 230V output voltage. It also has good thermal behavior under load with temperature values not exceeding 95°C for magnets and 102°C for windings. The designed generator is still under construction by ERNEO with a prototype expected in 2024.

An analytical model was used in the first pre-sizing stages to test many possibilities before performing the finite elements analysis, which is well known for its accuracy while being costly in terms of computation time.

The analytical model was used to conduct a parametric study in linear BH curve conditions to compute the torque, active mass and torque mass density for different internal and external radii in order to choose suitable radii for the machine. Also, the model was used to test different values for the design parameters to determine the best combination that satisfies the required specs.

After fixing the design parameters, a 3D finite elements simulation in nonlinear permeability conditions was performed using a commercial FE software to compute the magnetic flux density at load and no load conditions, flux, EMF, electromagnetic torque, electromagnetic power, iron losses and PM Eddy current loss.

As the study of the machines thermal behavior is important, it was also considered through simulation using a lumped parameter model to compute the temperatures in different regions of the machine where high temperature values can degrade machine performance. The most important regions are magnets and stator windings, as high temperatures in these regions can cause demagnetization of magnets and deterioration of winding insulation.

Finally a mechanical study was performed using a mechanical FE software to assess rotor disk deflection due to axial attraction forces. This was done to guarantee that the air gap will remain at acceptable values thus avoiding machine destruction.

References

- [1] J. Azzouzi, "Contribution à la modélisation et à l'optimisation des machines synchrones à aimants permanents à flux axial. Application au cas de l'aérogénérateur," Université du Havre, 2007.

- [2] N. Abdel Karim, “Optimisation multi-critères et multi-physique d’aérogénérateurs à aimants permanents à flux axial,” Université du Havre, 2008.
- [3] A. Mahyob, “Modélisation des machines électriques tournantes défectueuses par la méthode des réseaux de perméances : Application à la machine asynchrone,” L’École Nationale Supérieure d’Arts et Métiers, 2012.
- [4] A. Bellara, “Modélisation analytique par le formalisme de Maxwell des machines synchrones à aimants permanents à flux axial en vue de leur dimensionnement,” 2011.
- [5] H. Tiegna, “Contribution à la modélisation analytique des machines synchrones à flux axial à aimants permanents à attaque directe en vue de leur dimensionnement. Application aux éoliennes.,” Université Le Havre Normandie, 2013.
- [6] G. Verez, “Contribution à l’étude des émissions vibro-acoustiques des machines électriques : cas des machines synchrones à aimants dans un contexte automobile,” Université du Havre, 2014.
- [7] K. Atallah, S. D. Calverley, and D. Howe, “Design, analysis and realisation of a high-performance magnetic gear,” *Electr. Power Appl. IEE Proc. -*, vol. 151, pp. 135–143, 2004, doi: 10.1049/ip-epa:20040224.
- [8] J. Sepaseh, N. Rostami, M. R. Feyzi, and M. B. B. Sharifian, “Optimal design of an axial magnetic gear by using particle swarm optimisation method,” *IET Electr. Power Appl.*, vol. 16, no. 6, pp. 723–735, 2022, doi: <https://doi.org/10.1049/elp2.12189>.
- [9] C. Cester, “Etude des pertes magnétiques supplémentaires dans les machines asynchrones alimentées par onduleur à modulation de largeur d’impulsion,” Institut National Polytechnique de Grenoble (INPG), 1996.
- [10] T. Chevalier, “Modélisation et mesure des pertes fer dans les machines électriques, application à la machine asynchrone,” Institut National Polytechnique de Grenoble - INPG, 1999.
- [11] T. Gautreau, “Estimation des pertes fer dans les machines électriques : modèles d’hysteresis Loss Surface et application aux machines synchrones à aimants,” Institut National Polytechnique de Grenoble - INPG, 2005.
- [12] Y. Amara, J. Wang, and D. Howe, “Stator iron loss of tubular permanent magnet machines,” in *Conference Record of the 2004 IEEE Industry Applications Conference, 2004. 39th IAS Annual Meeting.*, Oct. 2004, vol. 3, pp. 2119–2124 vol.3, doi: 10.1109/IAS.2004.1348759.
- [13] G. Bertotti, A. Boglietti, M. Chiampi, D. Chiarabaglio, F. Fiorillo, and M. Lazzari, “An improved estimation of iron losses in rotating electrical machines,” *IEEE Trans. Magn.*, vol. 27, no. 6, pp. 5007–5009, Nov. 1991, doi: 10.1109/20.278722.
- [14] K. Atallah, D. Howe, P. H. Mellor, and D. A. Stone, “Rotor loss in permanent magnet brushless AC machines,” in *IEEE International Electric Machines and Drives Conference. IEMDC’99. Proceedings (Cat. No.99EX272)*, May 1999, pp. 60–62, doi: 10.1109/IEMDC.1999.769027.
- [15] Y. Amara, P. Reghem, and G. Barakat, “Analytical Prediction of Eddy-Current Loss in Armature Windings of Permanent Magnet Brushless AC Machines,” *Magn. IEEE Trans.*, vol. 46, pp. 3481–3484, 2010, doi: 10.1109/TMAG.2010.2046885.
- [16] W.-Y. Huang, A. Bettayeb, R. Kaczmarek, and J.-C. Vannier, “Optimization of Magnet Segmentation for Reduction of Eddy-Current Losses in Permanent Magnet Synchronous Machine,” *IEEE Trans. Energy Convers.*, vol. 25, no. 2, pp. 381–387, Jun. 2010, doi: 10.1109/TEC.2009.2036250.

- [17] T. D. Nguyen, K. J. Tseng, C. Zhang, and S. Zhang, "Loss study of a novel axial flux permanent magnet machine," in *2011 IEEE International Electric Machines & Drives Conference (IEMDC)*, May 2011, pp. 1143–1148, doi: 10.1109/IEMDC.2011.5994763.
- [18] R. Di Stefano and F. Marignetti, "Electromagnetic Analysis of Axial-Flux Permanent Magnet Synchronous Machines With Fractional Windings With Experimental Validation," *IEEE Trans. Ind. Electron.*, vol. 59, no. 6, pp. 2573–2582, 2012, doi: 10.1109/TIE.2011.2165458.
- [19] J. Li, D.-W. Choi, D.-H. Son, and Y.-H. Cho, "Effects of MMF Harmonics on Rotor Eddy-Current Losses for Inner-Rotor Fractional Slot Axial Flux Permanent Magnet Synchronous Machines," *IEEE Trans. Magn.*, vol. 48, no. 2, pp. 839–842, Feb. 2012, doi: 10.1109/TMAG.2011.2173923.
- [20] M. Aydin and M. Gulec, "Reduction of Cogging Torque in Double-Rotor Axial-Flux Permanent-Magnet Disk Motors: A Review of Cost-Effective Magnet-Skewing Techniques With Experimental Verification," *IEEE Trans. Ind. Electron.*, vol. 61, no. 9, pp. 5025–5034, 2014, doi: 10.1109/TIE.2013.2276777.
- [21] M.-F. Hsieh, Y.-C. Hsu, D. G. Dorrell, and K.-H. Hu, "Investigation on End Winding Inductance in Motor Stator Windings," *IEEE Trans. Magn.*, vol. 43, no. 6, pp. 2513–2515, Jun. 2007, doi: 10.1109/TMAG.2007.896209.
- [22] A. M. El-Refaie, Z. Q. Zhu, T. M. Jahns, and D. Howe, "Winding Inductances of Fractional Slot Surface-Mounted Permanent Magnet Brushless Machines," in *2008 IEEE Industry Applications Society Annual Meeting*, Oct. 2008, pp. 1–8, doi: 10.1109/08IAS.2008.61.
- [23] T. Cox, F. Eastham, and J. Proverbs, "End Turn Leakage Reactance of Concentrated Modular Winding Stators," *IEEE Trans. Magn.*, vol. 44, no. 11, pp. 4057–4061, Nov. 2008, doi: 10.1109/TMAG.2008.2002382.
- [24] M. J. Kamper and F. S. Van der Merwe, "Influence of laminations on axially directed flux in induction motors," in *Proc. ICEM*, 1988, pp. 413–416.
- [25] D. Žarko, D. Ban, and R. Klarić, "Finite Element Approach to Calculation of Parameters of an Interior Permanent Magnet Motor." 2005.
- [26] J. H. J. Potgieter and M. J. Kamper, "Calculation Methods and Effects of End-Winding Inductance and Permanent-Magnet End Flux on Performance Prediction of Nonoverlap Winding Permanent-Magnet Machines," *IEEE Trans. Ind. Appl.*, vol. 50, no. 4, pp. 2458–2466, Jul. 2014, doi: 10.1109/TIA.2013.2295468.
- [27] R. De Weerd and R. Belmans, "Squirrel cage induction motor end effects using 2D and 3D finite elements," in *1995 Seventh International Conference on Electrical Machines and Drives (Conf. Publ. No. 412)*, 1995, pp. 62–66, doi: 10.1049/cp:19950836.
- [28] A. Tounzi, T. Henneron, Y. Le Menach, R. Askour, E. Dumetz, and F. Piriou, "3-D approaches to determine the end winding inductances of a permanent-magnet linear synchronous motor," *IEEE Trans. Magn.*, vol. 40, no. 2, pp. 758–761, Mar. 2004, doi: 10.1109/TMAG.2004.825287.
- [29] R. Lin and A. Arkkio, "Calculation and Analysis of Stator End-Winding Leakage Inductance of an Induction Machine," *IEEE Trans. Magn.*, vol. 45, no. 4, pp. 2009–2014, Apr. 2009, doi: 10.1109/TMAG.2008.2010317.
- [30] B. Funieru and A. Binder, "Simulation of electrical machines end effects with reduced

- length 3D FEM models,” in *2012 XXth International Conference on Electrical Machines*, 2012, pp. 1430–1436, doi: 10.1109/ICEIMach.2012.6350066.
- [31] A. Hemeida, P. Sergeant, and H. Vansompel, “Comparison of Methods for Permanent Magnet Eddy-Current Loss Computations With and Without Reaction Field Considerations in Axial Flux PMSM,” *IEEE Trans. Magn.*, vol. 51, no. 9, pp. 1–11, 2015, doi: 10.1109/TMAG.2015.2431222.
- [32] H. Vansompel, P. Sergeant, and L. Dupré, “Effect of segmentation on eddy-current loss in permanent-magnets of axial-flux PM machines using a multilayer-2D — 2D coupled model,” in *2012 XXth International Conference on Electrical Machines*, 2012, pp. 228–232, doi: 10.1109/ICEIMach.2012.6349869.
- [33] A. Tessarolo, “A survey of state-of-the-art methods to compute rotor eddy-current losses in synchronous permanent magnet machines,” in *2017 IEEE Workshop on Electrical Machines Design, Control and Diagnosis (WEMDCD)*, Apr. 2017, pp. 12–19, doi: 10.1109/WEMDCD.2017.7947717.
- [34] M. Cheng and S. Zhu, “Calculation of PM Eddy Current Loss in IPM Machine Under PWM VSI Supply With Combined 2-D FE and Analytical Method,” *IEEE Trans. Magn.*, vol. 53, no. 1, pp. 1–12, Jan. 2017, doi: 10.1109/TMAG.2016.2611582.
- [35] S. S. Nair, J. Wang, L. Chen, R. Chin, I. Manolas, and D. Svehkarenko, “Computationally Efficient 3-D Eddy Current Loss Prediction in Magnets of Interior Permanent Magnet Machines,” *IEEE Trans. Magn.*, vol. 52, no. 10, pp. 1–10, Oct. 2016, doi: 10.1109/TMAG.2016.2582145.
- [36] K. Yamazaki and Y. Fukushima, “Effect of eddy-current loss reduction by magnet segmentation in synchronous motors with concentrated windings,” in *2009 International Conference on Electrical Machines and Systems*, Nov. 2009, pp. 1–6, doi: 10.1109/ICEMS.2009.5382795.
- [37] K. Yamazaki and A. Abe, “Loss Analysis of Interior Permanent Magnet Motors Considering Carrier Harmonics and Magnet Eddy Currents Using 3-D FEM,” in *2007 IEEE International Electric Machines & Drives Conference*, May 2007, vol. 2, pp. 904–909, doi: 10.1109/IEMDC.2007.382794.
- [38] K. Yamazaki, M. Shina, Y. Kanou, M. Miwa, and J. Hagiwara, “Effect of Eddy Current Loss Reduction by Segmentation of Magnets in Synchronous Motors: Difference Between Interior and Surface Types,” *IEEE Trans. Magn.*, vol. 45, no. 10, pp. 4756–4759, Oct. 2009, doi: 10.1109/TMAG.2009.2024159.
- [39] M. Mirzaei, A. Binder, B. Funieru, and M. Susic, “Analytical Calculations of Induced Eddy Currents Losses in the Magnets of Surface Mounted PM Machines With Consideration of Circumferential and Axial Segmentation Effects,” *IEEE Trans. Magn.*, vol. 48, no. 12, pp. 4831–4841, Dec. 2012, doi: 10.1109/TMAG.2012.2203607.
- [40] S. S. Nair, J. Wang, L. Chen, R. Chin, I. Manolas, and D. Svehkarenko, “Prediction of 3-D High-Frequency Eddy Current Loss in Rotor Magnets of SPM Machines,” *IEEE Trans. Magn.*, vol. 52, no. 9, pp. 1–10, 2016, doi: 10.1109/TMAG.2016.2574779.
- [41] L. Chen, J. Wang, and S. S. Nair, “An Analytical Method for Predicting 3-D Eddy Current Loss in Permanent Magnet Machines Based on Generalized Image Theory,” *IEEE Trans. Magn.*, vol. 52, no. 6, pp. 1–11, Jun. 2016, doi: 10.1109/TMAG.2015.2500878.
- [42] Y. Yoshida, K. Nakamura, and O. Ichinokura, “Basic examination of eddy current loss estimation in SPM motor based on electric and magnetic networks,” in *2012 XXth*

- International Conference on Electrical Machines*, 2012, pp. 1586–1591, doi: 10.1109/ICEIMach.2012.6350090.
- [43] H. Toda, Z. Xia, J. Wang, K. Atallah, and D. Howe, “Rotor eddy-current loss in permanent magnet brushless machines,” *IEEE Trans. Magn.*, vol. 40, no. 4, pp. 2104–2106, Jul. 2004, doi: 10.1109/TMAG.2004.832481.
- [44] H. Polinder and M. J. Hoeijmakers, “Eddy-current losses in the permanent magnets of a PM machine,” in *1997 Eighth International Conference on Electrical Machines and Drives (Conf. Publ. No. 444)*, 1997, pp. 138–142, doi: 10.1049/cp:19971054.
- [45] A. R. Tariq, C. E. Nino-Baron, and E. G. Strangas, “Iron and Magnet Losses and Torque Calculation of Interior Permanent Magnet Synchronous Machines Using Magnetic Equivalent Circuit,” *IEEE Trans. Magn.*, vol. 46, no. 12, pp. 4073–4080, Dec. 2010, doi: 10.1109/TMAG.2010.2074207.
- [46] J. Klötzl, M. Pyc, and D. Gerling, “Permanent magnet loss reduction in PM-machines using analytical and FEM calculation,” in *SPEEDAM 2010*, Jun. 2010, pp. 98–100, doi: 10.1109/SPEEDAM.2010.5544964.
- [47] J. Pyrhonen, H. Jussila, Y. Alexandrova, P. Rafajdus, and J. Nerg, “Harmonic Loss Calculation in Rotor Surface Permanent Magnets—New Analytic Approach,” *IEEE Trans. Magn.*, vol. 48, no. 8, pp. 2358–2366, Aug. 2012, doi: 10.1109/TMAG.2012.2190518.
- [48] Z. Q. Zhu and D. Howe, “Instantaneous magnetic field distribution in brushless permanent magnet DC motors. II. Armature-reaction field,” *IEEE Trans. Magn.*, vol. 29, no. 1, pp. 136–142, 1993, doi: 10.1109/20.195558.
- [49] S. Steentjes, S. Boehmer, and K. Hameyer, “Permanent Magnet Eddy-Current Losses in 2-D FEM Simulations of Electrical Machines,” *IEEE Trans. Magn.*, vol. 51, no. 3, pp. 1–4, Mar. 2015, doi: 10.1109/TMAG.2014.2362551.
- [50] P. Zhang, G. Y. Sizov, J. He, D. M. Ionel, and N. A. O. Demerdash, “Calculation of Magnet Losses in Concentrated-Winding Permanent-Magnet Synchronous Machines Using a Computationally Efficient Finite-Element Method,” *IEEE Trans. Ind. Appl.*, vol. 49, no. 6, pp. 2524–2532, Nov. 2013, doi: 10.1109/TIA.2013.2264652.
- [51] R. Benlamine, F. Dubas, S.-A. Randi, D. Lhotellier, and C. Espanet, “3-D Numerical Hybrid Method for PM Eddy-Current Losses Calculation: Application to Axial-Flux PMSMs,” *IEEE Trans. Magn.*, vol. 51, no. 7, pp. 1–10, Jul. 2015, doi: 10.1109/TMAG.2015.2405053.
- [52] W. C. Young, R. G. Budynas, and A. M. Sadegh, *Roark’s formulas for stress and strain; 8th ed.* New York, NY: McGraw Hill, 2012.

General Conclusion

In this thesis, a review of axial flux machines was presented including a classification of axial flux machines based on the integration or not of magnets, covering machines like classical AFPM machines, flux-switching PM machines, Vernier PM machines, switched reluctance machines, induction machines and wound rotor machines with their corresponding advantages and drawbacks. Also, the review included a classification based on the number of stator and rotor disks (SSSR, DSSR, SSSR, and MSMR), recent advances in the design of these machines, the different materials used in their design (soft materials, hard materials, composite materials, insulating materials and ferromagnetic alloys) and the magnetic, thermal and mechanical problems that arise in these machines (skewing, lamination, end winding heat evacuation, insulation heat evacuation, demagnetization of magnets, mechanical loss, axial attraction force, centrifugal force and vibration). This allowed for a wise choice when designing the actual machine especially the choice of topology, the choice of magnets, the air gap and the winding topology.

The methods used in the design of the machine were an analytical method for the pre-sizing phase and a finite element method for the validation phase. Both methods were explained stating assumptions and solved equation for the analytical model, followed by the solution in the different regions of the machine for the magnetic vector potential, which was then used to determine the expressions of the normal and tangential components of the magnetic flux density followed by the expressions for the flux, the EMF and the electromagnetic torque. As analytical models are machine specific and has to be worked every time when the machine type changes, attention was turned to reluctance networks. Building on a previously available model at GREAH Laboratory, a generic mesh based generated reluctance network model was implemented in a MATLAB code where the possibility to consider iron non linearity and the excitation of coils were added. The method was tested on a double stator single rotor switched reluctance axial flux machine where error on torque and magnetic flux density as well as computation time were the key indicators of the method's performance. Testing of the method was achieved by first dividing the machine into several slices and simulating the each model as a separate entity and then aggregating the obtained results. Then the slices were linked with reluctances in the radial direction and the whole quasi-3D network was simulated. Results were compared with 3D FEA and showed a reduction of up to 22 times in computation time with an acceptable accuracy.

The lumped parameter thermal model used to study the thermal behavior of the machine was presented illustrating heat transfer mechanisms (conduction, convection and radiation) and the solved heat equation with the corresponding matrix system.

The finite elements method with its different formulations was explained. First, Maxwell's equations were presented, then the magnetic scalar and magnetic vector formulations used in magneto-static simulations were detailed. This was followed by the A-V and T- ϕ formulations used in magneto-dynamic simulation and their corresponding equations.

The finite elements approach used to model mechanical systems was also exposed. Both strong and weak formulations were presented with their corresponding equations that are used to compute the displacement in a body undergoing mechanical stress.

The machine design methodology was elaborated justifying the choice of the design parameters through a parametric study using the analytical model in linear BH curve

conditions and based on similar designs. After fixing the design parameters that satisfy the required specifications, machine performances were evaluated using a nonlinear simulation in 3D finite elements. These parameters being the electromagnetic torque and power, the EMF, the copper, iron and PM Eddy current losses and finally the machine efficiency. Also, the deflection of the rotor disk was assessed through a finite elements simulation using a commercial mechanical FE software. The adopted design was an axial flux permanent magnet synchronous machine having a mean torque of 150 N.m with a 2% ripple and a mean power of 30 kW. The machine is rated to spin at 2000 RPM and has an efficiency exceeding 95%. It also has good thermal behavior under load with temperature values not exceeding 95°C for magnets and 102°C for windings.

A prototype of the designed machine is currently being manufactured by ERNEO and is expected to be available in 2024. This prototype will be an opportunity to conduct tests on the real thing and verify the accuracy of computations done using the analytical model as well as the finite elements model. This machine can be subjected to tests like open circuit test, short circuit test, phase resistance measurement, load test, mean power and losses measurements, efficiency and voltage regulation measure. Also the implemented reluctance network model can be tested on machines with permanent magnets to test its ability to model these kinds of machines and also to put the claim that it is “generic” to the test. Another important thing that can be done in this context is that the implemented model can be extended to generate directly the full 3D reluctance network model from a 3D mesh, this can be very useful for modelling the end winding region as the absence of this aspect can greatly impact results.